

**WA Schools of Mines: Minerals, Energy and Chemical Engineering**

**Stress Corrosion Cracking of Stainless Steel 316L Additively  
Manufactured using Sinter-based and Laser-based Technologies**

**Ricardo Andres Santamaria Torres**

**0000-0002-0272-8121**

**This thesis is presented for the Degree of**

**Doctor of Philosophy**

**of**

**Curtin University**

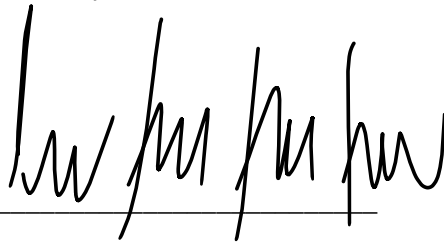
**August 2023**

## Declaration

To the best of my knowledge and belief, this thesis contains no material previously published by any other person except where due acknowledgment has been made.

This thesis contains no material which has been accepted for the award of any other degree or diploma in any university.

Signature:



Ricardo Andres Santamaria Torres

Date:

23 August 2023

## **Dedication**

This thesis is dedicated to my beloved wife Yurany, and my precious daughter Gaby, who have been my inspiration and driving force throughout this challenging journey. Without their infinite love, hugs, and smiles, I would not have reached this point. I also extend this dedication to my dear parents Ligia and Ricardo, and my dear sister Mary, who have always cheered me. I am truly grateful for their love and encouragement. Thank you.

## Abstract

Additive manufacturing (AM), also known as 3D printing, is a general term that includes the technologies used to fabricate objects with complex geometries from digital models by the successive addition of layers of material. Compared to traditional manufacturing, such as forming and subtractive processes, AM offers advantages in terms of supply chain complexity, quality, cost, speed, and design freedom. As a result, AM is increasingly being used in various industries, including biomedical, transportation, aerospace, and energy, to produce engineering-grade metals like copper, stainless steels, titanium, aluminium, and nickel-based alloys.

Austenitic stainless steel UNS S31603 (SS316L) is recognised for its high ductility, weldability, and good corrosion resistance in certain oxidising conditions. However, under tensile stress and exposure to halides, particularly chloride ions, SS316L can be prone to stress corrosion cracking (SCC). This type of environmentally assisted cracking (EAC) can affect SS316L when it is subjected to specific conditions above certain temperature and/or stress thresholds. SCC is either transgranular (TGSCC), or intergranular (IGSCC), and its direction of propagation is always normal to the tensile component. In TGSCC, the cracks propagate across the grains, usually in specific crystal planes with low indices such as {100}, {110}, and {210}. In IGSCC, chromium carbides precipitate along the grain boundaries of the steel, making it susceptible to intergranular corrosion. TGSCC is less common than IGSCC, but both may exist in the same system. There is significant interest in improving the properties and performance of SS316L produced with AM technologies. For instance, by using laser-based powder bed fusion (LPBF) which is known for producing SS316L with low porosity, good tensile properties, and high resistance to localised corrosion, albeit producing anisotropic microstructures with significant residual stresses due to the rapid melting and solidification of the printed layers. On the other hand, sinter-based material extrusion AM, which combines the low operating costs of fused deposition modelling (FDM) with the strengthening steps of powder metallurgy (PM) and metal injection moulding (MIM), is known for producing microstructures resembling the wrought SS316L in its annealed condition with some differences in porosity content and distribution.

This research aims to advance our understanding of SCC behaviour in 3D printed SS316L produced with sinter-based and laser-based AM methods. It addresses mechanical properties, resistance to localised corrosion, and establishes a correlation with the underlying structures at macro-, micro-, and nano-length scales. The conclusions from this research are expected to have an impactful contribution to the optimisation of printing strategies towards producing

more resistant alloys. In addition, the performance of 3D printed SS316L is compared with conventionally manufactured counterparts with the aim of developing more efficient, sustainable, and cost-effective solutions for the energy industry.

To achieve the proposed goal, test specimens of SS316L were additively manufactured with sinter-based material extrusion and LPBF methods. The 3D printed microstructures were characterised with advanced microanalysis techniques such as light optical microscopy (LOM), scanning electron microscopy (SEM), electron backscatter diffraction (EBSD), transmission electron microscopy (TEM), x-ray diffraction (XRD), and micro-computed tomography (micro-CT). The mechanical properties were determined through standardised tensile and microhardness tests. The SCC susceptibility was investigated using custom-designed C-ring specimens subjected to different levels of elastic stress while immersed in acidic chloride solutions at temperatures ranging from 30°C to boiling. Wrought SS316L specimens in cold-worked (CW) and solution-annealed (SA) conditions underwent identical testing and analysis for comparison.

The findings of this research work reveal that both sintered-based and LPBF-manufactured SS316L exhibit fully austenitic microstructures with elemental compositions meeting the standard requirements of UNS S31603. However, there are distinctive differences in the microscopy. For instance, the sinter-based SS316L produces equiaxed grains with an average size of 40  $\mu\text{m}$ , double that of its SA wrought counterpart. The relatively larger average grain size is attributed to the high temperature (1345 °C) and long dwell time (2 h) during the sintering step. These thermal conditions promote the formation of  $\Sigma 3$  twin boundaries, accounting for 53% of the total boundary length in the sintered SS316L, a higher content compared to SA wrought SS316L (46%). The sintering process also produces a weak, nearly random crystallographic texture ( $\times 1.26$  random in the  $\{111\}$  pole figure) in the 3D printed SS316L, attributable to the well-controlled heating and cooling rates (approx. 1.0 °C/min) of the thermal profile.

Nanoscale spherical non-metallic inclusions rich in Si-Mn-O (average size 20 nm), are present in the pre-alloyed SS316L powder feedstock. However, these inclusions undergo physical and chemical changes during sintering that increase their size of up to 70 times (final average size 1.4  $\mu\text{m}$ ). In addition, new irregularly shaped particles rich in Cr-Mn-O (average size 3.0  $\mu\text{m}$ ) are created after sintering. Moreover, the sinter-based AM process produces a combination of round and elongated pores, characteristic of PM/MIM and FDM technologies, respectively. This porosity accounts for a bulk porosity content of 5.21%. Results from this investigation reveal that porosity and non-metallic inclusions have a

significant impact on the localised corrosion resistance of the sintered SS316L by acting as favourable sites for pits to nucleate and grow, thus increasing its SCC susceptibility.

In contrast, the higher energy input and rapid solidification of the laser-based AM process yield SS316L with a notably low bulk porosity (0.74%), comparable to both its SA wrought (0.57%) and CW wrought (0.35%) counterparts. Microscopy analysis reveals the presence of columnar grains oriented along the printing direction with small cellular structures. Spherical inclusions rich in Si-Mn-O are also found in the as-printed LPBF SS316L, although there is no evidence of the irregularly shaped Cr-Mn-O particles. In addition, the LPBF-manufactured microstructures exhibit a stronger crystallographic texture ( $\times 2.32$  random in the  $\{111\}$  pole figure), similar to the SA wrought ( $\times 2.81$  random in the  $\{111\}$  pole figure) and CW wrought ( $\times 2.27$  random in the  $\{111\}$  pole figure) SS316L specimens. However, unlike its sinter-based counterpart, no twin boundaries are evident in the LPBF-manufactured SS316L due to the hindering effect of the rapid solidification rates, which have been reported to be in the range of  $10^3$  to  $10^7$  K/min. Moreover, the thermal cycle of the laser-based AM induce significant residual stresses in the as-printed microstructure of the SS316L, accelerating the crack initiation and, consequently, increasing the SCC susceptibility of the 3D printed specimens.

As expected, the distinctive microstructures of both 3D printed materials influence their tensile properties. For instance, the relatively large grains in the sinter-based SS316L are responsible for its reduced yield strength (167 MPa), which is below the minimum required for the standard UNS S31603 (170 MPa). However, its tensile strength (524 MPa) is within acceptable range (minimum 485 MPa). The extraordinary 96% ductility of the sinter-based alloy, higher than the 88% of its SA wrought counterpart, is attributed, in part, to the higher content of  $\Sigma 3$  twin boundaries, a correlation that has been reported elsewhere<sup>1-4</sup>. Moreover, the ductile fracture in pure tension of the sinter-based tensile specimens is attributed to the Si-Mn-O inclusions, which act as sites where voids simultaneously nucleate and coalesce into a single crack. The fracture surfaces show no evidence of secondary cracks or elongated dimples which are indicative of shear fracture. In contrast, the columnar grains, small cellular structures, high thermal residual stresses, and the absence of twin boundaries in LPBF-manufactured SS316L, contribute to its outstanding yield strength (529 MPa) and tensile strength (656 MPa), and reduced ductility (43%), mirroring the behaviour of its CW wrought counterpart (646 MPa yield strength, 717 MPa tensile strength, and 49% ductility). The porosity content and distribution, and their effect on the mechanical properties of 3D printed alloys is still debatable and will require further investigation.

The SCC susceptibility of both 3D printed SS316L is also distinctly different. For instance, in the sintered SS316L, the round porosity and oxide inclusions weaken the passive layer, thus increasing the number of sites for pit nucleation and growth. These pits grow further in length and depth during the immersion tests, which, in combination with the applied stress and high temperatures of the acidic chloride solution, lead to higher SCC susceptibility. Nevertheless, the elongated porosity and almost random crystallographic orientation of the grains act as barriers to the propagation of secondary cracks, thus reducing the crack-branching effect. On the other hand, LPBF-manufactured SS316L exhibits distinct results. For instance, the specimens show an extremely high susceptibility to SCC near the printed holes of the C-rings, with cracking occurring in both stressed and unstressed specimens when immersed in boiling solution. This behaviour is attributed to the distribution of thermal residual stresses near the printed holes caused by the printed supports, which create two highly stressed sites located perpendicular to the ends of these supports. Moreover, the cracking morphology changes after the residual stresses are reduced through stress-relieved heat treatment, although the crack location remains unchanged. However, by isolating the C-ring's printed holes from the solution through partial immersion testing, i.e., keeping them above the solution line, the cracks initiate from pits located on the upmost curved surface of the C-ring, where the maximum stress is applied. These results highlight the significance of considering printing parameters for complex geometries, as they can significantly impact the performance of the component.

Overall, this thesis provides comparative insights on the printing variables, defects, microstructures and mechanical/corrosion properties of SS316L printed with sinter-based and laser-based methods. The findings of this thesis will contribute to optimising the printing strategies and design aspects for producing of more corrosion resistant alloys with superior performance compared to the widely used wrought counterparts.

## Acknowledgements

I would like to extend my gratitude to my primary supervisor, Dr. Md Zakaria Quadir, for his guidance, knowledge, and contributions to this research. I am also deeply thankful to my co-supervisors, Dr. Ke Wang, Dr. Mariano Iannuzzi, Dr. Garry Leadbeater, and Dr. Mobin Salasi, for their guidance, motivation, and feedback throughout this project.

I am equally appreciative of Dr. Sam Bakhtiari and Dr. Thaneshan Sapanathan for their continuous advice and expertise during the project. Special thanks to Emeritus Professor Brian Kinsella for his enduring support not only to me but also to the entire Curtin Corrosion Centre team. His guidance, motivation, and encouragement have been invaluable during the time I met him as a student.

I want to acknowledge the Curtin Corrosion Centre for providing the resources essential for executing this project. My gratitude also extends to the Microscopy and Microanalysis Facility (MMF) and the Microfactory for Additive Manufacturing at the John de Laeter Centre (JDLC) for allowing me to use their research facilities.

I am immensely grateful to Woodside Energy Ltd., especially Mike Brameld, for recognizing the value of academia-industry interaction and sponsoring this research. Additionally, I want to thank Woodside Energy Ltd. for the two internships in which I participated, where I had the opportunity to learn and contribute my knowledge.

My heartfelt thanks to my colleagues at the Curtin Corrosion Centre, including Louis (Yu) Long, Marisa Yookhong, Ammar Al Helal, Darwin Hartono, Edgar Hornus, Francisco Vouilloz, Alex Liso, and Sheila Omar. I would also like to express my appreciation to my friends Mayra Gualteros, Juan Camilo Diaz, Esteban Rodoni, Erika Suarez, Silvia Chaparro, Lina Silva, Sofia Hazarabedian, Abraham Rojas, and Alex Kovacs for their support during this journey.

Lastly, I am deeply indebted to my wife and my daughter for their unwavering patience, unconditional love, and continuous support throughout my PhD studies. I am eternally grateful to my parents and sister for accompanying, encouraging, and praying for me from afar all these years. Without all of you, I could not have completed this work.



## **Acknowledgement of Country**

*We acknowledge that Curtin University works across hundreds of traditional lands and custodial groups in Australia, and with First Nations people around the globe. We wish to pay our deepest respects to their ancestors and members of their communities, past, present, and to their emerging leaders. Our passion and commitment to work with all Australians and peoples from across the world, including our First Nations peoples are at the core of the work we do, reflective of our institutions' values and commitment to our role as leaders in the Reconciliation space in Australia.*

# List of publications

## Journal articles

Santamaria R, Salasi M, Bakhtiari S, Leadbeater G, Iannuzzi M, Quadir MZ. Microstructure and mechanical behaviour of 316L stainless steel produced using sinter-based extrusion additive manufacturing. *Journal of Materials Science*. 2022 Jun 1:1-7

<https://doi.org/10.1007/s10853-021-06828-8>

Santamaria R, Salasi M, Rickard WD, Pojtanabuntoeng K, Leadbeater G, Iannuzzi M, Reddy SM, Quadir MZ. Crystallographic Texture and Substructural Phenomena in 316 Stainless Steel Printed by Selective Laser Melting. *Materials*. 2023 Jun 9;16(12):4289.

<https://doi.org/10.3390/ma16124289>

Santamaria R, Wang K, Salasi M, Iannuzzi M, Mendoza MY, Quadir MZ. Stress Corrosion Cracking of 316L Stainless Steel Additively Manufactured with Sinter-Based Material Extrusion. *Materials*. 2023 May 26;16(11):4006. <https://doi.org/10.3390/ma16114006>

Santamaria R, Wang K, Salasi M, Salem M, Lours P, Iannuzzi M, Quadir MZ. Stress corrosion cracking behavior of austenitic stainless steel 316L produced using laser-based powder bed fusion. *Corrosion*. 2023;4311. <https://doi.org/10.5006/4311>

## Statement of contribution by others

I, Ricardo Andres Santamaria Torres, as the first author of the publications included in this thesis, was primarily responsible for conceptualizing, planning, and conducting the experimental tests, analysing and interpreting the data, and preparing the manuscript. The contributions of the co-authors are summarised below, and their written statements can be found in Appendix 1.

- Mobin Salasi, Mariano Iannuzzi, Garry Leadbeater, and Md Zakaria Quadir made significant contributions to the investigation by providing input in research conception, supervision, manuscript review, and expertise in additive manufacturing, material science, corrosion science, metallurgy, and microanalysis.
- Sam Bakhtiari contributed with his background knowledge in materials and microstructure analysis, reviewed Chapter 2, and assisted in conducting the micro-computed tomography (micro-CT) in Chapter 4.
- Michael Y. Mendoza provided expertise in additive manufacturing, microstructure analysis, reviewed Chapter 4, and offered valuable insights.
- Ke Wang contributed with his expertise in additive manufacturing and corrosion science and engineering, reviewed Chapter 4 and Chapter 5, and provided overall valuable input to the investigation.
- Mehdi Salem and Philippe Lours from IMT Mines (France) supplied the 3D printed SS316L test specimens used in Chapter 5 and provided supervision.
- William Rickard, Kod Pojtanabuntoeng, and Steven Reddy provided their expertise in materials science and corrosion, as well as supervision and review of Chapter 3.

All mechanical testing, immersion experiments for stress corrosion cracking susceptibility, and sample preparation for microanalysis were carried out at the Corrosion Centre of Curtin University. Electron microscopy studies were conducted at the John de Laeter Centre (JDLC), Curtin University. The micro-CT scans were performed at the Centre for Microscopy, Characterization, and Analysis (CMCA), University of Western Australia. The sinter-based 3D printed SS316L used in Chapters 2 and 4 was fabricated at the Microfactory for Additive Manufacturing in JDLC, while the laser-based SS316L was produced in IMT Mines (France). Financial support for this research was provided by the Chevron and Woodside Chair in Corrosion, Curtin International Postgraduate Research Scholarship, and the Curtin University – Colombian Institute of Education (ICETEX) scholarship (11093).

## Table of contents

Declaration .....	i
Dedication .....	ii
Abstract .....	iii
Acknowledgements .....	vii
Acknowledgement of Country .....	viii
List of publications.....	ix
Statement of contribution by others .....	x
List of abbreviations.....	xiv
List of figures .....	xv
List of tables.....	xix
Chapter 1: Introduction .....	1
1.1 Aim and objectives .....	7
1.2 Significance of the research.....	7
1.3 Thesis overview and structure .....	7
Chapter 2: Sinter-based material extrusion of SS316L: Microstructures and tensile properties.....	11
Microstructure and mechanical behaviour of 316L stainless steel produced using sinter-based extrusion additive manufacturing.....	12
2.1 Abstract .....	12
2.2 Introduction .....	12
2.3 Experimental Procedure .....	14
2.3.1 Manufacturing technology .....	14
2.3.2 Sample manufacture .....	14
2.3.3 Microscopy sample preparation.....	15
2.3.4 Microstructure investigation .....	16
2.3.5 Tensile properties.....	17
2.4 Results .....	18
2.4.1 Microstructures and analysis .....	18
2.4.2 Tensile properties.....	23
2.5 Discussion .....	26
2.5.1 Influence of sintering on the microstructure.....	26
2.5.2 Influence of sintering on the mechanical properties.....	27
2.5.3 Influence of sintering on the fracture mode.....	28
2.6 Conclusions .....	30

Chapter 3: Laser-based powder bed fusion of SS316L: Microstructures and Crystallographic Texture.....	32
Crystallographic Texture and Substructural Phenomena in 316 Stainless Steel Printed by Selective Laser Melting .....	33
3.1 Abstract .....	33
3.2 Introduction .....	33
3.3 Materials and Methods .....	35
3.4 Results and Discussion .....	36
3.4.1 Structural Symmetry and Crystallographic Texture .....	36
3.4.2 Substructural Features.....	39
3.4.3 Solution treatment structures .....	43
3.5 Conclusions .....	46
Chapter 4: Sinter-based material extrusion of SS316L: Stress corrosion cracking susceptibility and crack-branching behaviour.....	48
Stress Corrosion Cracking of 316L Stainless Steel Additively Manufactured with Sinter-Based Material Extrusion .....	49
4.1 Abstract .....	49
4.2 Introduction .....	49
4.3 Materials and Methods .....	51
4.3.1 Materials .....	51
4.3.2 Analytical Characterization .....	52
4.3.3 Mechanical Testing.....	53
4.3.4 SCC Susceptibility and Crack-branching .....	54
4.4 Results .....	56
4.4.1 Analytical Characterization .....	56
4.4.2 Mechanical Testing.....	59
4.4.3 Pitting and Cracking Susceptibility .....	60
4.4.4 Crack-Branching Susceptibility.....	62
4.5 Discussion .....	64
4.5.1 Susceptibility to SCC Initiation: Pit-to-Crack Transition.....	65
4.5.2 Crack-Branching.....	66
4.6 Conclusions .....	66
Chapter 5: Laser-based powder bed fusion of SS316L: Stress Corrosion Cracking and the Effect of Residual Stresses .....	68
Stress Corrosion Cracking Behaviour of Austenitic Stainless Steel 316L Produced Using Laser-based Powder Bed Fusion.....	69
5.1 Abstract .....	69

5.2 Introduction .....	69
5.3 Experimental Procedures.....	71
5.3.1 Materials .....	71
5.3.2 Microstructure characterization .....	72
5.3.3 Mechanical properties.....	73
5.3.4 Stress corrosion cracking .....	74
5.4 Results .....	77
5.4.1 Microstructure characterization .....	77
5.4.2 Mechanical properties.....	79
5.4.3 Stress corrosion cracking .....	80
5.5 Discussion .....	86
5.6 Conclusions .....	88
Chapter 6: Summary, main conclusions and future research.....	89
6.1 Summary .....	89
6.2 Main conclusions.....	94
6.3 Study limitations.....	96
6.4 Future research .....	96
Chapter 7: References .....	98
Appendix 1: Written statements from co-authors of the publications .....	115
Appendix 2: Copyrights statements .....	120
Appendix 3: Original reprint of the publication included in Chapter 2 .....	128
Appendix 4: Original reprint of the publication included in Chapter 3 .....	146
Appendix 5: Original reprint of the publication included in Chapter 4 .....	162
Appendix 6: Original reprint of the publication included in Chapter 5 .....	181

## List of abbreviations

AM	Additive manufacturing
AYS	Actual yield strength
BMD	Bound metal deposition
BS	Backscatter
CD	Cold-drawn
CMT	Cold metal transfer
CW	Cold-worked
CT	Computer tomography
DED	Direct energy deposition
EAC	Environmentally assisted cracking
EBSD	Electron backscatter diffraction
EB-PBF	Electron beam powder bed fusion
EDS	Energy-dispersive X-ray spectroscopy
FE	Field emission
FIB	Focused-ion beam
KAM	Kernel average misorientation
LOM	Light optical microscopy
LPBF	laser powder bed fusion
PBF	Powder bed fusion
SA	Solution-annealed
SCC	Stress corrosion cracking
SEM	Scanning electron microscopy
SLM	Selective laser melting
SS	Stainless steel
TEM	Transmission electron microscopy
WAAM	Wire arc additive manufacturing
XRD	X-ray powder diffraction

## List of figures

Figure 1-1: Common representation of the necessary condition for SCC

Figure 1- 2: Thesis structure

Figure 2-1: a) Test specimen, 3D printing strategy, and b) thermal profile used for sintering

Figure 2-2: FE-SEM image of the feedstock showing the SS316L powder with a particle size distribution of d50 1.4  $\mu\text{m}$  and d90 5.0  $\mu\text{m}$

Figure 2-3: TEM image and corresponding EDS map of a SS316L particle showing a spherical inclusion rich in Si, Mn and O content found in the SS316L precursor powder

Figure 2-4: XRD spectra of SS316L powder showing an  $\gamma$  (FCC) austenite phase with a small presence of retained  $\delta$  (BCC) ferrite (top), SS316L sintered sample (XY plane) showing a fully  $\gamma$  (FCC) austenite phase (middle), and SS316L wrought also showing a fully  $\gamma$  (FCC) (bottom)

Figure 2-5: SEM images showing large recrystallised microstructures in the a) SS316L wrought, and b) sintered samples, with the later showing distributed porosity, inclusions and twin interfaces

Figure 2-6: Micro-CT scans of a SS316L sintered sample showing the presence of elongated macroporosity, a) as a 3D mesh-like pattern at the bulk volume, b) as a layer-by-layer pattern at the contour shell, and c) as a layer-by-layer pattern skewed  $45^\circ$  in the XY plane at the bulk

Figure 2-7: SEM image of a SS316L sintered sample and corresponding EDS elemental maps showing the distribution of Si-Mn-O-rich spherical and Cr-Mn-O-rich irregular inclusions

Figure 2-8: EBSD measured inverse pole figure maps of the (a) SS316L sintered and (b) SS316L wrought sample with corresponding  $\{111\}$  pole figures

Figure 2-9: Engineering stress-strain curves of both sintered and wrought SS316L materials along with the dimensions of the test specimens

Figure 2-10: SEM images of the tensile fractured surfaces in the a) SS316L wrought and b) sintered specimen showing their microscopy features

Figure 2-11: SEM image of a SS316L sintered fractured specimen and corresponding EDS elemental map showing a Si-Mn-O inclusion inside a spherical dimple



Figure 2-12: Photographic image of both fractured SS316L sintered tensile specimen (top) and SS316L wrought specimen (bottom) showing two types of necked regions

Figure 3-1: EBSD-measured color-coded IPF map of the as-printed SLM sample, taken from the transverse direction (TD), showing the orientation along the (a) BD and (b) SD. The insets in Figure 1a show the optical microscopy image and the EBSD cross-section

Figure 3-2: Higher-resolution EBSD maps of the as-printed SLM sample showing (a) color-coded IPF map of SD to illustrate the inhomogeneities in the high ( $>15^\circ$ ) and low-angle ( $3\text{--}15^\circ$ ) boundary distribution and their alignments with the SD and (b) the corresponding inhomogeneities in the KAM plot

Figure 3-3: HAADF STEM images showing (a) particle decorations in the dislocation-constituted boundaries of the commonly found fine cell structures (in the inset) in the SLM-printed sample. (b) Particle pinning at the dislocation boundary in a higher-magnification HAADF STEM image of the white rectangular area located in subfigure (a). (c) BF STEM image showing the strain field width of the dislocation boundaries at the boundaries edge on tilted condition

Figure 3-4: HAADF STEM image (top) of the nanoparticles and corresponding EDS-measured elemental maps (bottom) of the white rectangular area, showing that the particles are rich in Si, Mn and O content in the as-printed SLM sample

Figure 3-5: EBSD-measured high-resolution KAM map showing the differences in the stored energy distribution between the (a) as-printed and (b) solution-treated SLM samples in the BD-SD cross-section. TEM investigation of the solution-treated sample shows (c) the changes in the dislocation boundary structures in a BF STEM image and (d) the retention of boundaries by particle pinning in a magnified HAADF STEM image of the rectangular area marked in subfigure (c)

Figure 3-6: The structural and chemical heterogeneity of inclusions in the solution-treated SLM-printed sample is shown in (a) the HAADF STEM image, and (b–e) the corresponding elemental mapping for Si, Mn, O, and Cr, respectively. The insets in (a) show the inclusion from which the TEM sample was prepared, and the indexed SAD pattern of  $\text{Cr}_3\text{O}_4$  from the SAD-labelled area

Figure 4-1: Drawings of the specimens used for tensile testing BMD SS316L and CD wrought SS316L (top), and SA wrought SS316L with snug-fitting metallic plugs (bottom).

Figure 4-2: Drawings of the C-ring type specimen used to investigate the SCC susceptibility in the BMD SS316L and its wrought SS316L counterparts. Units in millimetres

Figure 4-3: Schematics of the constant-strain setup used to stress the C-rings under different levels of AYS. The circumferential strain gauge is located at the uppermost curved surface of the C-ring

Figure 4-4: Representative XRD patterns of BMD SS316L, SA wrought SS316L, and CD SS316L showing predominance of the  $\gamma$ -austenitic with small fractions of  $\delta$ -ferrite

Figure 4-5: Representative EDS elemental map of (a) BMD SS316L showing inclusions rich in O, Si, Mn, and Cr, (b) SA wrought SS316L showing slight presence of round pores and lack of non-metallic inclusions, and (c) CD wrought SS316L showing elongated MnS inclusions

Figure 4-6: Representative EBSD maps with corresponding  $\{111\}$  pole figures, with respect to the build direction (Y-axis), of (a) BMD SS316L, (b) SA wrought SS316L, and (c) CD wrought SS316L C-rings taken from their uppermost curved surfaces

Figure 4-7: Representative KAM maps, with respect to the build direction (Y-axis), with a maximum misorientation angle of  $5^\circ$  in (a) BMD SS316L, (b) SA wrought SS316L, and (c) CD wrought SS316 C-rings taken from their uppermost curved surfaces

Figure 4-8: Stress–strain curves within the elastic region of BMD SS316L, SA wrought SS316L, and CD wrought SS316L showing their corresponding 60% and 90% AYS

Figure 4-9: Pitting and cracking susceptibility map of BMD SS316L and its wrought SS316L counterparts at different test conditions over a period of six weeks

Figure 4-10: LOM images of unstressed C-rings after one week in boiling solution, showing different sizes of corrosion pits in (a) BMD SS316L, (b) SA wrought SS316L, and (c) CD wrought SS316L. The top images correspond to the C-rings' flat surfaces, while the curved ones are presented at the bottom

Figure 4-11: LOM images of etched microstructures in (a) BMD SS316L, (b) SA wrought SS316L, and (c) CD wrought SS316L C-rings after exposure to boiling solution, showing SCC initiated from pits and propagated perpendicular to the applied stress of 90% AYS

Figure 4-12: Representative (a) EBSD map, (b) KAM map, and (c) phase map with overlaid band contrast of BMD SS316L, showing transgranular cracking, twin boundaries, oxide inclusions, round porosity, and area of  $\delta$ -ferrite

Figure 4-13: Photographic and SEM image of the curved surface of a BMD SS316L C-ring after exposure to boiling solution under 90% AYS, showing SCC crossing perpendicular to the elongated porosity

Figure 5-1: Geometry of the rectangular specimens used for the tensile tests a) LPBF-manufactured SS316L, and b) machined CD wrought SS316L. The extrusion direction of the rod bar is in the X axis. Units in millimetres

Figure 5-2: a) Geometry of the custom C-ring specimen used to investigate the SCC susceptibility of LPBF and CD wrought SS316L, and b) schematics of the constant-strain assembly according to ASTM G38

Figure 5-3: Schematic of the partial immersion test applied to the as-printed LPBF SS316L C-ring

Figure 5-4: XRD patterns of LPBF and CD wrought SS316L showing the presence of  $\gamma$  (FCC) austenite as the only phase in their microstructures

Figure 5-5: EBSD maps and color-coded inverse pole figures of untested C-rings showing textured microstructures in the a) as-printed LPBF SS316L perpendicular to its printing direction, and b) CD wrought SS316L

Figure 5-6: Engineering stress-strain curves within the elastic region of a) LPBF SS316L and b) CD wrought SS316L along with the location of their corresponding AYS

Figure 5-7: Photographs of as-printed LPBF SS316L C-rings fully immersed in boiling solution showing similar SCC morphologies under a) unstressed (0% AYS), and b) stressed (90% AYS) conditions. The red arrows indicate the location of the hole/support interfaces

Figure 5-8: Photographs of LPBF SS316L C-rings with a) as-printed holes and b) polished holes, showing similar SCC that initiated from pits near their printed holes in the unstressed (0% AYS) and stressed (90% AYS) conditions, respectively

Figure 5-9: Band contrast image and corresponding EBSD map of SCC in as-printed unstressed (0% AYS) LPBF SS316L specimens after full immersion in boiling solution showing transgranular cracking

Figure 5-10: KAM maps of untested LPBF SS316L C-rings in their a) as-printed, and b) stress-relieved conditions. The KAM histogram in c) shows the redistribution of local misorientations after the stress relief process

Figure 5-11: Photographs of an unstressed (0% AYS) stress-relieved LPBF SS316L C-ring after full immersion in boiling solution showing identical SCC morphology and crack location as its as-printed counterparts

Figure 5-12: As-printed LPBF SS316L C-ring stressed at 90% AYS showing a) its partial immersion setup, b) SCC located at the middle of its uppermost curved surface, and c) an etched imaged showing the resulting transgranular SCC morphology

Figure 5-13: CD wrought SS316L 90% C-ring showing a) full immersion setup, b) photograph illustrating SCC that started from the edge of the uppermost curved surface, and c) a micrograph showing the resulting transgranular SCC morphology

Figure 5-14: Hypothesized: a) residual stresses produced in the hole/support interface of the C-rings, b) unstressed C-ring with SCC initiating from corrosion pits at the 3 and 9 O'clock sites, and c) "stress relieving" effect of the applied load over the residual stresses

## List of tables

Table 1-1: Key studies on the correlation between printing variables and properties/performance of SS316L produced using different AM technologies

Table 2-1: Quantitative EDS chemical composition of SS316L powder, SS316L wrought and nominal UNS S31603

Table 2-2: Grain size measurements of SS316L sintered and SS316L wrought samples

Table 2-3: Mechanical properties of the SS316L sintered and SS316L wrought samples

Table 2-4: Summary of mechanical properties, powder size, grain size and final porosity of SS316L manufactured by Metal FFF, PBF, DED, MIM, PM and standard requirements for UNS S31603 and MIM-316L grade

Table 4-1: Summary of parameters used to manufacture all BMD SS316L test specimens

Table 4-2: Elemental composition in wt% of BMD SS316L, SA wrought SS316L, CD wrought SS316L, and nominal composition of UNS S31603

Table 4-3: Content of non-metallic inclusions,  $\delta$ -ferrite (BCC) phase, and grain size measurements of BMD SS316L, SA wrought SS316L, and CD wrought SS316L

Table 4-4: Average mechanical properties of BMD SS316L and its wrought counterparts

Table 4-5: Average pit size and pit depth measurements made on stressed and unstressed BMD SS316L C-rings and wrought counterparts

Table 5-1: Elemental composition of the pre-alloyed SS316L powder, LPBF-manufactured SS316L, CD wrought SS316L, and nominal composition of UNS S31603

Mechanical properties of as-printed LPBF SS316L, CD wrought SS316L, and standard requirements for UNS S31603

Table 5-3: SCC behaviour of LPBF SS316L and CD wrought SS316L C-rings tested at different conditions in acidified chloride boiling solution. The number in the cells corresponded to the week when the cracks were observed. Ndash correspond to untested conditions

## Chapter 1: Introduction

Stress corrosion cracking (SCC) is considered one of the most aggressive manifestations of corrosion, and it represents a prominent form of environmentally assisted cracking (EAC) <sup>5</sup>. This type of failure occurs when the susceptible materials are subjected to specific environments that exceed certain tensile stress thresholds <sup>6-8</sup>. Figure 1-1 provides a common representation of the conditions necessary for SCC, namely: susceptible material, suitable environment, and tensile stress. In a sequence of events, cracks frequently initiate from localised corrosion, leading to SCC when the operating conditions surpass the critical temperature for pitting corrosion <sup>6, 9-12</sup>.

SCC poses a significant challenge to the integrity of assets within the oil and gas industry sector, with an estimated annual cost of £1.372 billion <sup>13</sup>. It particularly impacts buried pipelines <sup>5, 14-16</sup>, and occasionally leads to sudden catastrophic failures <sup>17-21</sup>. However, despite extensive research efforts to explain the mechanism involved in SCC <sup>7, 22-25</sup>, a comprehensive understanding still remains unresolved. Consequently, relying solely on knowledge-based material selection tailored to specific applications proves challenging.

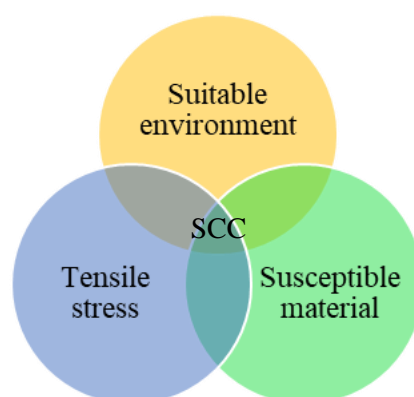


Figure 1-1: Common representation of the necessary condition for SCC

The risk of SCC can potentially be managed through strategies such as increasing the material's protection (via surface treatment, coating, cathodic protection, etc.), reducing the environmental severity, or modifying the operating conditions <sup>26-29</sup>. However, implementing these measurements can often be impractical. Therefore, one notable approach is to utilise materials less susceptible to SCC. This can be achieved through material development or process optimisation, leading to more resistant alloy versions. Regardless of the approach, a thorough understanding of the material's susceptibility to SCC under specific operating conditions remains imperative. Since SCC occurs in components exposed to corrosive surroundings while subjected to tensile stresses exceeding their resistance thresholds <sup>6, 9-12</sup>,

the critical aspect to comprehend is how these two conditions interact to influence the material, shedding light on the SCC mechanism within the given application environment.

Numerous studies have looked into the link between the SCC of different alloys, their microstructures, and mechanical properties with the objective of better understanding this damage mechanism<sup>30-37</sup>. For instance, Y. Hou et al.<sup>30</sup> explored the artificial aging of high-strength 7A99 Al alloy (AA) and found that the increased SCC resistance in over-aged alloys was due to coarse, discontinuous grain boundary precipitates (GBPs) and wide precipitate-free zones, which enhanced mechanical properties and hindered active corrosion paths. Similarly, Huang et al.<sup>31</sup> studied the SCC of Al-Zn-Mg-Zr alloy and found a clear connection between aging treatment, mechanical properties, microstructures, and SSC susceptibility. Other researchers, such as P.B. Srinivasan et al.<sup>32</sup> and H. Jia et al.<sup>33</sup> discovered that the presence of precipitates increased the SCC resistance in AA2219 friction stir weldment and a novel Mg-6Zn-1Y-0.5Cu-0.5Zr alloy, respectively. D.P. Braga et al.<sup>34</sup> reported that equal-channel angular pressing (ECAP), which enhances AA's mechanical properties through intense grain refinement, led to improved mechanical properties and SCC resistance. However, no general relationship between grain size and SCC resistance was established, as microstructural heterogeneities often impact localised corrosion susceptibility in various ways. However, T.C. Tsai and T.H. Chuang<sup>38</sup> found a clear link between grain refinement, microstructure, and SCC susceptibility in AA7475. They determined that a more homogeneous slip mode and smaller GBP sizes led to reduced SCC susceptibility. Nevertheless, SCC resistance could not be enhanced through grain refinement for superplastic AA7475 with GBPs smaller than a critical size. L. Huang et al.<sup>39</sup> studied the effects of grain size on AZ80 magnesium alloy friction-stir processing and concluded that grain refinement increased stress corrosion resistance in 3.5 wt% NaCl solution for mainly three reasons: improved interfacial cohesive force, increased nucleation resistance for stress corrosion cracks, and enhanced growth resistance for such cracks. Lastly, Z. Li et al.<sup>40</sup> studied annealed AA5083 and concluded that samples with a dominant brass texture showed greater SCC resistance than those with weaker textures. Additionally, SCC in the brass-dominant samples followed a more convoluted path. Consequently, cracks were deflected at brass texture grains, which was ascribed to the combined effects of the relatively large twist angle between grain boundaries of brass grains and adjacent grains, as well as the low grain boundary energy configuration of {011} oriented grains.

Consequently, alloys with well-documented mechanical performance and resistance to pitting corrosion, such as UNS S31603 (SS316L), are commonly employed<sup>41-45</sup>, although this alloy is also susceptible to SCC when it is subjected to stress in the presence of chloride

ions at elevated temperatures <sup>7, 9, 46-49</sup>. Therefore, enhancing the material's performance becomes an appealing option via optimising the fabrication process or through post-processing stages. For example, M. Yasir et al. <sup>50</sup> observed a reduction in SCC susceptibility and crack density of SS316L by improving the material's surface quality through end-milling. T. Ming et al. <sup>51</sup> enhanced the SCC resistance of SS316L by introducing high-level residual compressive stresses and forming a nano-sized deformation layer through water jet cavitation peening (WJP). A.B. Rhouma et al., achieved similar outcomes using shot blasting and wire brushing <sup>52</sup>, whereas B. Krawczyk et al., achieved them through aqua blasting <sup>53</sup>. D.N. Wasnik et al. reported a reduction of the intergranular SCC achieved by randomisation of grain boundaries via sensitisation heat treatment <sup>54</sup>. L. Zhang, and J. Wang, concluded that SCC crack growth rates in cold-worked SS316L decreased by reducing the dissolved oxygen content in the simulated pressurised water reactor (PWR) primary water environment <sup>55</sup>. L. Vehovar et al, reported a significant increase in the resistance to SCC in nitrogen-alloyed stainless steels, attributed in part to the rise of local pH at the interface between the passive film and the electrolyte caused by NH<sub>4</sub><sup>+</sup> ions. In summary, there have been numerous approaches involving post-processing of the material to reduce its susceptibility to SCC.

While the aforementioned approaches have yielded some improvements, practical limitations remain in achieving substantial changes with conventionally manufactured SS316L. Therefore, attention has turned towards alternative manufacturing methods, notably additive manufacturing (AM) technologies. To provide a general definition of AM, it is a collection of methods that involve the transformation of digital data into physical objects through the successive addition of material layer by layer <sup>56-58</sup>. Regardless of the feedstock nature or binding mechanism, current AM technologies are classified into seven basic categories: i) Binder Jetting, ii) Direct Energy Deposition (DED), iii) Material Extrusion, iv) Material Jetting, v) Powder Bed Fusion (PBF), vi) Sheet Lamination, and vii) Photopolymerisation <sup>57-59</sup>. The general advantages of AM include the reduction of operational costs, enhanced productivity, and the ability to produce complex designs <sup>58, 60, 61</sup>. Moreover, AM offers a streamlined optimisation of manufacturing parameters, thus reducing the time needed for iterative optimisation and the development of improved properties and performance through tailored microstructures <sup>62-67</sup>.

One of the most popular AM technologies for producing SS316L is laser powder bed fusion (LPBF) <sup>68-70</sup>. This technology is used to fabricate near-net shape SS316L components through the consecutive melting and solidification of layers of pre-alloyed loose powder <sup>58, 59, 71-73</sup>. The cyclic manufacturing process involves a high-intensity laser energy input, followed by a near-instant solidification (approximately 10<sup>3</sup> K/s to 10<sup>7</sup> K/s <sup>72, 73</sup>). LPBF is capable of



yielding SS316L engineering-grade components with high tensile properties<sup>74-76</sup>, minimal porosity<sup>74, 75, 76</sup>, and reasonably good resistance to pitting corrosion<sup>77-79</sup>. However, LPBF-manufactured materials have two major drawbacks: i) components exhibit anisotropic microstructures oriented in the build direction<sup>80-82</sup>, and ii) they contain significant residual stresses<sup>75, 83, 84</sup>.

In contrast, a less common AM technology is sinter-based material extrusion, which combines the extrusion approach of fused deposition modelling (FDM) with the strengthening steps of high-temperature sintering of powder compacted components, such as powder metallurgy (PM) and metal injection moulding (MIM)<sup>58, 60, 85-89</sup>. The well-controlled and steady sintering and gradual cooling steps of this technology produce SS316L components that exhibit relatively lower yield strength<sup>86, 89, 90</sup>, and high bulk porosity<sup>86, 88, 91, 92</sup>, that might limit their resistance to localised corrosion<sup>92</sup>. However, this process yields isotropic microstructures characterised by large equiaxed grains and twin boundaries<sup>89, 92-94</sup>, which can accommodate more elongation before fracture<sup>95, 96</sup>, potentially increasing the material's toughness<sup>97-99</sup>. Consequently, these laser-based and sinter-based technologies have gathered attention for their potential to enhance mechanical properties, reduce susceptibility to pitting corrosion, and, ultimately, increase resistance to SCC through the optimisation of the process parameters.

It is pertinent to note that, despite significant research into 3D printing of SS316L using various methods, there is still a need for a holistic investigation that correlates the printing variables with the material's properties and performance. This is because many elements of this knowledge are interconnected, representing a critical knowledge gap. An effort has been made to summarise the literature in tabular form, Table 1-1, illustrating the extensive research studies on localised corrosion and mechanical properties in connection with the material microscopy. However, when it comes to SCC, there are only a handful of available investigations. Furthermore, these investigations have been primarily carried out on SS316L fabricated through PBF methods, such as laser PBF (LPBF) and electron-beam PBF (EB-PBF), as well as DED and its variations, including cold metal transfer (CMT) and wire-arc AM (WAAM). However, there is minimal literature on sinter-based methods. Therefore, Table 1-1 places this thesis within the context of these other research studies, demonstrating a more comprehensive approach to addressing the aforementioned knowledge gap.

In summary, SCC poses a substantial risk to the integrity of SS316L alloy-made components. The solution to this challenge is widely agreed to be the development of new materials or the implementation of novel manufacturing processes that result in unique

microstructures, enabling the material to better withstand environments susceptible to SCC. Recent advancements in 3D metal printing technologies, particularly LPBF and sinter-based material extrusion, are considered promising pathways for enhancing the material's properties and performance. This research aims to investigate the influence of AM process parameters on printed microstructures to develop improved alloys capable of resisting SCC.

Table 1-1: Key studies on the correlation between printing variables and properties/performance of SS316L produced using different AM technologies

Reference	Investigated the correlation among printing variables and				AM method	
	Microstructures	Mechanical properties	Localised corrosion	SCC resistance		
A.S. Wu et al. <sup>100</sup> , M. Sprengel et al. <sup>101</sup> , S. Zhang et al. <sup>102</sup>	X				LPBF	
M.S. Pham et al. <sup>103</sup> , J. Bedmar, et al. <sup>104</sup> , M. Godec et al. <sup>105</sup> , H. Gong et al. <sup>106</sup> , W. Zhai et al. <sup>107</sup> , M. Mokhtari et al. <sup>108</sup> , M.R. Jandaghi et al. <sup>109</sup> , M. Ahmed Obeidi et al. <sup>110</sup> , X. Wang et al. <sup>111</sup>	X	X				
R.I. Revilla et al. <sup>112</sup> , J.R. Trelewicz et al. <sup>113</sup> , Yeganeh et al. <sup>114</sup> , K. Wang et al. <sup>115</sup> , E.C. Bordinassi et al. <sup>116</sup> , S. Santa-aho et al. <sup>117</sup>	X		X			
V. Cruz et al. <sup>118</sup> , Z. Que et al. <sup>119</sup> , E.K. Karasz et al. <sup>120</sup>	X			X		
X. Lou et al. <sup>121</sup>	X	X		X		
P. Dong et al. <sup>83</sup> , A. Yazdanpanah et al. <sup>122-125</sup> , S. Zhang et al. <sup>126</sup>	X		X	X		
L.-E. Rannar et al. <sup>127</sup>	X					EB-PBF
Y. Zhong et al. <sup>128</sup> , I.A. Segura et al. <sup>129</sup>	X	X				
J. Bedmar et al. <sup>104</sup> , N. Yang et al. <sup>130</sup> , B.M. Morrow et al. <sup>131</sup> , L. Zhang et al. <sup>132</sup> , X. Chen et al. <sup>133</sup>	X	X				DED
M. McMurtrey et al. <sup>134</sup>	X	X		X		
R. I. Revilla et al. <sup>112</sup> , Q. Xiao et al. <sup>135</sup>	X		X			
J. Yang at al. <sup>136, 137</sup>	X			X		
M. Bassis, et al. <sup>138</sup>	X	X	X	X		
X. Chen et al. <sup>139</sup>	X				WAAM	
L. Wang et al. <sup>140</sup> , C. Wang et al. <sup>141</sup> , T.A. Rodrigues et al. <sup>142</sup> , W. Wu et al. <sup>143</sup>	X	X				
C. Wang et al. <sup>144</sup> , D. Wen et al. <sup>145</sup>	X		X			
S.H. Lee <sup>146</sup>	X				CMT	
J. Chen et al. <sup>147</sup> , C. Wang et al. <sup>141</sup>	X	X				
B. Xie et al. <sup>148</sup>	X	X	X			
D. Jiang and F. Ning <sup>149</sup>	X				Sinter-based material extrusion	
H. Gong et al. <sup>106</sup> , M. Sadaf et al. <sup>150</sup> , Y. Thompson et al. <sup>151</sup> , M.A. Caminero et al. <sup>94</sup> , M.A. Wagner et al. <sup>93</sup>	X	X				
J. Jansa et al. <sup>92</sup>	X		X			
Present work	X	X	X	X	LPBF & sinter- based material extrusion	

## **1.1 Aim and objectives**

This investigation aims to evaluate the 3D printed properties and performance of SS316L alloy produced using LPBF and sinter-based material extrusion methods, and correlate those properties with the underlying structures at macro-, micro-, and nano-scales. The outcomes of this research contribute to the optimisation of the process parameters towards producing more SCC resistant materials. The specific objectives of the research are:

- Establish a correlation between the printing variables and the properties/performance of 3D printed SS316L alloy.
- Examine the material's susceptibility to pitting and cracking initiation at different exposure conditions of stress and temperature.
- Assess the role of 3D printed microstructural elements on the susceptibility to SCC initiation and crack propagation behaviour.

## **1.2 Significance of the research**

The significance of this investigation primarily revolves around understanding the additive manufacturing of SS316L using two distinctive technologies: laser-based and sinter-based methods. It aims to contribute to the existing body of knowledge concerning the correlation between printing parameters and the engineering performance of the manufactured components. The findings are scientifically explained with advanced microscopy and microanalytical methods. The insights gained from this research have the potential to reduce the risk of SCC-related failures by optimising the printing strategy to produce components with improved resistance. Tailored properties, such as yield strength and pitting resistance, can be achieved by establishing correlations between the printing variables and the 3D printed microstructures of SS316L. This is possible due to the high flexibility of AM technologies that enable the fine-tuning of variables to produce prompt results, thus facilitating timely decision-making.

## **1.3 Thesis overview and structure**

This thesis consists of six chapters: It starts by introducing the subject matter (Chapter 1). The core of the research is presented in four peer-reviewed journal articles each forming a chapter (Chapter 2 to 5). The research summary is presented, followed by the overall main conclusions that are not specific to the individual chapters but highlight the broader findings of the research. Finally, an outline of the future research is provided (Chapter 6). The

structure of the thesis is illustrated in Figure 1- 2. The subject matter of each chapter is summarised in detail below:

**Chapter 2** consists of a study that aims to gain insight into the influence of the sinter-based material extrusion technology on the microstructures and mechanical properties of 3D printed SS316L. The initial part of the study comprises research on determining various microstructural aspects, including chemical composition, primary and secondary phases, grain size distribution, structural boundary content including twin boundaries, crystallographic textures, nature of non-metallic inclusions, as well as, structural defects such as porosity. To achieve the objectives, microanalysis techniques, including SEM, EDS, XRD, and EBSD were employed. Additionally, non-metallic inclusions in the pre-alloyed SS316L feedstock powder were examined using TEM. The second part of the study involves evaluating the mechanical properties of 3D printed materials, specifically the elastic modulus, yield strength, tensile strength, and ductility. The tests were conducted per ASTM E8<sup>152</sup>, and the findings correlated with the microstructures to achieve a better understanding of the structure-property relationship. The last part of the study investigates the fracture mode of the tensile samples through fractography and establishes connections between the findings and the microstructures. This chapter has been published in the Journal of Materials Science<sup>153</sup>.

**Chapter 3** involves a comprehensive study of the crystallographic textures and microstructures of the LPBF-manufactured SS316L at macro-, micro-, and nano-scales. The investigation demonstrates that some of the reported findings on the crystallographic textures are oversimplified and do not capture the anomalies in the texture-related phenomena. This investigation, therefore, identifies these features and explains how they are created through the formation of the microstructures, illustrating them using a set of advanced characterisation tools such as SEM, EBSD, and TEM. The research study also incorporates stress relief heat treatments. The findings are compared with the as-printed conditions to observe changes resulting from the heat treatment process. Structural analysis in this study includes distribution of misorientation boundaries, twin boundary content, nature and size of non-metallic inclusions, crystallographic textures, and grain morphology. This chapter has been published in the journal of Materials<sup>154</sup>.

**Chapter 4** focuses on investigating the impact of the microstructures on the susceptibility to pitting, SCC, and crack-branching, of SS316L produced using sinter-based material extrusion. The investigation employs C-ring specimens designed per ASTM G38<sup>155</sup>, which are subjected to three levels of elastic loading (0%, 60%, 90% of actual yield strength

(AYS)), and immersed in 25% w.t. acidic chloride solution, per ASTM G123 <sup>156</sup> at four different temperatures (0 °C, 30 °C, 60 °C, boiling). The initial part of the study involves mapping the pitting and cracking susceptibility of the C-rings when exposed to the different test conditions of stress and temperature. Susceptibility is assessed based on the time taken for the C-rings to exhibit evidence of pitting or cracking. This analysis aims to determine the influence of the printed microstructures on the susceptibility to pit and crack initiation. In the second part of the study, cracked specimens are investigated using microanalysis techniques, including LOM, SEM, and EBSD. This part of the study aims to correlate the crack-branching behaviour with the microstructures and microstructural attributes of the printed alloy. Furthermore, to enhance the understanding of SS316L's susceptibility to pitting, SCC, and crack-branching, C-rings manufactured from wrought SS316L at SA and CD conditions, are identically tested and investigated. This chapter has been published in the journal of *Materials* <sup>157</sup>.

**Chapter 5** comprises two studies that explore the influence of the manufacturing process and microstructures on the SCC susceptibility of LPBF-manufactured SS316L. The initial part of the study focuses on investigating the printed microstructures using microanalysis techniques, including SEM, XRD, and EBSD, to determine aspects such as grain size distribution, primary and secondary phases, crystallographic textures, and residual stresses. In addition, tensile properties are determined per ASTM E8 <sup>152</sup>, and the results are benchmarked with CD wrought SS316L, known for its high-strength. In the second part of the study, similar to Chapter 4, the SCC susceptibility of LPBF-manufactured SS316L is investigated using C-rings designed per ASTM G38 <sup>155</sup>. The C-rings are also subjected to three levels of elastic loading (0%, 60%, 90% AYS) and immersed in boiling acidic chloride solution (25% w.t.), per ASTM G123 <sup>156</sup>. This investigation explores the role of residual stresses and printed supports in the C-ring's SCC susceptibility. To achieve this, stress relief heat-treatment and partial immersion tests are conducted on test specimens. Finally, a mechanism is proposed to explain the consistent cracking occurring at the same location in the C-ring, irrespective of the test conditions. This chapter has been published in the journal of *Corrosion* <sup>158</sup>.

**Chapter 6** presents the primary accomplishments and limitations of the study, summarising the key findings and conclusions. In addition, it outlines future research directions aimed at advancing the understanding of SCC in 3D printed SS316L and developing more SCC resistant materials.

**Appendix 1** presents the written attribution statements from co-authors of the manuscripts.

**Appendix 2** presents the copyright statements related to all publications included in this thesis.

**Appendix 3** presents the original reprint of the publication included in Chapter 2

**Appendix 4** presents the original reprint of the publication included in Chapter 3

**Appendix 5** presents the original reprint of the publication included in Chapter 4

**Appendix 6** presents the original reprint of the publication included in Chapter 5

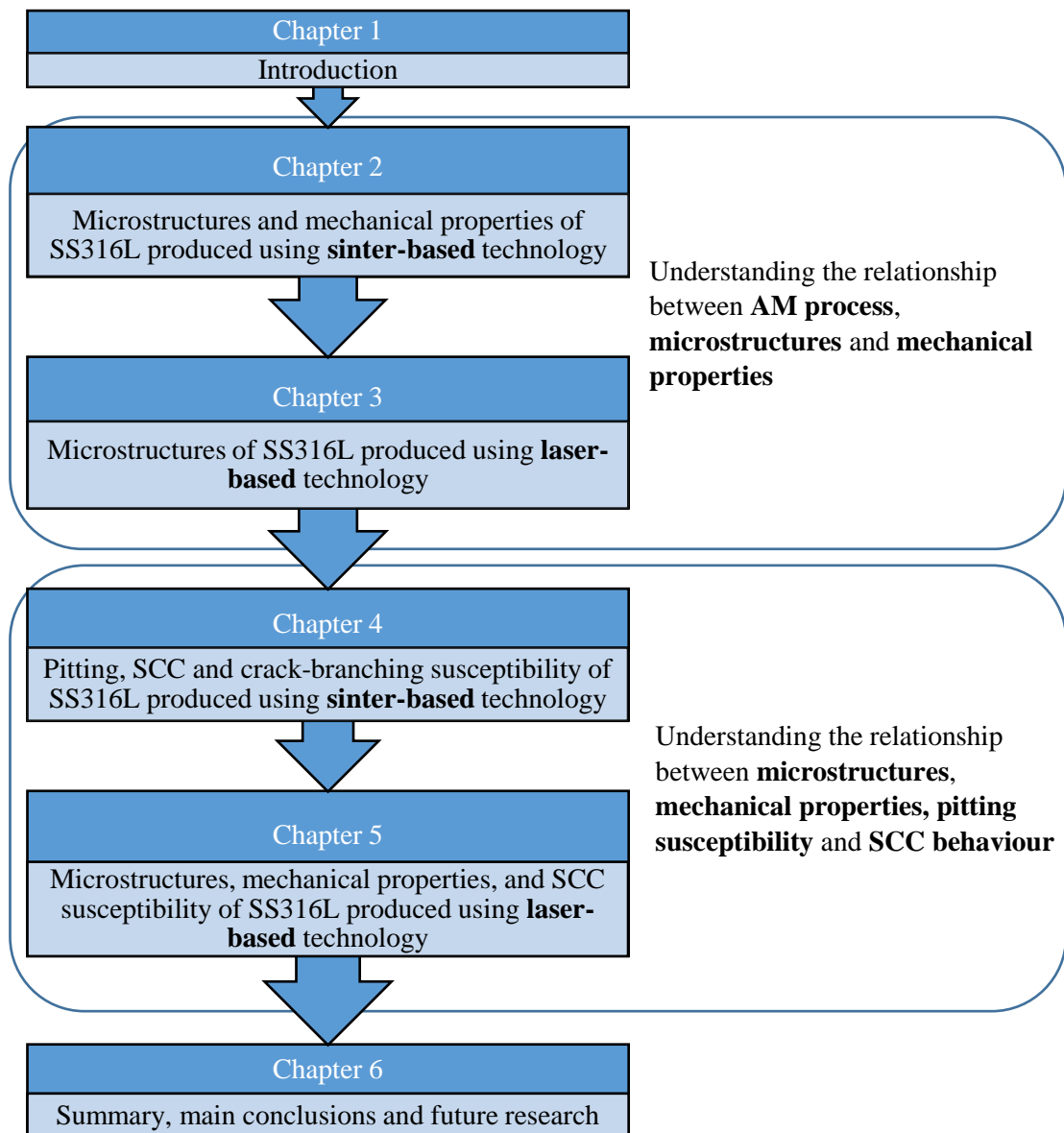


Figure 1- 2: Thesis structure

## **Chapter 2: Sinter-based material extrusion of SS316L: Microstructures and tensile properties**

This chapter corresponds to a publication that has been reformatted to align with the overall style of the thesis and to address the comments raised by the examiners. This publication is reproduced with permission from Spring Nature.

### **Publication:**

Santamaria R, Salasi M, Bakhtiari S, Leadbeater G, Iannuzzi M, Quadir MZ. Microstructure and mechanical behaviour of 316L stainless steel produced using sinter-based extrusion additive manufacturing. *Journal of Materials Science*. 2022 Jun 1:1-7

<https://doi.org/10.1007/s10853-021-06828-8>



# **Microstructure and mechanical behaviour of 316L stainless steel produced using sinter-based extrusion additive manufacturing**

## **2.1 Abstract**

Specimens were additively manufactured in 316L stainless steel (SS316L) with a technology that combines the extruding method of fused filament fabrication (FFF) with the strengthening stages of metal injection moulding (MIM). A thorough metallographic analysis and tensile testing were carried out to investigate the effect of sintering in the final microstructures, mechanical properties, and fracture modes of the manufactured material. SS316L wrought specimens were also characterised and tested for comparison. Results showed that the sinter-based technology produced a near-fully dense material with a microstructure and mechanical properties comparable to the standard requirements of the UNS S31603 grade. The sintered specimens were characterised at as annealed condition, with fully austenitic microstructures, annealing twins, and sintering defects such as i) scattered round microporosity, ii) elongated macroporosity, iii) spherical inclusions rich in Si, Mn and O —also found in the precursor powder— and iv) irregularly-shaped inclusions rich in Cr, Mn and O. The average mechanical properties of the printed SS316L were Young's modulus (E) 196 GPa, 0.2% offset yield strength (Sy) 166 MPa, tensile strength (Su) 524 MPa, elongation after fracture 85% and reduction of area 51%. Based on the findings, a mechanism is outlined explaining the departure from the typical cup-and-cone ductile fracture in the necked region observed in the printed samples.

## **2.2 Introduction**

Additive manufacturing (AM), also known as 3D printing, is a general term covering those technologies that allow the fabrication of complex physical objects from digital data by the successive addition of material <sup>56-58</sup>. Regardless of the type of feedstock or binding mechanism, current AM technologies are classified into seven basic categories, i.e., (i) binder jetting, (ii) direct energy deposition (DED), (iii) material extrusion, (iv) material jetting, (v) powder bed fusion (PBF), (vi) sheet lamination and (vii) vat photopolymerisation <sup>57-59</sup>.

SS316L is a widely used stainless steel in the resource sector, due to its favourable corrosion behaviour and good formability. Studies on SS316L fabricated via PBF and DED, showed that the manufacturing parameters have a direct impact on the final microstructures, porosity characteristics and mechanical properties <sup>72, 74, 76, 94, 159-165</sup>. Issues with these AM technologies include their initial capital costs and safety concerns in relation to the handling of loose powder and high-energy sources. Although these issues have seen recent improvements,

there are also challenges associated with the anisotropic nature of microstructures, which produce columnar grains<sup>74, 76, 160, 165, 166</sup>. Hence, in recent years, investigations have been carried out to address these issues by combining the low cost of extrusion 3D printing techniques using fused filament fabrication (FFF) with the strengthening process of metal injection moulding (MIM). This combined AM technology is referred as metal FFF<sup>58, 60, 85-89</sup>.

Manufacturing of SS316L via metal FFF starts with loading the feedstock of pre-alloyed powder embedded in a binder into the 3D printer. The feedstock is then heated just above its binder's melting point, 210 °C to 290 °C<sup>89, 150, 151, 167</sup>, allowing it to be extruded line-by-line and layer-by-layer<sup>57-59</sup>. At this point the as-printed object, known as green-part, lacks all the mechanical properties of the final densified metal. Therefore to achieve the required strength, the green-part subsequently undergoes a series of post-print processing stages similar to those used in MIM and powder metallurgy (PM) technologies<sup>58, 60, 150, 151</sup>. Solvent debinding is the first stage in metal FFF. Debinding involves removing the primary binder material by dissolving it in a suitable solvent, typically a liquid or gas<sup>94, 151, 168, 169</sup>. The obtained structure, known as brown-part, undergoes the next stage of the process inside a furnace. During this next stage, the remaining secondary binder is burnt off through the porous structures at 425 to 600 °C temperature range, a process known as thermal debinding<sup>88, 150, 167, 169</sup>. The heating rate during thermal debinding is optimised to avoid blistering or cracking of the part. A vacuum atmosphere is used to prevent the oxidation of the steel particles; however, a reducing atmosphere using hydrogen gas can also be employed<sup>151, 167-169</sup>. During the final stage, i.e., sintering, the temperature reaches between 1250 and 1380 °C<sup>150, 167, 168</sup>. During sintering, the specimen is held at this peak temperature for 120 to 180 min<sup>88, 94, 150, 151, 168, 169</sup>. Finally, the sintered part is cooled down to room temperature either inside the furnace or by air quenching<sup>88, 94</sup>. It has been observed that a higher peak temperature and a longer sintering result in microstructures with larger grains and reduced porosity<sup>151, 170, 171</sup>.

Recent investigations have reported the microstructure and mechanical properties of FFF fabricated SS316L<sup>85, 86, 88, 89, 91, 94, 106, 150, 151, 167-169, 172, 173</sup>. Results show that metal FFF produces porous sintered materials<sup>88, 151, 169</sup>, with a relatively large distribution of austenitic grains<sup>94, 151, 169</sup> displaying a ductile behaviour<sup>88, 89</sup> with varying other tensile properties, which are a function of the building orientation<sup>85, 88, 94</sup>. For instance, the porosity varied between less than 1% to 16%<sup>85, 168</sup>, the average grain size ranged between 25 and 75 µm<sup>85, 94</sup>, the yield strength (Sy) varied between 93 and 252 MPa<sup>86, 150</sup>, and the tensile strength (Su) ranged between 219 and 561 MPa<sup>86, 172</sup>.

The objective of this work was to investigate the relationship between the microstructures, tensile properties and the fracture mechanism of the FFF additively manufactured SS316L. A detailed morphological and microstructural characterisation was carried out using scanning and transmission electron microscopy (SEM and TEM, respectively) and microanalytical techniques, such as electron backscattered diffraction (EBSD), and energy dispersive spectroscopy (EDS). The wrought condition of the SS316L specimens was also tested and analysed, and the results were compared to gain a better understanding of the mechanical and chemical performance of the sintered SS316L material. Results were benchmarked with the literature covering SS316L manufactured by PBF and DED.

## **2.3 Experimental Procedure**

### **2.3.1 Manufacturing technology**

The SS316L used in this investigation was additively manufactured with a sinter-based extrusion process known as Bound Metal Deposition™ (Desktop Metal®, DM) using the Studio System™ (DM) technology. The system comprises three units, printer, debinder and sintering furnace. The printer uses cartridges containing the feedstock in the form of 6×150 mm rods made of pre-alloyed SS316L powder embedded in the wax- and polymer-based binders. The Studio Printer comprises a build volume of 300×200×200 mm<sup>3</sup> and a dual extrusion capability for the ceramic-based media. This media creates an interface between the part and its support structures that is removed after sintering. Once the printing of an object is done, it is moved to the Studio Debinder unit which is an atmospheric pressure, low emission, vapour and odour-tight distillation tank that uses a proprietary solvent solution at 50 °C to remove the wax-based binder and create an open-pore structure. Then, the debound part is moved to the Studio Furnace for sintering. The furnace, which operates under vacuum in an argon-rich atmosphere, eliminates the remaining binder in the brown-part during the heating process and then sinters the part at high temperature, followed by some degree of densification. The entire process is controlled by the cloud-based software Fabricate™ (DM).

### **2.3.2 Sample manufacture**

The dimensions of the SS316L samples for microscopy analysis were 10×10×3 mm. Subsize tensile specimens were produced per ASTM E8 recommendations<sup>152</sup>, i.e., 100 mm overall length, 6 mm width, 32 mm length in the parallel section, and a 3 mm thickness. All specimens were 3D printed in the XY orientation and Z direction with the longest dimension laying parallel to the X axis as shown in the schematic Figure 2-1a. The extruded line width was 0.50 mm, the deposited layer height was 0.15 mm and the contour shell thickness was

1.50 mm. The top-to-bottom bulk volume was achieved with a linear raster pattern than changed its extruding direction  $+45^\circ$  and  $-45^\circ$  with respect to the Y axis with each deposited layer. The other printing parameters were: extruding temperature  $175^\circ\text{C}$ , extrusion nozzle size 0.40 mm diameter, extrusion rate 30 mm/s, and build plate temperature  $65^\circ\text{C}$ . The sinter scale factors were  $X=1.16$ ,  $Y=1.16$  and  $Z=1.15$ . This indicates the material allowance of the green-part to compensate for the contractions during the sintering stage. The solvent debinding was conducted for 15 h and the thermal debinding at  $550^\circ\text{C}$  for 2 h. The sintering was performed at a peak temperature of  $1350^\circ\text{C}$  with a dwell time of 2 h. The process ended with furnace-cooling the sintered parts down to room temperature. Figure 2-1b shows the sintering furnace temperature profile.

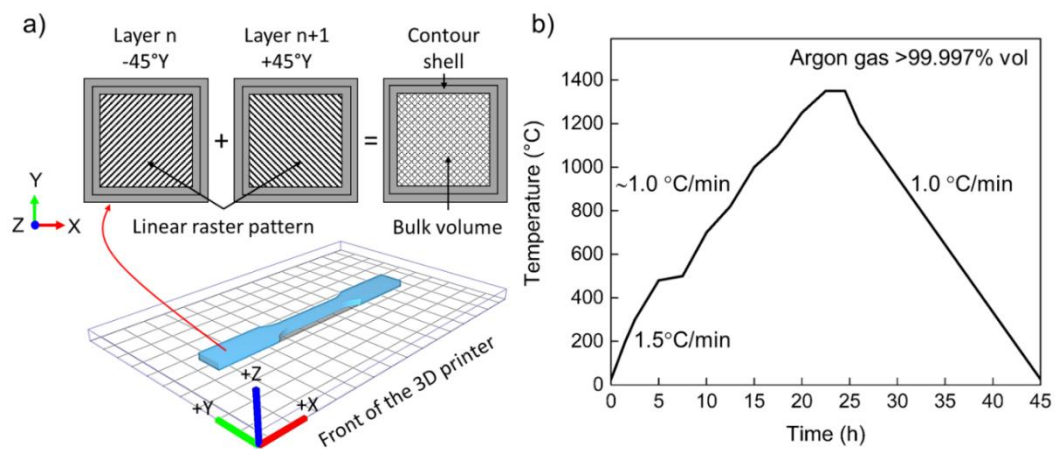


Figure 2-1: a) Test specimen, 3D printing strategy, and b) thermal profile used for sintering

### 2.3.3 Microscopy sample preparation

Feedstock rods (cut longitudinally), brown-part and sintered samples were mounted in cold epoxy resin. Then, they were wet ground from 80 to 1200 grit SiC abrasive paper and then mechanically polished down to a final polish with  $0.02\ \mu\text{m}$  alumina suspension. All polished samples were rinsed with ethanol, sonicated in deionized water, dried with nitrogen and placed inside a vacuum desiccator for at least 12 h before the microscopy analysis. Sintered samples for EBSD analysis were additionally ion-milled for 30 minutes using a beam voltage of 8 kV at a glancing angle of  $4^\circ$  with full cycle rotational movements (TECHNOORG Linda, SEMPrep2). Samples for TEM analysis were prepared using the focused ion beam (FIB) lift-out technique on a Dual Beam FIB/SEM instrument (FEI Helios Nanolab G3 CX). The prepared TEM lamella was a strip of  $10\times 10\ \mu\text{m}^2$  with a thickness below 100 nm. A carbon protective layer was deposited on top of the region of interest using an ion beam with a 30 kV voltage and 0.43 nA current. Trenching, cutting, and thinning steps were carried out at 30 kV and ion beam currents of 9.50-0.23 nA, as the thinning was progressed. After

thinning the TEM lamella to a thickness of 100 nm at 30 kV, a final cleaning was applied in two steps: the first step was at a lower voltage of 5 kV for 1 min on each side, followed by a low voltage of 2 kV cleaning for 30 seconds on either side.

### **2.3.4 Microstructure investigation**

The chemical composition of the powder used in this investigation was verified by quantitative EDS. The analysis was performed on exposed particles on a section of a brown part. Measurements were taken with a cobalt calibrated standard using a high sensitivity Oxford EDS detection system coupled to a field emission-scanning electron microscope (FE-SEM) (TESCAN system, CLARA). The quantification was conducted using the Oxford Aztec software. The chemical composition of a SS316L wrought sample was also quantified for comparison. The microstructure of the sintered material was imaged using the SE detector in the FE-SEM and its chemical composition was mapped using EDS. The microstructure of the SS316L wrought sample was also obtained by FE-SEM for comparison. The particle size of the SS316L powder was measured with the open-source ImageJ software by analysing the FE-SEM images of the feedstock taken at different magnifications using both secondary electron (SE) and backscatter (BS) detectors. Imaging and elemental analysis at nanoscale were conducted on a TEM sample with a Field Emission TEM operating at 200 kV beam voltage (FEI, Talos).

The phases present in the SS316L powder and SS316L sintered material were identified via X-ray diffraction (XRD) analysis using a Cobalt K alpha powder diffractometer radiation source operating at 35 kV 40 mA using a LynxEye detector (Bruker D8 Discover). The XRD data were collected over an angular range of 15° to 135° at a step size of 0.015° and a time interval of 0.7 s. Likewise, a SS316L wrought sample was also analysed in the same analytical conditions for comparison.

The volumetric porosity fraction of the SS316L sintered material was determined with X-ray micro computed tomography (micro-CT) in a 5×5×3 mm<sup>3</sup> sample cut from the corner of a square specimen to ensure having part of its contour shell and bulk volume. The analysis was conducted using a 3D X-ray microscope with an exposure energy of 140 kV, during an exposure time of 24 h and at a pixel resolution of 2.2 μm (Zeiss 520 Versa). The fraction area of the samples' porosity was quantified with ImageJ by analysing cross-sectional SEM images at different magnifications. The density of the SS316L sintered material was calculated using the Archimedes principle, as described in ASTM B311<sup>174</sup>.

The crystallographic orientation of the SS316L sintered microstructures was mapped with respect to the build direction (Z) using an Oxford symmetry EBSD detector in the Tescan Clara FE-SEM. The data was acquired at 2  $\mu\text{m}$  step size, 28 kV beam energy, and 21.2 mm working distance. Both EDS and EBSD data acquisition was conducted with Aztec data acquisition software, and the EDS and EBSD data post processing was undertaken using the Aztec and AztecCrystal software, respectively. A clean-up process was applied to the EBSD data to assimilate any non- or mis-indexed points into the surrounding neighbourhood grains. Less than 10% of the points were modified in the process. The grain boundaries were detected with a threshold misorientation of  $10^\circ$  in conjunction with a minimum of 8 pixel of fractional difference of misorientation variation and a kernel size of 3 by 3. The grain size was measured as the maximum Feret diameter. The average grain aspect ratio was calculated as the fitted ellipse aspect ratio with the  $\Sigma 3$  twins ( $\langle 111 \rangle / 60^\circ$ ) boundaries excluded. The same analysis was conducted on a SS316L wrought sample for comparison.

### **2.3.5 Tensile properties**

The tensile properties (yield and tensile strength) of the sintered SS316L samples were measured by tensile testing on triplicate specimens at room temperature ( $25^\circ\text{C}$ ). Tests were conducted on rectangular subsize specimens using a 50 kN universal testing machine (UTM, Shimadzu) equipped with 50 kN manual non-shift wedge grips. The UTM crosshead speed was set to 0.48 mm/min within the elastic region, while the displacement was measured using an axial extensometer with a gauge length of 25 mm and a travel range of +100% (Epsilon Tech Corp). The test was paused once the proportional limit was surpassed, the extensometer was then removed, and the test was resumed at a UTM crosshead speed of 1.6 mm/min until the specimen fractured. Data were collected at a rate of 10 Hz in the elastic region and 5 Hz in the plastic region. The test was monitored with the Trapezium X software. The tensile test, the dimensions of the specimens, and the method to calculate the 0.2% offset yield strength ( $S_y$ ), tensile strength ( $S_u$ ), elongation after fracture and reduction of area were conducted as per standard ASTM E8<sup>152</sup>. The elongation at fracture was calculated from the engineering stress-strain curve. The Young's modulus (E) was approximated using the least-squares method from 25 MPa to 100 MPa using the stress-strain data as recommended in the standard ASTM E111<sup>175</sup>. All fracture specimens were cut transversely (YZ plane) to a length of 10 mm, sonicated in ethanol, rinsed with deionised water, dried with nitrogen and placed inside a vacuum desiccator for at least 12 h before the microscopy analysis. Fractured surfaces were imaged using the SE detector, and micro-chemical analysis was conducted by EDS. The wrought SS316L specimens used for comparison were wire-cut with the same dimensions from a 3 mm thick plate and similarly tested and analysed.

## 2.4 Results

### 2.4.1 Microstructures and analysis

Table 2-1 presents the chemical composition of SS316L powder and SS316L wrought samples measured by quantitative EDS along with the nominal composition of UNS S31603 per standard ASTM A240 <sup>176</sup>. From comparisons, the analysed powder metal met the UNS S31603 requirements. A representative FE-SEM image of the feedstock is shown in Figure 2-2. The measured average particle size distribution was d50 1.4  $\mu\text{m}$  and d90 5.0  $\mu\text{m}$ . A representative TEM image and corresponding EDS map of the SS316L precursor powder in Figure 2-3 shows the presence of spherical Si, Mn and O-rich inclusions. The inclusion size varies between 0.02 and 0.23  $\mu\text{m}$ . SEM-EDS analysis showed no evidence of sensitisation, i.e., Cr depletion in the vicinity of the grain boundaries, in any of the SS316L alloys. This is illustrated later in Chapter 4.

Table 2-1: Quantitative EDS chemical composition of SS316L powder, SS316L wrought and nominal UNS S31603

Material	Chemical composition in wt%					
	Fe	Cr	Ni	Mo	Mn	Si
SS316L Powder	Bal.	17.1	10.0	2.3	1.3	0.6
SS316L Wrought	Bal.	17.8	10.0	2.1	1.6	0.5
UNS S31603 <sup>176</sup>	Bal.	16-18	10-14	2-3	2 max.	0.75 max.

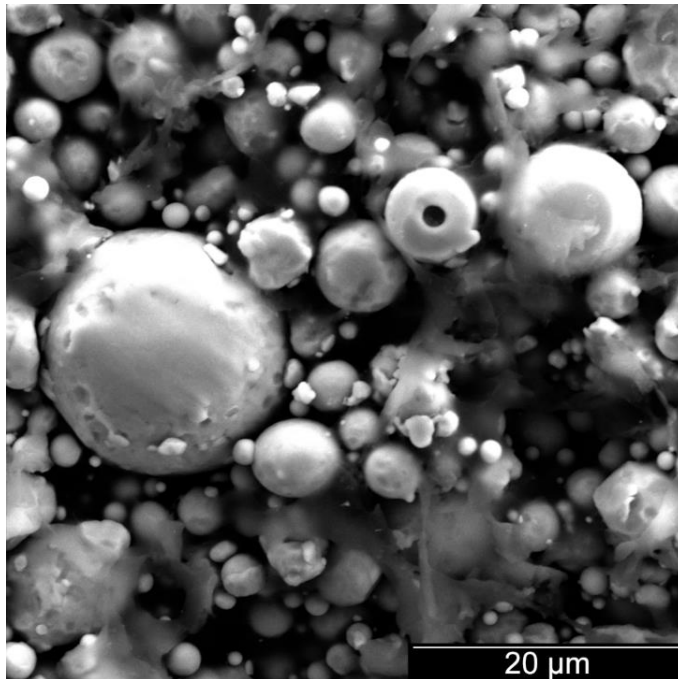


Figure 2-2: FE-SEM image of the feedstock showing the SS316L powder with a particle size distribution of d50 1.4  $\mu\text{m}$  and d90 5.0  $\mu\text{m}$

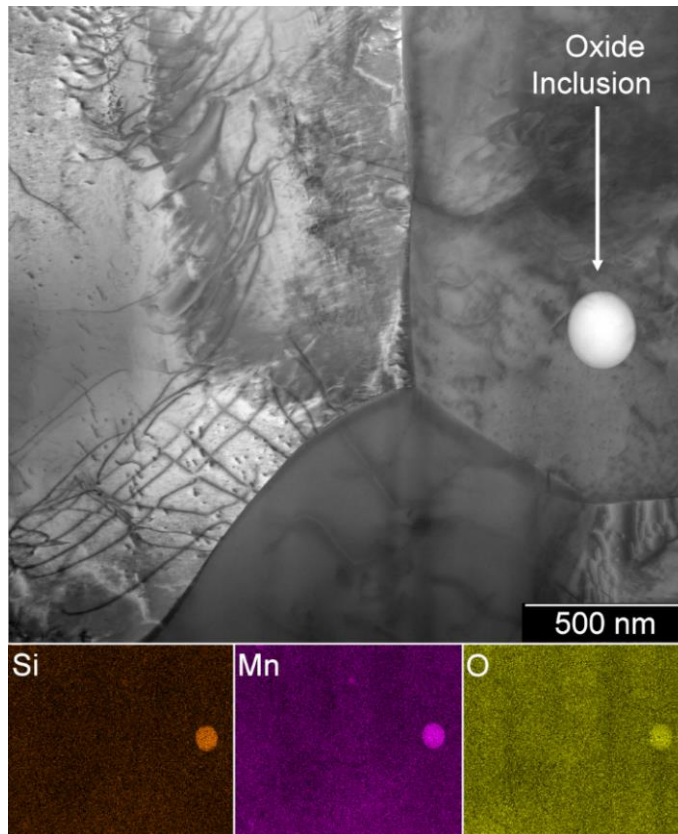


Figure 2-3: TEM image and corresponding EDS map of a SS316L particle showing a spherical inclusion rich in Si, Mn and O content found in the SS316L precursor powder

The XRD spectra of representative SS316L powder and sintered samples measured with respect to its build direction (Z) are shown in Figure 2-4. The SS316L wrought data was added for comparison. It can be seen from the figure that the SS316L powder consisted mainly of  $\gamma$  (FCC) austenite phase with a subtle presence of retained  $\delta$  (BCC) ferrite. According to T. Kurzynowski et al. <sup>76</sup>, the retention of  $\delta$ -ferrite in the powder feedstock results from the rapid solidification of molten SS316L during the gas atomisation process, when the  $\delta$ -ferrite stabilisers, such as Cr, Mo and Si, segregate to create later localised site-specific metastable conditions in the austenitic matrix <sup>76</sup>. The XRD data of the SS316L sintered sample solely shows  $\gamma$  (FCC) austenitic phase confirming the full dissipation of the  $\delta$ -ferrite. Wrought data was added for comparison.



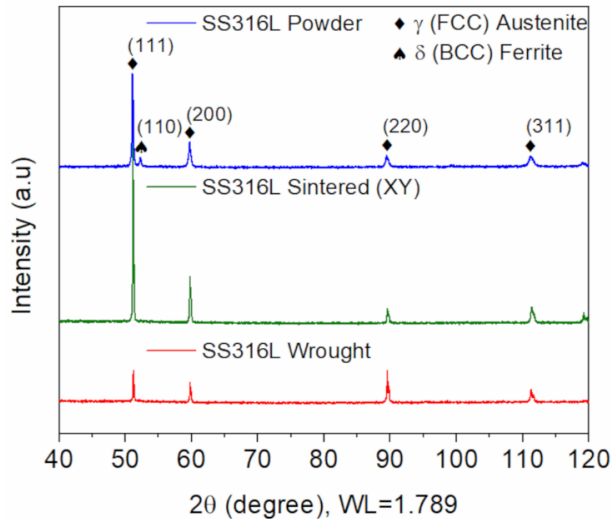


Figure 2-4: XRD spectra of SS316L powder showing an  $\gamma$  (FCC) austenite phase with a small presence of retained  $\delta$  (BCC) ferrite (top), SS316L sintered sample (XY plane) showing a fully  $\gamma$  (FCC) austenite phase (middle), and SS316L wrought also showing a fully  $\gamma$  (FCC) (bottom)

Figure 2-5 shows a large field of view SEM images of the SS316L wrought and sintered samples. The grayscale contrasts indicates the presence of larger austenitic grains in the sintered sample than the wrought sample. Both samples comprises twin boundaries. There is a high porosity and oxide inclusion content in the sintered sample.

The Micro-CT reconstruction in Figure 2-6 reveals the presence of the elongated defects correlated with the printing raster pattern. The scan from the contour shell shows a cumulative stack of parallel lines as expected from the layer-by-layer print built up. The total scanned volume was  $6.9 \times 10^9 \mu\text{m}^3$ , in which the porosity volume was  $8.75 \times 10^7 \mu\text{m}^3$ , i.e., 1.27% v/v. The total amount of macro- and microporosity were 0.85% and 0.43%, respectively. The threshold used to define micro pores was  $<10,000 \mu\text{m}^3$ . The fractional area of porosity measured from post-processed SEM cross-sectional images was  $4.8\% \pm 1.4$ . The bulk density measured with the Archimedes principle was  $7.43 \text{ g/cm}^3 \pm 0.07$ .

A SEM image of a SS316L sintered sample with corresponding EDS elemental maps are given in Figure 2-7. The images show the presence of two types of inclusions, namely, i) irregular Cr-rich particles with an average size of  $3 \mu\text{m}$ , and ii) spherical Si-rich particles with an average size of  $1.4 \mu\text{m}$ . Both types contain Mn and O. Identical findings are also reported in other investigations in 3D printed SS316L produced via PBF<sup>177</sup> and DED<sup>164</sup>. According to P. Deng et al.<sup>177</sup>, the Si-Mn-O particles in the precursor powder were generated during the gas atomisation process<sup>177</sup>. Yan et al.<sup>178</sup>, observed both inclusion types in PBF manufactured SS316L, and concluded the particles were Rhodonite ( $\text{MnSiO}_3$ ) and

Spinel ( $\text{MnCr}_2\text{O}_4$ )<sup>178</sup>. However, the absence of these phases in the XRD spectra might suggest an amorphous nature of these inclusions, which deserves further investigations.

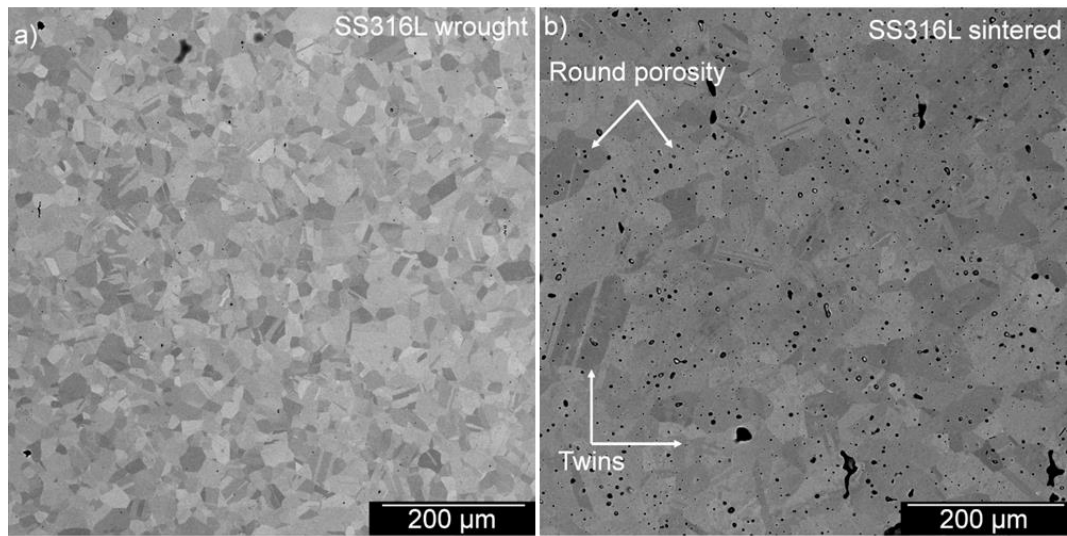


Figure 2-5: SEM images showing large recrystallised microstructures in the a) SS316L wrought, and b) sintered samples, with the later showing distributed porosity, inclusions and twin interfaces

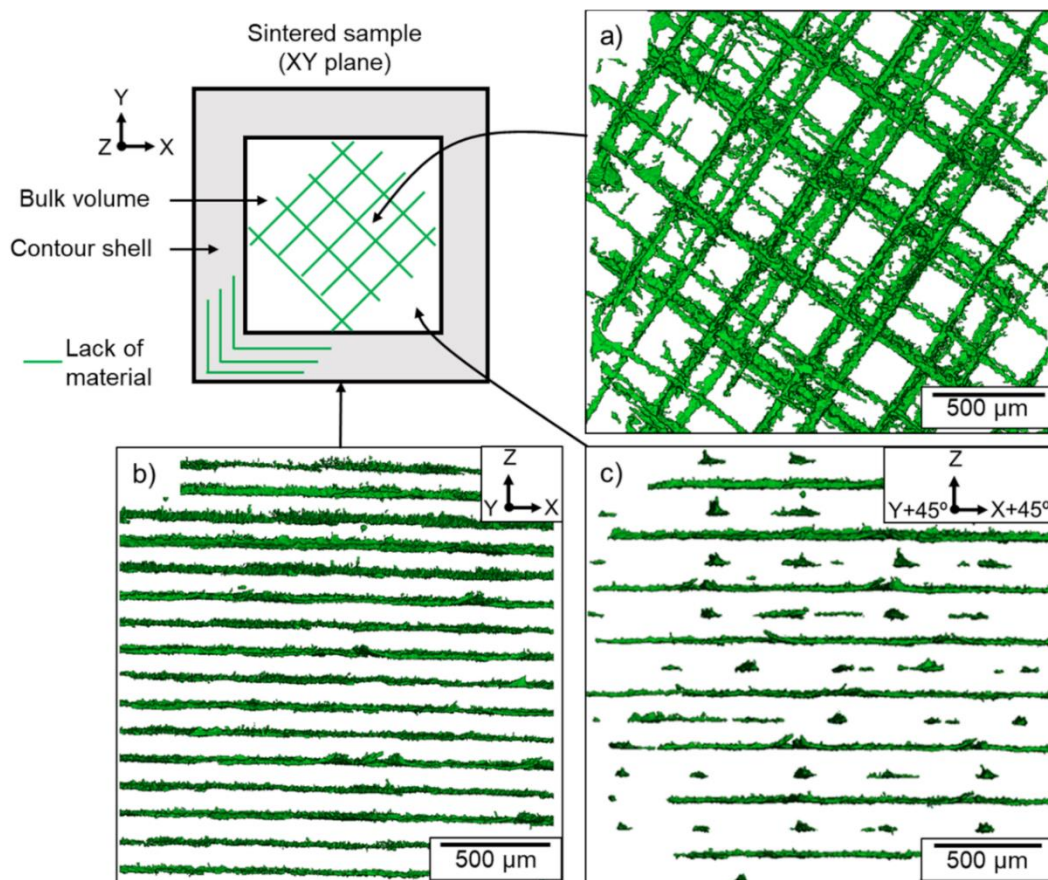


Figure 2-6: Micro-CT scans of a SS316L sintered sample showing the presence of elongated macroporosity, a) as a 3D mesh-like pattern at the bulk volume, b) as a layer-by-layer pattern at the contour shell, and c) as a layer-by-layer pattern skewed 45° in the XY plane at the bulk

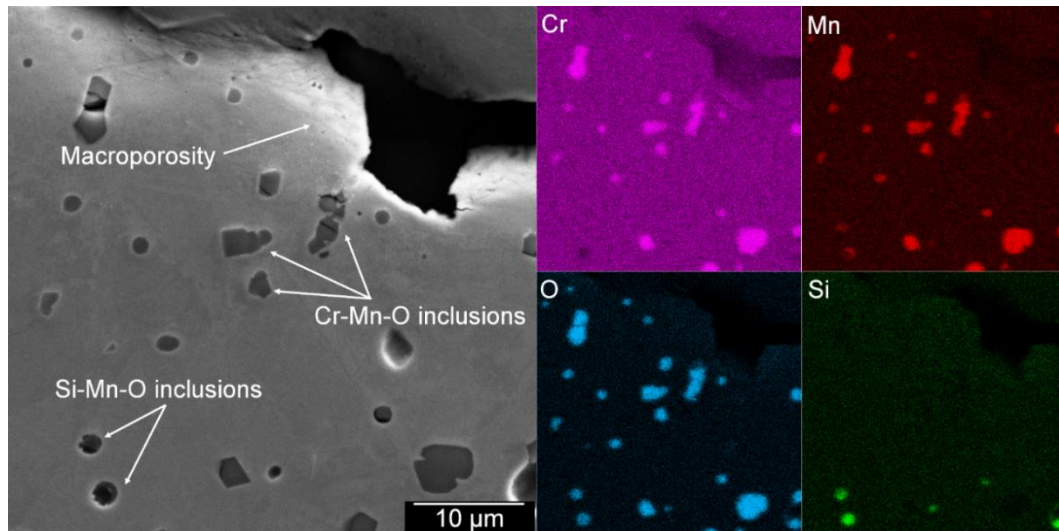


Figure 2-7: SEM image of a SS316L sintered sample and corresponding EDS elemental maps showing the distribution of Si-Mn-O-rich spherical and Cr-Mn-O-rich irregular inclusions

Figure 2-8 shows a wide area EBSD map of the Z-cross section (normal to the built direction) of a sintered sample is shown with the corresponding colour coded inverse pole, indicating a weakly-textured almost random orientation distribution. The almost random orientation is also consistent with the low intensity ( $\times 1.26$  random) in the  $\{111\}$  pole figure. It should be noted that the EBSD area covered is inadequate for the measured grain size, but as a non-textured characteristic was found, it was not regarded as critical. The twin content was measured as the length fraction of the  $\Sigma 3$  boundaries in the microstructure, which was 52.3% of  $>10^\circ$  boundaries. This finding is identical to the 53% reported by Irukuvarghula et al.<sup>179</sup> in hot isostatic pressing (HIP) processed SS316L steels<sup>179</sup>. The quantification made from the grain size measurement is shown in Table 2-2. In comparison, the SS316L wrought sample showed a slight strengthening of the texture as seen in the  $\{111\}$  pole figure, assumed to be caused by the processing history of the sample, the detail of which is beyond the scope of the manuscript. The grain size measurements are shown in Table 2-2.

Table 2-2: Grain size measurements of SS316L sintered and SS316L wrought samples

Material	Overall grain size distribution ( $\mu\text{m}$ )	Average grain size ( $\mu\text{m}$ )	ASTM grain size No <sup>180</sup>	Average grain aspect ratio
SS316L sintered	d50 35, d90 71	$40 \pm 23$	7.5	$3.0 \pm 2.4$
SS316L wrought	d50 18, d90 34	$20 \pm 10$	9.5	$2.3 \pm 1.3$

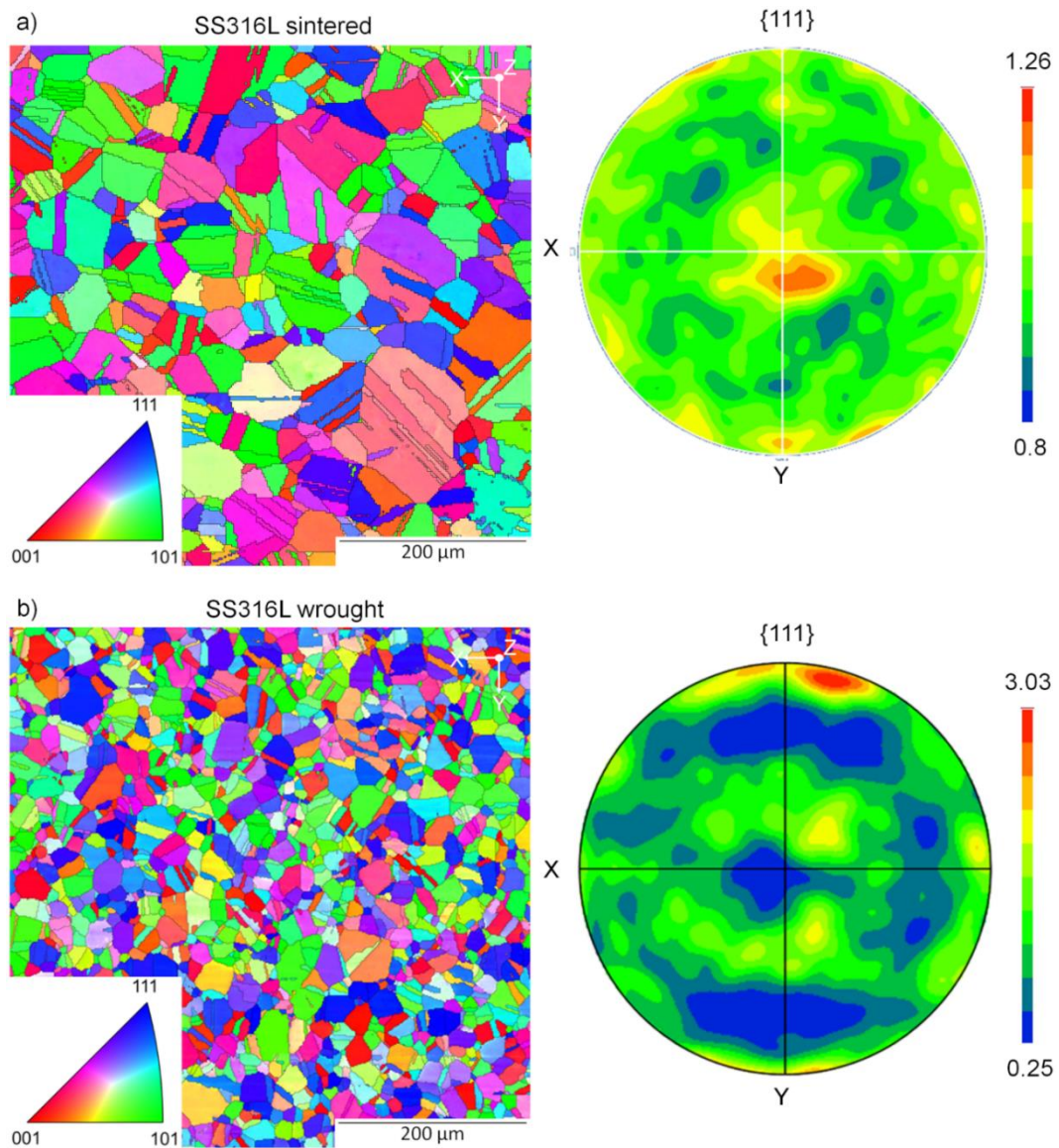


Figure 2-8: EBSD measured inverse pole figure maps of the (a) SS316L sintered and (b) SS316L wrought sample with corresponding  $\{111\}$  pole figures

#### 2.4.2 Tensile properties

Representative engineering stress-strain curves of both SS316L sintered and SS316L wrought samples are shown in Figure 2-9, along with the dimensions of the test specimens. Results have shown that the sintered specimens performed in a ductile manner, which is represented by an initial linear elastic deformation followed by a non-linear permanent deformation. The calculated average Young's modulus ( $E$ ,  $196 \text{ GPa} \pm 28$ ) matched with other's measurements, i.e.,  $202 \text{ GPa}$  conducted at  $25 \text{ }^\circ\text{C}$  room temperature<sup>181</sup>. The tensile strength ( $S_u$ ,  $524 \text{ MPa} \pm 1$ ) and elongation at fracture ( $96\% \pm 1$ ) met and exceeded the UNS S31603 standard requirements<sup>176</sup>. The 0.2% offset yield strength ( $S_y$ ,  $166 \text{ MPa} \pm 2$ ) was slightly lower ( $\sim 2\%$ ) than the minimum required. The mechanical properties are summarised in Table 2-3.

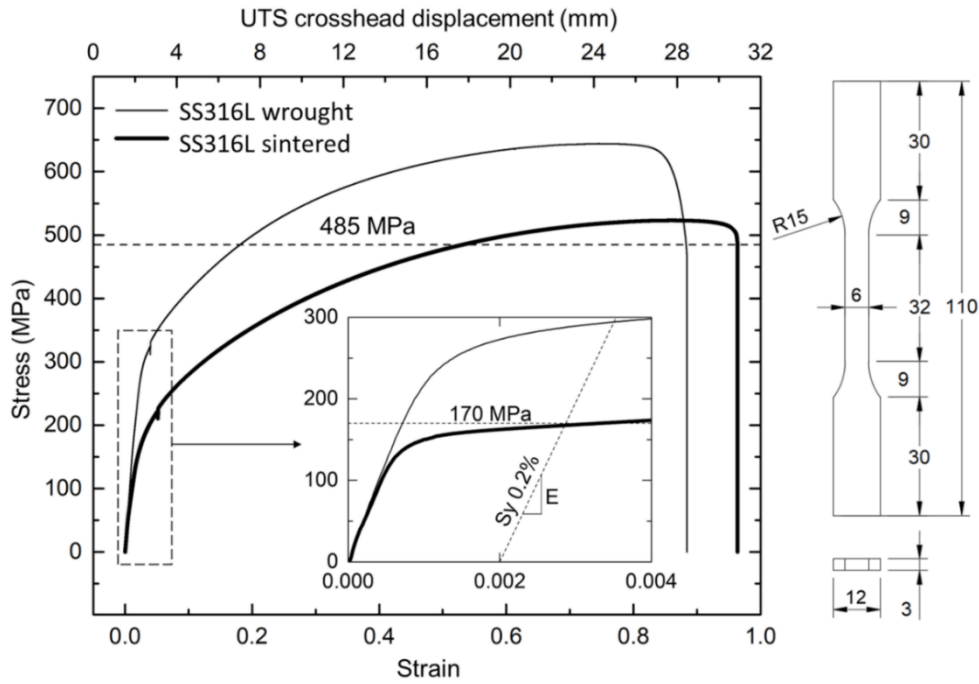


Figure 2-9: Engineering stress-strain curves of both sintered and wrought SS316L materials along with the dimensions of the test specimens

Table 2-3: Mechanical properties of the SS316L sintered and SS316L wrought samples

SS316L		Young's modulus (E)	Offset Yield strength (Sy)	Tensile strength (Su)	Elongation at fracture	Elongation after fracture	Reduction of area
		(GPa)	(MPa)	(MPa)	(%)	(%)	(%)
Sintered	Avg.	196 ± 28	166 ± 2	524 ± 1	96 ± 1	85 ± 3	51 ± 1
	Min.	156	163	523	95	80	50
	Max.	216	168	524	96	88	52
Wrought	Avg.	240	286	644	88	86	55
UNS S31603	<sup>176</sup>	202 <sup>181</sup>	min. 170	min. 485	min. 40	n/a	min. 40

SEM images of the fractured surface of both SS316L wrought and sintered tensile specimens are presented in Figure 2-10. The sintered specimens had a ductile fracture, which was characterised by small inclusions located inside the uniformly distributed spherical dimples. The magnified image at the contour shell and bulk volume shows the presence of elongated macro-porosity. No evidence of secondary central cracks or parabolic dimples, usually found from a shear fracture, were observed in the sintered sample; however, these features were found in the fractured surface of the SS316L wrought specimens. A SEM image and corresponding EDS map from the fractured surface of the SS316L sintered specimen confirming the presence of a Si-Mn-O rich inclusion inside a spherical dimple, can be seen in Figure 2-11. Finally, photographs of both SS316L sintered and wrought fractured tensile specimens are given in Figure 2-12. While both sintered and wrought sample fractured in a

ductile manner, the sintered specimen had a smaller necked region. A typical cup-and-cone characteristic is observed in the wrought specimen.

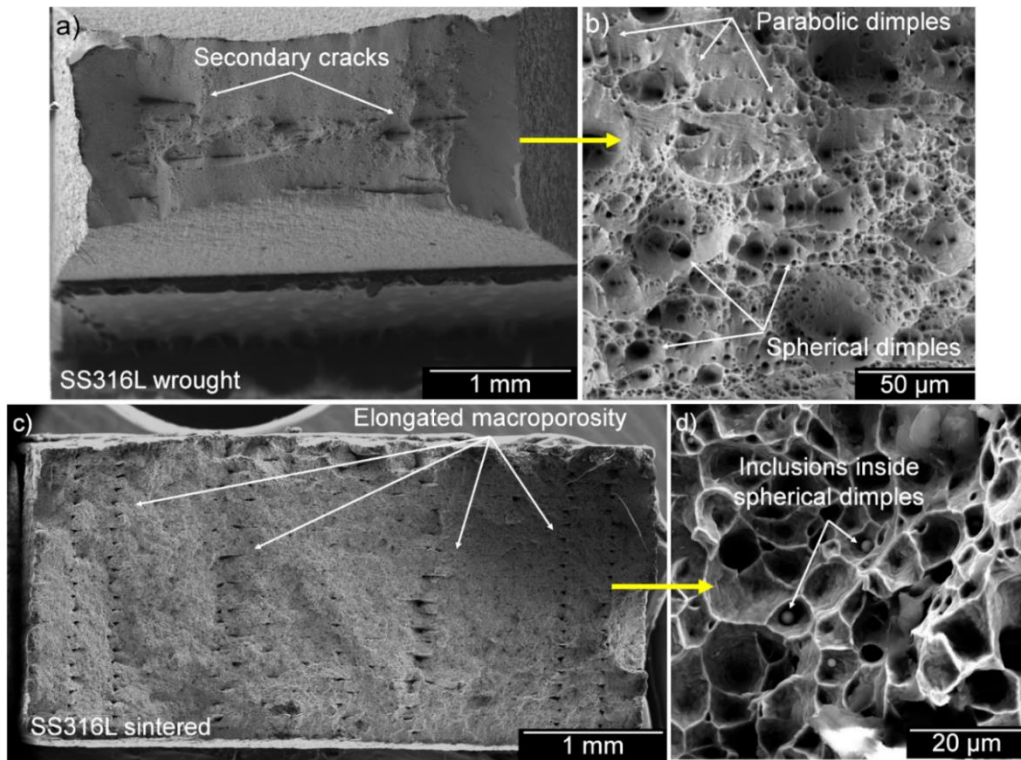


Figure 2-10: SEM images of the tensile fractured surfaces in the a) SS316L wrought and b) sintered specimen showing their microscopy features

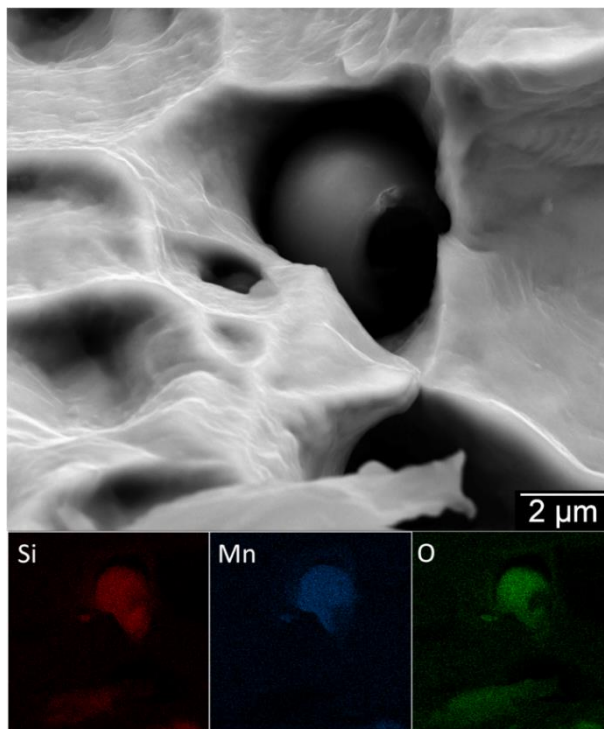


Figure 2-11: SEM image of a SS316L sintered fractured specimen and corresponding EDS elemental map showing a Si-Mn-O inclusion inside a spherical dimple



Figure 2-12: Photographic image of both fractured SS316L sintered tensile specimen (top) and SS316L wrought specimen (bottom) showing two types of necked regions

## 2.5 Discussion

The mechanical properties of the 3D printed SS316L in this work were compared with the literature of SS316L additively manufactured via FFF, PBF and DED techniques. The results are summarised in Table 2-4 which also includes the typical properties obtained from well-established powder-based processes such as MIM and PM. The MIM-316L and UNS standard requirements for the S31603 grade were also added for comparison. Ultimately some characteristics obtained from literature such as the size of the precursor powder, as well as the average grain size and amount of porosity of the densified SS316L obtained with FFF, PBF and DED processes are given in Table 2-4 for comparison.

### 2.5.1 Influence of sintering on the microstructure

This study revealed that the thermal profile in Figure 2-1b for sintering yielded an average grain size of 40  $\mu\text{m}$ , which is larger than the observed in the wrought sample. This can be seen in Figure 2-5 and Figure 2-8. The grain growth most likely took place as a result of the high temperature and long dwelling time inside the furnace. Similar grain growth has been reported in other FFF investigations<sup>85, 94, 150</sup>. It is pertinent to note, that the grain growth did not lead to the formation of a growth dependent texture. In contrast, due to different thermal processing with the PBF and DED involving a rapid melting followed by a rapid solidification, the produced material is strongly textured and the microstructure is also asymmetric containing elongated columnar grains in the build direction along with much smaller grains that could grow preferentially along the scanning directions<sup>103, 162</sup>.

The micro-CT analysis showed that after sintering, the final porosity of the additively manufactured SS316L was 1.27% v/v, which appears consistent with the findings by Y. Thompson et al.<sup>151</sup> showing less porosity is produced after sintering at higher peak temperatures and longer dwell time<sup>151</sup>. The porosity content also depends on the built orientation and printing raster patterns, as it was reported by Damon et al.<sup>85</sup> and Suwanprecha et al.<sup>87</sup>. Similar effects were also found for PBF and DED<sup>74, 161</sup>. The size of the pre-alloyed powder employed for making the feed material and used in this investigation

was 8 to 30 times smaller than the particles generally used in vast majority investigations with PBF and DED. Therefore it would be a subject of research how PBF and DED can produce denser objects with a porosity as low as 0.2%<sup>76, 162, 163</sup>. The elongated macroporosity found in the manufactured sintered SS316L is a common defect of the FFF technique due to the inherent nature of the line-by-line and layer-by-layer process, regardless of the feedstock or post-processing<sup>57, 182, 183</sup>. This pattern of porosity can be seen in Figure 2-6, creating a 3D mesh-like structure inside the bulk volume, and a stack of lines resembling the layer-by-layer printing process in the contour shell of the specimen. The same type of FFF defect is reported elsewhere<sup>85, 87-89, 169, 173, 184</sup>.

Spherical nanosized Si-, Mn- and O- rich inclusions, shown in Figure 2-3, were observed in the original feedstock before sintering, which might alter or create a new set of inclusions. Similar findings in the feed powder of AM and PM processes have been reported elsewhere<sup>170, 177, 178, 185</sup>. Some investigations suggest that these inclusions are formed in the powder during its atomisation process<sup>177, 185</sup>. During sintering, these inclusions may undergo physical and chemical changes, and may evolve into a new set of particles, as seen in Figure 2-7. The presence of this new type of irregular inclusions rich in Cr, Mn and O, suggests the importance of the sintering process on their morphology. The transformation from the fairly stable Si-Mn-O into the Cr-Mn-O-type after the heat treatment of Fe-Cr alloys has also been studied elsewhere<sup>186-189</sup>. These investigations observed that the chemical composition of the Si-Mn-O-type inclusions present in the as-cast Fe-Cr alloys will either remain or change during heat treatment between 1000 °C and 1300 °C, depending on the initial content of Cr and Si in the steel matrix. Further changes associated with new transformation phenomena—as those occurring post sintering in the 1100 to 1200 °C range for the PBF manufactured SS316L alloy—make the matter more complex<sup>189</sup>. The dwell time at peak temperature during the heat treatment was also found to play important roles for the transformation<sup>186, 189</sup>.

### **2.5.2 Influence of sintering on the mechanical properties**

The results presented herein showed that a sinter-based extrusion technology can be used to 3D print SS316L with a tensile strength ( $S_u$ ) and ductility in agreement with the standard requirements for the UNS S31603 grade, and a yield strength ( $S_y$ ) slightly lower (~2%) than the minimum specified<sup>176</sup>. The higher yield strength ( $S_y$ ) of SS316L wrought, see in Table 2-3, can be a contribution of the smaller grain size distribution as per the Hall-Petch equation<sup>98, 99</sup>. However, it should be noted here that many interdependent factors contribute the yield phenomena, and therefore it should not be further discussed based on the grain size only.



An attempt was made to predict the minimum grain size requirement to attain the UNS S31603 standard benchmark of 170 MPa, assuming the other factors remains constant. The analysis was done using the Hall-Petch parameters experimentally obtained for SS316L wrought alloys in the literature <sup>190, 191</sup>. However, it becomes clear that none of the reported data fit the performance of the sintered material of the present study, i.e., the calculated yield strength (Sy) for a 40 μm grain size was much higher than the 166 MPa obtained herein. The discrepancy of the results with those of the published data could be explained by the fact that there is a significant presence of twin boundaries that were not taken into account in the Hall-Petch calculations. Also, as it is noted earlier, while Hall-Petch provides a great framework for strength prediction, the complexity of the present materials due to the presence of porosity and inclusions makes it difficult to predict and it requires a dedicated approach to simulate.

In order to shed light on the effect of porosity on mechanical properties, it was shown that the PBF and DED processes can produce SS316L with a porosity content that can be as low as 0.2% <sup>76, 162, 163</sup>, and hence can exhibit improved yield and tensile strength. Porosity has a detrimental effect on these strength and ductility parameters because of the reduced area supporting the load and the stress concentration factor at each pore <sup>170</sup>. However, an investigation on the effects of sintering conditions on the mechanical properties of MIM SS316L showed that only the tensile strength and elongation were dependent on the porosity content <sup>192</sup>. Further details, on the influence of porosity in the strength of an additively manufactured SS316L via PBF and DED can be seen elsewhere <sup>1, 74</sup>.

Regarding ductility, this study indicated that the elongation at fracture of the sintered tensile specimens was in average 70% higher than other metal FFF studies, as shown in Table 2-4. However, in some of these studies, the reported elongation was not calculated per ASTM E8 standard <sup>152</sup>, which might explain the difference. When compared to the reported data of PBF and DED manufacturing, the elongation obtained in this study was 20% to 80% higher. The reason might be due to the fact that there is a significant strain field in the PBF and DED manufactured samples that makes a drop in ductility. Some improvements in ductility from the presence of annealing twins has also been reported elsewhere <sup>1-4</sup>.

### **2.5.3 Influence of sintering on the fracture mode**

The SS316L sintered specimens were fractured in a ductile manner. The spherical dimples observed in Figure 2-10d appeared similar in size and uniformly distributed throughout the fractured surface. This mode of fracture is predicted to be caused by the presence of oxide inclusions, as shown in Figure 2-7, which acted as the void nucleation sites <sup>98</sup>. The inclusion

content, compared to SS316L wrought, is suspected to have led to the voids coalescence into a single crack that lead to the fracture during in tension. As a result no secondary central cracks nor parabolic dimples were found in the fractography. It is pertinent to note that the presence of parabolic dimples indicates shear fracture <sup>193</sup>. Therefore, the absence of these features in the sintered fracture structure suggests that the material failed in pure tension <sup>193</sup>. The presence of larger voids indicates coalescence in both the wrought and sintered tensile specimens, as shown in Figure 2-10b and Figure 2-10d, respectively.

Another characteristic observation in the fracture surface of the SS316L sintered specimen was the lack of a cup-and-cone shape at the necked region, as shown in Figure 2-12, which is a common feature of a ductile fracture <sup>98,99</sup>. The reason can be explained by the tensile flow instability phenomena <sup>98</sup>. In short, for a tensile specimen with a rectangular cross-section two types of tensile flow instabilities can take place, i.e., diffuse and localised necking. The transition from diffuse to localised necking, as well as the final extent of each instability mode, depends on the capacity of the material to accommodate strains before the geometrical softening cancels its strain hardening <sup>98</sup>. In other words, when comparing two metals, the one with the higher strain-hardening exponent ( $n$ ) will tend to maintain the rectangular shape of its cross-section for a longer period during the tensile test before the fracture, than the metal with the smaller  $n$ -value. The  $n$ -value was calculated for both sintered and wrought materials to predict the mode of behaviour by using the tensile test data and following the procedure reported in <sup>98</sup>. The values were 0.56 and 0.44 for the sintered and wrought material, respectively. It can be seen from the different necked regions in the sintered and wrought specimens in Figure 2-12, that the final instability mode was affected by the different  $n$ -values. As a result, the sintered specimen showed a larger localised necking than the wrought. Furthermore, when comparing the present investigation results with those from pure copper (99.99%) rectangular tensile specimens, it was found that the instability of the copper specimens was dominated by localised necking, making no cup-and-cone shape <sup>194</sup>, because copper has an identical  $n$ -value of 0.54 <sup>98</sup>.

Table 2-4: Summary of mechanical properties, powder size, grain size and final porosity of SS316L manufactured by Metal FFF, PBF, DED, MIM, PM and standard requirements for UNS S31603 and MIM-316L grade

Manufacturing technology	Young's modulus (E)	Yield strength (Sy)	Tensile strength (Su)	Elongation at fracture	Powder size	Grain size	Final porosity
	(GPa)	(MPa)	(MPa)	(%)	( $\mu\text{m}$ )	( $\mu\text{m}$ )	(%)
Metal FFF (this work)	196	166	524	96	d90 5.0	40 $\pm$ 23	1.27
Metal FFF <sup>94</sup>	93 - 154	168 - 187	409 - 499	17 - 37	n/s	75 $\pm$ 20	1.9 - 2.1
Metal FFF <sup>85</sup>	185 $\pm$ 5	155 - 165	500 - 520	32 - 37	n/s	25 $\pm$ 3	0.5 - 1.7
Metal FFF <sup>86</sup>	n/s	93 - 105	219 - 312	6 - 13	n/s	n/s	4.6
Metal FFF <sup>88</sup>	n/s	n/s	412	56.3	3 - 15	n/s	7.5
Metal FFF <sup>89</sup>	157.2 $\pm$ 4.5	148.0 $\pm$ 4.5	443.9 $\pm$ 5.9	43.3 $\pm$ 2.5	1 - 10	n/s	9.8
Meta FFF <sup>150</sup>	198	252 $\pm$ 7	521 $\pm$ 16	9	20 - 53	45 $\pm$ 5	7
Metal FFF <sup>168</sup>	132 $\pm$ 65	n/s	296 $\pm$ 78	32 $\pm$ 16	n/s	n/s	16
Metal FFF <sup>172</sup>	n/s	251	561	53	n/s	n/s	n/s
Metal FFF <sup>91</sup>	n/s	194 $\pm$ 19	441 $\pm$ 27	29.5 $\pm$ 3.8	30 - 50	n/s	7.8
Metal FFF <sup>106</sup>	152	167	465	31	n/s	n/s	1.5
PBF <sup>76</sup>	219 $\pm$ 41	517 $\pm$ 38	687 $\pm$ 40	32 $\pm$ 5	20 - 63	n/s	< 0.2
PBF <sup>74</sup>	n/s	430 - 536	509 - 668	12 - 25	20 - 50	1	1.4 - 4.8
DED <sup>161</sup>	204 - 218	201 - 284	457 - 509	27 - 42	44 - 106	n/s	< 1.0
DED <sup>162</sup>	n/s	388 $\pm$ 42	588 $\pm$ 53	48 $\pm$ 6	50 - 150	$\leq$ 10	0.1 - 0.2
PM SS316L <sup>170</sup>	103 - 144	176 - 289	308 - 468	11 - 19	typ. 12	n/s	12.7 - 20.6
MIM SS316L <sup>171</sup>	185	180	520	40	n/s	n/s	n/s
UNS S31603 <sup>176</sup>	202 <sup>181</sup>	min. 170	min. 485	min. 40	n/a	n/s	n/a
MIM-316L <sup>195</sup>	190	min. 450	min. 450	min. 40	n/s	n/s	n/s

## 2.6 Conclusions

Stainless steel 316L was additively manufactured with a sinter-based extrusion technology. A detailed microstructure characterisation, tensile tests, and fractography were conducted to investigate the effects of sintering in the final microstructures and mechanical behaviour of the manufactured materials. Based on the results the following conclusions can be drawn:

1. The SS316L sintered samples revealed an annealed microstructure composed of fully austenitic grains with an average grain size of 40  $\mu\text{m}$  and 1.27% v/v of combined porosity. None-metallic particles, such as Si-Mn-O and Cr-Mn-O inclusions, were also obtained. Nanosized Si-Mn-O-type were found in the initial pre-alloyed SS316L powder, probably as a sub-product of its atomisation process. Further research is required to elucidate the mechanism responsible for the transformation of the Si-Mn-O inclusions into the Cr-Mn-O particles during sintering. Thermodynamic stability studies followed by different stages of sintering

and in-depth microstructural analyses using methods, such as TEM-based techniques, will bring new insights into this complex phenomenon.

2. The SS316L sintered samples had a Young's modulus, tensile strength, and ductility comparable to those of a standard UNS S31603 grade; nevertheless, with a yield strength 2% lower than the specified minimum value. The main reason for the lower yield strength was attributed to the relatively large grains as defined by the general Hall-Petch relationship. The detrimental effect of porosity content requires further investigation.
3. The SS316L sintered samples revealed a ductile fracture in pure tension with two distinctive features: i) a fractured surface with uniformly distributed spherical dimples and no secondary cracks, and ii) a necked region without the typical cup-and-cone shape. The first type of fracture surface was proposed to be the product of the larger number of oxide inclusions present in the microstructure compared to the wrought case, leading to the formation of multiple voids coalescing into a single crack. The second fracture surface case was associated with the capacity of the sintered samples to accommodate a larger amount of strain-hardening during the tensile test, compared to the SS316L wrought specimens, which reduced the effect of the diffuse necking while promoting the localised necking instead as the dominating instability mode.

## **Chapter 3: Laser-based powder bed fusion of SS316L: Microstructures and Crystallographic Texture**

This chapter corresponds to a publication that has been reformatted to align with the overall style of the thesis and to address the comments from the examiners.

### **Publication:**

Santamaria R, Salasi M, Rickard WD, Pojtanabuntoeng K, Leadbeater G, Iannuzzi M, Reddy SM, Quadir MZ. Crystallographic Texture and Substructural Phenomena in 316 Stainless Steel Printed by Selective Laser Melting. *Materials*. 2023 Jun 9;16(12):4289.

<https://doi.org/10.3390/ma16124289>

# Crystallographic Texture and Substructural Phenomena in 316 Stainless Steel Printed by Selective Laser Melting

## 3.1 Abstract

There is a fast-growing interest in the use of selective laser melting (SLM) for metal/alloy additive manufacturing. Our current knowledge of SLM-printed 316 stainless steel (SS316) is limited and sometimes appears sporadic, presumably due to the complex interdependent effects of a large number of process variables of the SLM processing. This is reflected in the discrepant findings in the crystallographic textures and microstructures in this investigation compared to those reported in the literature, which also vary among themselves. The as-printed material is macroscopically asymmetric in terms of both structure and crystallographic texture. The  $\langle 101 \rangle$  and  $\langle 111 \rangle$  crystallographic directions align parallel with the SLM scanning direction (SD) and build direction (BD), respectively. Likewise, some characteristic low-angle boundary features have been reported to be crystallographic, while this investigation unequivocally proves them to be non-crystallographic, since they always maintain an identical alignment with the SLM laser scanning direction, irrespective of the matrix material's crystal orientation. There are also  $500 \pm 200$  nm columnar or cellular features, depending on the cross-section, which are generally found all over the sample. These columnar or cellular features are formed with walls made of dense packing of dislocations entangled with Mn-, Si- and O-enriched amorphous inclusions. They remain stable after ASM solution treatments at a temperature of 1050 °C, and therefore, are capable of hindering boundary migration events of recrystallization and grain growth. Thus, the nanoscale structures can be retained at high temperatures. Large 2–4  $\mu\text{m}$  inclusions form during the solution treatment, with heterogeneous chemical and phase distribution.

## 3.2 Introduction

Selective laser melting (SLM) is a powder-based 3D printing/additive manufacturing (AM) technique for fabricating complex metallic parts with custom-designed internal and/or external structures. In SLM, a digital system drives a high-power laser beam, up to 1 kW, along a predesigned track to melt and fuse metallic powder particles layer by layer to build a complex metal/alloy shape and/or internal structures that otherwise would be impossible to fabricate with conventional metal processing techniques. SLM was initially developed almost two decades ago<sup>196</sup>, but until recently, it has primarily been used in laboratory-scale and industrial prototyping<sup>72, 197-199</sup>. Over the last ten years, the manufacturing sector has shown a keen interest in using SLM for industrial mass production. This is primarily due to improvements in SLM printing hardware, e.g., laser precision, powder manufacturing, etc., thus reducing time and production costs, as well as increasing the inherent metallurgical

benefits of SLM manufacturing<sup>72, 197, 198</sup>. SLM provides a high degree of freedom in alloy compositions, covering both conventional and exotic mixtures, e.g., high-entropy alloys, and provides for post-heating treatments<sup>200-202</sup>. There are also unique metallurgical benefits in terms of the lightweighting and strengthening of material via the control of solidification rates and compositional gradients. These benefits are not possible, or are highly restricted, in conventional metal casting and subsequent thermomechanical processing (TMP)<sup>203-205</sup>. As a result, the SLM technique is rapidly being incorporated into industrial manufacturing<sup>206-208</sup>, particularly in the aerospace, automotive, biomedical and energy sectors<sup>209-211</sup>.

The metallurgical process variables between conventional metal processing and SLM are significantly different<sup>212, 213</sup>. Consequently, the material properties, structures (at macro, micro and nano scales), and application performance have large differences, even for the same alloy composition. Nevertheless, it should be noted that the majority of metal AM techniques are developed from the concept of conventional techniques such as casting, welding, powder processing and/or cladding. These conventional techniques are not ideal when developing additive manufacturing process parameters and variables, and Aboulkhair et al.<sup>212</sup> recently summarized the SLM process variables, and their differences compared to conventional processing. For instance, castability and weldability are considered the primary characteristics for a given alloy's suitability for SLM fabrication. Indeed, there are marked differences between the solidification rates and conventional welding parameters and those involved in SLM. Likewise, the remelting and rewelding during subsequent SLM scanning creates a thermal effect that has some similarities to conventional TMP<sup>199</sup>.

Our current SLM knowledge is limited to a handful of alloy systems, including aluminium<sup>213-216</sup> and titanium<sup>204, 217, 218</sup> alloys, as well as some studies on stainless steel<sup>219-222</sup>, nickel<sup>223-226</sup>, cobalt<sup>227-230</sup>, copper<sup>231</sup> and magnesium<sup>232</sup> alloys. Consistent and systematic investigations are essential to developing a detailed understanding of the effect of process variables on the microstructures and ultimate physical properties of SLM-printed materials; as such, it has taken many decades of research to reach the current level of knowledge for a given alloy system for a given conventional processing. The SLM journey has commenced, and the processes, microstructures and properties of materials processed in this way are in high demand because of the significant benefits and rapid growth of the technique. This paper presents a comprehensive analysis of the crystallography and composition of structures in an SLM-printed 316 stainless steel (SS316) in the macro to the nano scales for advancing and rectifying our understanding on the structural and crystallographic texture phenomena.

### 3.3 Materials and Methods

SLM printing was conducted with a 3D system Pro X DMP 320 machine provided by a commercial 3D printing service company (Amiga Engineering, Tullamarine, VIC, Australia). A SS316 powder feed supplied by TLS Technik GmbH & Co (Bitterfeld-Wolfen, Germany) with  $45 \pm 10 \mu\text{m}$  average size was used to print a rectangular block  $40 \times 40 \times 2 \text{ mm}$  (X:Y:Z), see the schematic in Figure 3-1a inset. The other SLM parameters were  $30 \mu\text{m}$  layer thickness, 250 W laser power, 900 mm/s laser speed,  $30 \mu\text{m}$  scan resolution, parallel raster pattern with  $0^\circ$  rotation, and high-purity argon as the shielding gas. The feed chemical composition was provided by the supplier as 0.02 wt.% C, 0.51 wt.% Si, 1.0 wt.% Mn, 17.5 wt.% Cr, 2.3 wt.% Mo, 11.1 wt.% Ni, and Fe balance.

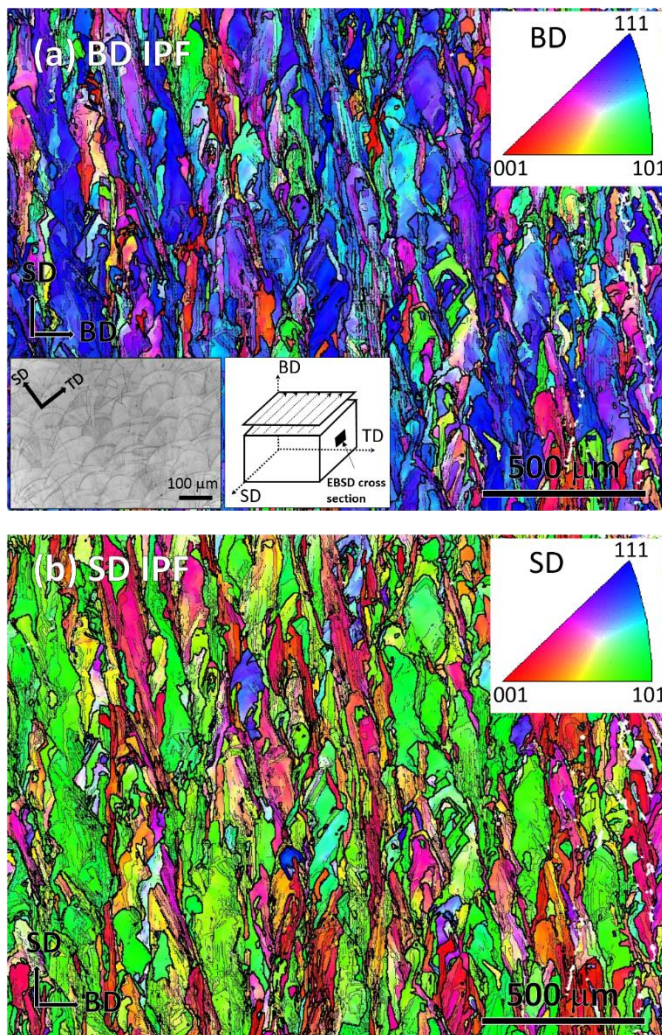


Figure 3-1: EBSD-measured color-coded IPF map of the as-printed SLM sample, taken from the transverse direction (TD), showing the orientation along the (a) BD and (b) SD. The insets in Figure 1a show the optical microscopy image and the EBSD cross-section

The printed material was subjected to an isothermal solution treatment at  $1050^\circ\text{C}$  for 4 h in an argon-purged furnace followed by immediate water-cooling. The longitudinal cross-



section, see the schematic in Figure 3-1a inset, of both the as-printed and heat-treated samples were cut, mechanically polished down to colloidal silica finish, and then ion milled with a Technoorg Linda SEMPRep II system (Budapest, Hungary) to obtain a defect-free surface suitable for investigation by electron backscattered diffraction (EBSD) investigation. The ion milling parameters were 8 kV, 6° tilt and 360° rotation. EBSD was conducted with an Oxford Instruments Symmetry™ system attached to a Tescan Mira (Brno, The Czech Republic) field emission scanning electron microscope (FE SEM) operated at 15 kV beam energy. Iron FCC (face-centred cubic) phase from the Oxford database was used for indexing EBSD patterns and the Oxford Instruments' AztecCrystal software v.2.1.259 was used to post-process and analyse the EBSD data.

Site-specific transmission electron microscopy (TEM) samples were prepared from bulk samples using a Tescan Lyra Ga+ (Brno, The Czech Republic) focused ion beam (FIB)-SEM. The final polishing step was performed with a low beam energy of 2 kV to minimize ion beam damage. A FEI Talos FS200X G2 (Waltham, MA, USA) FE TEM was used for the TEM investigation and was operated at 200 kV. Elemental mapping was conducted by an energy dispersive spectroscopy (EDS) attached as two pairs of a FEI Super X detection system. Location-specific diffraction analysis was performed using selective area diffraction (SAD) with an aperture with a diameter of 200 nm and convergent beam electron diffraction (CBED). A double tilt holder was used to tilt the sample to the intended crystallographic zone axis by navigating through the CBED generated Kikuchi pattern. TEM imaging was conducted both in conventional and scanning TEM (STEM) modes. For STEM, the bright field (BF) and high-angle annular dark-field (HAADF) mode were used to enhance diffraction and atomic number contrast, respectively. TEM data acquisition and analysis was undertaken using Velox software and diffraction data analysis was conducted using the international centre for diffraction data (ICDD) database.

### **3.4 Results and Discussion**

#### **3.4.1 Structural Symmetry and Crystallographic Texture**

Figure 3-1a,b show EBSD color-coded inverse pole figure (IPF) maps in the building direction (BD) and scanning direction (SD) in a BD-SD cross-section from an SLM-printed block. The investigated cross-section schematic is shown in the inset in Figure 3-1a, in which the terminology of the orthogonal print axes is shown, in convention with comparable studies, e.g.,<sup>233</sup>. In Figure 3-1, the optical micrograph shows the characteristic print features in an SD-TD surface previously reported in numerous investigations<sup>74, 105, 233, 234</sup>. From the IPF maps, it is clear that the BD and SD were predominantly oriented along the <111> and

$\langle 101 \rangle$  crystal directions, respectively. It has been well-established that crystallographic texture in iron controls its anisotropy in mechanical, thermal, magnetic and optical properties. The observed macroscopic crystallographic texture is therefore likely to play a fundamental control on the anisotropy of physical properties in SLM-printed SS316. The thick and thin black lines in the EBSD map represent the high-angle ( $>15^\circ$ ) and low-angle ( $3\text{--}15^\circ$ ) misorientation boundaries, respectively. The high-angle boundaries are broadly parallel to the laser scanning tracks associated with printing. There was no evidence of the formation of the  $\Sigma 9$  twin boundary ( $\langle 111 \rangle 60^\circ$ ) in the as-printed sample. This finding is consistent with the other literature, where no twin boundaries were reported in SLM-printed SS316, although the wrought form of the material contained annealing twins<sup>105, 234</sup>. The formation of twin boundaries is generally promoted by low solidification temperatures<sup>235, 236</sup>. Therefore, in the case of SLM-manufactured SS316, where solidification occurs almost instantly at cooling rates ranging from  $10^3$  to  $10^7$  K/s<sup>72, 73, 237, 238</sup>, the formation of twin boundaries is hindered. This rapid cooling prevents sufficient time for the atoms to rearrange, which in turn delays the nucleation and growth of twin boundaries. This is in contrast to wrought SS316L, where cooling rates are much slower and facilitate the formation of twin boundaries<sup>105, 234</sup>.

In the IPF map presented in Figure 3-1b, there are thin  $\langle 001 \rangle$ -oriented layers, coloured in red, between thicker  $\langle 101 \rangle$ -oriented printing tracks, coloured in green. These green and red layers are called ‘major’ and ‘minor layers’ by Sun et al.<sup>239</sup> (pp. 89–93). The thickness of the major and minor layers varied between 100 and 200  $\mu\text{m}$  and 50 and 100  $\mu\text{m}$ , respectively, suggesting an overall crystallographic relationship between the major and minor layers. In both IPF maps, there are other orientations in the major layers, which are present in the red and green regions in Figure 3-1a, and red and blue regions in Figure 3-1b. EBSD analysis in the TD revealed mixed orientation, not presented in the Figure 3-1. These findings suggest that a sample-scale macroscopic crystallographic texture forms in SLM-printed SS316, which is consistent overall with the recent literature, but the reported textures vary in terms of crystal orientation<sup>239-242</sup>. An epitaxial growth mechanism between the major and minor layers is regarded as the origin of the overall texture development<sup>239</sup>. However, lattice epitaxy requires a perfect match between two lattice interfaces with common coincident sites, which is somewhat unrealistic to imagine in the SLM-printed material, because it contains a continuous change in orientation, as reflected by a gradual change in colour within short distances in the EBSD maps. Hence, a separate in-depth investigation at a finer length scale is required to find out whether there are epitaxies over short distances, and if this collectively develops the overall texture.

In Figure 3-2a, the misorientation boundaries are elucidated in a higher-resolution, 100 nm step size, IPF map, whereby the SD is plotted as per the color-coded IPF section in the inset. As before, the high- ( $>15^\circ$ ) and low-angle ( $3\text{--}15^\circ$ ) boundaries are represented by thick and thin black lines, respectively. The corresponding Kernel average misorientation (KAM) map is shown in Figure 3-2b, in which each data point represents the mean orientation difference with the eight surrounding neighbouring points. The blue–yellow–red legend in Figure 3-2b indicates the relative KAM intensity. There is a correlation between Figure 3-2a,b, viz., comparison of the white encircled areas shows that the high-stored-energy spots have a higher density of misorientation boundaries. This observation can be understood in relation to dislocation density because a higher dislocation density is required to accommodate any misorientation. There were also regions of low stored energy. One such example is encompassed with a white rectangular box, within which there is a small orientation variation, represented by a minor change in the IPF colour variation. Such low misorientation variations indicate the presence of dislocation mesh and cell structures, which usually accommodate relatively less energy<sup>243</sup>. Therefore, the as-printed sample showed an overall heterogeneous distribution of the stored energy. This finding explains the spatial variation of the micro- and nano-scale mechanical data in the SLM-printed material<sup>244, 245</sup>.

Figure 3-2a also reveals several other morphological features of the boundary. For example, the majority of the boundaries were straight, though there were several high-angle boundaries that had convoluted trajectories, some of which are indicated with white arrows. This phenomenon indicates the occurrence of a thermally induced restoration process, perhaps from the heat flow from the subsequent SLM scanning<sup>243</sup>. It is important to note that the boundaries depicted in Figure 3-2 are also present in Figure 3-1. However, Figure 3-1 provides a broader field of view, making the details of the boundaries less apparent. Figure 3-2 complements Figure 3-1 by offering a closer view (or finer scale) that provides additional information about the boundary features. There was no sign of recrystallization, as noted by an absence of a trailed region with a uniform orientation behind a migrating high-angle boundary<sup>243</sup>. The convoluted high-angle boundaries are expected to have formed during solidification or due to subsequent thermal restoration<sup>243</sup>, although the process did not progress to the boundary migration stage of recrystallization.

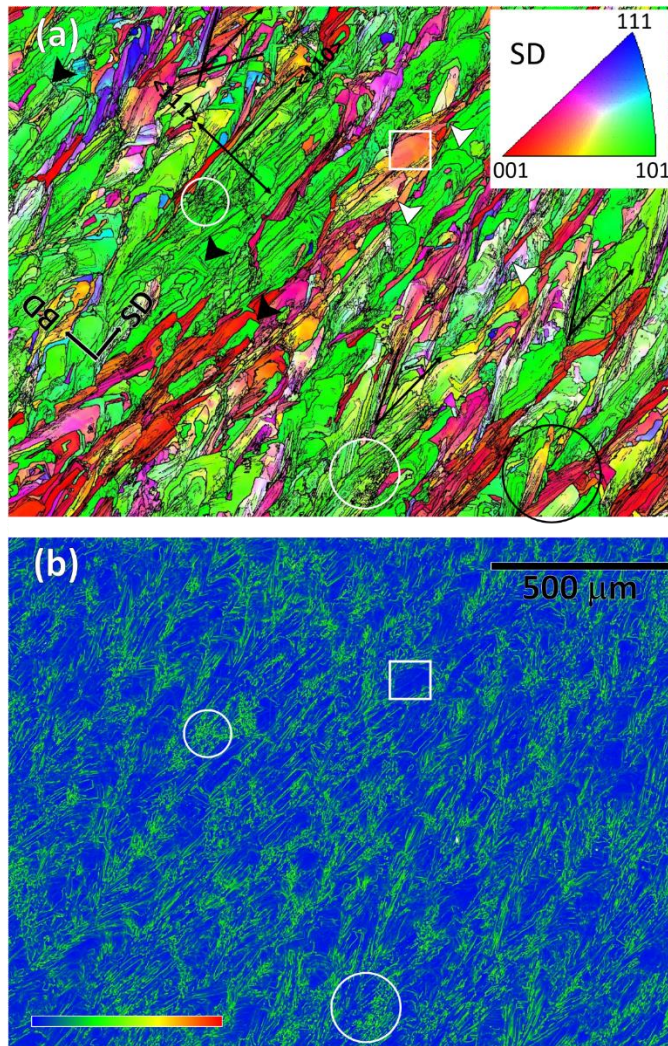


Figure 3-2: Higher-resolution EBSD maps of the as-printed SLM sample showing (a) color-coded IPF map of SD to illustrate the inhomogeneities in the high ( $>15^\circ$ ) and low-angle ( $3\text{--}15^\circ$ ) boundary distribution and their alignments with the SD and (b) the corresponding inhomogeneities in the KAM plot

### 3.4.2 Substructural Features

There is a profuse presence of straight misorientation boundaries in Figure 3-2a, which are aligned, within a certain angular range, with the SD, as indicated by the black lines. Some straight boundaries are aligned along the SD, as shown in Figure 3-2a, which is  $\langle 101 \rangle$  of the lattice direction. A small fraction also aligns at the right angle, in short segments indicated with the black arrows, which is along the BD  $\parallel \langle 111 \rangle$ . The remainder, accounting for the largest fraction of straight boundaries, are aligned in the  $\pm 30^\circ - 45^\circ$  angular range, with the highest frequency being around  $\pm 35^\circ$ . Some boundary combinations also resemble a leaf vein structure, with changing directions; one such example is circled in black at the right bottom of Figure 3-2a. Therefore, the overall alignment of the straight boundaries is rather complex, which Dinda et al. <sup>246</sup> (pp. 2152–2160) described as a function of the laser scanning strategy. In some recent studies, the boundaries appeared to have a coincidence with the

crystallographic planes, most commonly along the {100} plane trace, e.g., SS316-, Ni-25% (Mo, Nb and Ti)-, Al-, Ta-, Ti-Mo-Zr-Al- and Mo-Si-alloys<sup>239, 240, 246-251</sup>. A few mechanisms for the formation of these textures have been outlined in the published literature based on the formation of the solid/liquid interface in order to explain their crystallographic origin. The scan rate and laser energy have been reported to play a vital role in this regard<sup>252</sup>. In this investigation, however, the alignment of the straight boundaries invariably remained identical within an angular range with the SD, irrespective of the matrix orientation, as shown in Figure 3-2a. For instance, the boundary orientations in the blue-, located in the upper left, and red-oriented regions comprise the same angular alignments with SD as the boundaries found in the vast majority green regions. This suggests that the low-angle straight boundaries are non-crystallographic, viz., they do not preferentially form on a particular lattice plane trace(s). Although this conclusion is made based on unequivocal evidence, it should be noted that only a 3D EBSD can reveal the real crystallography of a 3D interface. There is evidence that 2D trace analysis of 3D boundary features may lead to misleading conclusions. One such example is the low-angle microband boundaries that form in high stacking fault energy materials that have been claimed to be both crystallographic<sup>253</sup> and non-crystallographic<sup>254</sup>. This debate continued until reconciliation was achieved on the basis of a 3D EBSD investigation<sup>255, 256</sup>.

A recent article by Pham et al.<sup>242</sup> (p. 749) accounts for the variations in boundary formation in SLM-printed SS316, such as those seen in Figure 3-2a. The fundamental basis remains identical to the previous reports, viz., the boundaries form along the solid-liquid interface during the solidification process<sup>239, 257, 258</sup>. In Pham et al.'s simulation work, it was demonstrated that side branching occurs, similarly to the current findings shown in Figure 3-1 and Figure 3-2, during the solidification process, and thus alters the shape of the solidifying boundary front. As a result, the alignment of the solidification interface changes, and therefore, the formation of low-angle boundaries takes place over a wider angular range. The magnitude of side branching depends on a number of factors, primarily on the thermal gradient and heat flux, and the SLM parameters that control these two. Each narrative in the literature on low-angle crystallographic boundary formation, including Pham et al.'s study, is overwhelmed by the assumption that the solid/liquid interface appears as a crystallographic lattice interface. However, physical details on the mechanism by which the habit plane or rotation axis correlate with a preferred crystal plane or direction are missing. Therefore, the mechanism of low-angle boundary formation is rather complicated, because of the simultaneous occurrence of rapid solidification with the complex mechanical interaction of the semi-solid pool by laser beam movement. In addition, there is thermal pulsing during the subsequent overlay of layers.

Numerous investigations have reported columnar structures that also appear as fine cellular structures in the transverse cross-section of SLM-printed SS316 <sup>74, 259, 260</sup>. An example of such a cell structure is shown as an SEM image in the inset of Figure 3-3a. Unlike the low- and high-angle boundary structures in Figure 3-1 and Figure 3-2, this structure was found homogeneously throughout the sample. These cellular structures have been reported to vary in size from 0.25 to 1.2  $\mu\text{m}$ , with the actual size having an inverse relationship with the laser scanning speed. <sup>238, 261, 262</sup> It has been observed that these structures exhibit a weaker strengthening effect compared to the grain boundaries of the microstructure <sup>262</sup>. Because of the submicron-scale fineness of the cellular structures, an electron-transparent TEM sample was prepared using FIB-SEM site-specific lift-out methods. Figure 3-3a shows a HAADF STEM image of the TEM sample, in which the columnar structures are sub-vertical in the cross-sectional lamellae. The walls of the columns are densely populated with dislocations, and the walls are spaced parallel at an average distance of 500 nm. These boundaries were also decorated with 5–30 nm spherical particles. The particles were tangled within the boundary dislocations, see higher magnification image in Figure 3-3b, and created a pinning effect. These particles are likely to have restricted any thermally activated migration, and thus, restricted the structures to the nanoscale. The dislocation walls were 50–150 nm in thickness and are expected to have created a strain field, which became apparent through the diffraction contrast in the BF STEM imaging in Figure 3-3c, which was taken after tilting the sample so that the boundaries were edge-on. These dislocation features are expected to provide elevated strengthening in the SLM-printed SS316 material over the conventionally processed grade that usually comprises large equiaxed grains, hundreds of  $\mu\text{m}$  in size, and twin boundaries. This is reflected in a 20–50% improvement in the tensile strength of SLM-printed SS316 over the conventional grade with an identical chemical composition <sup>74</sup>. The strength can also be improved by changing the laser strategy that works at a larger length scale. While further discussions of mechanical properties are outside the scope of this paper, it is expected from the results presented herein that superior strengthening at the micro and nano scale can be achieved in SLM-printed grade due to the retention of nanostructures and the formation of inclusions due to the rapid cooling ( $\sim 10^3$ – $10^5$  K/s) of SLM solidification <sup>263</sup>.

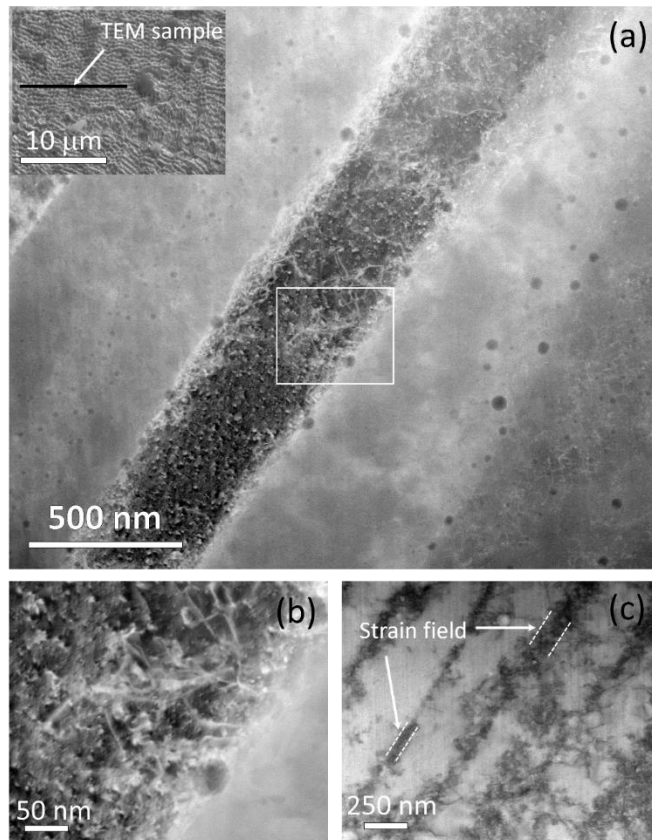


Figure 3-3: HAADF STEM images showing (a) particle decorations in the dislocation-constituted boundaries of the commonly found fine cell structures (in the inset) in the SLM-printed sample. (b) Particle pinning at the dislocation boundary in a higher-magnification HAADF STEM image of the white rectangular area located in subfigure (a). (c) BF STEM image showing the strain field width of the dislocation boundaries at the boundaries edge on tilted condition

The darker appearance of the particles in the HAADF STEM images in Figure 3-3 indicates that they had a lower average atomic weight than the matrix. In Figure 3-4, an area was selected that contained larger particles, and these were subjected to elemental analysis by STEM-EDS. Elemental maps revealed that the particles were rich in Mn, Si and O. Significant efforts were devoted to determining the crystallographic identity of the inclusions using SAD and CBED diffraction techniques, but no diffraction spots were observed other than those from the FCC iron matrix, and therefore, these particles are likely amorphous. This finding is consistent with the report by Salman et al.<sup>260</sup> (pp. 205–212). It is pertinent to note that Shibata et al.<sup>264</sup> (pp. 522–528) found larger particles, ~1 μm, with identical morphologies in cast SS316. These were characterized as MnO–SiO<sub>2</sub> particles, solely based on the chemical ratio measured by electron probe microanalysis and thermodynamic calculations. In some cases, they also found a small association of Cr<sub>2</sub>O<sub>3</sub>. In regard to the current study, it is important to note that Cr was not measured within the particles, and no Cr-C crystalline diffraction patterns were observed. Therefore, Cr is expected to remain in the solid solution to provide the intended stainless property in the SLM-printed SS316.

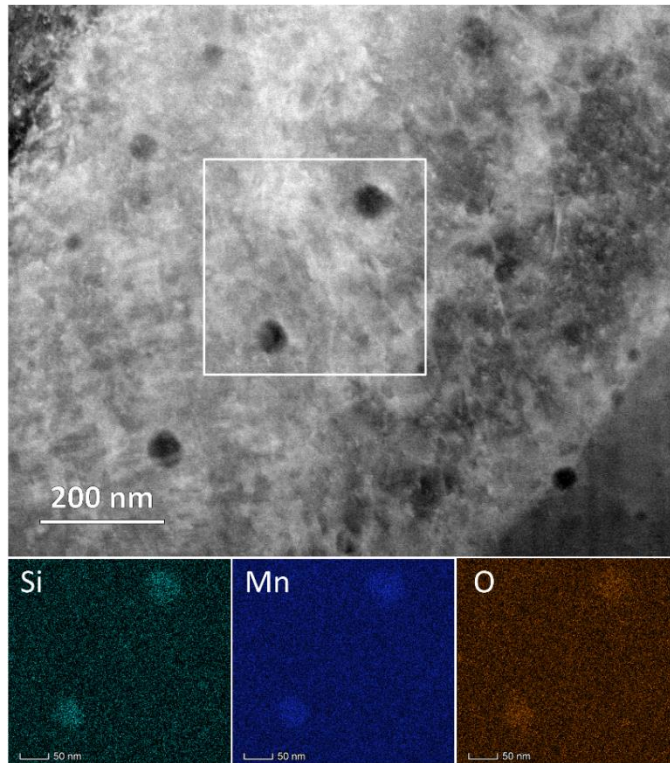


Figure 3-4: HAADF STEM image (top) of the nanoparticles and corresponding EDS-measured elemental maps (bottom) of the white rectangular area, showing that the particles are rich in Si, Mn and O content in the as-printed SLM sample

### 3.4.3 Solution treatment structures

A solution treatment at 1050 °C for 4 h, per ASM<sup>265</sup> recommendations, of the as-printed sample is expected to anneal any thermally unstable microstructures, and to ensure a uniform Cr dissolution into the matrix. It is pertinent to note that the stainless properties are impaired in conventional-grade SS316 because of the inadequate presence of atomic Cr in the solution that occurs due to Cr-C formation. The solution treatment brings the Cr atoms back to the matrix as solutes. Cr-containing inclusions were not observed in the samples in this study, see Figure 3-3 and Figure 3-4, which suggests that the solution treatment is not needed for Cr dissolution purposes in the SLM material. However, the heterogeneous boundary structures shown in Figure 3-2 may result in an uneven Cr distribution, because dislocations are naturally preferable sites for solute atoms. Therefore, the solution treatment may indeed promote an even Cr concentration.

Interestingly, only a subtle change took place in the substructures during the 1050 °C solution treatment. Figure 3-5a,b present a comparative view in the form of KAM maps that reveal an overall reduction in the KAM-intensive boundary density after the solution treatment. The solution-treated structure is also shown in the BF STEM micrograph in Figure 3-5c, in which the dislocation-constituted boundaries underwent a thermal relaxation



process, compared with Figure 3-3, viz., the boundaries were curved and the dislocations were dissociated. The rectangular area in Figure 3-5c is magnified in the HAADF STEM image in Figure 3-5d. Analysis revealed boundary pinning by the inclusions that were found in the as-printed sample in Figure 3-3 and Figure 3-4. They were measured to contain Mn, Si and O as per the as-printed sample. Overall, the inclusion density was significantly reduced by the solution treatment, perhaps because of some degree of dissolution and/or agglomeration. The high stability of the inclusions after the solution treatment at 1050 °C explains why recrystallization and grain growth did not take place in the SLM-printed material. Previously, Shibata et al. <sup>264</sup> (pp. 522–528) reported that amorphous Mn-Si-O particles remain stable even after 1200 °C solution treatment in cast SS316, where grain growth was not prevented because the density was low and the inclusions size was large, >1 μm.

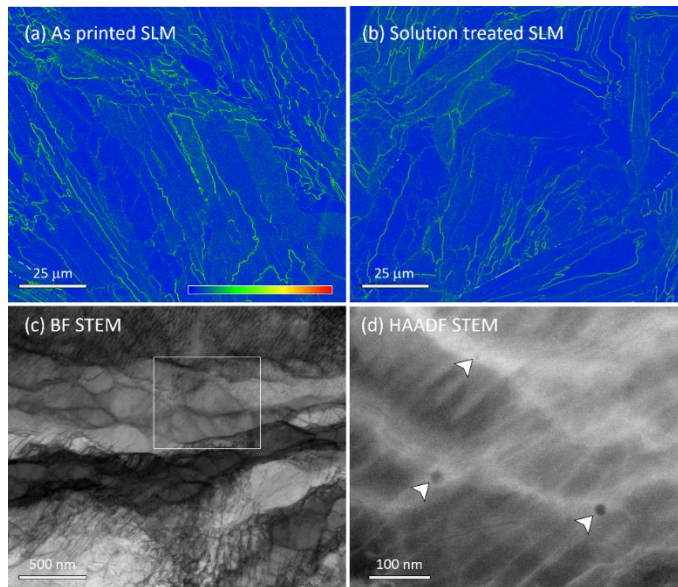


Figure 3-5: EBSD-measured high-resolution KAM map showing the differences in the stored energy distribution between the (a) as-printed and (b) solution-treated SLM samples in the BD-SD cross-section. TEM investigation of the solution-treated sample shows (c) the changes in the dislocation boundary structures in a BF STEM image and (d) the retention of boundaries by particle pinning in a magnified HAADF STEM image of the rectangular area marked in subfigure (c)

It is important to note that inclusions 2–4 μm in size were also observed in the solution-treated sample that were absent under as-printed conditions. An example is shown in the upper inset in Figure 3-6a, whereby a TEM lamella was prepared by FIB and presented as a STEM HAADF image (Figure 3-6a) in order to determine the chemical distribution within the inclusion. The surrounding iron matrix appears brighter. It should be noted that it was identified via TEM-EDS that the inclusions were rich in Mn, Si, and O, although there were also Cr- and O-rich regions within the inclusions, which can also be seen as brighter regions, as indicated by arrows, in the darker overall matrix. An SAD pattern was taken of the

marked area and indexed as  $\text{Cr}_3\text{O}_4$ , as illustrated in the lower inset of Figure 3-6a. The iron matrix also contained Cr, which was expected as the solute. These findings suggest that during the solution treatment, a large fraction of the nano-sized inclusions agglomerate into large 2–4  $\mu\text{m}$  inclusions. The Cr from the solid solution also diffused and participated in the formation of inclusions, since Cr was not found in the inclusions in the as-printed sample. Overall, the localized corrosion resistance of the as-printed SLM-manufactured SS316 is excellent, which has been attributed to factors such as the absence of sulphides, the presence of a more stable passive film, lower rates of metastable pitting, and a higher pitting potential compared to its wrought counterpart<sup>77-79</sup>. However, the presence of these large inclusions with heterogeneous chemical and structural distribution after heat treatment, as reported in this work, has been shown to be detrimental to the alloy's resistance to localized corrosion by decreasing its pitting potential<sup>115</sup>. Therefore, the solution treatment recommended by ASM<sup>265</sup> for conventional SS316 is, indeed, expected to be detrimental to the SLM-printed material.

SLM-manufactured SS316 components have shown excellent mechanical properties<sup>74-76</sup> and localized corrosion resistance<sup>77-79</sup>, often surpassing their conventionally manufactured wrought counterparts. Therefore, it is crucial to evaluate their performance against common damage mechanisms observed in the energy sector, such as stress corrosion cracking (SCC) or hydrogen-induced cracking (HIC), in both as-printed and heat-treated microstructures. Additionally, exploring the optimization of properties through variations in printing parameters or the utilization of post-processing steps would be of great significance.

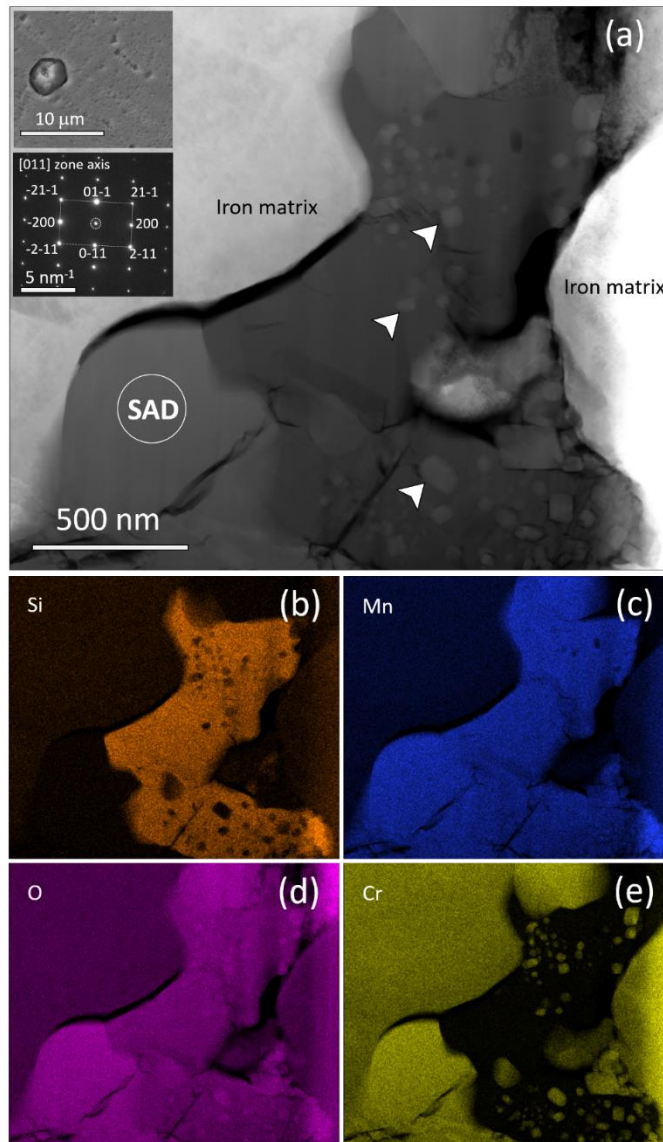


Figure 3-6: The structural and chemical heterogeneity of inclusions in the solution-treated SLM-printed sample is shown in (a) the HAADF STEM image, and (b–e) the corresponding elemental mapping for Si, Mn, O, and Cr, respectively. The insets in (a) show the inclusion from which the TEM sample was prepared, and the indexed SAD pattern of  $\text{Cr}_3\text{O}_4$  from the SAD-labelled area

### 3.5 Conclusions

In this investigation, a thorough microscopic characterization of SLM SS316 under as-printed and solution-annealed conditions was conducted at the macro, micro and nano scales. The findings suggest some of the existing findings are inconclusive or imprecise, and require further investigation to mature our knowledge in this area. The conclusions of this study can be summarized as follows:

1. SLM-printed material possesses an asymmetric crystallographic texture and material structure. The microstructure has a distinctive structural morphology along the

orthogonal axes of the sample, and develops crystallographic textures in SD  $\parallel \langle 101 \rangle$  and BD  $\parallel \langle 111 \rangle$ .

2. Heterogeneous distribution of misorientation boundaries and stored energy were found throughout the SLM-printed structures. Twin boundary formation was not observed in either the as-printed or solution-annealed samples.
3. In the as-printed structures, the typical straight misorientation boundaries were characterized as being non-crystallographic. The boundaries maintained general alignment with the SD within an angular range, irrespective of the matrix's crystal orientation, although there were occasional coincidences with crystal plane traces.
4. The high-angle boundaries in the SLM substructures underwent thermal restoration, which was activated by the heat originating from the printing of the subsequent layer. Pinning by the nano inclusions hindered classical recrystallization, and thus, prevented the formation of a defect-free annealing structure, even after 4 h of solution treatment at 1050 °C.
5. A nano-scale lamellar structure with a width of  $500 \pm 200$  nm formed homogeneously throughout the printed material. Depending on the orientation, the structures appeared with cellular or columnar morphologies in SEM and TEM images. Their boundaries contained dense dislocation structures tangled with fine amorphous inclusions containing Mn, Si and O. Cr was not found above the limit of detection in the inclusions. Hence, Cr remains in the matrix to provide the stainless properties.
6. Some degree of dissociation of the dislocation boundaries occurred during the solution treatment, but the overall refined structures were retained. Additionally, inclusions with a size of 2–4  $\mu\text{m}$  formed, consisting of composite structures and chemical distribution. These inclusions can have detrimental effects on the localized corrosion resistance of the alloy.

## **Chapter 4: Sinter-based material extrusion of SS316L: Stress corrosion cracking susceptibility and crack- branching behaviour**

This chapter corresponds to a publication that has been reformatted to align with the overall style of the thesis and to address the comments from the examiners.

### **Publication:**

Santamaria R, Wang K, Salasi M, Iannuzzi M, Mendoza MY, Quadir MZ. Stress Corrosion Cracking of 316L Stainless Steel Additively Manufactured with Sinter-Based Material Extrusion. *Materials*. 2023 May 26;16(11):4006. <https://doi.org/10.3390/ma16114006>

# **Stress Corrosion Cracking of 316L Stainless Steel Additively Manufactured with Sinter-Based Material Extrusion**

## **4.1 Abstract**

This study investigates the stress corrosion cracking (SCC) behaviour of type 316L stainless steel (SS316L) produced with sinter-based material extrusion additive manufacturing (AM). Sinter-based material extrusion AM produces SS316L with microstructures and mechanical properties comparable to its wrought counterpart in the annealed condition. However, despite extensive research on SCC of SS316L, little is known about the SCC of sinter-based AM SS316L. This study focuses on the influence of sintered microstructures on SCC initiation and crack-branching susceptibility. Custom-made C-rings were exposed to different stress levels in acidic chloride solutions at various temperatures. Solution-annealed (SA) and cold-drawn (CD) wrought SS316L were also tested to understand the SCC behaviour of SS316L better. Results showed that sinter-based AM SS316L was more susceptible to SCC initiation than SA wrought SS316L but more resistant than CD wrought SS316L, as determined by the crack initiation time. Sinter-based AM SS316L showed a noticeably lower tendency for crack-branching than both wrought SS316L counterparts. The investigation was supported by comprehensive pre- and post-test microanalysis using light optical microscopy (LOM), scanning electron microscopy (SEM), electron backscatter diffraction (EBSD), and micro-computed tomography (micro-CT).

## **4.2 Introduction**

Additive manufacturing (AM) encompasses the technologies used to create physical objects from digital data by successively joining materials<sup>56</sup>. Sinter-based material extrusion, one of the AM technologies categorized by the International Organization for Standardization (ISO)<sup>59</sup>, is gaining popularity due to its ease of use, low running and maintenance costs, and reduced safety risks<sup>58,60</sup>. Sintered-based AM involves a multi-step approach that incorporates the principles of fused filament fabrication (FFF), also known as fused deposition modelling (FDM), powder metallurgy (PM), and metal injection moulding (MIM). The process starts by heating the pre-alloyed powder-bound feedstock to the binder's melting point, and then extruding it through a nozzle to fabricate the so-called "green part". In the subsequent step, the primary binder is removed through full immersion in a solvent bath that leaves a component consisting of powder held by the secondary binder. This so-called "brown part" is still incomplete in terms of engineering properties. Therefore, in the final step, the component is strengthened by heating it just below the alloy's melting point, allowing the metal particles to sinter and create a structure that requires minimal post-processing or machining. The resulting sintered microstructure has been reported to have a

weak crystallographic texture, relatively large equiaxed grains, and a high population of  $\Sigma 3$  twin boundaries, pores, and oxide inclusions<sup>88, 94, 149, 151, 153</sup>. These characteristics diverge from the typical columnar grains found in other AM technologies where the heat follows the dissipation route, such as laser-engineered net shaping (LENS)<sup>266, 267</sup>, electron beam additive manufacturing (EBAM)<sup>268, 269</sup>, and laser-based powder bed fusion (LPBF)<sup>270, 271</sup>.

Stress corrosion cracking (SCC) is a form of environmentally-assisted cracking (EAC), typically nucleating from localized corrosion sites when susceptible materials are exposed above a threshold stress in specific corrosive environments<sup>6, 9-12</sup>. For instance, in conventional austenitic stainless steels, cracks originate from pits that create the stress concentration and acidic environment required for cracking<sup>272-278</sup>. The trajectory of the crack is determined by the energy associated with its propagation process. Therefore, secondary cracks, or crack-branching, occur due to the presence of an obstacle or a more energetically favourable path<sup>279</sup>. The presence of a tensile stress, either residual, applied, or both, along with a specific corrodent, are required for SCC to occur. Moreover, the cracks can grow and propagate at much lower stress levels than those needed to fracture the material without the corrodent<sup>6, 10, 46, 48, 280, 281</sup>. Therefore, brittle SCC fracture can occur on otherwise highly ductile materials<sup>10, 47, 48</sup>.

Austenitic stainless steel UNS S31603 (SS316L) is considered an excellent material for engineering applications due to its exceptional ductility, weldability, and corrosion resistance<sup>8, 10, 282</sup>. Its low carbon content (max. 0.035%<sup>283</sup>) has largely eliminated sensitization of its microstructure, which is responsible for intergranular SCC<sup>8, 10, 282</sup>. However, when exposed to hot environments containing halides, stressed SS316L can still experience transgranular SCC<sup>7, 9, 12, 46</sup>. Consequently, SCC poses a significant threat to the integrity and reliability of equipment in the energy sector. Thus, it is crucial to understand the influence of the AM process on SCC susceptibility.

Among the AM technologies, there has been a significant increase in the use of LPBF to investigate SCC in SS316L due to its ability to produce an alloy with a fully austenitic microstructure<sup>75, 284, 285</sup>, extremely low porosity<sup>74-76</sup>, excellent resistance to localized corrosion<sup>77-79, 286</sup>, and outstanding mechanical properties<sup>74-76</sup>. This is due to the distinctive manufacturing process of LPBF, in which a high-intensity laser is programmed to melt layers of powder feedstock that solidify into near-net-shape parts<sup>58, 59, 71</sup> at cooling rates ranging from  $10^3$  to  $10^7$  K/S<sup>72, 73, 237, 238</sup>. However, this heating and cooling cycle at each deposited layer results in LPBF-manufactured SS316L with high thermal residual stresses<sup>75, 83, 84</sup>, which are known to increase its susceptibility to SCC<sup>83, 122, 124</sup>.

The objective of this work was to determine the SCC behaviour of SS316L additively manufactured with sinter-based material extrusion when exposed to different stress levels and temperatures in an acidic chloride environment. The study focused on the impact of the sintered microstructure on the SCC initiation and crack-branching susceptibility. The SCC response was compared with those obtained from similarly tested wrought SS316L samples in solution-annealed (SA), and cold-drawn (CD) conditions. The investigation was supported by comprehensive pre- and post-test microanalyses that included LOM, SEM, EBSD, and micro-CT.

### 4.3 Materials and Methods

#### 4.3.1 Materials

The AM SS316L samples used in this investigation were fabricated using Bound Metal Deposition (BMD) (Desktop Metal, Studio System; Burlington, MA, USA). The technology includes the following: (i) rods of pre-alloyed SS316L powder held in a mix of polymer and wax binder, (ii) an FDM 3D printer, (iii) a solvent-based debinding unit, (iv) a sintering furnace, and (v) a cloud-based software (Live Studio v3.0) to control the process from digital object to sintered part. Further information regarding the manufacturing process can be found in a previous publication by Santamaria, R., et al. <sup>153</sup>. All BMD SS316L specimens for tensile and SCC testing were produced with the parameters summarized in Table 4-1. For comparison, commercially available SA wrought SS316L seamless tubes and CD wrought SS316L rod bars were included in the investigation. The tubes were 22 mm in diameter and 2 mm in thickness, while the rod bars were 25 mm in diameter. The dimensions of all BMD-manufactured specimens, including thickness, width, and length, were within 10% of the original design after sintering.

Table 4-1: Summary of parameters used to manufacture all BMD SS316L test specimens

<b>Printing Parameters</b>		<b>Debinding Parameters</b>	
Extrude line width:	0.5 mm	Debinding time:	15 h
Deposited layer height:	0.15 mm	Debinding temperature:	50 °C
Contour shell thickness:	1.50 mm	Debinding pressure:	Atmospheric
Extrusion nozzle size:	0.40 mm	<b>Sintering parameters</b>	
Extrusion rate:	30 mm/s	Heating rate:	~1.0 °C/min
Extrusion temperature:	175 °C	Thermal debinding temperature:	550 °C
Build plate temperature:	60 °C	Thermal debinding dwell time:	2 h
Sintering scale factors:	X = Y = Z = 1.15	Sintering temperature:	1350 °C
Bulk volume raster pattern:	+45°/-45° each layer (see Figure 2-1)	Sintering atmosphere:	Ar > 99.997% vol.
Infill density:	100%	Sintering dwell time:	2 h
Print orientation:	Vertical (Z)	Cooling rate:	Furnace cooling



### 4.3.2 Analytical Characterization

Table 4-2 presents the elemental composition of the BMD SS316L used in this investigation determined with inductively coupled plasma atomic emission spectroscopy (ICP-AES) analysis. The chemical compositions of SA wrought SS316L and CD wrought SS316L, as given in their material test reports (MTR), are also presented in Table 4-2. The UNS S31603 nominal chemical composition range is added for comparison.

Table 4-2: Elemental composition in wt% of BMD SS316L, SA wrought SS316L, CD wrought SS316L, and nominal composition of UNS S31603

Alloy	Source	Fe	C	Cr	Ni	Mo	Si	Mn	P	S
BMD SS316L	ICP-AES	Bal.	0.020	16.3	10.4	2.12	0.61	1.22	0.010	0.010
SA SS316L	MTR	Bal.	0.012	16.1	10.1	2.03	0.46	0.92	0.036	0.002
CD SS316L	MTR	Bal.	0.019	16.7	10.1	2.03	0.41	1.72	0.024	0.025
UNS S31603	ASTM A213 <sup>283</sup>	Bal.	Max. 0.035	16.0 18.0	10.0 14.0	2.00 3.00	Max. 1.00	Max. 2.00	Max. 0.045	Max. 0.030

The constituent phases were identified via X-ray diffraction (XRD) analysis using a Cobalt K alpha ( $\lambda = 0.179$  nm) powder diffractometer radiation source operating at 35 kV 40 mA with a LynxEye detector (Bruker, Billerica, MA, USA, D8 Discover). All XRD data were collected within  $2\theta$  ranging from  $40^\circ$  to  $130^\circ$ , using a step size of  $0.015^\circ$ , and a time interval of 0.7 s. Content of  $\gamma$ -austenite (FCC) and  $\delta$ -ferrite (BCC) phases were quantified from the XRD patterns as the area of each crystalline peak over the total area of crystalline peaks. Micro-CT analysis was performed on a  $2 \times 2 \times 2$  mm<sup>3</sup> cut sample using a 3D X-ray microscope with an exposure energy of 140 kV, during an exposure time of 24 h, and at a pixel resolution of 2.2  $\mu$ m (Zeiss 520 Versa, Oberkochen, Germany).

Microstructural characterization was conducted on representative samples, which were cut, mounted in cold epoxy resin, manually wet-ground with SiC abrasive papers, and mechanically polished down to 1  $\mu$ m surface finish. LOM analysis was conducted on samples chemically etched with a solution containing 100 mL H<sub>2</sub>O, 10 mL HNO<sub>3</sub>, and 100 mL HCl. The concentration of nitric acid and hydrochloric acid was 70% and 32%, respectively.

EBSD analysis was conducted on samples that were polished to a mirror surface finish with 0.02  $\mu$ m colloidal silica, and then ion-milled for 30 min using a beam voltage of 8 kV at a glancing angle of  $4^\circ$  with full cycle rotational movements (TECHNOORG Linda, Budapest, Hungary, SEMPrep2). Samples were surface-coated with a carbon film 5  $\mu$ m thick to prevent electrostatic charging. Microstructures were imaged using secondary electron (SE)

and backscatter (BS) detectors coupled to a field emission scanning electron microscope (FE-SEM) (TESCAN system, CLARA, Brno, The Czech Republic). Elemental composition was mapped with a high-sensitivity Oxford energy-dispersive X-ray spectroscopy (EDS) detection system attached to the FE-SEM. The content of non-metallic inclusions was quantified from EDS elemental maps by dividing the area of oxides or sulphides over the total area of the map, per ASTM E1245<sup>287</sup>.

EBSD was conducted with an Oxford symmetry EBSD detector in the FE-SEM on 70° tilted samples, at a working distance of 20 mm, with a beam energy of 28 kV, and a beam current of 1 nA. A clean-up process was applied to the data to assimilate any non- or mis-indexed points, ensuring that a maximum of 10% of the points were modified. Grain boundaries were detected with a threshold misorientation of 10° in conjunction with a minimum of 8 pixels of fractional difference of misorientation variation and a kernel size of 3 by 3. Kernel average misorientation (KAM) maps were used to investigate the presence of local strain in the microstructures. This analysis was conducted using a 3 by 3 kernel size, a square kernel shape, and a maximum misorientation angle of 5°.

The average grain size was measured as the maximum Feret diameter. The average grain aspect ratio was calculated as the fitted ellipse aspect ratio. Twin content was measured as the fraction length of  $\Sigma 3$  ( $\langle 111 \rangle / 60^\circ$ ) boundaries over the total length of  $\gamma$ -austenite (FCC) boundaries. The Schmid factor on the  $\gamma$ -austenite (FCC) phase was measured in the plane/direction  $\{111\} \langle 110 \rangle$ . All data acquisition and subsequent post-processing were conducted using the software Aztec v.5.1 and AztecCrystal v.2.1.259, respectively.

### **4.3.3 Mechanical Testing**

Tensile tests were conducted according to ASTM E8<sup>152</sup>. BMD SS316L and CD wrought SS316L were tested with rectangular specimens, while SA wrought SS316L was tested using tubular specimens with metallic plugs inserted in their ends to ensure a proper grip. All tests were conducted with a 50 kN universal testing machine (UTM, Shimadzu, Kyoto, Japan, AGS-X series). Displacements were measured using an axial extensometer with 25 mm of gauge length and +25 mm of travel length (Epsilon TechCorp, Jackson, WY, USA). The UTM crosshead speed was set to 0.375 mm/min, and the test was stopped once a clear deviation from the initial linear behaviour was observed. The actual yield strength (AYS) of each alloy was calculated by intersecting their corresponding stress–strain curves with an 0.2% offset line running parallel to their elastic portion, as per ASTM E8 requirements<sup>152</sup>. Figure 4-1 shows the geometries and dimensions of the tensile specimens.

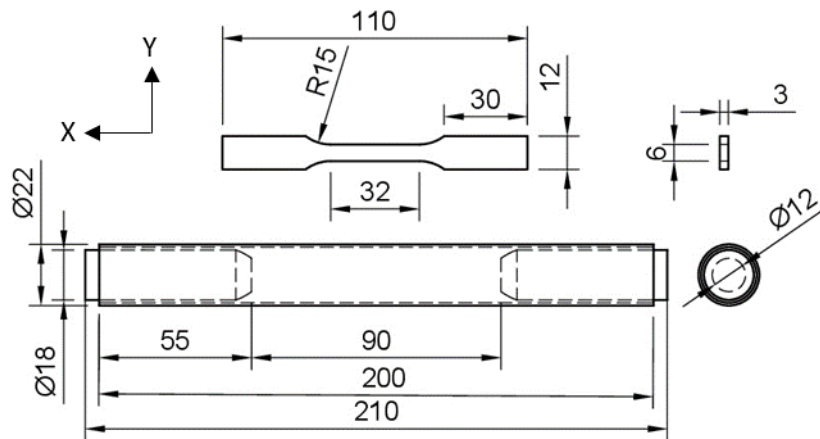


Figure 4-1: Drawings of the specimens used for tensile testing BMD SS316L and CD wrought SS316L (top), and SA wrought SS316L with snug-fitting metallic plugs (bottom). The extrusion direction of the tube is in the X axis. Units in millimetres.

Microhardness was measured on cut samples of untested C-rings prepared similarly to the microstructural characterization procedure that removes the sample preparation induced artefacts. The samples were obtained from the middle of the uppermost curved surface of the C-ring. This test was conducted as per ASTM E384<sup>288</sup> using a microhardness tester (Duramin-4, Struers, Copenhagen, Denmark), an applied load of 2 Kg (HV2), and a dwell time of 15 s. The bulk density was determined according to ASTM B962<sup>289</sup> using a density kit coupled to an analytical balance with a readability of 0.001 g and a linearity of  $\pm 0.002$  g (Mettler-Toledo, ME203, Columbus, OH, USA). The relative bulk porosity content was calculated as the ratio of the measured bulk density and the standard density of UNS S31603 given in ASTM G15<sup>290</sup>.

#### 4.3.4 SCC Susceptibility and Crack-branching

The SCC susceptibility of BMD SS316L and its wrought SS316L counterparts was investigated by exposing C-ring samples to different applied stresses and temperatures. The C-rings were designed following ASTM G38 guidelines<sup>155</sup>, see Figure 4-2. This type of specimen was selected due to its versatility to be elastically deformed at different magnitudes, unlike the U-bent type suggested by ASTM G123<sup>156</sup>. Duplicate BMD and wrought SS316 C-ring specimens were stressed to 60% and 90% of their AYS to study the effect of stress level on SCC susceptibility. Unstressed C-rings, i.e., 0% AYS, were also tested for comparison and to investigate the possible influence of residual stresses on SCC. Tests were performed in a 25% (by mass) sodium chloride (NaCl) solution, which was acidified to pH 1.5 with phosphoric acid ( $H_3PO_4$ ), as per ASTM G123<sup>156</sup>. In addition to the standard boiling condition, tests were conducted at different temperatures, i.e., 30, 60, and 80 °C, to define the stress–temperature SCC thresholds. Magnesium chloride (MgCl) was not used because it is more severe than NaCl.

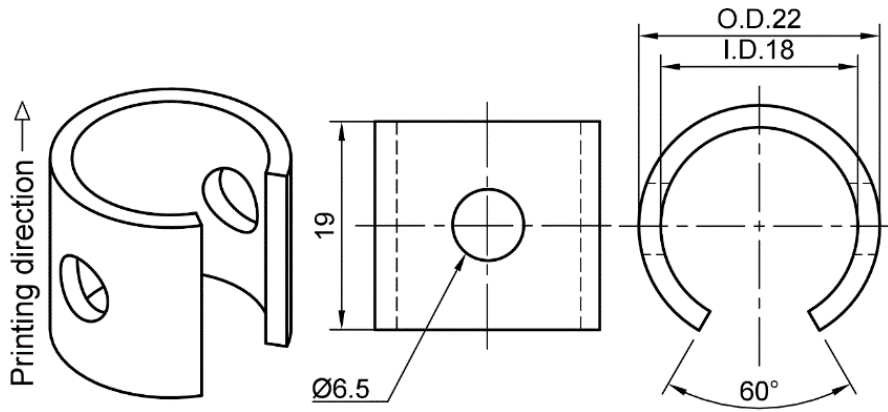


Figure 4-2: Drawings of the C-ring type specimen used to investigate the SCC susceptibility in the BMD SS316L and its wrought SS316L counterparts. Units in millimetres

BMD SS316L C-rings were 3D printed in the vertical direction as shown in Figure 4-2. All surfaces were wet-ground from 80-grit to 600-grit with SiC abrasive paper, avoiding any excessive removal of material. Subsequently, C-rings were constant-strained to the required level, as per ASTM G38<sup>155</sup>. The constant-strain setup, which is shown in Figure 4-3, consisted of two PEEK washers, two M6 titanium flat washers, one M6 titanium socket cap bolt, one M6 titanium flanged lock nut, and a strip of clear PTFE heat shrinkable tube moulded to the bolt. The required strain level was obtained by attaching a 0.3 mm circumferential strain gauge (Tokyo Measuring Instruments, Tokyo, Japan, FLAB-03-11-1LJC-F) to the uppermost curved surface at the middle of the C-ring's arc and width, as shown in Figure 4-3. Then, the bolt was tightened until the reading in the data logger (Ahlborn, Sayner, WI, USA, Almemo 2590) indicated the required strain value corresponding to 60% and 90% AYS. All traces of the strain gauges and adhesive were manually removed with 600-grit SiC abrasive paper. The electrical insulation between the titanium bolt and the C-ring was verified with a digital multimeter. The C-rings tested at 0% AYS were also prepared, as shown in Figure 4-3, but no strain was applied in this case. SA wrought SS316L and CD wrought SS316L C-rings were prepared following an identical procedure.

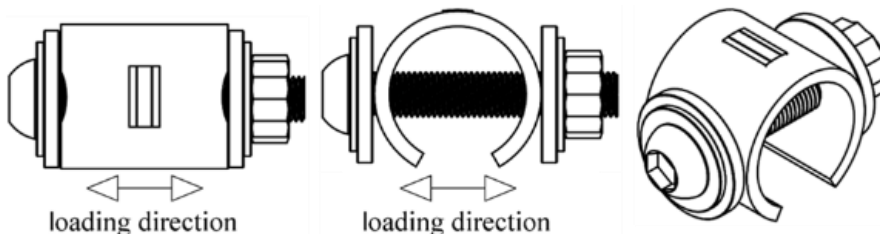


Figure 4-3: Schematics of the constant-strain setup used to stress the C-rings under different levels of AYS. The circumferential strain gauge is located at the uppermost curved surface of the C-ring. The applied load creates a hoop stress that is perpendicular to the print direction.

SCC tests were conducted by immersing the C-rings in a series of Erlenmeyer flasks containing 750 mL of solution at the set constant temperatures. Each temperature was monitored regularly with a thermocouple. Duplicate specimens of stressed and unstressed BMD SS316L C-rings and their wrought counterparts were immersed in the solution. Each Erlenmeyer flask contained three different C-rings, i.e., one from each alloy stressed at the same level. The volume of solution per exposed C-ring surface area ratio was 11 mL/cm<sup>2</sup>, which is twice the minimum ratio according to the ASTM G123 standard<sup>156</sup>. All C-rings were standing on their washers to prevent stagnant solution spots at the contact points. C-rings were removed weekly from the solution and inspected for cracks at a magnification of 20× using a LOM. If no cracks were observed, the specimens continued the test in a freshly prepared solution. If cracks were found, cracked specimens were removed from the test and prepared for microscopy analysis. The tests continued for a maximum of six weeks, as per ASTM G123<sup>156</sup>. The degree of crack-branching was calculated by dividing the total crack length, which includes both the primary and secondary cracks, by the length of the primary crack. LOM images at 10× magnifications were used for this purpose. This approach is consistent with other investigations<sup>83, 291</sup>. Size and depth of pits were measured according to the ASTM G46 standard<sup>292</sup>.

## **4.4 Results**

### **4.4.1 Analytical Characterization**

Representative BMD and wrought SS316 XRD patterns are presented in Figure 4-4, as indicated. The XRD patterns indicated that all the alloys contained almost entirely  $\gamma$ -austenite (FCC) with a minor presence of  $\delta$ -ferrite (BCC) phase. The amount of  $\delta$ -ferrite is summarized in Table 4-3. Retained  $\delta$ -ferrite in a relatively low temperature powder-based additively manufactured SS316L can originate from the gas atomization process of the pre-alloyed powder feedstock due to the ferrite-stabilizer effect of Cr, Mo, and Si<sup>76</sup>. Therefore, the small amount of  $\delta$ -ferrite found in BMD SS316L suggests that its allotropic transformation into the  $\gamma$ -austenite was incomplete during the sintering stage.

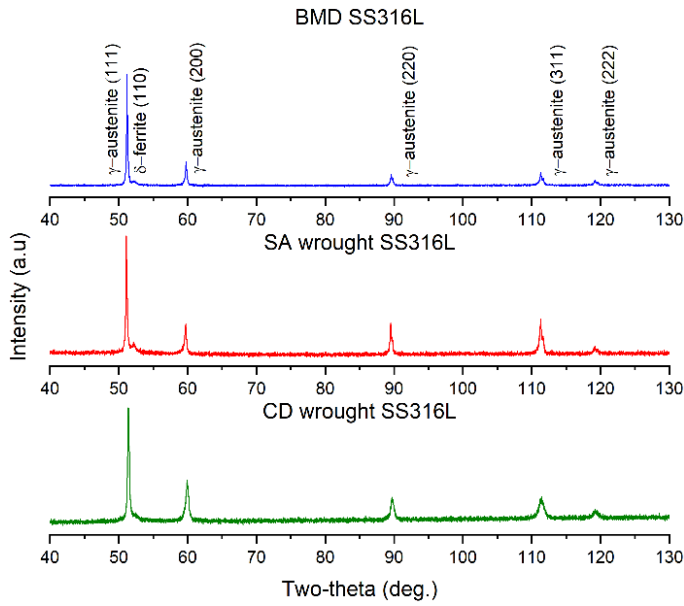


Figure 4-4: Representative XRD patterns of BMD SS316L, SA wrought SS316L, and CD wrought SS316L showing predominance of the  $\gamma$ -austenitic with small fractions of  $\delta$ -ferrite

Table 4-3: Content of non-metallic inclusions,  $\delta$ -ferrite (BCC) phase, and grain size measurements of BMD SS316L, SA wrought SS316L, and CD wrought SS316L

Alloy	Non-Metallic Inclusions (%)	$\delta$ -Ferrite Phase (%)	Average Grain Size ( $\mu\text{m}$ )	Aspect Ratio	Twin Boundaries (%)	Schmid Factor $\{111\}\langle 110\rangle$
BMD SS316L	3.23	6.09	$40.8 \pm 23.8$	$3.1 \pm 2.4$	53.2	0.69
SA SS316L	0.01	7.86	$16.2 \pm 8.5$	$2.2 \pm 1.3$	45.5	0.94
CD SS316L	0.39	0.95	$43.5 \pm 33.6$	$3.9 \pm 3.6$	39.4	0.96

SEM-EDS analysis showed no evidence of sensitization, i.e., Cr depletion in the vicinity of the grain boundaries, in any of the SS316L alloys, as illustrated in the elemental map in Figure 4-5. BMD SS316L contained non-metallic particles rich in O, Si, Mn, and Cr, as seen in Figure 4-5a, which are inherent to PM and MIM manufacturing processes<sup>170, 171, 185</sup>. SA wrought SS316L had an almost negligible amount of round pores, and no oxide inclusions were found, Figure 4-5b. CD wrought SS316L contained manganese sulphide inclusions (MnS), Figure 4-5c, common in cold-worked austenitic stainless steels<sup>282, 293, 294</sup>. Table 4-3 summarizes the content of non-metallic inclusions in BMD SS316L and its wrought counterparts.

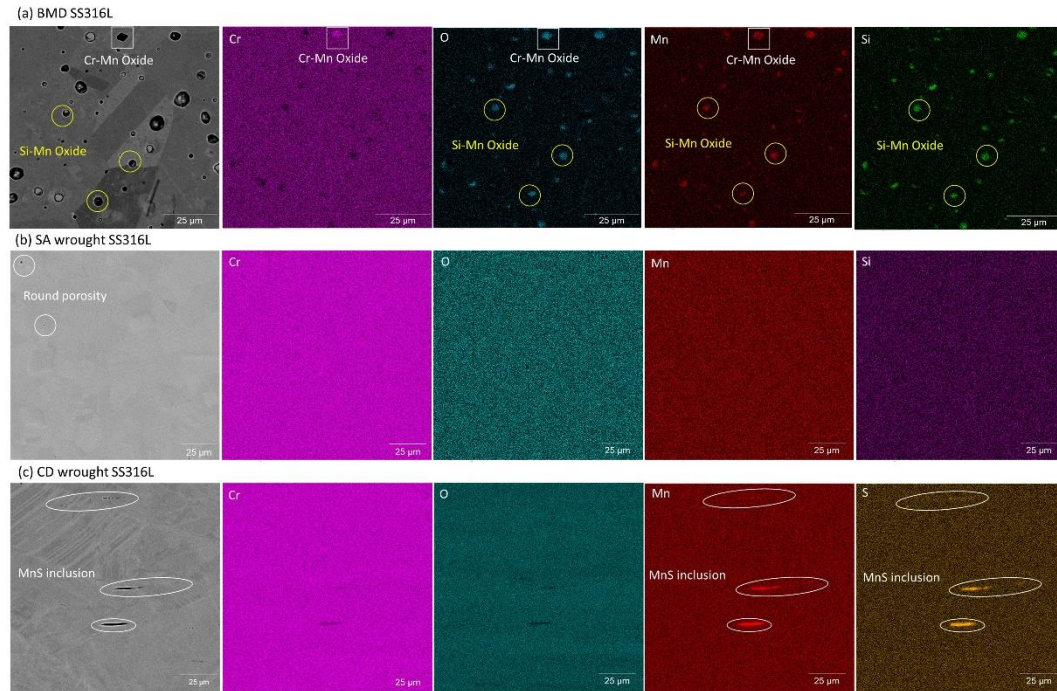


Figure 4-5: Representative EDS elemental map of (a) BMD SS316L showing inclusions rich in O, Si, Mn, and Cr, (b) SA wrought SS316L showing slight presence of round pores and lack of non-metallic inclusions, and (c) CD wrought SS316L showing elongated MnS inclusions

Figure 4-6 shows representative inverse pole figure EBSD maps with respect to the build direction (Y-axis) of BMD SS316L and its wrought SS316L counterparts. The corresponding BMD SS316L  $\{111\}$  pole figures in Figure 4-6a show a weakly textured, almost randomly oriented distribution with low intensity (x1.17 random). In comparison, Figure 4-6b,c shows a slight texture strengthening in wrought SS316L (x2.81 random) and CD wrought SS316 (x2.27 random), as indicated. These texture developments are assumed to be caused by the processing history, which is beyond the scope of this study. Figure 4-6a also shows an elongated pore in the BMD SS316L sample, perpendicular to its build direction. This type of porosity is inherent to the extruding nature of FDM manufacturing<sup>57, 182</sup>.

Figure 4-7 shows the KAM maps of the corresponding EBSD scans in Figure 4-6, illustrating areas of slight local plastic deformation, i.e., residual stresses, in the microstructure of BMD SS316L. Figure 4-7b shows negligible local straining in SA wrought SS316L, as opposed to CD wrought SS316L which contained substantial residual stresses, Figure 4-7c. The distinct degree of residual stresses observed in the wrought materials is caused by their processing conditions<sup>295</sup>, which are also beyond the scope of this study. Grain measurements, such as average grain size, aspect ratio, twin boundary content, and Schmid factors are included in Table 4-3. Further information regarding the influence of the

sintering process on the microscopy of the BMD-manufactured SS316L can be found in a previous publication by Santamaria, R., et al. <sup>153</sup>.

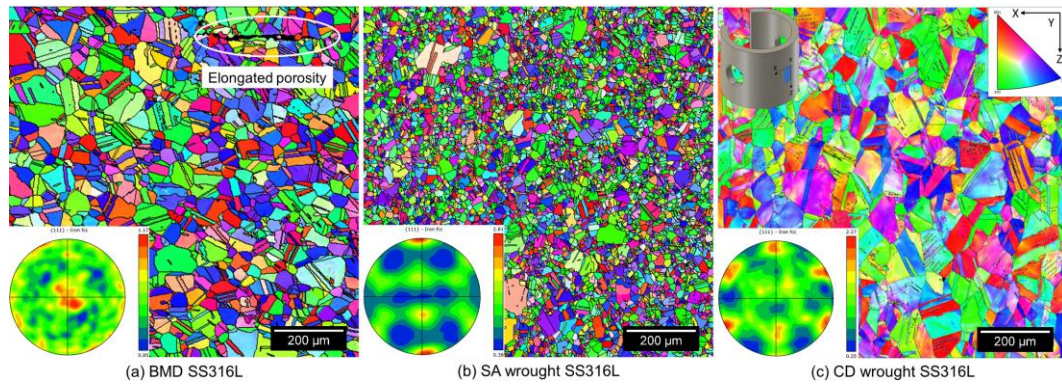


Figure 4-6: Representative EBSD maps with corresponding  $\{111\}$  pole figures, with respect to the build direction (Y-axis), of (a) BMD SS316L, (b) SA wrought SS316L, and (c) CD wrought SS316L C-rings taken from their uppermost curved surfaces

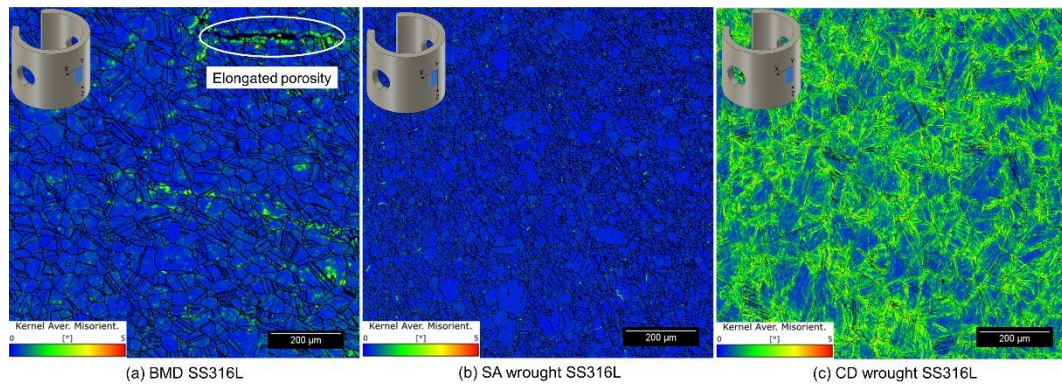


Figure 4-7: Representative KAM maps, with respect to the build direction (Y-axis), with a maximum misorientation angle of  $5^\circ$  in (a) BMD SS316L, (b) SA wrought SS316L, and (c) CD wrought SS316 C-rings taken from their uppermost curved surfaces

#### 4.4.2 Mechanical Testing

Figure 4-8 presents the elastic regions of the engineering stress–strain curves of BMD SS316L and SA and CD wrought SS316L, indicating their corresponding 60% and 90% AYS values. As shown in Figure 4-8, CD wrought SS316L had the highest average AYS due to cold working, i.e.,  $646 \pm 8$  MPa, followed by the SA wrought SS316L, i.e.,  $293 \pm 6$  MPa, and lastly, the BMD SS316L with an AYS of  $167 \pm 2$  MPa. Similar values of AYS in AM sinter-based SS316L have been reported elsewhere <sup>85, 91, 94, 106</sup>. Table 4-4 summarizes microhardness, bulk density, and relative bulk porosity content.



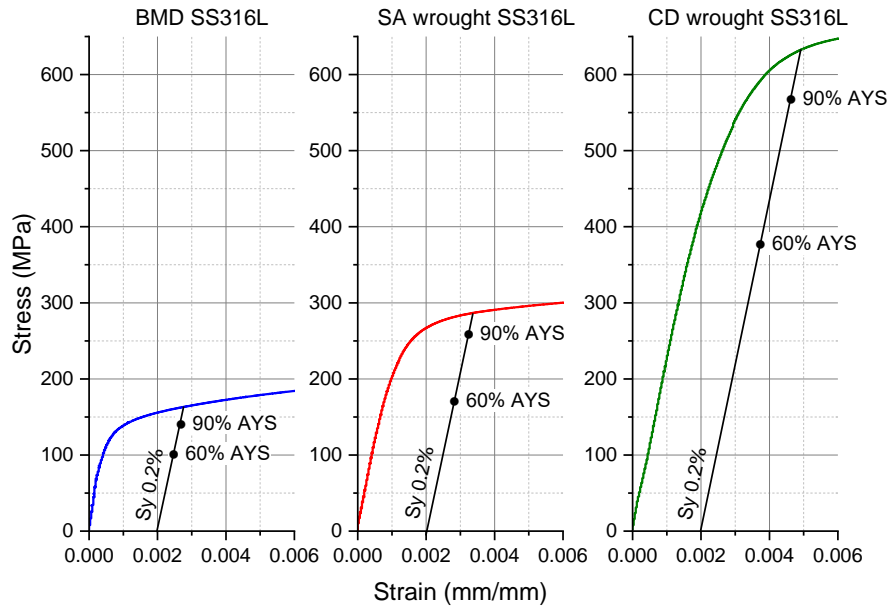


Figure 4-8: Stress–strain curves within the elastic region of BMD SS316L, SA wrought SS316L, and CD wrought SS316L showing their corresponding 60% and 90% AYS

Santamaria et al. <sup>153</sup> conducted a detailed investigation on the impact of the sintering process on the tensile properties and fracture behaviour of the BMD-manufactured SS316L. They found that the AM SS316L had a lower yield and tensile strength, caused by its relatively larger grain sizes. However, AM SS316L showed excellent ductility attributed to the abundance of twin boundaries. The AM SS316L fractured in a ductile manner, with spherical dimples uniformly distributed throughout the fracture surface, containing evidence of oxide inclusions rich in Mn and Si. No secondary cracks or parabolic dimples were observed, indicating that the fracture was due to pure tension. Additionally, the necked region exhibited no cup and cone shape, attributed to the tensile flow instability phenomena.

Table 4-4: Average mechanical properties of BMD SS316L and its wrought counterparts

Alloy	AYS (MPa)	Microhardness (HV2)	Bulk Density (g/cm <sup>3</sup> )	Relative Bulk Porosity (%)
BMD SS316L	167 ± 2	117.1 ± 3.2	7.564 ± 0.013	5.21
SA SS316L	293 ± 6	163.9 ± 2.5	7.935 ± 0.025	0.57
CD SS316L	646 ± 8	277.3 ± 3.2	7.953 ± 0.027	0.35

#### 4.4.3 Pitting and Cracking Susceptibility

Figure 4-9 summarizes the susceptibility to pitting and cracking initiation of BMD and SA and CD wrought SS316L at different stress and temperature levels over six weeks, as indicated. In Figure 4-9, cells coloured in green represent no pitting, cells coloured in yellow indicate that pitting was observed, and cells coloured in red indicate SCC had occurred. At 30 °C, none of the C-rings showed evidence of pitting for the duration of the tests. However,

pits were observed in all alloys within the first week when exposed to higher temperatures, i.e., 60 °C and above. In boiling solution (~106 °C), pits quickly (Week 1) transitioned into cracks for BMD and CD wrought SS316L at 90% AYS. The SCC resistance of all alloys decreased with increasing time, stress, and temperature, in agreement with the literature<sup>6, 11, 47, 296</sup>. Figure 4-9 also shows that SA wrought SS316L had the highest SCC resistance, as indicated by only 2 out of 12 test conditions that led to cracking, followed by BMD SS316L with 4 conditions, and finally, CD wrought SS316L with 7 conditions. It is noteworthy to mention that in stressed CD wrought SS316L specimens, all cracks started from the sharp edges of their curved surface, whereas in unstressed specimens, cracks initiated at their flat surface. The difference in crack initiation location was attributed to the residual stresses introduced during the manufacturing process and subsequent machining of the C-rings<sup>296-299</sup>.

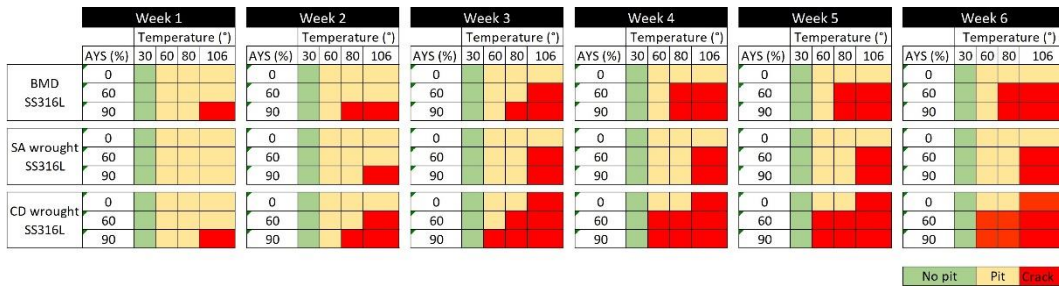


Figure 4-9: Pitting and cracking susceptibility map of BMD SS316L and its wrought SS316L counterparts at different test conditions over a period of six weeks

Figure 4-10 illustrates the size and distribution of corrosion pits in unstressed BMD and SA and CD wrought SS316L C-rings on their flat and curved surfaces after a week of exposure to the boiling solution. As shown in Figure 4-10, the printed material had the largest pits, while both wrought counterparts exhibited smaller pits that were similar in size. However, CD wrought SS316L had more pits than the other two alloys. Figure 4-10 also confirmed that residual stresses were sufficient to cause SCC in the unstressed CD wrought SS316L specimens after a week of immersion in the boiling solution. Table 4-5 summarizes the average pit size measurements made on unstressed C-rings after one week in boiling solution, as well as the average pit depth in cracked specimens under stress. As seen in Table 4-5, BMD SS316L had the largest and deepest pits in both measured conditions, while SA wrought had the smallest ones.

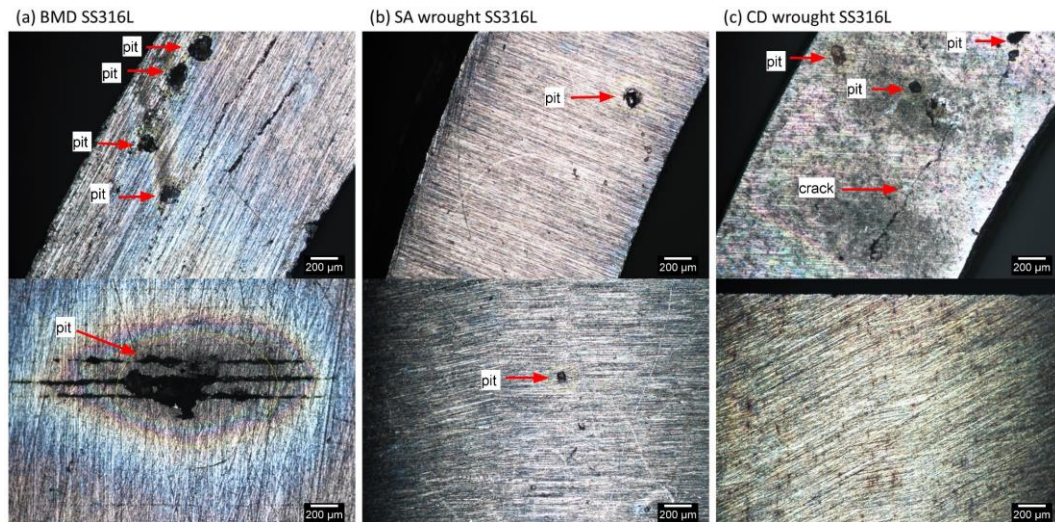


Figure 4-10: LOM images of unstressed C-rings after one week in boiling solution, showing different sizes of corrosion pits in (a) BMD SS316L, (b) SA wrought SS316L, and (c) CD wrought SS316L. The top images correspond to the C-rings' flat surfaces, while the curved ones are presented at the bottom

Table 4-5: Average pit size and pit depth measurements made on stressed and unstressed BMD SS316L C-rings and wrought counterparts

Alloy	Unstressed C-ring (0% AYS) in boiling solution after 1 week		Stressed C-ring (90% AYS) in boiling solution after cracking	
	Pit size in flat surface ( $\mu\text{m}$ )	Pit size in curved surface ( $\mu\text{m}$ )	Pit size ( $\mu\text{m}$ )	Pit depth ( $\mu\text{m}$ )
BMDSS3 16L	$112 \pm 117$	$89 \pm 154$	$406 \pm 359$	$190 \pm 135$
SA SS316L	$31 \pm 27$	$28 \pm 16$	$213 \pm 178$	$58 \pm 27$
CD SS316L	$88 \pm 61$	$27 \pm 11$	$205 \pm 118$	$130 \pm 84$

#### 4.4.4 Crack-Branching Susceptibility

Figure 4-11 shows transgranular SCC in BMD, SA and CD wrought SS316L after exposure to the boiling solution under a stress of 90% AYS. Identical crack morphology was observed in all specimens regardless of the applied stress and temperature. SCC started from pits and propagated perpendicularly to the applied stress direction, in agreement with the literature<sup>47, 296, 300, 301</sup>. Figure 4-11 also shows that BMD SS316L had the least amount of crack-branching while both wrought SS316L counterparts cracked in a similar fashion. The calculated crack-branching ratio for BMD and SA and CD wrought SS316L was  $1.84 \mu\text{m}/\mu\text{m}$ ,  $4.29 \mu\text{m}/\mu\text{m}$ , and  $4.64 \mu\text{m}/\mu\text{m}$ , respectively. No intergranular (IG) cracking was observed during the analysis. IG might have been present at some extent initially; however, since it was not clearly detected, it was considered negligible in comparison to the total length of the transgranular (TG) cracking. Therefore, the length of the crack was considered TG.

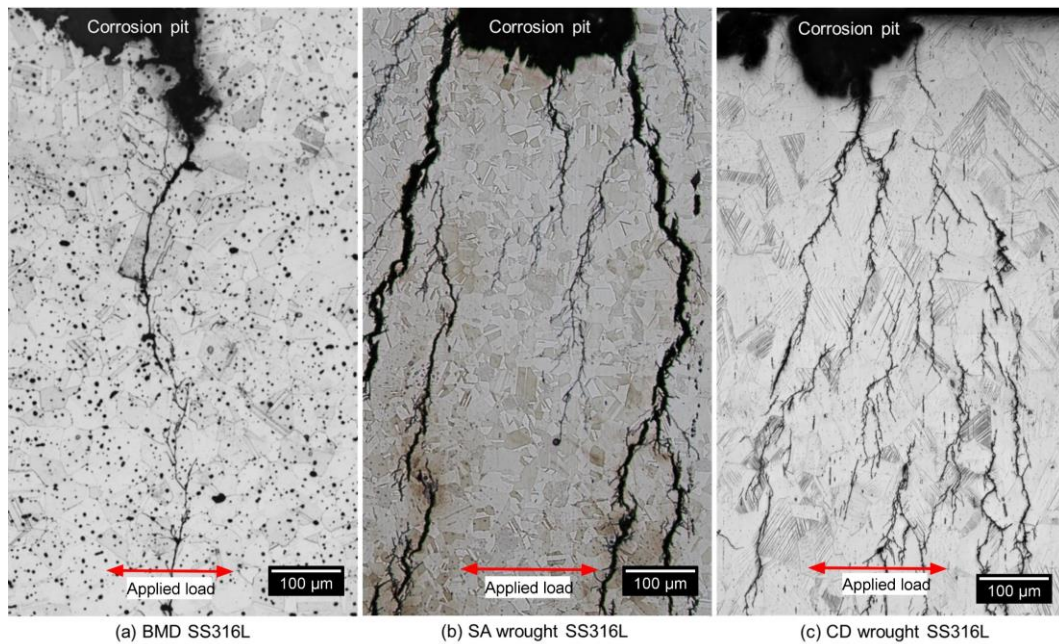


Figure 4-11: LOM images of etched microstructures in (a) BMD SS316L, (b) SA wrought SS316L, and (c) CD wrought SS316L C-rings after exposure to boiling solution, showing SCC initiated from pits and propagated perpendicular to the applied stress of 90% AYS

The transgranular nature of SCC in BMD SS316L was also confirmed by the EBSD analysis shown in Figure 4-12, which include all Euler map, KAM, and phase distribution along with the overlaid band contrast images to facilitate locating crack propagation through the grains. Figure 4-12 also illustrates some of the characteristic features of the BMD SS316L microstructure, such as twin boundaries, round porosity, oxide inclusions, and  $\delta$ -ferrite (BCC). Additionally, Figure 4-13 shows an SEM image of a crack that propagated through elongated pores of a BMD SS316L sample without branching. The lack of branching was attributed to the arresting effect of the pores, which is also visible in the micro-CT scan in Supplementary Video S1 ([link](#)).

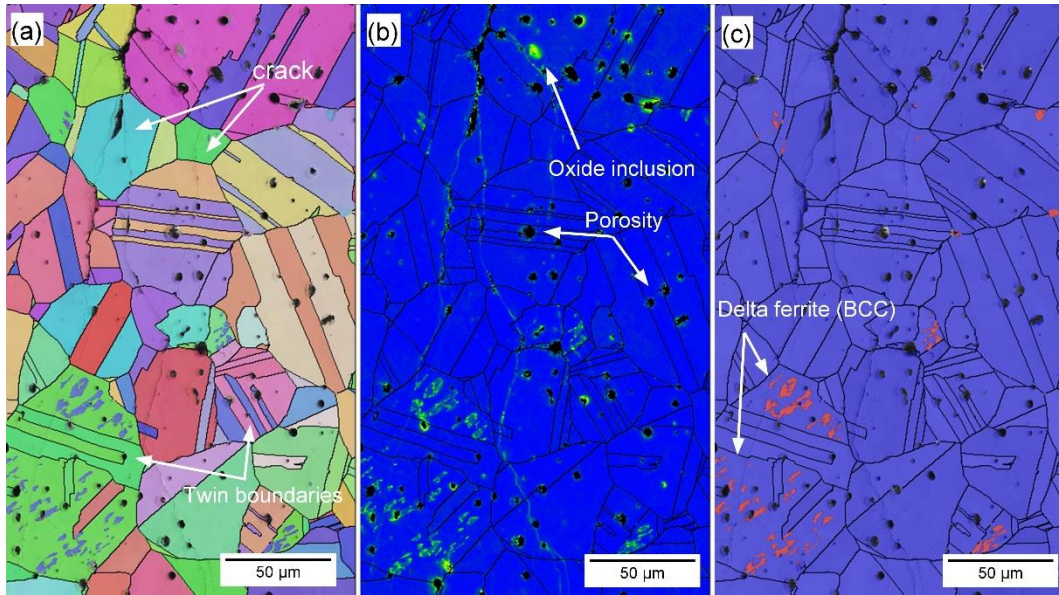


Figure 4-12: Representative (a) EBSD map, (b) KAM map, and (c) phase map with overlaid band contrast of BMD SS316L, showing transgranular cracking, twin boundaries, oxide inclusions, round porosity, and area of  $\delta$ -ferrite

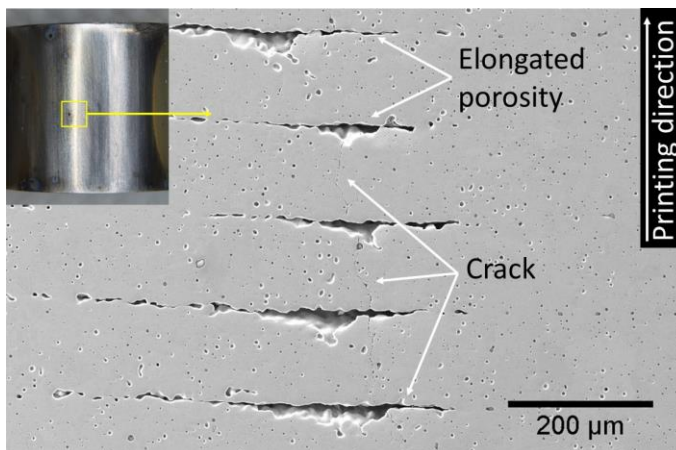


Figure 4-13: Photographic and SEM image of the curved surface of a BMD SS316L C-ring after exposure to boiling solution under 90% AYS, showing SCC crossing perpendicular to the elongated porosity

## 4.5 Discussion

The results from this study are consistent with the established body of knowledge showing that non-sensitized austenitic stainless steels under tensile stress are susceptible to transgranular SCC when exposed to hot acidic chloride solutions, i.e., 60 °C or above<sup>6, 8, 10, 11</sup>. Additionally, results demonstrated that, when tested under the same conditions, BMD SS316L was more susceptible to SCC initiation than SA wrought SS316L but, given its much lower strength, more resistant than CD wrought SS316L, Figure 4-9. It is important to note that samples were stressed at a fixed percentage of their AYS. Thus, the actual stress level of CD wrought SS316L was substantially higher at 60% and 90% AYS (i.e., 388 MPa

and 581 MPa) than SA wrought (i.e., 176 MPa and 264 MPa) and BMD (i.e., 100 MPa and 150 MPa) samples. Nevertheless, the results are considered valid since the loading conditions represent the reasonable utilization values for the materials in service, where designers take advantage of the higher yield strength of the CD wrought material. Results of unstressed samples also highlighted the influence of residual stresses on SCC susceptibility, with CD wrought samples experiencing SCC cracks after three weeks of exposure to the boiling conditions.

The manufacturing route influenced SCC morphology. Highly branched cracks are a frequent SCC characteristic of austenitic SS in chloride solutions<sup>7, 47, 98</sup>. SA and CD wrought samples exhibited the expected branched morphology. In contrast, BMD SS316L showed transgranular cracking with little to no branching, Figure 4-11. Given that all alloy compositions met the requirements of the UNS S31603 alloy type<sup>283</sup>, the different crack morphologies can be attributed to differences in alloy microstructure features such as defects and chemistry-phase-crystallography distribution.

#### **4.5.1 Susceptibility to SCC Initiation: Pit-to-Crack Transition**

The susceptibility map in Figure 4-9 shows that CD wrought SS316L had the lowest SCC resistance. As discussed above, SCC susceptibility depends on the extent of plastic deformation of the cold-worked condition<sup>98, 99, 282</sup>. Cold working introduced substantial residual stresses, as shown in the KAM map in Figure 4-7, promoting SCC nucleation<sup>297</sup>. High-strength SSs, such as CD wrought SS316L, are known to have a low threshold stress intensity factor for SCC ( $K_{I_{SCC}}$ ), an indication of their low SCC arrest capacity<sup>10, 278, 281, 302</sup>. Due to their lower strength and applied loads, SA wrought and BMD SS316L had improved resistance to SCC initiation. However, BMD exhibited a relatively lower SCC resistance than SA wrought SS316L, especially considering the AM samples' lower strength.

The lower SCC resistance of BMD SS316L was attributed to the higher content of microstructural heterogeneities, such as pores and oxide inclusions, Figure 4-5 and Table 4-3 and Table 4-4. These defects serve as preferred stable pit nucleation sites<sup>177, 185, 303-305</sup>. Faster sharp pit propagation, in turn, facilitates the so-called pit-to-crack transition<sup>272-277</sup>. The more extensive and deeper pits in BMD SS316L, Figure 4-10 and Table 4-5, negatively affected SCC resistance. The SCC resistance of BMD SS316L could be markedly improved by decreasing porosity and oxide inclusions. Strategies to reduce SCC susceptibility include using low-oxygen powder feedstock and prolonging the sintering time to reduce pore size, albeit at the expense of grain growth<sup>170, 171, 185</sup>. Post-processing steps such as high isostatic

pressure (HIP) could also be introduced to close the bulk porosity<sup>88, 306-309</sup>. Lastly, shot-peening could also close surface pores and introduce compressive residual stresses<sup>90, 310-312</sup>.

#### 4.5.2 Crack-Branching

The noticeable difference in SCC morphology between wrought and BMD SS316L samples, illustrated in Figure 4-11, was attributed to the presence of randomly oriented equiaxed grain aggregates—with minimal or no influence of special boundaries—and to a high content of twin boundaries in the BMD microstructure, Figure 4-6 and Table 4-3. These features are commonly found in materials processed with sinter-based manufacturing technologies<sup>85, 88, 91, 94, 106, 153</sup>, which act as barriers for crack-branching of transgranular SCC.

The weakly crystallographic textured microstructure of BMD SS316L resulted in an overall reduction of the Schmid factor, as given in Table 4-3. The Schmid factor indicates the increased resolved shear stress to initiate the slip across grains<sup>313-317</sup>. Furthermore, the equiaxed grains are crystallographically randomly oriented and comprise a larger amount of twin boundary fractions in BMD SS316L, thus enhancing the resistance to crack propagation via branching in non-localized directions<sup>314, 316-319</sup>. In addition, the higher porosity in BMD SS316L acted as an obstacle to crack-branching. A similar arrestor effect, caused by the blunting of the crack tips, has been reported elsewhere in additively manufactured porous alloys<sup>320-322</sup>. The influence of the non-metallic inclusions and retained  $\delta$ -ferrite (BCC) on the resistance to crack-branching could not be determined since no clear relationship was observed.

#### 4.6 Conclusions

This work determined the SCC behaviour of SS316L additively manufactured by sinter-based material extrusion. Tests were conducted in an acidified chloride solution (25 wt% NaCl, pH 1.50) at different stress levels and temperatures to identify SCC thresholds. Results were compared with the SCC response of conventional SA and CD wrought SS316L. Results were supported by a thorough characterization that included LOM, SEM-EDS, EBSD, and micro-CT. The following conclusions were drawn based on the evidence presented above:

1. SCC resistance increased in the following order: SA wrought > BMD > CD wrought SS316L.

2. The sinter-based manufacturing process used to produce BMD SS316L resulted in lower residual stresses and lower strength, contributing to a higher SCC initiation resistance than the highly stressed CD wrought condition.
3. The large grain aggregates, equiaxed grain morphology, weak crystallographic texture, and a large content of twin boundaries decreased the SCC crack-branching of BMD SS316L when compared to SA and CD wrought SS316L.
4. The porosity distribution of BMD SS316L had a mixed impact on its SCC resistance. While these defects facilitated the pit-to-crack transition, they also acted as crack arrestors by blunting the crack tips.



## **Chapter 5: Laser-based powder bed fusion of SS316L: Stress Corrosion Cracking and the Effect of Residual Stresses**

This chapter corresponds to a publication that has been reformatted to align with the overall style of the thesis and to address the comments raised by the examiners.

### **Publication:**

Santamaria R, Wang K, Salasi M, Salem M, Lours P, Iannuzzi M, Quadir MZ. Stress corrosion cracking behavior of austenitic stainless steel 316L produced using laser-based powder bed fusion. *Corrosion*. 2023;4311. <https://doi.org/10.5006/4311>

# Stress Corrosion Cracking Behaviour of Austenitic Stainless Steel 316L Produced Using Laser-based Powder Bed Fusion

## 5.1 Abstract

Austenitic stainless steel UNS S31603 (SS316L) is widely used in the resources industry due to its excellent corrosion resistance, ductility, and weldability. Recently, laser-based powder bed fusion (LPBF) manufacturing has gained popularity for creating SS316L components with complex geometries and superior mechanical properties. However, the rapid melting and solidification of the deposited layers during the thermal cycle of LPBF produce residual stresses. Components manufactured through LPBF are frequently used under applied stress in corrosive environments. Thus, it is crucial to understand their susceptibility to stress corrosion cracking (SCC) and the impact of residual stresses. This study investigated the combined effects of applied stress and temperature on the SCC behaviour of LPBF SS316L using custom-made C-ring test specimens. Cold-drawn wrought SS316L was included for comparison. Stress relief heat treatment, microhardness testing, partial immersion testing, and microanalysis techniques, such as light optical microscopy (LOM), scanning electron microscopy (SEM), and electron backscatter diffraction (EBSD), were used to quantify the SCC behaviour. The outcomes of this study showed that stressed and unstressed LPBF SS316L specimens were highly susceptible to cracking around the printed holes of the C-ring. The SCC susceptibility was attributed to the residual stresses introduced by the printed supports, as similar cracking behaviour was observed in both polished and as-printed holes. This work provides valuable insights and lays a foundation for further research into the impact of using C-ring samples to investigate SCC susceptibility and sheds light on the SCC susceptibility of as-printed components of complex geometry printed with supports due to the influence of residual stresses.

## 5.2 Introduction

Additive manufacturing (AM) encompasses the technologies used to produce physical objects from digital data by adding layers-upon-layers of material <sup>56-58</sup>. Compared to traditional manufacturing, AM has the potential to reduce complexity in the supply chain in terms of quality, impact, cost, speed, and innovation <sup>61</sup>. AM technologies include binder jetting, direct energy deposition, material extrusion, material jetting, sheet lamination, vat photopolymerisation, and powder bed fusion (PBF) <sup>57-59</sup>. Nowadays, it is common to use AM to produce engineering grade metals such copper <sup>323-325</sup>, stainless steels <sup>153, 284, 326, 327</sup>, titanium-base <sup>266, 328-330</sup>, aluminium-based <sup>212, 331, 332</sup>, and nickel-based alloys <sup>226, 333, 334</sup>. Thus, AM technologies have gathered growing interest from different industries such as biomedical, transport, aerospace, and energy among others <sup>61, 335-339</sup>.

Stainless steel UNS S31603 (SS316L) is widely known for its ductility, weldability, and good corrosion resistance in certain oxidizing conditions<sup>340-343</sup>. However, when exposed to halides, such as chloride ions, while being stressed under tension, SS316L can be susceptible to stress corrosion cracking (SCC)<sup>7, 9, 47-49, 297, 344</sup>. SCC is a form of environmentally assisted cracking (EAC) that occurs when a susceptible material is exposed to a specific environment above a certain tensile stress level. Cracks often nucleate from localized corrosion; thus, SCC occurs when the service temperature exceeds a critical localized corrosion temperature<sup>6, 9-12</sup>. In SCC, cracks can initiate and propagate at much lower stress levels than those required to fracture the material in the absence of a corrodent, i.e., once the cracking initiates, it propagates until the applied stress exceeds the fracture strength of the remaining ligament<sup>7, 47</sup>. Therefore, using AM technologies, such as PBF, to produce SS316L components with improved properties is of great interest<sup>1, 74, 160, 165</sup>.

In PBF, a high-intensity energy source, such as a laser (LPBF) or an electron beam (EB) PBF, is employed to melt layers of powdered feedstock that solidify at a calculated rate of approximately  $10^3$  to  $10^7$  K/s<sup>72, 73, 237, 238</sup> into near net shape parts<sup>58, 59, 71</sup>. LPBF-manufactured SS316L is known to be produced with fully austenitic microstructures<sup>75, 284, 285</sup>, extremely low porosity content<sup>74-76</sup>, and nano-size non-metallic inclusions<sup>75, 77, 345</sup>. Moreover, LPBF SS316L has shown excellent localized corrosion resistance<sup>77-79</sup>, and outstanding tensile properties<sup>74-76</sup>. However, the cyclic process of melting and rapid cooling through the deposited layers leaves LPBF SS316L parts with a metastable microstructure containing a high degree of thermal residual stresses<sup>75, 83, 84</sup>. These stresses, which can be between 250 MPa (36 ksi) and 500 MPa (72 ksi)<sup>75, 83, 100, 346, 347</sup>, usually start as tension loads at the external surfaces of the component, and gradually turn into compressive loads at its core<sup>75, 84</sup>. The magnitude of these process-induced residual stresses in LPBF-manufactured SS316L can be high enough for SCC to start at an applied stress lower than the material's yield strength or even in the absence of an externally applied load<sup>11, 83, 348</sup>. In addition, residual porosity and a rough surface finish, which are inherent in the LPBF manufacturing process, are factors known to increase the SCC susceptibility<sup>124, 349-352</sup>, as they facilitate localized corrosion initiation<sup>272-277</sup>. Yazdanpanah et al.<sup>122</sup> observed that SCC in LPBF-manufactured SS316L with high levels of residual stress started from microstructural heterogeneities, such as melt pool boundaries and grain boundaries, and from machining marks and pore sites, whereas for annealed specimens, only pitting was observed. Therefore, it is possible to decrease the SCC susceptibility by improving the surface finish of the printed material throughout grinding or machining. However, the localized plastic deformation from these processes may also introduce additional residual stresses that could further increase their SCC susceptibility<sup>9, 122-124, 298, 344</sup>. A more practical route to improve the SCC resistance

of LPBF-manufactured components is reducing their intrinsic residual stresses by optimizing the printing parameters such as laser power, scanning strategy, and printing orientation<sup>84, 353-356</sup>, or by adding post-processing steps to the as-printed object, e.g., stress relief heat treatment<sup>75, 357-360</sup>, or shock peening<sup>347, 361-363</sup>.

This study investigated how the residual stresses on LPBF-manufactured SS316L C-rings printed with supports influenced their high SCC susceptibility. To assess this, stressed and unstressed test specimens were immersed in an acidified chloride solution at boiling temperature, and their time-to-crack was monitored. Furthermore, stress relief heat treatment and partial immersion tests were conducted to mitigate the impact of residual stresses on the SCC susceptibility around the printed holes. A detailed post-testing characterization was carried out using light optical microscopy (LOM), scanning electron microscopy (SEM), and electron backscattered diffraction (EBSD) analysis. The cracking behaviour of cold-drawn wrought SS316L C-rings was used as a comparison.

## **5.3 Experimental Procedures**

### **5.3.1 Materials**

The SS316L used in this investigation was produced with LPBF. The material was additively manufactured using fresh nitrogen-atomized pre-alloyed SS316L powder with an average particle size of 35.7  $\mu\text{m}$ , and a particle size distribution of D50 33.1  $\mu\text{m}$  and D90 55.2  $\mu\text{m}$ . The SS316L powder was kept for at least 12 h in an oven at 50°C (122°F) to remove moisture prior to use. Before printing, the build plate was preheated at 100°C (212°F) to decrease thermal gradients, the oxygen content was reduced to less than 0.2%, and the chamber was filled with high-purity argon. All LPBF SS316L specimens were produced with a layer thickness of 50  $\mu\text{m}$ , no fill contour, no down-skin layer, and using a zig-zag pattern without rotation between layers to achieve the bulk volume. The laser power (P) was 275 W, the scanning speed (V) was 700 mm/s, and the hatching space (h) was 120  $\mu\text{m}$ . Commercially available cold-drawn (CD) wrought SS316L, which is known for its high yield strength and residual stresses resulting from its plastic deformation process<sup>98, 99, 282</sup>, was used for comparison.

The LPBF SS316L elemental composition was determined with inductively coupled plasma atomic emission spectroscopy (ICP-AES). Table 5-1 summarizes the elemental composition of the pre-alloyed SS316L powder used in the LPBF process and the CD wrought SS316L rod bar, as reported in their manufacturer certificates. Table 5-1 also shows the externally

analysed composition of the as-printed LPBF SS316L and the nominal composition of UNS S31603 for comparison.

Table 5-1: Elemental composition of the pre-alloyed SS316L powder, LPBF-manufactured SS316L, CD wrought SS316L, and nominal composition of UNS S31603

Material	Source	Fe	C	Cr	Ni	Mo	Si	Mn	P	S
Powder SS316L	Material certificate	Bal.	0.01	17.7	12.6	2.36	0.65	0.90	0.007	0.01
LPBF SS316L	ICP-AES analysis	Bal.	0.02	17.5	12.3	2.02	0.06	0.62	<0.01	0.01
CD Wrought SS316L	Material certificate	Bal.	0.02	16.7	10.1	2.03	0.04	1.72	0.024	0.02
UNS S31603	ASTM	Bal.	Max.	16.0	10.0	2.00	Max.	Max.	Max.	Max.
	A276 <sup>364</sup>		0.03	18.0	14.0	3.00	1.00	2.00	0.045	0.03

### 5.3.2 Microstructure characterization

The phased composition of the LPBF and CD wrought SS316L were identified via X-ray diffraction (XRD) using a Cobalt K alpha powder diffractometer radiation source operating at 35 kV and 40 mA with a LynxEye† detector (Bruker D8 Discover†). The XRD data were collected over an angular range of 40° to 130°, a step size of 0.015°, and a time interval of 0.7 s. The microscopy analysis was conducted on tested and untested samples that were cut, mounted in cold epoxy resin, wet ground with SiC abrasive paper, and mechanically polished down to 1 µm surface finish. Samples intended for LOM analysis were chemically etched with a solution containing 100 ml H<sub>2</sub>O, 10 ml HNO<sub>3</sub>, and 100 ml HCl. The concentration of nitric acid and hydrochloric acid was 70% and 32%, respectively. Samples for EBSD analysis were polished to a mirror surface finish with 0.02 µm colloidal silica and then ion-milled for 30 min using a beam voltage of 8 kV at a glancing angle of 4° with full cycle rotational movements (TECHNOORG Linda, SEMPrep2†). All samples for EBSD analysis were surface coated with a 5 µm carbon film to prevent electrostatic charging.

The microstructures were imaged using secondary electron (SE) and backscatter (BS) detectors in a field emission-scanning electron microscope (FE-SEM) (TESCAN system, CLARA†). The crystallographic orientations were mapped using an Oxford† symmetry EBSD detector in the FE-SEM, on samples tilted 70°, with a working distance of 20 mm, a beam energy of 28 kV, and a beam current of 1 nA. A clean-up process was applied to the EBSD data to assimilate any non- or mis-indexed points into the surrounding neighbourhood grains, ensuring that less than 10% of the points were modified. Grain boundaries were detected with a threshold misorientation of 10°, a minimum of 8 pixels of fractional

† Trade name.

difference of misorientation variation, and a kernel size of 3-by-3. Grain size was measured as the maximum Feret diameter. The kernel average misorientation (KAM) maps were obtained using 3 by 3 square kernels and a maximum misorientation angle of 5°. All data acquisition and subsequent post-processing were conducted using the software Aztec† and Aztec Crystal†, respectively.

### **5.3.3 Mechanical properties**

Mechanical properties, including yield strength ( $S_y$ ), tensile strength ( $S_u$ ), elongation at fracture, elongation after fracture, reduction of area, and elastic modulus ( $E$ ), were measured at room temperature. The tests were conducted in triplicate specimens. The LPBF SS316L, provided by IMT Mines Albi (France), was tested using rectangular specimens that were 55 mm long (2.20 in), 8 mm wide (0.30 in), and 2 mm thick (0.08 in) manufactured in the horizontal orientation. The displacement during the tensile test was measured using an axial extensometer with a 15 mm (0.60 in) gauge length and +5 mm (0.20 in) travel length (Epsilon TechCorp†). The crosshead speed in the universal testing machine (UTM) was set to 0.225 mm/min within the elastic region and 0.750 mm/min within the plastic region. The CD wrought SS316L was tested according to ASTM(1) E8<sup>152</sup> using custom rectangular sub-size tensile specimens that were 100 mm long (4 in), 6 mm wide (0.24 in), and 3 mm thick (0.12 in), also as per ASTM E8. The specimens were machined from a 25 mm (1 in) diameter rod bar. The displacement during the tensile test was measured with an axial extensometer with a 25 mm (1 in) gauge length and +25 mm (1 in) travel length (Epsilon TechCorp†). The UTM crosshead speed was set to 0.375 mm/min within the elastic region, and 1.25 mm/min within the plastic region. The displacement rates were different in both materials since their gauge lengths were different, as defined in ASTM E8. Figure 5-1 shows the geometry and dimensions of the LPBF SS316L and CD wrought SS316L tensile specimens.

---

<sup>(1)</sup> ASTM International, 100 Barr Harbor Dr., West Conshohocken, PA 19428-2959

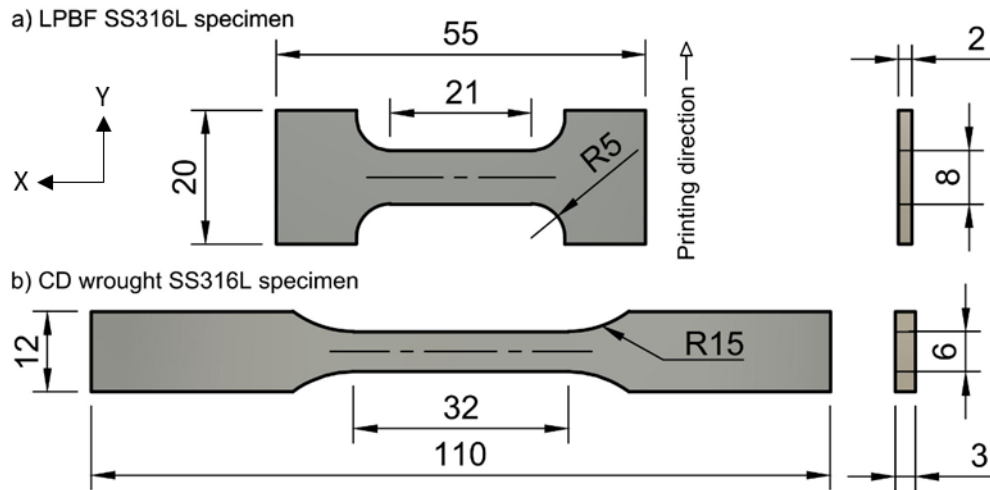


Figure 5-1: Geometry of the rectangular specimens used for the tensile tests a) LPBF-manufactured SS316L, and b) machined CD wrought SS316L. The extrusion direction of the rod bar is in the X axis. Units in millimetres.

All tensile tests were conducted using a 50 kN Shimadzu† UTM equipped with 50 kN manual non-shift wedge grips. All data were collected at a rate of 10 Hz using the Trapezium X† software. The actual yield strength (AYS) of the LPBF SS316L and the wrought SS316L were calculated by intersecting their corresponding engineering stress-strain curves with an 0.2% offset line running parallel to the elastic portion of their curves, per ASTM E8<sup>152</sup>. The slope of the offset line, i.e., an approximation of the material's elastic modulus (E), was calculated using the least-squared method per ASTM E111<sup>175</sup>. The microhardness was measured according to ASTM E384<sup>288</sup> using a microhardness tester (Duramin-4, Struers†), an applied load of 2 Kg (HV2), and a dwell time of 15 s. The bulk density was calculated using the Archimedes principle per standard ASTM B962<sup>289</sup> with a density kit coupled to an analytical balance with a readability of 0.001 g and a linearity of  $\pm 0.002$  g (ME203, Mettler-Toledo†).

### 5.3.4 Stress corrosion cracking

The SCC behaviour was investigated by monitoring the time required by the materials to crack when subjected to a stress level corresponding to 60% and 90% of their AYS while immersed in a boiling solution, i.e., 106 °C (223 °F). Unstressed specimens, i.e., 0% AYS, were also tested for comparison. The test solution was 25 wt% NaCl acidified to pH 1.50 with phosphoric acid (H<sub>3</sub>PO<sub>4</sub>), per ASTM G123<sup>156</sup>. The test specimens used in this investigation were C-rings designed per ASTM G38<sup>155</sup>. Magnesium chloride (MgCl) was not used because it is more severe than NaCl. The LPBF SS316L C-rings were manufactured, as shown in Figure 5-2a, and their holes were re-bored with a slightly larger drill bit to remove the printed supports. All surfaces of the C-rings were sequentially wet-ground with abrasive papers from 80- to 600-grit SiC. Although the dimensions of the C-

rings were not measured after surface finishing, the grinding process produced no excessive material removal. Notably, during the initial stages of this investigation, the printed holes were left in their as-printed condition. However, after preliminary results (not shown), it was decided to polish them in the same way as the rest of the C-rings. All tests were carried out at least in duplicate, as explained below.

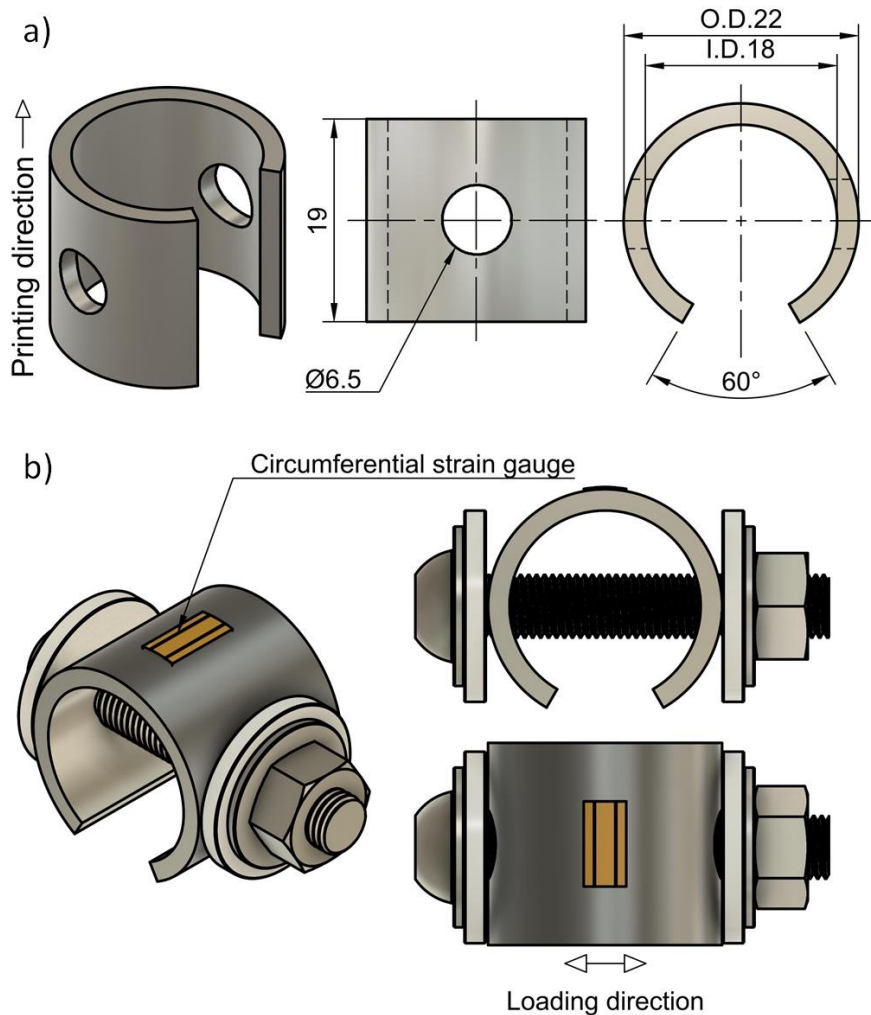


Figure 5-2: a) Geometry of the custom C-ring specimen used to investigate the SCC susceptibility of LPBF and CD wrought SS316L, and b) schematics of the constant-strain assembly according to ASTM G38

The C-rings were stressed to their corresponding material's AYS using a constant-strain setup, per ASTM G38<sup>155</sup>. The assembly, shown in Figure 5-2b, consisted of two PEEK washers, two M6 titanium flat washers, one M6 titanium socket cap bolt, one M6 titanium flanged lock nut, and a strip of clear PTFE heat shrinkable tube moulded to the bolt. The stress levels of 60% and 90% AYS were obtained by attaching a 0.3 mm (1/64 in) circumferential strain gauge (FLAB-03-11-1LJC-F, Tokyo Measuring Instruments†) to the middle of the uppermost curved surface of the C-ring, as shown in Figure 5-2b. Then, the bolt was tightened until the reading in the data logger (Almemo 2590, Ahlborn†) indicated



the strain value corresponding to the required stress level. This procedure was conducted according to the Stress Considerations outlined in ASTM G38<sup>155</sup>, which states that the nominal stress exists only along a line that runs across the C-ring at the middle of its arc. Therefore, the strain should be measured at that location, where the strain is maximum. However, the circumferential stress may vary across the width of the C-ring, and the extent of the variation depends on the width-to-thickness and diameter-to-thickness ratios of the specimen. In general, the stress is greater at the edges than in the middle, but only finite element modelling (FEM) can determine the actual location of the maximum stress for a given C-ring's configuration, which was outside the scope of our work. All traces of the strain gauges were manually removed with 600-grit SiC abrasive paper. The electrical insulation between the bolt and the C-ring was verified with a digital multimeter. All the C-rings tested at 0% AYS were also prepared, as shown in Figure 5-2b, although no stress was applied to the bolt. The CD wrought SS316L C-rings were similarly prepared and included as a control.

Each test condition consisted of a flask containing 750 ml of the test solution and two C-rings, one from each material stressed to the same corresponding AYS. The ratio of the volume of solution per exposed surface area of specimens was 17 mL/cm<sup>2</sup> (109 mL/in<sup>2</sup>), which is more than threefold the minimum required by ASTM G123<sup>156</sup>. The SCC susceptibility of each material was assessed as the time required to observe the first cracks. Therefore, longer exposure times without cracking indicated a lower SCC susceptibility. All C-rings were removed from their test solution weekly, cleaned, and inspected for cracks at a magnification of 20× using LOM. C-rings showing SCC were cut and prepared for post-test microscopy analysis, while C-rings with no cracks continued the test in freshly prepared solution until the next inspection for a maximum of six weeks, per ASTM G123<sup>156</sup>. Since removing the specimens for inspection is expected to disturb the local corrosion cells and may affect the results<sup>156</sup>, and due to the aggressive nature of the test solution for most stainless steels, a one-week inspection frequency was considered sufficient to determine the onset of cracking.

Two different methods were used to investigate how residual stresses affect the cracking behaviour of LPBF-manufactured SS316L. The first method involved subjecting duplicate C-rings to a stress relief heat treatment in a vertical tube furnace under vacuum at 650°C (1200°F) for 2 h. After stress relieving, the C-rings were manually wet ground down to 600-grit using SiC abrasive paper, left overnight to recover the passive film, and tested unstressed, i.e., 0% AYS, in boiling solution (approximately 106 °C (223 °F)). In the second method, duplicate C-rings were manually wet-ground down to 600-grit, stressed to 90% of

their AYS, and left to passivate overnight. The specimens were then partially immersed in boiling solution while hanging upside-down, with the uppermost curved surface immersed in the solution, while the printed holes were kept above the solution level, Figure 5-3. Weekly inspections were conducted on all C-rings to determine the onset of cracking.

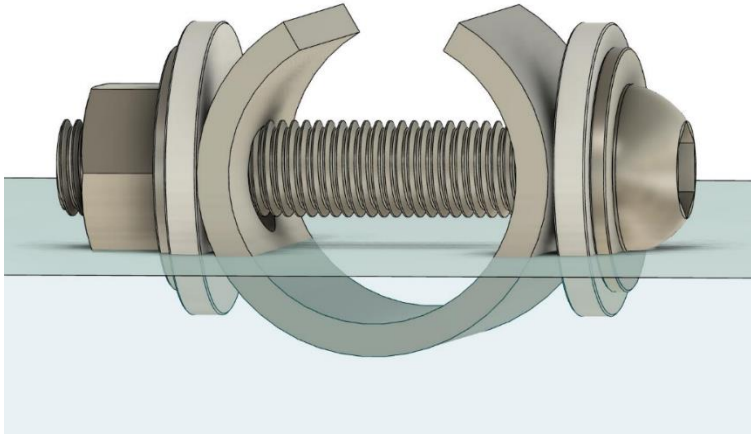


Figure 5-3: Schematic of the partial immersion test applied to the as-printed LPBF SS316L C-ring

## 5.4 Results

### 5.4.1 Microstructure characterization

Figure 5-4 shows representative XRD patterns of LPBF and CD wrought SS316L. Both materials consisted entirely of  $\gamma$ -austenite (FCC), i.e.,  $\delta$ -ferrite (BCC) was not detected within the resolution of the technique. Figure 5-5 shows EBSD maps perpendicular to the build direction and corresponding color-coded inversed pole figures (IPF) of the LPBF and the CD wrought SS316L microstructures obtained from untested C-rings. The IPF showed strongly textured LPBF and wrought SS316L microstructures indicated by the high-intensity poles in the  $\{111\}$  pole figure, i.e., 2.32 and 2.27 times random, respectively. Figure 5-5 also indicates relatively large austenitic grains in the LPBF and the CD wrought SS316L microstructures. Their average grain sizes were  $57 \pm 52 \mu\text{m}$  in the LPBF SS316L and  $44 \pm 34 \mu\text{m}$  in the CD wrought SS316L. The overall grain size distribution was D50  $39 \mu\text{m}$  and D90  $124 \mu\text{m}$  for the LPBF SS316L, and D50  $34 \mu\text{m}$  and D90  $90 \mu\text{m}$  for the CD wrought SS316L. The fitted ellipse aspect ratios were  $3.0 \pm 1.8$  for the LPBF SS316L and  $3.9 \pm 3.6$  for the CD wrought SS316L. SEM-EDS elemental mapping did not show relevant presence of non-metallic inclusions.

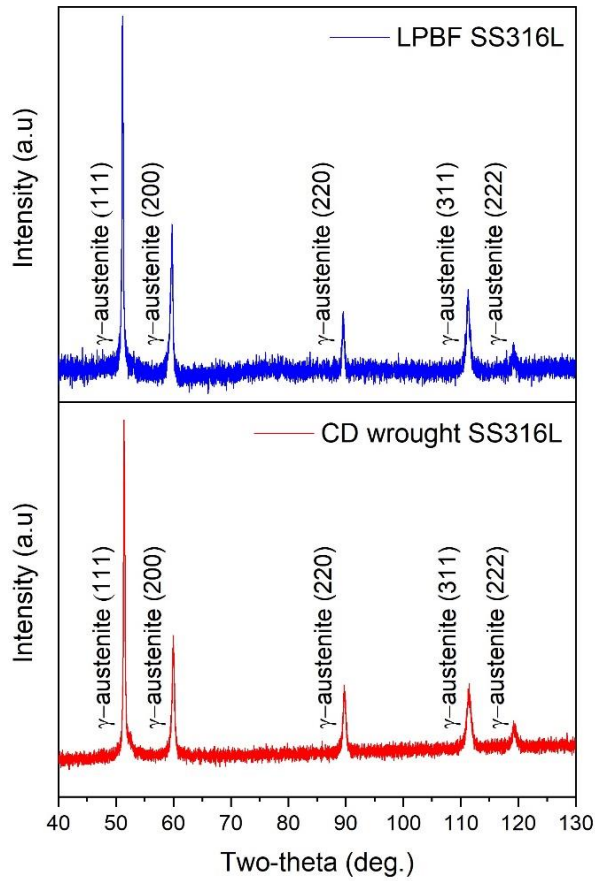


Figure 5-4: XRD patterns of LPBF and CD wrought SS316L showing the presence of  $\gamma$  (FCC) austenite as the only phase in their microstructures

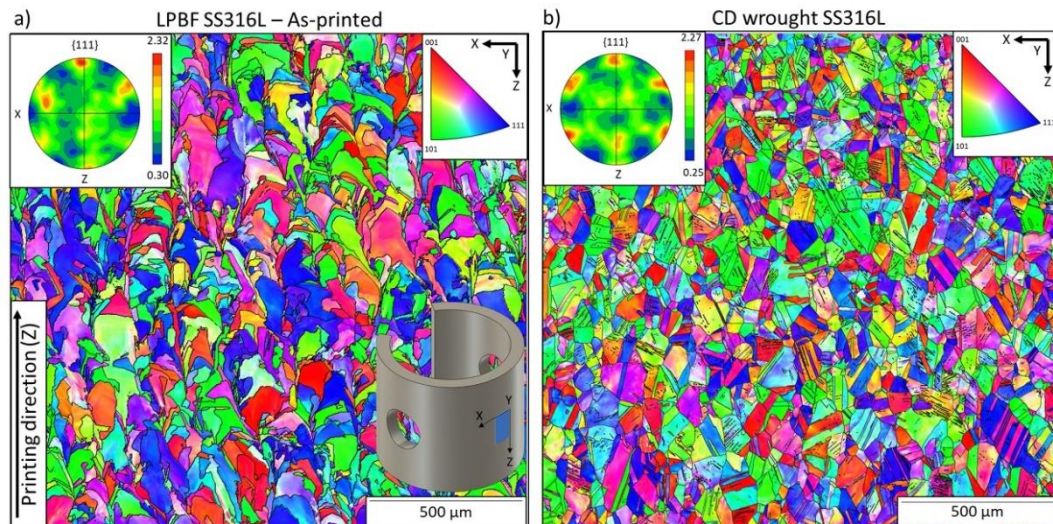


Figure 5-5: EBSD maps and color-coded inverse pole figures of untested C-rings showing textured microstructures in the a) as-printed LPBF SS316L perpendicular to its printing direction, and b) CD wrought SS316L

### 5.4.2 Mechanical properties

Figure 5-6 shows representative engineering stress-strain curves of LPBF SS316L and its CD wrought counterpart in their elastic regions and corresponding AYS. The AYS of LPBF and CD wrought SS316L were 529 MPa (77 ksi) and 646 MPa (94 ksi), respectively. Although the displacement rates differed for each material due to their different gauge lengths, which may affect their tensile properties<sup>152</sup>, the C-rings were stressed to their corresponding material's AYS, which allowed a proper evaluation of SCC susceptibility despite the difference in geometry and displacement rates. The bulk density of LPBF and CD wrought SS316L were  $7.894 \pm 0.013 \text{ g/cm}^3$  and  $7.953 \pm 0.027 \text{ g/cm}^3$ , respectively. The bulk porosity of LPBF SS316L was less than 1%.

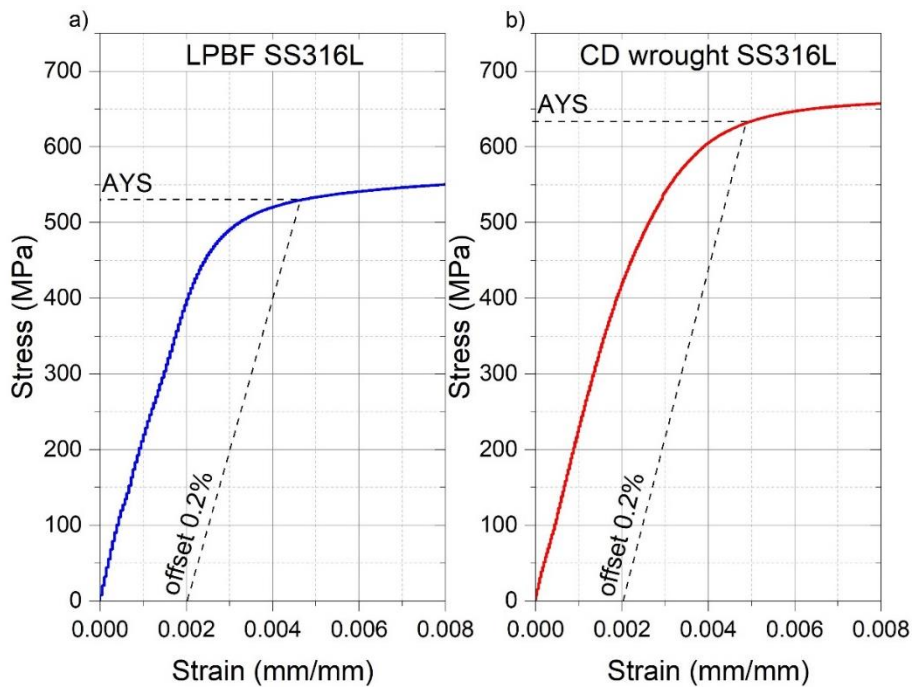


Figure 5-6: Engineering stress-strain curves within the elastic region of a) LPBF SS316L and b) CD wrought SS316L along with the location of their corresponding AYS

Table 5-2 summarizes additional tensile properties, such as elastic modulus, tensile strength, elongation at fracture, elongation after fracture, and reduction of area. The average microhardness of the as-printed LPBF SS316L, the stress relieved LPBF SS316L, and the CD wrought SS316L were  $224 \pm 3 \text{ HV}_2$ ,  $195 \pm 2 \text{ HV}_2$ , and  $282 \pm 3 \text{ HV}_2$ , respectively.

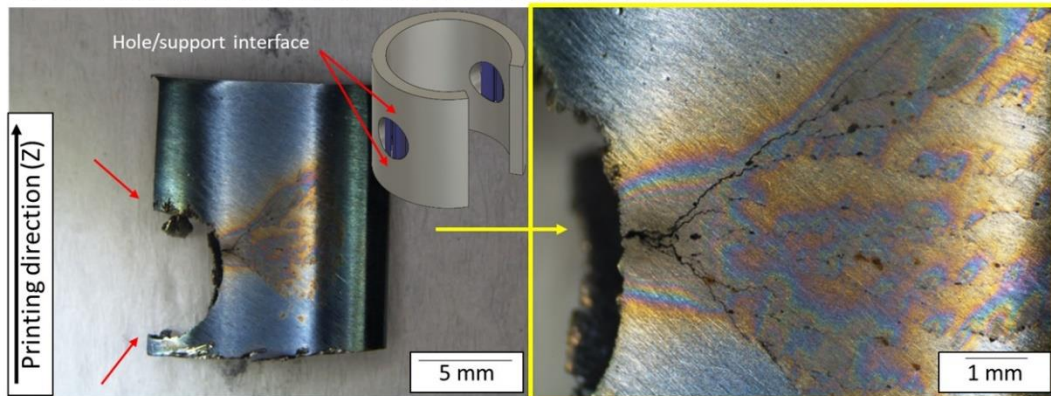
Table 5-2: Mechanical properties of as-printed LPBF SS316L, CD wrought SS316L, and standard requirements for UNS S31603

Material	Elastic Modulus (E)	Yield Strength (Sy)	Tensile Strength (Su)	Elongation at fracture	Elongation after fracture	Reduction of area	Bulk density
	GPa (ksi)	MPa (ksi)	MPa (ksi)	%	%	%	g/cm <sup>3</sup>
LPBF SS316L	211 ± 12 (30.6 ± 1.7)10 <sup>3</sup>	529 ± 4 (77 ± 0.6)	656 ± 7 (95 ± 1.0)	43 ± 1	12 ± 2	45 ± 1	7.894 ± 0.013
CD Wrought SS316L	214 ± 7 (31.0 ± 1.0)10 <sup>3</sup>	646 ± 8 (96 ± 1.2)	717 ± 6 (104 ± 0.9)	49 ± 5	13 ± 2	66 ± 2	7.953 ± 0.027
UNS S31603 <sup>364</sup>	202 <sup>181</sup> (29.3)10 <sup>3</sup>	Min. 170 (25)	Min. 485 (70)	Min. 40	n/a	Min. 40	7.98 <sup>290</sup>
UNS S31603 (strain-hardened) <sup>365</sup>	202 <sup>181</sup> (29.3)10 <sup>3</sup>	Min. 450 (65)	Min. 585 (85)	Min. 30	n/a	Min. 40	n/s

### 5.4.3 Stress corrosion cracking

Evidence of SCC in the as-printed LPBF SS316L C-rings tested in boiling solution while stressed to 0% and 90% AYS is shown in Figure 5-7a and Figure 5-7b, respectively. The figures show that regardless of the applied stress, the stressed and unstressed C-rings cracked with similar morphology, initiating from corrosion pits near the edges of their printed holes. Figure 5-8a illustrates the results of one of the initial C-ring tests with as-printed holes, whereas Figure 5-8b corresponds to one with the as-printed surface removed by grinding. Interestingly, both initiation sites were perpendicular to the hole/support interfaces, as depicted by the inset images in Figure 5-9. Highly branched SCC initiated near the printed holes from corrosion pits on unstressed and stressed LPBF SS316L C-rings with the holes in as-printed and polished conditions, respectively (Figure 5-8). SCC initiated from the polished surface of the C-ring near the holes regardless of the stress state and surface condition. Figure 5-9 shows an EBSD map and corresponding band contrast, revealing transgranular SCC in an unstressed (0% AYS) LPBF SS316L C-ring that cracked from the same location around the printed holes.

a) Unstressed (0% AYS) as-printed LPBF SS316L, fully immersed in boiling solution



b) Stressed (90% AYS) as-printed LPBF SS316L, fully immersed in boiling solution

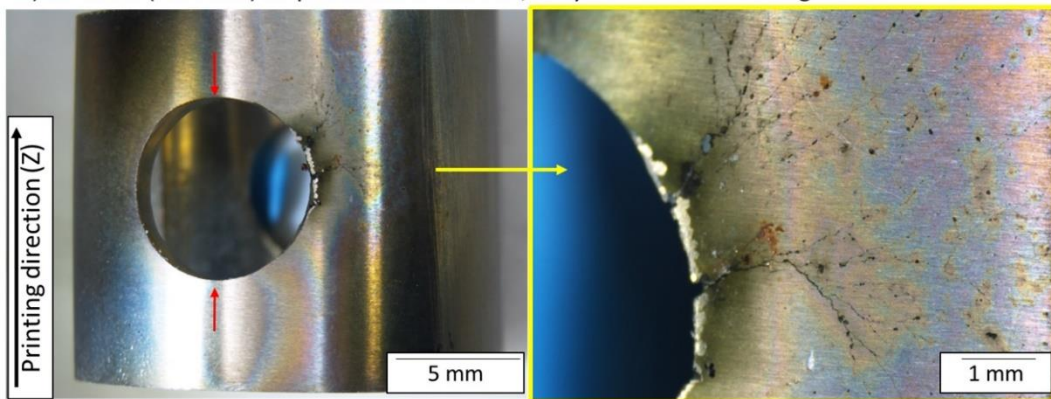


Figure 5-7: Photographs of as-printed LPBF SS316L C-rings fully immersed in boiling solution showing similar SCC morphologies under a) unstressed (0% AYS), and b) stressed (90% AYS) conditions. The red arrows indicate the location of the hole/support interfaces

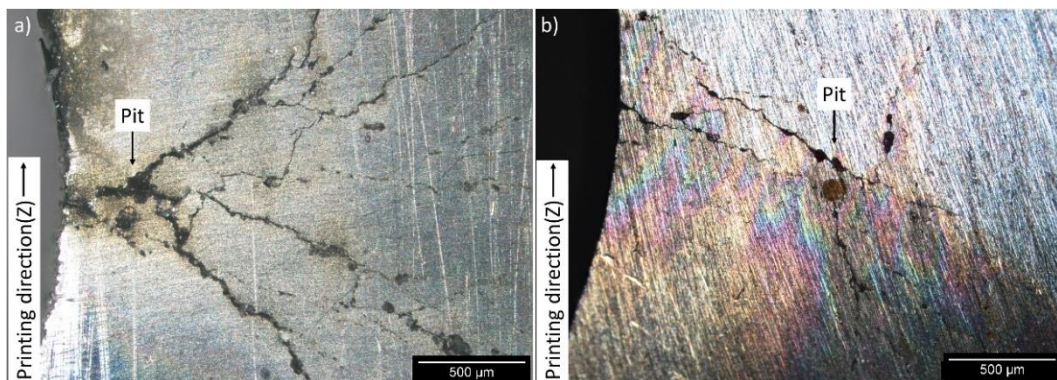


Figure 5-8: Photographs of LPBF SS316L C-rings with a) as-printed holes and b) polished holes, showing similar SCC that initiated from pits near their printed holes in the unstressed (0% AYS) and stressed (90% AYS) conditions, respectively

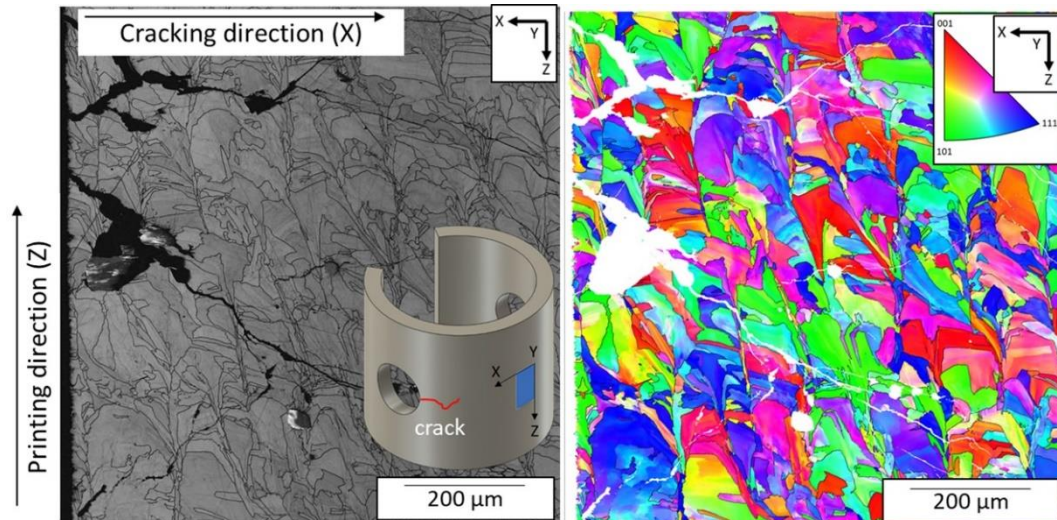


Figure 5-9: Band contrast image and corresponding EBSD map of SCC in as-printed unstressed (0% AYS) LPBF SS316L specimens after full immersion in boiling solution showing transgranular cracking

The SCC behaviour of fully immersed as-printed LPBF and CD wrought SS316L C-rings under different applied stress levels is summarised in Table 5-3. As seen in Table 5-3, a trend was observed between the immersion condition and time to crack initiation. In this regard, fully immersed as-printed LPBF C-rings took longer to crack when stressed to higher stress levels than partially immersed samples. Nevertheless, cracks always initiated near the same locations around their printed holes and perpendicular to the printed supports, regardless of the applied stress. The SCC resistance of the CD wrought SS316L decreased with applied load, in agreement with the literature <sup>6, 11, 47, 296</sup>, and the cracks always initiated on the curved surface.

Table 5-3: SCC behaviour of LPBF SS316L and CD wrought SS316L C-rings tested at different conditions in acidified chloride boiling solution. The number in the cells corresponded to the week when the cracks were observed. Ndash correspond to untested conditions

Stainless steel 316L C-rings in boiling solution				
	Partially immersed		Fully immersed	
Stress level	LPBF As-printed	Wrought Cold-drawn	LPBF As-printed	LPBF Stress-relieved
0% AYS	-	3 weeks	1 week	2 weeks
60% AYS	-	2 weeks	2 weeks	-
90% AYS	2 weeks	1 week	3 week	-
Crack location	Arch	Arch	Hole	Hole

The role of residual stresses on the unexpected SCC behaviour in LPBF SS316L C-ring samples was investigated by conducting a stress relief heat treatment on as-printed C-rings.

Figure 5-10 shows KAM maps perpendicular to the build direction of the as-printed and stress-relieved LPBF SS316L C-rings, as indicated. The as-printed LPBF SS316L microstructure contained local strain around their grain boundaries caused by its processing history. This local strain, depicted by the green areas in Figure 5-10a, indicates a high degree of residual stresses<sup>366, 367</sup>. Inversely, the microstructure of the heat-treated LPBF SS316L showed fewer areas with local strain, Figure 5-10b. A quantitative representation of the reduction in residual stresses due to the heat treatment is shown in Figure 5-10c. As seen in this figure, the stress relief effect of the heat treatment reduced the magnitude of the KAM angles. The overall KAM distribution went from D50 0.96°, D90 1.89° in the as-printed LPBF SS316L, to D50 0.64°, D90 1.43° in the heat-treated LPBF SS316L. A Kolmogorov-Smirnov (K-S) test using OriginLab's† statistical tools was conducted to confirm that both distribution were significantly different, and the results are presented in Figure 5-10c.

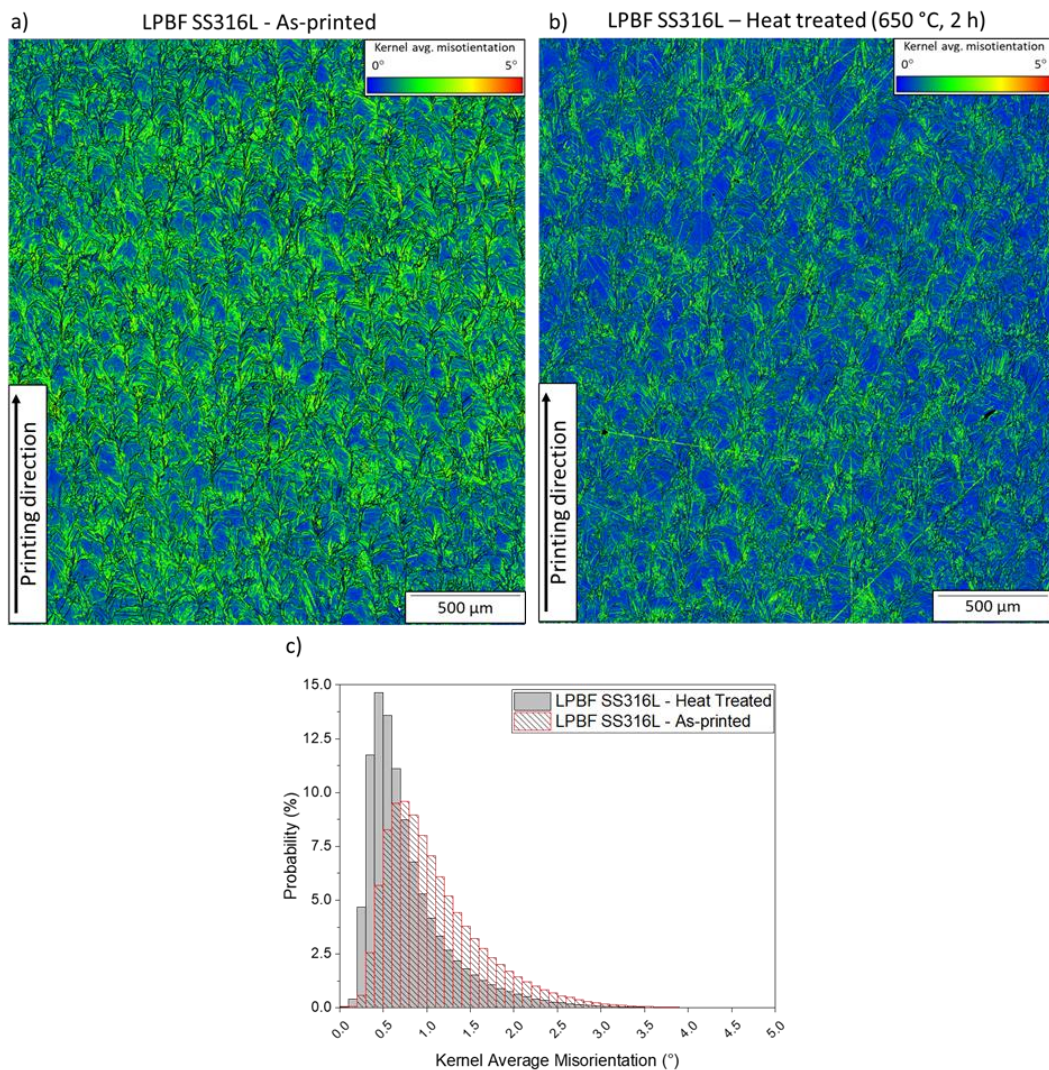


Figure 5-10: KAM maps of untested LPBF SS316L C-rings in their a) as-printed, and b) stress-relieved conditions. The KAM histogram in c) shows the redistribution of local misorientations after the stress relief process



Figure 5-11 illustrates the SCC of a stress-relieved LPBF SS316L C-ring when tested in boiling solution without applied stress, i.e., 0% AYS. As shown in Figure 5-11, in the absence of applied stress, cracking still occurred at the same locations near the printed holes and perpendicular to the printed supports. Moreover, the crack morphology was similar to its as-printed counterparts, although the initial main crack propagated longer before branching in the annealed specimen. As seen in Table 5-3, the heat-treated specimens cracked one week after the as-printed counterparts. These findings indicated that the SCC resistance of unstressed LPBF SS316L C-rings slightly improved after stress relief.

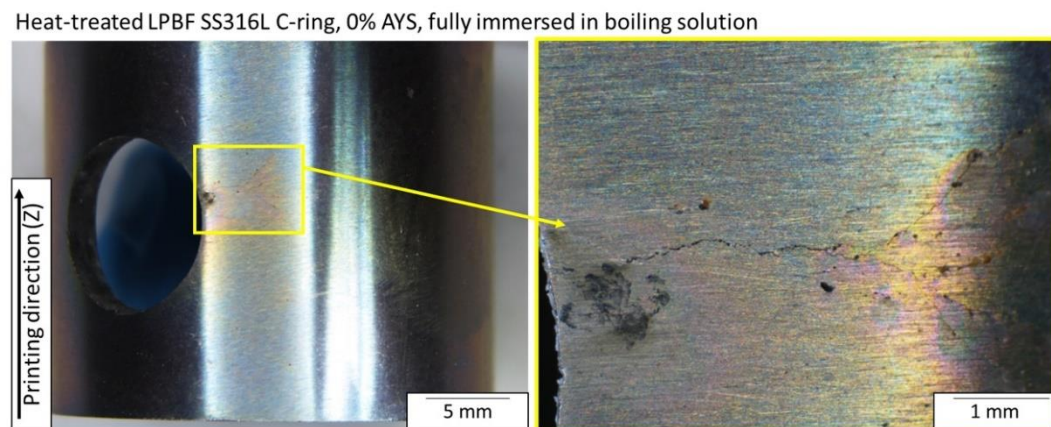


Figure 5-11: Photographs of an unstressed (0% AYS) stress-relieved LPBF SS316L C-ring after full immersion in boiling solution showing identical SCC morphology and crack location as its as-printed counterparts

The as-printed LPBF SS316L C-rings stressed to 90% AYS were also partially immersed in boiling 25% NaCl (pH 1.5), as shown in Figure 5-3. Since the dissolved oxygen concentration is much lower at the boiling temperature (106 °C (223 °F)) than at room temperature<sup>368</sup>, pitting and SCC were supported by the hydrogen evolution reaction rather than the oxygen reduction reaction, which allows a direct comparison between fully and partially immersed tests. After exposure, the partially immersed printed material cracked transgranularly from its uppermost curved surface, i.e., where the nominal applied stress is maximum<sup>155, 369</sup>, Figure 5-12. Figure 5-13 shows the SCC behaviour of the fully immersed 90% AYS CD wrought samples. As seen in Figure 5-13, the CD wrought SS316L samples cracked perpendicular to the direction of the applied stress from its curved surface. However, cracking initiated from the edges of the C-ring rather than from its middle area. Cracking from the edges of the samples was attributed to the residual stresses introduced during the machining process<sup>9, 344, 370</sup>. Nevertheless, both materials cracked along the line of maximum applied stress when stressed to 90% AYS. Notably, the percentage of the total pitted area in the fully immersed samples (approximately 0.22%) was, on average, 4 to 5 times higher than the percentage of pitted area in the partially immersed samples (approximately 0.05%).

Therefore, considering that the immersed area of the fully immersed sample is about 3 times larger compared to the partially immersed sample, this suggests that the difference in the immersed surface of the samples had no impact on the distribution of pitting or the onset of cracking.

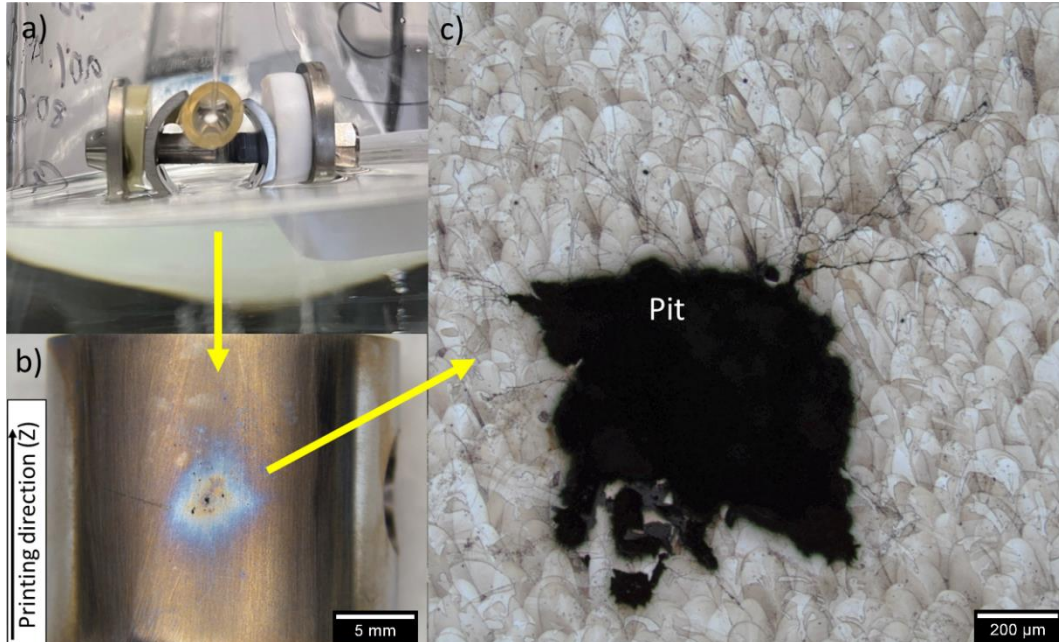


Figure 5-12: As-printed LPBF SS316L C-ring stressed at 90% AYS showing a) its partial immersion setup, b) SCC located at the middle of its uppermost curved surface, and c) an etched imaged showing the resulting transgranular SCC morphology



Figure 5-13: CD wrought SS316L 90% C-ring showing a) full immersion setup, b) photograph illustrating SCC that started from the edge of the uppermost curved surface, and c) a micrograph showing the resulting transgranular SCC morphology

## 5.5 Discussion

All LPBF SS316L C-rings manufactured with printed supports were consistently susceptible to SCC. Regardless of whether the specimens were stressed (90% AYS) or unstressed (0% AYS), as-printed or heat-treated, they all developed cracks from the same location near the printed holes and perpendicular to the hole/support interface, as illustrated in Figure 5-7, Figure 5-8 and Figure 5-11. All cracks exhibited a highly branched morphology, indicating a similar fracture behaviour across the different test conditions and, thus, suggesting the presence of highly localized residual stresses at the cracking sites. The stress relief heat treatment applied to the specimens reduced residual stresses, as evidenced by the KAM maps and distribution shown in Figure 5-10, as well as the 13% reduction in microhardness. Interestingly, the stress-relieved specimens exhibited a slightly different cracking behaviour than their as-printed counterparts, as can be seen in Figure 5-7 and Figure 5-11, in which the length of the main crack before branching was around 3 times longer than in the as-printed condition. Nevertheless, the cracking location remained consistent near the printed holes, indicating that the stress relief process was only partially effective at reducing SCC susceptibility. The surface finish of the printed holes did not play a role in SCC initiation, as evidenced by Figure 5-7 and Figure 5-8 where all cracks occurred in the same location—i.e., from pits located on the polished surface of the C-rings and near the printed holes—regardless of the hole's surface roughness. These observations suggested that factors other than the hole's surface roughness, particularly residual stresses, may be influencing the SCC behaviour of the LPBF SS316L C-rings.

The influence of residual stresses around the printed holes was further demonstrated through partial immersion tests conducted on stressed C-rings (90% AYS). Since the printed holes were positioned above the solution line, Figure 5-3, the specimens cracked along the axis of maximum applied stress, Figure 5-12. This SCC behaviour, characterized by highly branched transgranular cracks, was comparable to that observed in CD wrought C-rings, Figure 5-13, although the wrought specimens cracked from the edges instead of the centre or the curved surface. The different crack initiation site was attributed to the residual stresses introduced during the machining process of the CD wrought SS316L C-rings<sup>9, 122-124, 298, 344</sup>. These results underscore the significant role of residual stresses in dictating the path of crack propagation, regardless of the manufacturing method employed.

The results from the partial immersion tests summarized in Table 5-3 indicated that the LPBF C-rings developed SCC one week after the CD wrought samples. Notably, no cracks were observed at the printed holes, confirming the absence of residual stress influencing the

SCC of the material at those locations. This apparent marginal improvement in the SCC resistance of the printed material compared to its wrought counterpart could be attributed, for instance, to a delay in pit nucleation and the lower applied stress<sup>371, 372</sup>. However, to provide a comprehensive understanding of this phenomenon, further analysis would be necessary, for instance, by including testing LPBF C-rings manufactured at different orientations and specimens with drilled holes instead of printed ones.

It is hypothesized that the hole/support interface, located at the 12 and 6 o'clock positions, as shown in Figure 5-14, experienced volumetric contraction during the rapid cooling from the melting temperatures during the production of the C-rings, resulting in the observed residual stress effect. This phenomenon may have introduced compressive stresses through the supporting structure, forming two additional sites of maximum tensile residual stress at the 3 and 9 o'clock positions, as shown in Figure 5-14. This stress effect, resembling a "C-ring within the C-ring" scenario, is believed to be the primary cause of the systematic cracking of the C-rings at the 3 and 9 o'clock positions.

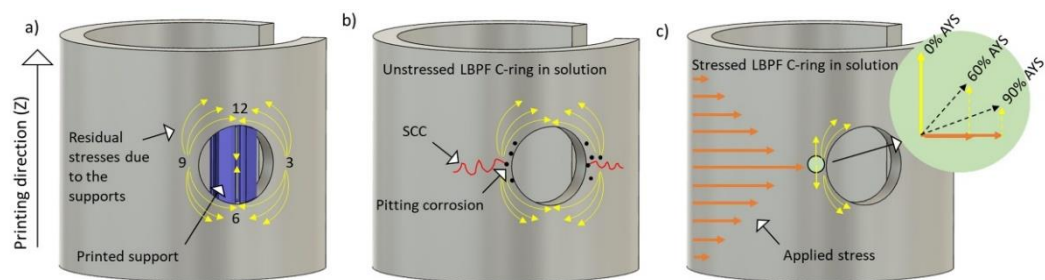


Figure 5-14: Hypothesized: a) residual stresses produced in the hole/support interface of the C-rings, b) unstressed C-ring with SCC initiating from corrosion pits at the 3 and 9 O'clock sites, and c) "stress relieving" effect of the applied load over the residual stresses

Finally, this study found that the SCC susceptibility of the LPBF C-rings decreased as the applied stress increased, particularly in the unstressed LPBF C-rings, which exhibited faster crack initiation than their stressed counterparts, as reported in Table 5-3. In the absence of rigorous FEM, which is beyond the scope of this investigation, these unexpected results can be explained using vector analysis. In this regard, the 3 and 9 o'clock positions are the locations of the highest tensile residual stress in unstrained C-ring, Figure 5-14a-b. In contrast, in stressed C-rings, Figure 5-14c, the stress acts perpendicular to the main component of the residual stress, reducing the magnitude and changing the direction of the stress. This unintentional "stress relieving" effect is hypothesized to have lowered the SCC propensity (measured as a longer crack initiation time) around the printed holes. Nevertheless, since all stressed LPBF C-rings continued to crack at their printed holes suggests that the resulting "vector stress" in this area was above the externally applied stress.

## 5.6 Conclusions

This study investigated the SCC behaviour of LPBF-manufactured SS316L using stressed and unstressed C-rings immersed in boiling, 106 °C (223 °F), 25% NaCl (pH 1.5). The analysis included a stress relief heat treatment and a partial immersion test to elucidate the effect of residual stresses, as well as a comprehensive microstructure characterization to analyse the cracking behaviour. The following conclusions were drawn based on the results presented above:

1. Localized residual stresses introduced by the printed supports reduced the SCC resistance of SS316L C-rings manufactured by LPBF. This observation has important implications, as it suggests that LPBF-manufactured components with complex geometries that require printed supports may also contain residual stresses, leading to decreased SCC resistance.
2. Provided that the effect of residual stresses is mitigated or removed by a stress relief heat treatment, LPBF SS316L had a marginally better SCC resistance than CD wrought SS316L when stressed at 90% of their corresponding AYS values, as determined by a 1-week delay in crack initiation time.
3. A stress relief heat treatment improved the SCC resistance of LPBF SS316L. However, more research is needed to determine the degree of improvement that can be achieved and to identify the best temperature and duration of the heat treatment process.

# Chapter 6: Summary, main conclusions and future research

## 6.1 Summary

SCC is a type of environmentally-assisted cracking that affects susceptible materials when exposed to specific conditions above certain temperature/stress thresholds<sup>6, 9-12</sup>. For instance, a susceptible material that is ductile under regular operational conditions would fracture in a brittle manner at stresses below its yield point if SCC takes place. This phenomenon is observed in conventional austenitic SS316L, which typically exhibits excellent ductility and resistance to localised corrosion under nominal conditions. However, when SS316L is stressed and exposed to chloride ions at high temperatures, it becomes susceptible to SCC<sup>272-275, 277, 278</sup> and therefore experiences brittle fracture.

Given the importance of improving SCC resistance in SS316L, AM has emerged as a promising approach to produce engineering-grade alloys. AM also offers several advantages over conventional manufacturing processes, including reduced supply chain complexity, lower running costs, faster production, and greater design flexibility<sup>58, 60</sup>. Additionally, 3D printed materials can sometimes outperform their conventionally-manufactured counterparts since the printing parameters directly influence the material's characteristics such as microstructures, crystallographic textures, porosity and oxide inclusions content, mechanical properties, and corrosion resistance<sup>72, 74, 76, 94, 159-165</sup>. For instance, sinter-based material extrusion, an AM process that combines FDM with PM/MIM, has shown the ability to produce SS316L with isotropic microstructures and excellent ductility<sup>58, 60, 85-89</sup>. However, it has lower tensile strength and resistance to pitting corrosion caused by its relatively large grains and high bulk porosity content, respectively. Inversely, the rapid melting and near-instant solidification during the layering process involved in LPBF produce high-strength SS316L with good resistance to pit initiation<sup>74-79, 115, 284-286</sup>. However, LPBF SS316L components are anisotropic in the build direction and contain significant residual stresses, which limit their suitability for certain applications<sup>74, 76, 165, 166</sup>.

This investigation underpins the foundations for understanding the relationship between the 3D printed structures of SS316L produced using sinter-based and laser-based technologies at macro-, micro-, and nano-scales, and their impact on mechanical properties, pitting corrosion, SCC, and crack-branching susceptibility. Therefore, the first objective of this research was to characterise the microstructures of the as-printed SS316L, aiming to establish a correlation between the microstructures and the printing parameters. The microstructures' investigation was conducted using a suit of advanced imaging and crystallographic characterising techniques such as SEM, EDS, XRD, TEM, and EBSD. The major findings from this study are consistent with the existing literature, and support the

findings in relation to the influence of the AM process on the printed microstructures of the alloy<sup>58, 72, 94, 164, 165</sup>. Although both AM technologies, sinter-based and laser-based, produced SS316L with the chemical composition of UNS S31603, their distinct process parameters led to distinct microstructures.

For instance, sinter-based AM, with its high sintering temperature (1350 °C) and long dwell time (2 h), promotes the growth of large equiaxed austenitic grains (avg. 40 μm). The controlled heating and cooling rates inside the furnace (approx. 1 °C/min) produce a weakly textured microstructure ( $\times 1.17$  random in the {111} pole figure) that facilitate the formation of  $\Sigma 3$  twin boundaries (52.3%), and contribute to the reduction of the thermal residual stresses, as evidenced through the KAM analysis. In addition, the steady sintering stage allows the nano-spherical inclusions rich in Si-Mn-O (ranging from 20 to 230 nm), originally present in the precursor powder, to evolve both physically and chemically to form two sets of larger inclusions: i) spherical and Si-Mn-O-rich (avg. 1.4 μm), and ii) irregularly shaped and Cr-Mn-O-rich (avg. 3 μm). Moreover, the FDM and PM/MIM nature of the technology influence the bulk porosity content (5.21%) of the as-printed microstructure. In this context, two types of porosity are present: a round-type, resulting from the voids left between the feedstock powder during the necking process in the sintering stage, and an elongated-type, corresponding to the interstitial air gaps left between the extruded lines of material during the first stage of the printing process.

In comparison, the laser-based technology, with its rapid energy input (275 W at a scanning speed of 700 mm/s), followed by a near-instant solidification of the melted layers (cooling rates between  $10^3$  and  $10^7$  K/s<sup>72, 73, 237, 238</sup>), produce SS316L with significant columnar grain growth (avg. 57 μm) oriented in the build direction as influenced by the heat dissipation route. These elongated grains end in fine cellular structures, not measured in this investigation, but reported to range between 0.25 μm and 1.2 μm depending on the scanning parameters<sup>238, 261, 262</sup>. In addition, the rapid solidification of LPBF yields microstructures that exhibit a grain growth-dependent texture ( $\times 2.32$  random in the {111} pole figure), hinders the formation of  $\Sigma 3$  twin boundaries, and induces high thermal residual stresses<sup>75, 76, 83, 105, 234</sup>. However, the selected scanning strategy reduces the bulk porosity content to 0.74%. The as-printed LPBF-manufactured SS316L also contains nano-sized inclusions rich in Si-Mn-O. These particles experience size growth (reaching an average of 3 μm) upon undergoing solution treatment (1050 °C for 4 h), thereby reinforcing observations regarding the morphological evolution of such inclusions under controlled heat input conditions<sup>186, 188, 189, 264</sup>.

The second part of this research aimed to determine the mechanical properties of the 3D printed SS316L and establish their correlation with their as-printed microstructures. To achieve this, standard tensile tests were conducted on as-printed SS316L rectangular specimens, and their properties were measured. The results indicate that the sinter-based SS316L exhibits a low yield strength of 167 MPa, attributed to the presence of large equiaxed austenitic grains within its microstructure, as described by the classical Hall-Petch equation<sup>98,99</sup>. However, several independent factors might also contribute to the decreased strength. For instance, the bulk porosity content could have a combined effect, reducing the supporting area of the acting load and inducing an stress concentration factor at each pore<sup>170</sup>. Nonetheless, further investigations are necessary, as this statement still lacks consensus among researchers, likely due to the absence of a universally accepted qualification of defects and their distribution. These findings imply that the yield strength of sinter-based SS316L could potentially be improved by reducing the average grain size, achievable by diminishing the sintering time and/or sintering temperature, albeit at the expense of potentially increasing the size of round pores.

The sinter-based SS316L meets UNS S31603 requirements for elastic modulus (196 GPa), tensile strength (524 MPa), and ductility (51%, measured as the reduction of area). The remarkable elongation at fracture (96%) and after fracture (85%) of the sintered specimens can be attributed to the relatively high content of  $\Sigma 3$  twin boundaries and their ability to accommodate plastic deformation<sup>1-4</sup>. In addition, the rectangular cross-section of the test specimens and the high strain-hardening exponent (0.56) of the printed alloy contribute to its ability to maintain the rectangular shape for an extended period of time during tensile testing before fracture, in accordance with the tensile flow instability phenomenon<sup>98</sup>. The fracture behaviour of the 3D printed alloy is evidently ductile and occurs purely under tension, lacking the parabolic dimples on the fracture surface, indicative of shear fracture<sup>193</sup>. This fracture mode is influenced by Si-Mn-O-rich inclusions within the uniformly distributed spherical dimples. These particles act as multiple sites for void nucleation and subsequent coalescence into a single crack, preventing secondary cracks.

Conversely, the high yield strength (529 MPa) of LPBF-manufactured SS316L can be attributed to the fine cell structures perpendicular to the print direction<sup>74-76</sup>. The remaining tensile properties, i.e., elastic modulus (211 GPa), tensile strength (656 MPa), and ductility (45%), fall within standard ranges<sup>365</sup>. The reduced elongation at fracture (43%) and after fracture (12%) are attributed to the absence of  $\Sigma 3$  twin boundaries, which are hindered by the rapid solidification of the printed layers<sup>1-4, 75, 76, 83, 105, 234</sup>.



The third part of the research involved determining the pitting corrosion susceptibility in the printed materials, quantified as the time taken by pits to nucleate in an acidic chloride solution (1.5 pH and 25% w.t.). This study was conducted in conjunction to the SCC immersion tests. The findings from this investigation align with the existing literature, reinforcing that both 3D printed SS316L and wrought counterparts are susceptible to pitting corrosion at temperatures starting from 60 °C<sup>6, 8, 10, 11</sup>. While both 3D printed alloys meet the elemental composition of UNS S31603<sup>176</sup>, their distinctive pitting susceptibilities are attributed to the presence of surface heterogeneities. Notably, the considerable higher number of pits observed in sinter-based SS316L is attributed to its significantly higher porosity content, which weakens the passive layer. Moreover, larger pores facilitate the rapid growth of wider and deeper pits. These results suggest the potential for enhancing the pitting resistance of sinter-based SS316L by using shot-peening to close external porosity<sup>90, 310-312</sup>, or by reducing its bulk porosity through HIPing<sup>88, 306, 307, 309</sup>. In contrast, the low porosity content of LPBF-manufactured SS316L restricts the number of pit nucleation sites, effectively delaying pit growth. This phenomenon has been reported in the literature as a contributing factor to the high pitting resistance of LPBF SS316L<sup>77, 78</sup>. This observation was evident during the testing, as the samples exhibited fewer and smaller pores compared to the sinter-based counterparts tested under identical conditions.

The final part of the investigation aimed to determine the SCC susceptibility of the 3D printed alloys and establish its correlation with their microstructures, mechanical properties, and pitting corrosion resistance. To attain this objective, custom-made C-rings of SS316L were 3D printed and subjected to three stress levels (0%, 60%, 90% AYS). These C-rings were subsequently immersed in test solutions spanning temperatures from 30°C to boiling. For the purpose of comparison and to gain a deeper insights into SCC behaviour, wrought SS316L counterparts in both SA and CD conditions underwent identically testing. The findings of this investigation are in line with existing literature, reaffirming that non-sensitised austenitic stainless steels under tensile stress are susceptible to transgranular SCC in hot acidic chloride solutions<sup>6, 8, 10, 11</sup>. This investigation revealed that both sinter-based SS316L and SA wrought SS316L require applied stress to initiate cracking. However, although the printed alloy exhibited cracking from 80°C, the wrought material cracked only at boiling temperature. Consequently, it was established that the sinter-based SS316L is more susceptible to SCC initiation compared to its SA wrought counterpart. The higher susceptibility of sinter-based SS316L is attributed to its notably higher content of microstructural heterogeneities, specifically pores and oxide inclusions, which increase the number pit nucleation sites. This potentially increases the number of locations for pits to

grow towards a critical size, which in combination with the externally applied stress, facilitated the so-called pit-to-crack transition.

The aforementioned findings indicate that enhancing the SCC resistance of sinter-based SS316L might be potentially achievable through the reduction of its porosity content using the methods previously mentioned, i.e., HIPing or shot-peening. Comparatively, the lower strength of sinter-based SS316L led to a reduced applied stress when considering a percentage of AYS, making it more resistant to SCC initiation than its CD wrought counterpart, which experienced a higher load. These results hold validity as the loading conditions of the tests represent reasonable utilisation values for both materials in service.

This study also highlights the influence of residual stresses on the susceptibility to SCC. It was observed that the CD wrought SS316L C-rings under 0% AYS cracked in boiling conditions, attributed to the significant residual stresses induced during the material's cold-working manufacturing process and subsequent machining of the test specimen<sup>295-299</sup>. High-strength stainless steels, like CD wrought SS316L, tend to have a low threshold stress intensity factor for SCC ( $K_{I,SCC}$ ), indicating low SCC resistance<sup>10, 278, 281, 302</sup>. Similar observations are applicable to high-strength LPBF-manufactured SS316L, which exhibited high residual stresses as evidenced through the KAM analysis. These residual stresses increase its susceptibility to SCC. Notably, the LPBF C-rings exhibited constant cracking near the printed holes in areas perpendicular to the ends of the printed supports. Moreover, the unstressed printed samples cracked at boiling temperatures, mirroring the behaviour of their CD wrought unstressed counterparts. Although LPBF SS316L exhibited smaller pits compared to its sinter-based counterparts, the thermal residual stresses induced by the laser-based technology were sufficient to surpass the pit-to-crack transition threshold.

This investigation provides evidence of the impact of residual stresses on the SCC susceptibility. Significantly, LPBF C-rings subjected to stress relief heat treatment exhibited improved SCC resistance, as evidenced by the additional week needed for the material to crack. In addition to this, the partial immersion test, in which LPBF C-rings were suspended upside down with the printed holes above the solution line, established that the samples did not exhibit SCC near the printed holes. Instead, the cracking occurred in the region of maximum applied stress<sup>155, 369</sup>, resulting in a delay of one week before cracking occurred. These findings suggest mitigating or removing the effect of residual stresses could enhance the SCC resistance of LPBF-manufactured SS316L. These observations hold significant implications, as LPBF-manufactured components with complex geometries requiring support structures could contain residual stresses not considered during the material's qualification

for SCC susceptibility. This is particularly relevant when the test specimens involve printed supports.

Finally, the cracking behaviour of the 3D printed alloys was investigated in relation to their microstructures using fractography and micro-CT analysis techniques. The results of this investigation demonstrate that the presence of large aggregates of equiaxed grains, a high content of  $\Sigma 3$  twin boundaries, and a weak crystallographic textures can act as barriers for the propagation of secondary cracks (crack-branching), in sinter-based SS316L.

Consequently, sinter-based SS316L exhibit reduced crack-branching compared to both its laser-based and wrought counterparts. This investigation concluded that the microstructures of sinter-based SS316L, lead to an overall decrease in the Schmid factor, indicating an increased resolved shear stress required to initiate the slip across grains<sup>313-317</sup>. As a result, their nearly randomly oriented grains, coupled with the large number of twin boundaries, enhanced its resistance to crack propagation via branching in non-localised directions<sup>314, 316-319</sup>. Furthermore, this study suggests that despite the negative impact of porosity content on the resistance to SCC initiation in sinter-based SS316L, there is an additional crack-arrestor effect due to the blunting of crack tips, primarily attributed to the elongated pores<sup>320-322</sup>.

Conversely, since the microstructures of LPBF-manufactured SS316L lack effective crack barriers, the printed material exhibits more susceptibility to crack-branching. The impact of non-metallic inclusions and secondary phases, such as retained  $\delta$ -ferrite (BCC), on crack-branching resistance could not be definitively determined, as no clear correlation was observed. Therefore, the findings from this investigation indicate that the primary role in the material's resistance to crack-branching is played by the crystallographic texture.

## 6.2 Main conclusions

This thesis draws a number of holistic conclusions on the broader subject matter in addition to the specific conclusions detailed in the respective chapters. These conclusions are outlined below:

- There is a clear influence of the AM process variables on the microstructures and mechanical properties of the 3D printed SS316L. The controlled slow rate heating and cooling steps of the sinter-based technology results in the generation of a porous and isotropic microstructure, large equiaxed grains, high content of twin boundaries, low yield strength and high ductility. In contrast, the rapid energy input and near-instant solidifications of LPBF produce materials with anisotropic microstructures, elongated grains, absence of twin boundaries, high yield strength, and low ductility.

- In general, 3D printed SS316L alloys with a high content of porosity and surface heterogeneities, inherent to the 3D printing process, are more susceptible to SCC than the conventionally manufactured grade material. These heterogeneities weaken the corrosion-protective passive layer of the alloy, thereby facilitating the rapid nucleation and growth of pits. In this context, the sintered-based 3D printed SS316L is more susceptible than the LPBF-manufactured material due to the higher bulk porosity content.
- In 3D printed materials, cracking as a consequence of pitting is further aggravated by the presence of applied stresses, which accelerates pit-to-crack transition. This phenomenon is particularly noticeable in the sinter-based 3D printed material, primarily due to its high porosity content, which serves as multiple sites for pit nucleation.
- The crack-branching behaviour is also influenced by the porosity, including factors such as microscopy, morphology, quantity, and crack propagation dynamics. The round and elongated pores present in the sinter-based SS316L, situated within an environment of pseudo-random or relatively weak crystallographic texture, serve as barriers to the propagation of secondary cracks that result from the branching of the primary crack. These secondary cracks are eventually arrested, preventing further sub-branching. In contrast, the absence of this arresting behaviour is evident in the low-porosity (<1% bulk porosity) LPBF-SS316L and wrought alloys, as observed in this investigation. A definitive threshold value for porosity content in relation to this arresting behaviour could not be established.
- The high residual stresses present in both LPBF-manufactured and CD wrought SS316L significantly accelerate their susceptibility to SCC. This observation became evident when stressed and unstressed C-rings produced through these two methods cracked upon exposure to acidified chloride solution at boiling temperature. The considerable tensile loads induced by the residual stresses induced by their distinctive manufacturing methods facilitated the pit-to-crack transition. In contrast, materials with minimal residual stresses, like the sinter-based 3D printed and SA wrought SS316L, exhibited no cracking in their unstressed samples throughout the duration of the test.

### **6.3 Study limitations**

As previously stated, the complex interplay of the parameters in the AM technologies influence the microstructures of the 3D printed alloys, consequently affecting their mechanical properties, pitting resistance, and, therefore, SCC susceptibility. One of the aims of the investigation was to optimise the printing strategy for producing SS316L with improved properties and performance. However, there was a time constraint for manufacturing test samples under a wider range of printing variables in an iterative process. Moreover, there are secondary effects of one printing variable on others, making it difficult to manipulate multiple variables simultaneously and draw conclusive remarks. Conducting tests on 3D printed samples to generate distinctively different microstructures, thus exploring the influence of the parameters and their effects on properties/performance, would have provided a comprehensive understanding. However, this was beyond the scope of the project's timeframe. Overall, the thesis findings offer a clear view that AM technologies involve complex and interdependent printing variables, making the iterative process intricate and time-consuming. Drawing conclusions solely from an experimental-only approach might prove challenging. Therefore, it is crucial to consider a simulation-based investigation in conjunction with the experimental approach. Simulations could include a wider range of parameter variations, providing narrower windows for exploration. The results from simulations can then be validated through experiments. Nevertheless, based on the current experimentation, common parameters were fixed to establish a baseline of results that can be used for addressing new investigations.

Another limitation of this investigation is that, due to time constraints, the influence of post-processing was only briefly incorporated to understand the resulting microstructures and their impact on their material's properties and performance. Similarly, the actual effect of non-metallic inclusions and secondary phases on the crack-branching behaviour of the 3D printed SS316L remains largely unexplored. The control over inclusions morphology, distribution, and quantity is also unknown, necessitating thorough investigation.

In summary, the subject matter of this investigation is novel, and each aspect requires dedicated investigations, drawing upon our existing knowledge of conventional materials as a strong baseline.

### **6.4 Future research**

The results obtained in this dissertation could serve as a foundations for enhancing the resistance of 3D printing SS316L to SCC. While this investigation addresses certain

knowledge gaps related to the interplay between 3D printed microstructures, SCC susceptibility, and crack-branching behaviour, it also raises questions about the potential of improving these properties through the refinement of printing strategies and the implementation of post-processing techniques, as previously discussed.

It has been suggested that the SCC resistance of sinter-based SS316L could be significantly improved by minimising structural defects and oxide inclusions through the careful selection of appropriate feedstock. Strategies aimed at reducing SCC susceptibility might involve using low-oxygen powder feedstock, combined with extended sintering times and the optimisation of defect content and structural elements, such as grain size, defect morphology, surface characteristics, etc.

The susceptibility of LPBF-manufactured SS316L to SCC could potentially be mitigated by minimising the impact of the thermal residual stresses. This objective could be achieved by employing commercial software to simulate various scanning strategies, aiming to produce components with minimal residual stresses. Additionally, residual stresses could be reduced through the optimisation of post-process stress relief heat treatments, or by avoiding the introduction of residual stresses near the component/support interface through the manufacture of supportless structures. The latter approach would also require the use of software to determine the optimal printing strategy.

Further investigations could also explore the potential impact of post-processing steps on improving the SCC resistance of 3D printed SS316L. For instance, one approach could involve reducing the porosity content through surface treatments such as mechanical attrition, thereby minimising susceptibility to pitting and subsequently increase the SCC resistance of sinter-based manufactured SS316L. Some suggest the application of HIP to printed specimens. However, applying the high force of HIP in the final printed components might be impractical and could lead to geometrical distortions. Nevertheless, this approach contributes to a deeper scientific understanding and provides valuable insights into fundamental material science.

## Chapter 7: References

1. T. Ronneberg, C.M. Davies, P.A. Hooper, *Materials & Design* 189 (2020): p. 108481.
2. S. Ma, L. Fu, A. Shan, *Materials Characterization* 177 (2021): p. 111057.
3. H.W. Deng, Z.M. Xie, B.L. Zhao, Y.K. Wang, M.M. Wang, J.F. Yang, T. Zhang, Y. Xiong, X.P. Wang, Q.F. Fang, C.S. Liu, *Materials Science and Engineering: A* 744 (2019): p. 241-246.
4. S. Kheiri, H. Mirzadeh, M. Naghizadeh, *Materials Science and Engineering: A* 759 (2019): p. 90-96.
5. M. Wasim, M.B. Djukic, *Journal of Natural Gas Science and Engineering* 100 (2022): p. 104467.
6. E. McCafferty, *Introduction to corrosion science*, Springer Science & Business Media, 2010).
7. R.C. Newman, in *Corrosion Mechanisms in Theory and Practice*, CRC Press, 2011), p. 511-556.
8. H.S. Khatak, B. Raj, *Corrosion of austenitic stainless steels: mechanism, mitigation and monitoring*, Woodhead publishing, 2002).
9. W. Zhang, K. Fang, Y. Hu, S. Wang, X. Wang, *Corrosion Science* 108 (2016): p. 173-184.
10. D.A. Jones, *Principles and Prevention of Corrosion. New international edition*, 2nded., (Essex, England: Pearson, 1996).
11. D. Spencer, M. Edwards, M. Wenman, C. Tsitsios, G. Scatigno, P. Chard-Tuckey, *Corrosion Science* 88 (2014): p. 76-88.
12. R.C. Newman, *CORROSION TECHNOLOGY-NEW YORK AND BASEL-* 17 (2002): p. 399-450.
13. S. Papavinasam, *Corrosion control in the oil and gas industry*, Elsevier, 2013).
14. R. Pourazizi, M.A. Mohtadi-Bonab, J.A. Szpunar, *Engineering Failure Analysis* 109 (2020): p. 104400.
15. C. Manfredi, J.L. Otegui, *Engineering Failure Analysis* 9, 5 (2002): p. 495-509.
16. C.E. Jaske, J.A. Beavers, *1998 2nd International Pipeline Conference Volume 1: Risk Assessment and Management; Emerging Issues and Innovative Projects; Operations and Maintenance; Corrosion and Integrity Management* (1998): p. 439-445.
17. TheAdvertiser, "Epic Energy finds gas pipeline rupture was caused by stress corrosion cracking," The Abvertiser, 2015, <https://www.adelaidenow.com.au/news/south-australia/epic-energy-finds-gas-pipeline-rupture-was-caused-by-stress-corrosion-cracking/news-story/7c901d3fa3ae0a5e5742a8c88c456093> (Access date: 19/08/2023).
18. MP\_Materials\_Performance, "Stress Corrosion Cracking Led to Canadian Pipeline Rupture, Fire," Materials Performance Magazine, 2020, <https://www.materialsperformance.com/articles/coating-linings/2020/04/stress-corrosion-cracking-led-to-canadian-pipeline-rupture-fire> (Access date: 19/08/2023).
19. Reuters, "Stress, corrosion caused 2018 Enbridge gas pipeline blast: Canadian agency," Reuters, 2020, <https://www.reuters.com/article/us-canada-pipeline-enbridge-inc-idUSKBN20R2M3> (Access date: 19/08/2023 ).

20. Prince\_George\_Daily\_News, "Stress corrosion cracking led to pipeline explosion near Prince George in 2018," Prince George Daily News, 2020, <https://pgdailynews.ca/index.php/2020/03/04/stress-corrosion-cracking-led-to-pipeline-explosion-near-prince-george-in-2018/> (Access date: 19/08/2023).
21. ISS\_Source, "Stress Cracking Fatal AZ Pipeline Blast Cause," Copyright 2023, 2023, <https://www.isssource.com/stress-cracking-fatal-az-pipeline-blast-cause/> (Access date: 19/08/2023).
22. B.Y. Fang, A. Atrens, J.Q. Wang, E.H. Han, Z.Y. Zhu, W. Ke, *Journal of Materials Science* 38, 1 (2003): p. 127-132.
23. J. Galvele, *Corrosion Science* 27, 1 (1987): p. 1-33.
24. C.A. Loto, *The International Journal of Advanced Manufacturing Technology* 93, 9 (2017): p. 3567-3582.
25. Y.F. Cheng, *Stress corrosion cracking of pipelines*, John Wiley & Sons, 2013).
26. W. Chen, *Corrosion* 72, 7 (2016): p. 962-977.
27. R.M. Horn, G.M. Gordon, F.P. Ford, R.L. Cowan, *Nuclear Engineering and Design* 174, 3 (1997): p. 313-325.
28. J.T. Busby, G.S. Was, E.A. Kenik, *Journal of Nuclear Materials* 302, 1 (2002): p. 20-40.
29. Z. Abbasi, H. Niazi, M. Abdolrazzaghi, W. Chen, M. Daneshmand, *IEEE Sensors Journal* 20, 13 (2020): p. 7033-7043.
30. Y. Hou, L. Chen, Z. Li, G. Zhao, C. Zhang, *Materials Science and Engineering: A* 780 (2020): p. 139217.
31. X. Huang, Q. Pan, B. Li, Z. Liu, Z. Huang, Z. Yin, *Journal of Alloys and Compounds* 650 (2015): p. 805-820.
32. P.B. Srinivasan, K.S. Arora, W. Dietzel, S. Pandey, M.K. Schaper, *Journal of Alloys and Compounds* 492, 1 (2010): p. 631-637.
33. H. Jia, J. Li, Y. Li, M. Wang, S. Luo, Z. Zhang, *Journal of Alloys and Compounds* 911 (2022): p. 164995.
34. D.P. Braga, D.C.C. Magalhães, A.M. Kliauga, C.A. Della Rovere, V.L. Sordi, *Materials Science and Engineering: A* 773 (2020): p. 138865.
35. H. Ming, R. Zhu, Z. Zhang, J. Wang, E.H. Han, W. Ke, M. Su, *Materials Science and Engineering: A* 669 (2016): p. 279-290.
36. Z. Zhu, X. Jiang, G. Wei, X. Fang, Z. Zhong, K. Song, J. Han, Z. Jiang, *Acta Metallurgica Sinica (English Letters)* 33, 10 (2020): p. 1369-1378.
37. L. Romero-Resendiz, V. Amigó-Borrás, A. Vicente-Escuder, S. Elizalde, J.M. Cabrera, D. Pineda-Ruiz, I.A. Figueroa, G. Gonzalez, *Journal of Materials Research and Technology* 15 (2021): p. 4564-4572.
38. T.C. Tsai, T.H. Chuang, *Materials Science and Engineering: A* 225, 1 (1997): p. 135-144.
39. L. Huang, K. Wang, W. Wang, J. Yuan, K. Qiao, T. Yang, P. Peng, T. Li, *Engineering Failure Analysis* 92 (2018): p. 392-404.
40. Z. Li, D. Yi, C. Tan, B. Wang, *Journal of Alloys and Compounds* 817 (2020): p. 152690.
41. X. Guo, K. Chen, W. Gao, Z. Shen, P. Lai, L. Zhang, *Corrosion Science* 127 (2017): p. 157-167.



42. J. Ding, L. Zhang, D. Li, M. Lu, J. Xue, W. Zhong, *Journal of Materials Science* 48, 10 (2013): p. 3708-3715.
43. B. Panda, M. Sujata, M. Madan, S.K. Bhaumik, *Engineering Failure Analysis* 36 (2014): p. 379-389.
44. R. Novotny, P. Hähner, J. Siegl, P. Haušild, S. Ripplinger, S. Penttilä, A. Toivonen, *Journal of Nuclear Materials* 409, 2 (2011): p. 117-123.
45. G. Cragolino, D.S. Dunn, N. Sridhar, *Corrosion* 52, 03 (1996):
46. V. Raja, T. Shoji, *Stress corrosion cracking: theory and practice*, (Cambridge, UK: Woodhead Publishing Limited, 2011).
47. R.H. Jones, *Stress-Corrosion Cracking: Materials Performance and Evaluation*, ed., R.H. Jones, ASM International, 2017).
48. H.J. Russell, *Stress Corrosion Cracking*, (Materials Park, Ohio: ASM International, 1992).
49. S. Ghosh, "Effect of surface working operations on electrochemical corrosion and susceptibility to stress corrosion cracking of 304L stainless steel" (Doctor of Philosophy Doctoral, Homi Bhabha National Institute, June 2012, 2012).
50. M. Yasir, M. Danish, M. Mia, M.K. Gupta, M. Sarikaya, *The International Journal of Advanced Manufacturing Technology* 112, 3 (2021): p. 1065-1076.
51. T. Ming, H. Xue, T. Zhang, Y. Han, Q. Peng, *Surface and Coatings Technology* 438 (2022): p. 128420.
52. A.B. Rhouma, H. Sidhom, C. Braham, J. Lédion, M. Fitzpatrick, *Journal of materials engineering and performance* 10 (2001): p. 507-514.
53. B. Krawczyk, P. Cook, J. Hobbs, D.L. Engelberg, *Corrosion Science* 142 (2018): p. 93-101.
54. D.N. Wasnik, I. Samajdar, V. Kain, P.K. De, B. Verlinden, *Journal of Materials Engineering and Performance* 12, 4 (2003): p. 402-407.
55. L. Zhang, J. Wang, *Journal of Nuclear Materials* 446, 1 (2014): p. 15-26.
56. "Additive manufacturing — General principles — Fundamentals and vocabulary" (CH-1211 Geneva 20: ISO, 2015).
57. L. Yang, K. Hsu, B. Baughman, D. Godfrey, F. Medina, M. Menon, S. Wiener, *Additive manufacturing of metals: the technology, materials, design and production*, Springer, 2017).
58. B. Redwood, F. Schöffner, B. Garret, *The 3D printing handbook: technologies, design and applications*, (Amsterdam: 3D Hubs B.V., 2017).
59. "Additive Manufacturing - General Principles - Part 2: Overview of process categories and feedstock" (CH-1211 Geneva 20: ISO International, 2015).
60. G. Poszvek, G. Stattler, E. Markl, R. Seemann, M. Lackner, "Fused Filament Fabrication of Metallic Components for Semi-professional and Home Use," *Digital Conversion on the Way to Industry 4.0* Springer International Publishing, 2021), p. 140-149.
61. M. Attaran, *Business Horizons* 60, 5 (2017): p. 677-688.
62. B. Wu, Z. Pan, D. Ding, D. Cuiuri, H. Li, J. Xu, J. Norrish, *Journal of Manufacturing Processes* 35 (2018): p. 127-139.
63. Y. Kok, X.P. Tan, P. Wang, M.L.S. Nai, N.H. Loh, E. Liu, S.B. Tor, *Materials & Design* 139 (2018): p. 565-586.

64. D. Liu, D. Wu, R. Wang, J. Shi, F. Niu, G. Ma, *Additive Manufacturing* 50 (2022): p. 102554.
65. Y. Tang, Y.F. Zhao, *Rapid Prototyping Journal* 22, 3 (2016): p. 569-590.
66. H. Cheng, Z. Liu, H. Luo, Z. Pan, X. Wang, Q. Zhao, X. Qi, X. Li, *Corrosion Science* 213 (2023): p. 110969.
67. H. Chen, Y.F. Zhao, *Rapid Prototyping Journal* 22, 3 (2016): p. 527-538.
68. H. Chen, Y. Sun, W. Yuan, S. Pang, W. Yan, Y. Shi, *Chinese Journal of Mechanical Engineering: Additive Manufacturing Frontiers* 1, 1 (2022): p. 100017.
69. K.S. Ramani, E. Malekipour, C.E. Okwudire, "Toward Intelligent Online Scan Sequence Optimization for Uniform Temperature Distribution in LPBF Additive Manufacturing," ASME 2021 16th International Manufacturing Science and Engineering Conference(V001T01A023: 2021).
70. J.G. Pauza, W.A. Tayon, A.D. Rollett, *Modelling and Simulation in Materials Science and Engineering* 29, 5 (2021): p. 055019.
71. L. Bian, N. Shamsaei, J.M. Usher, *Laser-based additive manufacturing of metal parts: modeling, optimization, and control of mechanical properties*, CRC Press, 2017).
72. T. DebRoy, H.L. Wei, J.S. Zuback, T. Mukherjee, J.W. Elmer, J.O. Milewski, A.M. Beese, A. Wilson-Heid, A. De, W. Zhang, *Progress in Materials Science* 92 (2018): p. 112-224.
73. Y. Tsutsumi, T. Ishimoto, T. Oishi, T. Manaka, P. Chen, M. Ashida, K. Doi, H. Katayama, T. Hanawa, T. Nakano, *Additive Manufacturing* 45 (2021): p. 102066.
74. J. Suryawanshi, K.G. Prashanth, U. Ramamurty, *Materials Science and Engineering: A* 696 (2017): p. 113-121.
75. Q. Chao, S. Thomas, N. Birbilis, P. Cizek, P.D. Hodgson, D. Fabijanic, *Materials Science and Engineering: A* 821 (2021): p. 141611.
76. T. Kurzynowski, K. Gruber, W. Stopyra, B. Kuźnicka, E. Chlebus, *Materials Science and Engineering A* 718 (2018): p. 64-73.
77. C. Man, C. Dong, T. Liu, D. Kong, D. Wang, X. Li, *Applied Surface Science* 467-468 (2019): p. 193-205.
78. G. Sander, S. Thomas, V. Cruz, M. Jurg, N. Birbilis, X. Gao, M. Brameld, C.R. Hutchinson, *Journal of The Electrochemical Society* 164, 6 (2017): p. C250-C257.
79. M.H. Shaeri Karimi, M. Yeganeh, S.R. Alavi Zaree, M. Eskandari, *Optics & Laser Technology* 138 (2021): p. 106918.
80. S. Dixit, S. Liu, H.A. Murdoch, P.M. Smith, *Materials Science and Engineering: A* 880 (2023): p. 145308.
81. Z. Pitrmuc, J. Šimota, L. Beránek, P. Mikeš, V. Andronov, J. Sommer, F. Holešovský, *Materials* 15, 2 (2022): p. 551.
82. J. Fu, S. Qu, J. Ding, X. Song, M.W. Fu, *Additive Manufacturing* 44 (2021): p. 102067.
83. P. Dong, F. Vecchiato, Z. Yang, P.A. Hooper, M.R. Wenman, *Additive Manufacturing* 40 (2021): p. 101902.
84. P. Bian, J. Shi, Y. Liu, Y. Xie, *Optics & Laser Technology* 132 (2020): p. 106477.
85. J. Damon, S. Dietrich, S. Gorantla, U. Popp, B. Okolo, V. Schulze, *Rapid Prototyping Journal* 25, 7 (2019): p. 1319-1327.

86. I. Ait-Mansour, N. Kretzschmar, S. Chekurov, M. Salmi, J. Rech, *Progress in Additive Manufacturing* 5, 1 (2020): p. 51-57.
87. C. Suwanpreecha, P. Seensattayawong, V. Vadhanakovint, A. Manonukul, *Metallurgical and Materials Transactions A* 52, 5 (2021): p. 1999-2009.
88. Y. Wang, L. Zhang, X. Li, Z. Yan, *Materials Letters* 296 (2021): p. 129854.
89. C. Tosto, J. Tirillò, F. Sarasini, G. Cicala, *Applied Sciences* 11, 4 (2021): p. 1444.
90. J. Damon, S. Dietrich, F. Vollert, J. Gibmeier, V. Schulze, *Additive Manufacturing* 20 (2018): p. 77-89.
91. B. Liu, Y. Wang, Z. Lin, T. Zhang, *Materials Letters* 263 (2020): p. 127252.
92. J. Jansa, A. Volodarskaja, J. Hlinka, L. Zárbynická, S. Polzer, M. Kraus, J. Hajnyš, D. Schwarz, M. Pagáč, *Journal of Manufacturing Processes* 88 (2023): p. 232-245.
93. M.A. Wagner, J. Engel, A. Hadian, F. Clemens, M. Rodriguez-Arbaizar, E. Carreño-Morelli, J.M. Wheeler, R. Spolenak, *Additive Manufacturing* 59 (2022): p. 103147.
94. M.Á. Caminero, A. Romero, J.M. Chacón, P.J. Núñez, E. García-Plaza, G.P. Rodríguez, *Rapid Prototyping Journal* 27, 3 (2021): p. 583-591.
95. W. Wang, T. Liu, X. Cao, Y. Lu, T. Shoji, *Materials Characterization* 132 (2017): p. 169-174.
96. R. Zheng, M. Liu, Z. Zhang, K. Ameyama, C. Ma, *Scripta Materialia* 169 (2019): p. 76-81.
97. R.W. Hertzberg, R.P. Vinci, J.L. Hertzberg, *Deformation and fracture mechanics of engineering materials*, John Wiley & Sons, 2020).
98. G.E. Dieter, D.J. Bacon, *Mechanical metallurgy*, vol. 3, (New York: McGraw-hill, 1976).
99. W.D. Callister, D.G. Rethwisch, A. Blicblau, K. Bruggeman, M. Cortie, J. Long, J. Hart, R. Marceau, M. Ryan, R. Parvizi, *Materials science and engineering: an introduction*, wiley, 2021).
100. A.S. Wu, D.W. Brown, M. Kumar, G.F. Gallegos, W.E. King, *Metallurgical and Materials Transactions A* 45, 13 (2014): p. 6260-6270.
101. M. Sprengel, A. Ulbricht, A. Evans, A. Kromm, K. Sommer, T. Werner, J. Kelleher, G. Bruno, T. Kannengiesser, *Metallurgical and Materials Transactions A* 52, 12 (2021): p. 5342-5356.
102. S. Zhang, F. Bi, T. Wu, Y. Wang, Z. Que, L. Chang, *Materials Characterization* 197 (2023): p. 112716.
103. M.S. Pham, B. Dovgyy, P.A. Hooper, *Materials Science and Engineering: A* 704 (2017): p. 102-111.
104. J. Bedmar, A. Riquelme, P. Rodrigo, B. Torres, J. Rams, *Materials* 14, 21 (2021): p. 6504.
105. M. Godec, S. Zaefferer, B. Podgornik, M. Šinko, E. Tchernychova, *Materials Characterization* 160 (2020): p. 110074.
106. H. Gong, D. Snelling, K. Kardel, A. Carrano, *JOM* 71, 3 (2019): p. 880-885.
107. W. Zhai, W. Zhou, S.M.L. Nai, *Materials Science and Engineering: A* 840 (2022): p. 142912.
108. M. Mokhtari, P. Pommier, Y. Balcaen, J. Alexis, *Journal of Manufacturing and Materials Processing* 5, 4 (2021): p. 136.

109. M.R. Jandaghi, H. Pouraliakbar, S.H. Shim, V. Fallah, S.I. Hong, M. Pavese, *Materials Science and Engineering: A* 857 (2022): p. 144114.
110. M. Ahmed Obeidi, S.M. Uí Mhurchadha, R. Raghavendra, A. Conway, C. Souto, D. Tormey, I.U. Ahad, D. Brabazon, *Journal of Materials Research and Technology* 13 (2021): p. 2361-2374.
111. X. Wang, O. Sanchez-Mata, S.E. Atabay, J.A. Muñoz-Lerma, M. Attarian Shandiz, M. Brochu, *Additive Manufacturing* 46 (2021): p. 102104.
112. R.I. Revilla, M. Van Calster, M. Raes, G. Arroud, F. Andreatta, L. Pyl, P. Guillaume, I. De Graeve, *Corrosion Science* 176 (2020): p. 108914.
113. J.R. Trelewicz, G.P. Halada, O.K. Donaldson, G. Manogharan, *JOM* 68, 3 (2016): p. 850-859.
114. M. Yeganeh, M.H. Rezvani, S.M. Laribaghal, *Colloids and Surfaces A: Physicochemical and Engineering Aspects* 627 (2021): p. 127120.
115. K. Wang, Q. Chao, M. Annasamy, P.D. Hodgson, S. Thomas, N. Birbilis, D. Fabijanic, *Corrosion Science* 197 (2022): p. 110060.
116. É.C. Bordinassi, S.U. Mhurchadha, V. Seriacopi, S. Delijaicov, S.M.G. Lebrão, K. Thomas, G.F. Batalha, R. Raghavendra, *Journal of the Brazilian Society of Mechanical Sciences and Engineering* 44, 10 (2022): p. 491.
117. S. Santa-aho, M. Kiviluoma, T. Jokiahho, T. Gundgire, M. Honkanen, M. Lindgren, M. Vippola, *Metals* 11, 2 (2021): p. 182.
118. V. Cruz, Y. Qiu, N. Birbilis, S. Thomas, *Corrosion Science* 207 (2022): p. 110535.
119. Z. Que, T. Riipinen, S. Goel, A. Revuelta, T. Saario, K. Sipilä, A. Toivonen, *Corrosion Science* 214 (2023): p. 111022.
120. E.K. Karasz, J. Taylor, D.M. Autenrieth, P. Reu, K. Johnson, M. Melia, P. Noell, *Corrosion* 78, 1 (2021): p. 3-12.
121. X. Lou, P.L. Andresen, R.B. Rebak, *Journal of Nuclear Materials* 499 (2018): p. 182-190.
122. A. Yazdanpanah, M. Lago, C. Gennari, M. Dabalà, *Metals* 11, 2 (2021): p. 327.
123. A. Yazdanpanah, F.R. Biglari, A. Fallahi Arezoodar, M. Dabalà, *Corrosion Engineering, Science and Technology* 56, 1 (2021): p. 81-92.
124. A. Yazdanpanah, M. Franceschi, G. Bergamo, M. Bonesso, M. Dabalà, *Engineering Failure Analysis* 136 (2022): p. 106192.
125. A. Yazdanpanah, M. Franceschi, P. Rebesan, M. Dabalà, *Materials* 15, 20 (2022): p. 7151.
126. S. Zhang, S. Wang, X. Feng, Z. Ning, J. Hou, W. Kuang, *Acta Materialia* 244 (2023): p. 118561.
127. L.-E. Rännar, A. Koptuyug, J. Olsén, K. Saeidi, Z. Shen, *Additive Manufacturing* 17 (2017): p. 106-112.
128. Y. Zhong, L.-E. Rännar, L. Liu, A. Koptuyug, S. Wikman, J. Olsen, D. Cui, Z. Shen, *Journal of Nuclear Materials* 486 (2017): p. 234-245.
129. I.A. Segura, J. Mireles, D. Bermudez, C.A. Terrazas, L.E. Murr, K. Li, V.S.Y. Injeti, R.D.K. Misra, R.B. Wicker, *Journal of Nuclear Materials* 507 (2018): p. 164-176.
130. N. Yang, J. Yee, B. Zheng, K. Gaiser, T. Reynolds, L. Clemon, W.Y. Lu, J.M. Schoenung, E.J. Lavernia, *Journal of Thermal Spray Technology* 26, 4 (2017): p. 610-626.

131. B.M. Morrow, T.J. Lienert, C.M. Knapp, J.O. Sutton, M.J. Brand, R.M. Pacheco, V. Livescu, J.S. Carpenter, G.T. Gray, *Metallurgical and Materials Transactions A* 49, 8 (2018): p. 3637-3650.
132. L. Zhang, W. Zhai, W. Zhou, X. Chen, L. Chen, B. Han, L. Cao, G. Bi, *Materials Science and Engineering: A* 853 (2022): p. 143767.
133. X. Chen, J. Li, X. Cheng, B. He, H. Wang, Z. Huang, *Materials Science and Engineering: A* 703 (2017): p. 567-577.
134. M. McMurtrey, C. Sun, R.E. Rupp, C.H. Shiau, R. Hanbury, N. Jerred, R. O'Brien, *Journal of Nuclear Materials* 545 (2021): p. 152739.
135. Q. Xiao, J. Chen, H.B. Lee, C. Jang, K. Jang, *Corrosion Science* 210 (2023): p. 110830.
136. J. Yang, L. Hawkins, L. He, S. Mahmood, M. Song, K. Schulze, X. Lou, *Journal of Nuclear Materials* 577 (2023): p. 154305.
137. J. Yang, L. Hawkins, M. Song, L. He, M. Bachhav, Q. Pan, L. Shao, D. Schwen, X. Lou, *Journal of Nuclear Materials* 560 (2022): p. 153493.
138. M. Bassis, A. Kotliar, R. Koltiar, T. Ron, A. Leon, A. Shirizly, E. Aghion, *Metals* 11, 12 (2021): p. 1930.
139. X. Chen, J. Han, J. Wang, Y. Cai, G. Zhang, L. Lu, Y. Xin, Y. Tian, *Materials Letters* 300 (2021): p. 130141.
140. L. Wang, J. Xue, Q. Wang, *Materials Science and Engineering: A* 751 (2019): p. 183-190.
141. C. Wang, T.G. Liu, P. Zhu, Y.H. Lu, T. Shoji, *Materials Science and Engineering: A* 796 (2020): p. 140006.
142. T.A. Rodrigues, F.W. Cipriano Farias, K. Zhang, A. Shamsolhodaei, J. Shen, N. Zhou, N. Schell, J. Capek, E. Polatidis, T.G. Santos, J.P. Oliveira, *Journal of Materials Research and Technology* 21 (2022): p. 237-251.
143. W. Wu, J. Xue, L. Wang, Z. Zhang, Y. Hu, C. Dong, *Metals* 9, 1 (2019): p. 109.
144. C. Wang, P. Zhu, F. Wang, Y.H. Lu, T. Shoji, *Corrosion Science* 206 (2022): p. 110549.
145. D. Wen, P. Long, J. Li, L. Huang, Z. Zheng, *Vacuum* 173 (2020): p. 109131.
146. S.H. Lee, *Metals* 10, 2 (2020): p. 278.
147. J. Chen, H. Wei, K. Bao, X. Zhang, Y. Cao, Y. Peng, J. Kong, K. Wang, *Journal of Materials Research and Technology* 11 (2021): p. 170-179.
148. B. Xie, J. Xue, X. Ren, *Metals* 10, 11 (2020): p. 1419.
149. D. Jiang, F. Ning, *Journal of Manufacturing Science and Engineering* 143, 9 (2021):
150. M. Sadaf, M. Bragaglia, F. Nanni, *Journal of Manufacturing Processes* 67 (2021): p. 141-150.
151. Y. Thompson, J. Gonzalez-Gutierrez, C. Kukla, P. Felfer, *Additive Manufacturing* 30 (2019): p. 100861.
152. "Standard Test Methods for Tension Testing of Metallic Materials" (West Conshohocken, PA: ASTM International, 2016).
153. R. Santamaria, M. Salasi, S. Bakhtiari, G. Leadbeater, M. Iannuzzi, M.Z. Quadir, *Journal of Materials Science* 57 (2022): p. 1-17.

154. R. Santamaria, M. Salasi, W.D. Rickard, K. Pojtanabuntoeng, G. Leadbeater, M. Iannuzzi, S.M. Reddy, M.Z. Quadir, *Materials* 16, 12 (2023): p. 4289.
155. "Standard practice for making and using C-ring stress-corrosion test specimens" (West Conshohocken, PA: ASTM International, 2013).
156. "Standard test method for evaluationg stress-corrosion cracking of stainless steel alloys with different nickel content in boiling acidified sodium chloride solution" (West Conshohocken, PA: ASTM International, 2015).
157. R. Santamaria, K. Wang, M. Salasi, M. Iannuzzi, M.Y. Mendoza, M.Z. Quadir, *Materials* 16, 11 (2023): p. 4006.
158. R. Santamaria, K. Wang, M. Salasi, M. Salem, P. Lours, M. Iannuzzi, M.Z. Quadir, *Corrosion* 4311, 8 (2023):
159. B. Rankouhi, K.M. Bertsch, G. Meric de Bellefon, M. Thevamaran, D.J. Thoma, K. Suresh, *Materials Science and Engineering: A* 776 (2020): p. 139050.
160. R. Casati, J. Lemke, M. Vedani, *Journal of Materials Science & Technology* 32, 8 (2016): p. 738-744.
161. S. Kersten, M. Pranievicz, T. Kurfess, C. Saldana, *Procedia Manufacturing* 48 (2020): p. 730-736.
162. D.R. Feenstra, V. Cruz, X. Gao, A. Molotnikov, N. Birbilis, *Additive Manufacturing* 34 (2020): p. 101205.
163. K. Benarji, Y. Ravi Kumar, A.N. Jinoop, C.P. Paul, K.S. Bindra, *Metals and Materials International* 27, 3 (2021): p. 488-499.
164. A. Aversa, A. Saboori, E. Librera, M. de Chirico, S. Biamino, M. Lombardi, P. Fino, *Additive Manufacturing* 34 (2020): p. 101274.
165. Y.n. Song, Q. Sun, K. Guo, X. Wang, J. Liu, J. Sun, *Materials Science and Engineering: A* 793 (2020): p. 139879.
166. B. Barkia, P. Aubry, P. Haghi-Ashtiani, T. Auger, L. Gosmain, F. Schuster, H. Maskrot, *Journal of Materials Science & Technology* 41 (2020): p. 209-218.
167. F. Cerejo, D. Gatões, M.T. Vieira, *The International Journal of Advanced Manufacturing Technology* 115, 7 (2021): p. 2449-2464.
168. T. Rosnitschek, A. Seefeldt, B. Alber-Laukant, T. Neumeyer, V. Altstädt, S. Tremmel, *Materials* 14, 18 (2021): p. 5173.
169. D. Jiang, F. Ning, *Journal of Manufacturing Science and Engineering* 143, 9 (2021): p. 091007.
170. R.M. German, *Powder metallurgy of iron and steel*, 1998).
171. D.F. Heaney, *Handbook of Metal Injection Molding*, (Philadelphia, PA: Woodhead Publishing, 2012).
172. J. Šafka, M. Ackermann, J. Machacek, M. Seidl, F. Vélé, V. Truxova, *MM Science Journal* 2020 (2020): p. 4216-4222.
173. K. Gante Lokesh Renukaradhya, "Metal Filament 3D Printing of SS316L : Focusing on the printing process" (Independent thesis Advanced level (degree of Master (Two Years)) Student thesis, KTH Royal Institute of Technology, 2019, 2019).
174. "Standard Test Method for Density of Powder Metallurgy (PM) Materials Containing Less Than Two Percent Porosity" (West Conshohocken, PA: ASTM International, 2017).

175. "Standard Test Method for Young's Modulus, Tangent Modulus, and Chord Modulus" (West Conshohocken, PA: ASTM International, 2017).
176. "Standard Specification for Chromium and Chromium-Nickel Stainless Steel Plate Sheet and Strip for Pressure Vessels and for General Applications" (West Conshohocken, PA: ASTM International, 2020).
177. P. Deng, M. Karadge, R.B. Rebak, V.K. Gupta, B.C. Prorok, X. Lou, *Additive Manufacturing* 35 (2020): p. 101334.
178. F. Yan, W. Xiong, E. Faierson, G.B. Olson, *Scripta Materialia* 155 (2018): p. 104-108.
179. S. Irukuvarghula, H. Hassanin, C. Cayron, M.M. Attallah, D. Stewart, M. Preuss, *Acta Materialia* 133 (2017): p. 269-281.
180. "Standard Practice for Determining Average Grain Size Using Electron Backscatter Diffraction (EBSD) in Fully Recrystallized Polycrystalline Materials" (West Conshohocken, PA: ASTM International, 2019).
181. H.M. Ledbetter, *Journal of Applied Physics* 52, 3 (1981): p. 1587-1589.
182. J.L. Colón Quintana, A. Redmann, G.A. Mazzei Capote, A. Pérez-Irizarry, A. Bechara, T.A. Osswald, R. Lakes, *Additive Manufacturing* 28 (2019): p. 704-710.
183. M. Montero, S. Roundy, D. Odell, S.-H. Ahn, P.K. Wright, *Society of Manufacturing Engineers* 10, 13552540210441166 (2001): p. 1-21.
184. P. Singh, "Materials-processing relationships for metal fused filament fabrication of Ti-6Al-4V alloy" University of Louisville, (2020).
185. E. Klar, P.K. Samal, *Powder metallurgy stainless steels: processing, microstructures, and properties*, (Ohio: ASM international, 2007).
186. H. Shibata, K. Kimura, T. Tanaka, S.-y. Kitamura, *ISIJ International* 51, 12 (2011): p. 1944-1950.
187. H. Shibata, T. Tanaka, K. Kimura, S.Y. Kitamura, *Ironmaking & Steelmaking* 37, 7 (2010): p. 522-528.
188. Y. Ren, L. Zhang, P.C. Pistorius, *Metallurgical and Materials Transactions B* 48, 5 (2017): p. 2281-2292.
189. M. Laleh, A.E. Hughes, W. Xu, P. Cizek, M.Y. Tan, *Corrosion Science* 165 (2020): p. 108412.
190. R. Varin, K. Kurzydowski, *Materials Science and Engineering: A* 101 (1988): p. 221-226.
191. K.K. Singh, S. Sangal, G. Murty, *Materials Science and Technology* 18 (2002): p. 165-172.
192. T.S. Yoon, Y.H. Lee, S.H. Ahn, J.H. Lee, C.S. Lee, *ISIJ international* 43, 1 (2003): p. 119-126.
193. K. Mills, J.R. Davis, *ASM Handbook, Volume 12-Fractography*, ASM International, 1987).
194. S. Ifergane, Z. Barkay, O. Beerli, N. Eliaz, *Journal of Materials Science* 45, 23 (2010): p. 6345-6352.
195. "Standard Specification for Metal Injection Molded (MIM) Materials" (West Conshohocken, PA: ASTM International, 2019).
196. W. Meiners, K. Wissenbach, A. Gasser, *DE Patent* 19 (1998):

197. W. Harun, M. Kamariah, N. Muhamad, S. Ghani, F. Ahmad, Z. Mohamed, *Powder Technology* 327 (2018): p. 128-151.
198. B. Song, S. Dong, S. Deng, H. Liao, C. Coddet, *Optics & Laser Technology* 56 (2014): p. 451-460.
199. E.O. Olakanmi, R.F. Cochrane, K.W. Dalgarno, *Progress in Materials Science* 74 (2015): p. 401-477.
200. Z. Liu, D. Zhang, S. Sing, C. Chua, L. Loh, *Materials Characterization* 94 (2014): p. 116-125.
201. R. Shi, S.A. Khairallah, T.T. Roehling, T.W. Heo, J.T. McKeown, M.J. Matthews, *Acta Materialia* 184 (2020): p. 284-305.
202. T.M. Mower, M.J. Long, *Materials Science and Engineering: A* 651 (2016): p. 198-213.
203. T. Maconachie, M. Leary, B. Lozanovski, X. Zhang, M. Qian, O. Faruque, M. Brandt, *Materials & Design* 183 (2019): p. 108137.
204. I. Maskery, A. Aremu, M. Simonelli, C. Tuck, R. Wildman, I. Ashcroft, R. Hague, *Experimental Mechanics* 55 (2015): p. 1261-1272.
205. I. Maskery, N. Aboulkhair, A. Aremu, C. Tuck, I. Ashcroft, R.D. Wildman, R. Hague, *Materials Science and Engineering: A* 670 (2016): p. 264-274.
206. R.F. Hamilton, B.A. Bimber, M.T. Andani, M. Elahinia, *Journal of Materials Processing Technology* 250 (2017): p. 55-64.
207. C.W. Visser, R. Pohl, C. Sun, G.W. Römer, B. Huis in 't Veld, D. Lohse, *Advanced materials* 27, 27 (2015): p. 4087-4092.
208. Y. Li, D. Gu, *Materials & design* 63 (2014): p. 856-867.
209. M. Averyanova, E. Cicala, P. Bertrand, D. Grevey, *Rapid Prototyping Journal* (2012):
210. P. Lott, H. Schleifenbaum, W. Meiners, K. Wissenbach, C. Hinke, J. Bültmann, *Physics Procedia* 12 (2011): p. 683-690.
211. C. Brecher, *Advances in production technology*, Springer Nature, 2015).
212. N.T. Aboulkhair, M. Simonelli, L. Parry, I. Ashcroft, C. Tuck, R. Hague, *Progress in materials science* 106 (2019): p. 100578.
213. N.T. Aboulkhair, N.M. Everitt, I. Ashcroft, C. Tuck, *Additive manufacturing* 1 (2014): p. 77-86.
214. M. Langelaar, *Additive manufacturing* 12 (2016): p. 60-70.
215. N. Read, W. Wang, K. Essa, M.M. Attallah, *Materials & Design (1980-2015)* 65 (2015): p. 417-424.
216. N.T. Aboulkhair, N.M. Everitt, I. Maskery, I. Ashcroft, C. Tuck, *MRS Bulletin* 42, 4 (2017): p. 311-319.
217. M. Simonelli, Y.Y. Tse, C. Tuck, *Materials Science and Engineering: A* 616 (2014): p. 1-11.
218. M. Simonelli, Y.Y. Tse, C. Tuck, *Metallurgical and Materials Transactions A* 45 (2014): p. 2863-2872.
219. C. Kamath, B. El-Dasher, G.F. Gallegos, W.E. King, A. Sisto, *The International Journal of Advanced Manufacturing Technology* 74 (2014): p. 65-78.



220. M. Garibaldi, I. Ashcroft, J. Lemke, M. Simonelli, R. Hague, *Scripta Materialia* 142 (2018): p. 121-125.
221. M. Garibaldi, I. Ashcroft, M. Simonelli, R. Hague, *Acta Materialia* 110 (2016): p. 207-216.
222. J. Lemke, M. Simonelli, M. Garibaldi, I. Ashcroft, R. Hague, M. Vedani, R. Wildman, C. Tuck, *Journal of Alloys and Compounds* 722 (2017): p. 293-301.
223. S. Catchpole-Smith, N. Aboulkhair, L. Parry, C. Tuck, I.A. Ashcroft, A. Clare, *Additive Manufacturing* 15 (2017): p. 113-122.
224. J.-P. Choi, G.-H. Shin, S. Yang, D.-Y. Yang, J.-S. Lee, M. Brochu, J.-H. Yu, *Powder Technology* 310 (2017): p. 60-66.
225. G. Marchese, X. Garmendia Colera, F. Calignano, M. Lorusso, S. Biamino, P. Minetola, D. Manfredi, *Advanced Engineering Materials* 19, 3 (2017): p. 1600635.
226. L.N. Carter, C. Martin, P.J. Withers, M.M. Attallah, *Journal of Alloys and Compounds* 615 (2014): p. 338-347.
227. J. Ciurana, L. Hernandez, J. Delgado, *The International Journal of Advanced Manufacturing Technology* 68 (2013): p. 1103-1110.
228. Y. Pupo, J. Delgado, L. Serenó, J. Ciurana, *Procedia Engineering* 63 (2013): p. 370-378.
229. K. Monroy, J. Delgado, J. Ciurana, *Procedia Engineering* 63 (2013): p. 361-369.
230. A. Takaichi, T. Nakamoto, N. Joko, N. Nomura, Y. Tsutsumi, S. Migita, H. Doi, S. Kurosu, A. Chiba, N. Wakabayashi, *Journal of the mechanical behavior of biomedical materials* 21 (2013): p. 67-76.
231. I. Yadroitsev, A. Gusarov, I. Yadroitsava, I. Smurov, *Journal of Materials Processing Technology* 210, 12 (2010): p. 1624-1631.
232. B. Zhang, H. Liao, C. Coddet, *Materials & Design* 34 (2012): p. 753-758.
233. C. Galy, E. Le Guen, E. Lacoste, C. Arvieu, *Additive Manufacturing* 22 (2018): p. 165-175.
234. M. Michiuchi, H. Kokawa, Z. Wang, Y. Sato, K. Sakai, *Acta materialia* 54, 19 (2006): p. 5179-5184.
235. A. Mahata, M.A. Zaeem, *Computational Materials Science* 163 (2019): p. 176-185.
236. J. Shen, R. Gonçalves, Y.T. Choi, J.G. Lopes, J. Yang, N. Schell, H.S. Kim, J.P. Oliveira, *Scripta Materialia* 222 (2023): p. 115053.
237. M. Ma, Z. Wang, X. Zeng, *Materials Science and Engineering: A* 685 (2017): p. 265-273.
238. N. Diaz Vallejo, C. Lucas, N. Ayers, K. Graydon, H. Hyer, Y. Sohn, *Metals* 11, 5 (2021): p. 832.
239. S.-h. Sun, T. Ishimoto, K. Hagihara, Y. Tsutsumi, T. Hanawa, T. Nakano, *Scripta Materialia* 159 (2019): p. 89-93.
240. S.-H. Sun, K. Hagihara, T. Nakano, *Materials & Design* 140 (2018): p. 307-316.
241. L. Thijs, M.L.M. Sistiaga, R. Wauthle, Q. Xie, J.-P. Kruth, J. Van Humbeeck, *Acta Materialia* 61, 12 (2013): p. 4657-4668.
242. M.-S. Pham, B. Dovgvy, P.A. Hooper, C.M. Gourlay, A. Piglione, *Nature communications* 11, 1 (2020): p. 749.

243. F. Humphreys, M. Hatherly, *Recrystallization and Related Annealing Phenomena, second ed., Elsevier, Oxford* (2004): p. 379e413.
244. K. Prashanth, H.S. Shahabi, H. Attar, V. Srivastava, N. Ellendt, V. Uhlenwinkel, J. Eckert, S. Scudino, *Additive Manufacturing* 6 (2015): p. 1-5.
245. T. Qi, H. Zhu, H. Zhang, J. Yin, L. Ke, X. Zeng, *Materials & Design* 135 (2017): p. 257-266.
246. G. Dinda, A. Dasgupta, J. Mazumder, *Surface and Coatings Technology* 206, 8-9 (2012): p. 2152-2160.
247. H. Wei, J. Mazumder, T. DebRoy, *Scientific reports* 5, 1 (2015): p. 1-7.
248. S. Bhattacharya, G.P. Dinda, A.K. Dasgupta, J. Mazumder, *Journal of Materials Science* 49 (2014): p. 2415-2429.
249. L.L. Parimi, G. Ravi, D. Clark, M.M. Attallah, *Materials Characterization* 89 (2014): p. 102-111.
250. A. Yadollahi, N. Shamsaei, S.M. Thompson, D.W. Seely, *Materials Science and Engineering: A* 644 (2015): p. 171-183.
251. G. Dinda, A. Dasgupta, S. Bhattacharya, H. Natu, B. Dutta, J. Mazumder, *Metallurgical and Materials Transactions A* 44 (2013): p. 2233-2242.
252. T. Ishimoto, K. Hagihara, K. Hisamoto, S.-H. Sun, T. Nakano, *Scripta Materialia* 132 (2017): p. 34-38.
253. G. Winther, D.J. Jensen, N. Hansen, *Acta materialia* 45, 12 (1997): p. 5059-5068.
254. P. Hurley, P. Bate, F. Humphreys, *Acta Materialia* 51, 16 (2003): p. 4737-4750.
255. N. Afrin, M.Z. Quadir, W. Xu, M. Ferry, *Acta materialia* 60, 18 (2012): p. 6288-6300.
256. N. Afrin, M.Z. Quadir, L. Bassman, J. Driver, A. Albou, M. Ferry, *Scripta Materialia* 64, 3 (2011): p. 221-224.
257. H. Wei, J. Elmer, T. DebRoy, *Acta Materialia* 115 (2016): p. 123-131.
258. Y. Wang, J. Shi, *Materials Characterization* 165 (2020): p. 110372.
259. Y.M. Wang, T. Voisin, J.T. McKeown, J. Ye, N.P. Calta, Z. Li, Z. Zeng, Y. Zhang, W. Chen, T.T. Roehling, *Nature materials* 17, 1 (2018): p. 63-71.
260. O. Salman, C. Gammer, A. Chaubey, J. Eckert, S. Scudino, *Materials Science and Engineering: A* 748 (2019): p. 205-212.
261. S. Gao, Z. Hu, M. Duchamp, P.S.R. Krishnan, S. Tekumalla, X. Song, M. Seita, *Acta Materialia* 200 (2020): p. 366-377.
262. D. Kong, C. Dong, X. Ni, L. Zhang, X. Li, *Materials Letters* 279 (2020): p. 128524.
263. C. Huang, X. Yan, L. Zhao, M. Liu, W. Ma, W. Wang, J. Soete, A. Simar, *Materials Science and Engineering: A* 755 (2019): p. 85-96.
264. H. Shibata, T. Tanaka, K. Kimura, S.-Y. Kitamura, *Ironmaking & Steelmaking* 37, 7 (2010): p. 522-528.
265. J. Dossett, G. Totten, (2014):
266. M.Y. Mendoza, P. Samimi, D.A. Brice, B.W. Martin, M.R. Rolchigo, R. LeSar, P.C. Collins, *Metallurgical and Materials Transactions A* 48, 7 (2017): p. 3594-3605.
267. M. Ziętała, T. Durejko, M. Polański, I. Kunce, T. Płociński, W. Zieliński, M. Łazińska, W. Stępniewski, T. Czujko, K.J. Kurzydłowski, Z. Bojar, *Materials Science and Engineering: A* 677 (2016): p. 1-10.

268. P. Edwards, A. O'Conner, M. Ramulu, *Journal of Manufacturing Science and Engineering* 135, 6 (2013):
269. X. Wang, K. Chou, *Journal of Alloys and Compounds* 748 (2018): p. 236-244.
270. S.M. Zaharia, C. Lancea, L.A. Chicos, M.A. Pop, G. Caputo, E. Serra, *Transactions of FAMENA* 41, 4 (2017): p. 11-24.
271. R. Guzmán-Nogales, F. Estupiñán-López, C. Gaona-Tiburcio, O.E. Lopez-Botello, J.G. Ramírez-Rodríguez, P.C. Zambrano-Robledo, *Materials* 14, 16 (2021): p. 4509.
272. C.R. Bryan, R.P.M. Dingreville, D. Enos, "Estimating Bounding Corrosion Pit Sizes on Stainless Steel SNF Interim Storage Canisters," Sandia National Lab.(SNL-NM), Albuquerque, NM (United States) Report, 2016.
273. U. Martin, D.M. Bastidas, *Engineering Failure Analysis* 147 (2023): p. 107159.
274. D.A. Horner, B.J. Connolly, S. Zhou, L. Crocker, A. Turnbull, *Corrosion Science* 53, 11 (2011): p. 3466-3485.
275. R. Katona, E. Karasz, R. Schaller, *Corrosion* 79, 1 (2023): p. 72-96.
276. X.-g. Huang, J.-q. Xu, *Journal of Zhejiang University SCIENCE A* 14, 4 (2013): p. 292-299.
277. B.Y. Fang, R.L. Eadie, W.X. Chen, M. Elboujdaini, *Corrosion Engineering, Science and Technology* 45, 4 (2010): p. 302-312.
278. P. Marcus, *Corrosion mechanisms in theory and practice*, CRC press, 2011).
279. G.G. Scatigno, M.P. Ryan, F. Giuliani, M.R. Wenman, *Materials Science and Engineering: A* 668 (2016): p. 20-29.
280. A.J. Sedriks, *Corrosion of Stainless Steels*, 2nded., (New York: John Wiley & Sons, Inc, 1996).
281. R.W. Revie, *Uhlig's Corrosion Handbook*, 3rded., (Pennington, NJ: John Wiley & Sons, 2011).
282. M.F. McGuire, *Stainless steels for design engineers*, Asm International, 2008).
283. "Standard Specification for Seamless Ferritic and Austenitic Alloy-Steel Boiler, Superheater, and Heat-Exchanger Tubes" (West Conshohocken, PA: ASTM International, 2022).
284. E. Liverani, S. Toschi, L. Ceschini, A. Fortunato, *Journal of Materials Processing Technology* 249 (2017): p. 255-263.
285. A. Woźniak, M. Adamiak, G. Chladek, J. Kasperski, *Archives of Metallurgy and Materials* 65 (2020):
286. M.J.K. Lodhi, K.M. Deen, W. Haider, *Materialia* 2 (2018): p. 111-121.
287. "Standard Practice for Determining the Inclusion or Second-Phase Constituent Content of Metals by Automatic Image Analysis" (West Conshohocken, PA: ASTM International, 2016).
288. "Standard Test Method for Microindentation Hardness of Materials" (West Conshohocken, PA: ASTM International, 2017).
289. "Standard Test Methods for Density of Compacted or Sintered Powder Metallurgy (PM) Products Using Archimedes' Principle" (West Conshohocken, PA: ASTM International, 2017).
290. "Standard Terminology Relating to Corrosion and Corrosion Testing" (West Conshohocken, PA 19428-2959 USA: ASTM International, 2010).

291. F. Matsuda, H. Nakagawa, I. Kato, Y. Murata, *Welding International* 2, 6 (1988): p. 529-535.
292. ASTM-G46, in *Standard Guide for Examination and Evaluation of Pitting Corrosion*, ed.(West Conshohocken, PA 19428-2959 USA: ASTM International, 2018).
293. J.D. Verhoeven, *Steel metallurgy for the non-metallurgist*, ASM International, (2007).
294. W.F. Hosford, *Iron and steel*, Cambridge University Press, (2012).
295. B. Ravi Kumar, B. Mahato, R. Singh, *Metallurgical and Materials Transactions A* 38, 9 (2007): p. 2085-2094.
296. S. Ghosh, V.P.S. Rana, V. Kain, V. Mittal, S.K. Baveja, *Materials & Design* 32, 7 (2011): p. 3823-3831.
297. S.G. Acharyya, A. Khandelwal, V. Kain, A. Kumar, I. Samajdar, *Materials Characterization* 72 (2012): p. 68-76.
298. A. Turnbull, K. Mingard, J.D. Lord, B. Roebuck, D.R. Tice, K.J. Mottershead, N.D. Fairweather, A.K. Bradbury, *Corrosion Science* 53, 10 (2011): p. 3398-3415.
299. M.R. Wenman, K.R. Trethewey, S.E. Jarman, P.R. Chard-Tuckey, *Acta Materialia* 56, 16 (2008): p. 4125-4136.
300. A. Turnbull, L.N. McCartney, S. Zhou, *Corrosion Science* 48, 8 (2006): p. 2084-2105.
301. A. Turnbull, L.N. McCartney, S. Zhou, *Scripta Materialia* 54, 4 (2006): p. 575-578.
302. J. Galvele, G. Duffó, *Cursos ECOMAR, Comisión Nacional de Energía Atómica* (1975):
303. M.K. Abbass, S.A. Ajeel, H.M. Wadullah, "Biocompatibility, bioactivity and corrosion resistance of stainless steel 316L nanocoated with TiO<sub>2</sub> and Al<sub>2</sub>O<sub>3</sub> by atomic layer deposition method," *Journal of Physics: Conference Series* IOP Publishing, (2018), p. 012017.
304. Z. Abdullah, A. Ismail, S. Ahmad, "The influence of porosity on corrosion attack of Austenitic stainless steel," *Journal of Physics: Conference Series* IOP Publishing, (2017), p. 012013.
305. C. García, F. Martín, P. de Tiedra, L.G. Cambronero, *Corrosion Science* 49, 4 (2007): p. 1718-1736.
306. Y. Mao, J. Yuan, Y. Heng, K. Feng, D. Cai, Q. Wei, *Virtual and Physical Prototyping* 18, 1 (2023): p. e2174703.
307. H. Atkinson, S. Davies, *Metallurgical and materials transactions A* 31 (2000): p. 2981-3000.
308. Q. Teng, Y. Xie, S. Sun, P. Xue, A. Long, T. Wu, C. Cai, J. Guo, Q. Wei, *Journal of Alloys and Compounds* 909 (2022): p. 164668.
309. C. Cai, X. Gao, Q. Teng, R. Kiran, J. Liu, Q. Wei, Y. Shi, *Materials Science and Engineering: A* 802 (2021): p. 140426.
310. B. AlMangour, J.-M. Yang, *Materials & Design* 110 (2016): p. 914-924.
311. T. Rautio, M. Jaskari, T. Gundgire, T. Iso-Junno, M. Vippola, A. Järvenpää, *Materials* 15, 10 (2022): p. 3517.
312. N. Jemaa, J. Shu, S. Kaliaguine, B.P. Grandjean, *Industrial & engineering chemistry research* 35, 3 (1996): p. 973-977.
313. J. Lépinoux, T. Magnin, in *Fundamental Aspects of Dislocation Interactions*, eds. G. Kosterz, H.A. Calderon, J.L. Martin, Elsevier, (1993), p. 266-269.

314. H. Qu, "Effect of Crystallography On Stress Corrosion Cracking Growth in Austenitic Stainless Steels" (Master of Science Purdue University Graduate School, 2020).
315. W. Hosford, *Mechanical behavior of materials* (2009): p. 36-64.
316. G.N. Haidemenopoulos, *Physical metallurgy: principles and design*, CRC Press, 2018).
317. H.J. Qu, F. Tao, N. Gu, T. Montoya, J.M. Taylor, R.F. Schaller, E. Schindelholz, J.P. Wharry, *npj Materials Degradation* 6, 1 (2022): p. 43.
318. M. Koyama, T. Ogawa, D. Yan, Y. Matsumoto, C.C. Tasan, K. Takai, K. Tsuzaki, *International Journal of Hydrogen Energy* 42, 42 (2017): p. 26423-26435.
319. T.L. Anderson, *Fracture mechanics: fundamentals and applications*, CRC press, 2017).
320. K.M. Conway, C. Kunka, B.C. White, G.J. Pataky, B.L. Boyce, *Materials & Design* 205 (2021): p. 109696.
321. P. Kumar, R. Jayaraj, J. Suryawanshi, U.R. Satwik, J. McKinnell, U. Ramamurty, *Acta Materialia* 199 (2020): p. 225-239.
322. B. Vieille, C. Keller, M. Mokhtari, H. Briatta, T. Breteau, J. Nguejio, F. Barbe, M. Ben Azzouna, E. Baustert, *Materials Science and Engineering: A* 790 (2020): p. 139666.
323. S.D. Jadhav, L.R. Goossens, Y. Kinds, B. Van Hooreweder, K. Vanmeensel, *Additive Manufacturing* 42 (2021): p. 101990.
324. H. Miyajima, D. Ma, M.A. Atwater, K.A. Darling, V.H. Hammond, C.B. Williams, *Additive Manufacturing* 32 (2020): p. 100960.
325. J. Huang, X. Yan, C. Chang, Y. Xie, W. Ma, R. Huang, R. Zhao, S. Li, M. Liu, H. Liao, *Surface and Coatings Technology* 395 (2020): p. 125936.
326. D. Karlsson, C.-Y. Chou, N.H. Pettersson, T. Helander, P. Harlin, M. Sahlberg, G. Lindwall, J. Odqvist, U. Jansson, *Additive Manufacturing* 36 (2020): p. 101580.
327. J.W. Elmer, J. Vaja, J.S. Carpenter, D.R. Coughlin, M.J. Dvornak, P. Hochanadel, P. Gurung, A. Johnson, G. Gibbs, *Welding Journal* 99, LLNL-JRNL-771645; LA-UR-19-23147 (2020):
328. Z. Lin, K. Song, X. Yu, *Journal of Manufacturing Processes* 70 (2021): p. 24-45.
329. B. Dutta, F.S. Froes, *Metal powder report* 72, 2 (2017): p. 96-106.
330. D. Zhang, D. Qiu, M.A. Gibson, Y. Zheng, H.L. Fraser, D.H. StJohn, M.A. Easton, *Nature* 576, 7785 (2019): p. 91-95.
331. E. Louvis, P. Fox, C.J. Sutcliffe, *Journal of Materials Processing Technology* 211, 2 (2011): p. 275-284.
332. L. Pantělejev, D. Koutný, D. Paloušek, J. Kaiser, "Mechanical and microstructural properties of 2618 Al-Alloy processed by SLM remelting strategy," *Materials science forum* Trans Tech Publ, 2017), p. 343-349.
333. C.Y. Yap, H.K. Tan, Z. Du, C.K. Chua, Z. Dong, *Rapid Prototyping Journal* 23 (2017): p. 750-757.
334. E. Martin, A. Natarajan, S. Kottilingam, R. Batmaz, *Additive Manufacturing* 39 (2021): p. 101894.
335. S.C. Altıparmak, B. Xiao, *Journal of Manufacturing Processes* 68 (2021): p. 728-738.
336. A.J. Pinkerton, *Optics & Laser Technology* 78 (2016): p. 25-32.

337. C. Fredriksson, *Procedia manufacturing* 33 (2019): p. 139-144.
338. A.J. Sheoran, H. Kumar, P.K. Arora, G. Moona, *Procedia Manufacturing* 51 (2020): p. 663-670.
339. T.D. Ngo, A. Kashani, G. Imbalzano, K.T. Nguyen, D. Hui, *Composites Part B: Engineering* 143 (2018): p. 172-196.
340. P. Marshall, *Austenitic stainless steels: microstructure and mechanical properties*, Springer Science & Business Media, 1984).
341. A. Di Schino, in *Manufacturing and applications of stainless steels*, ed., vol. 10 MDPI, 2020), p. 327.
342. A. Outokumpu Stainless, *Avesta Research Centre, Avesta, Sweden* (2013):
343. M.F. McGuire, *Stainless Steel for Design Engineers*, (Materials Park, OH: ASM International, 2008).
344. S. Wang, Y. Hu, K. Fang, W. Zhang, X. Wang, *Corrosion Science* 126 (2017): p. 104-120.
345. V.B. Vukkum, J. Christudasjustus, A.A. Darwish, S.M. Storck, R.K. Gupta, *npj Materials Degradation* 6, 1 (2022): p. 2.
346. R.J. Williams, F. Vecchiato, J. Kelleher, M.R. Wenman, P.A. Hooper, C.M. Davies, *Journal of Manufacturing Processes* 57 (2020): p. 641-653.
347. N. Alharbi, *The International Journal of Advanced Manufacturing Technology* 119, 3 (2022): p. 2285-2299.
348. T. Magnin, A. Chambreuil, B. Bayle, *Acta Materialia* 44, 4 (1996): p. 1457-1470.
349. D. Kong, C. Dong, X. Ni, X. Li, *npj Materials Degradation* 3, 1 (2019): p. 24.
350. X.-q. Ni, D.-c. Kong, Y. Wen, L. Zhang, W.-h. Wu, B.-b. He, L. Lu, D.-x. Zhu, *International Journal of Minerals, Metallurgy, and Materials* 26 (2019): p. 319-328.
351. Y. Liu, Y. Yang, D. Wang, *The International Journal of Advanced Manufacturing Technology* 87 (2016): p. 647-656.
352. X. Lou, M. Song, P.W. Emigh, M.A. Othon, P.L. Andresen, *Corrosion Science* 128 (2017): p. 140-153.
353. J. Hajnys, M. Pagáč, J. Měsíček, J. Petru, M. Król, *Materials* 13, 7 (2020): p. 1659.
354. X. Yan, J. Pang, Y. Jing, *Materials* 12, 17 (2019): p. 2719.
355. E. Malekipour, H. El-Mounayri, *ASME International Mechanical Engineering Congress and Exposition* 84485 (2020): p. V02AT02A055.
356. P. Pant, *Residual stress distributions in additively manufactured parts: effect of build orientation*, vol. 1869, Linköping University Electronic Press, 2020).
357. M. Kumaran, V. Senthilkumar, T. Sathies, C.T. Justus Panicker, *Materials Letters* 313 (2022): p. 131766.
358. M. Kamariah, W. Harun, N. Khalil, F. Ahmad, M. Ismail, S. Sharif, *IOP Conference Series: Materials Science and Engineering* 257, 1 (2017): p. 012021.
359. K. Burdová, H. Jirková, L. Kučerová, I. Zetková, J. Mach, *Manufacturing Technology* 22, 3 (2022): p. 261-266.
360. S. Leuders, T. Lieneke, S. Lammers, T. Tröster, T. Niendorf, *Journal of Materials Research* 29, 17 (2014): p. 1911-1919.

361. T. Gundgire, T. Jokiahho, S. Santa-aho, T. Rautio, A. Järvenpää, M. Vippola, *Materials Characterization* 191 (2022): p. 112162.
362. N. Kalentics, E. Boillat, P. Peyre, C. Gorny, C. Kenel, C. Leinenbach, J. Jhabvala, R.E. Logé, *Materials & Design* 130 (2017): p. 350-356.
363. N. Kalentics, E. Boillat, P. Peyre, S. Ćirić-Kostić, N. Bogojević, R.E. Logé, *Additive Manufacturing* 16 (2017): p. 90-97.
364. "Standard Specification for Stainless Steel Bars and Shapes" (West Conshohocken, PA: ASTM International, 2015).
365. "Standard Specification for Stainless Steel Bars and Shapes for Use in Boilers and Other Pressure Vessels" (West Conshohocken, PA: ASTM International, 2021).
366. M. Tong, X. Di, C. Li, D. Wang, *Materials Characterization* 144 (2018): p. 631-640.
367. M. Calcagnotto, D. Ponge, E. Demir, D. Raabe, *Materials Science and Engineering: A* 527, 10-11 (2010): p. 2738-2746.
368. W. Xing, M. Yin, Q. Lv, Y. Hu, C. Liu, J. Zhang, *Rotating Electrode Methods and Oxygen Reduction Electrocatalysts* (2014): p. 1-31.
369. S. Huzni, M. Ridha, A.K. Ariffin, *Key Engineering Materials* 462 (2011): p. 194-199.
370. D.Y. Jang, T.R. Watkins, K.J. Kozaczek, C.R. Hubbard, O.B. Cavin, *Wear* 194, 1 (1996): p. 168-173.
371. Q. Chao, V. Cruz, S. Thomas, N. Birbilis, P. Collins, A. Taylor, P.D. Hodgson, D. Fabijanic, *Scripta Materialia* 141 (2017): p. 94-98.
372. G. Sander, S. Thomas, V. Cruz, M. Jurg, N. Birbilis, X. Gao, M. Brameld, C. Hutchinson, *Journal of the electrochemical society* 164, 6 (2017): p. C250.

**Every reasonable effort has been made to acknowledge the owners of copyright material. I would be pleased to hear from any copyright owner who has been omitted or incorrectly acknowledged.**

## **Appendix 1: Written statements from co-authors of the publications**



To whom it may concern,

I, Ricardo Santamaria, contributed by conducting the research, interpreting the obtained data and writing the contents in the publication entitled "**Stress Corrosion Cracking of 316L Stainless Steel Additively Manufactured with Sinter-Based Material Extrusion**".

\_\_\_\_\_  
Signature of candidate

Date: 04/08/2023

I, as Co-Author, endorse that this level of contribution by the candidate indicated above is appropriate.

Ke Wang  
Full name of Co-author 1

\_\_\_\_\_  
Signature of Co-author 1

Date:  
08/08/2023

Mobin Salasi  
Full name of Co-author 2

\_\_\_\_\_  
Signature of Co-author 2

Date:  
10-Aug-2023

Mariano Iannuzzi  
Full name of Co-author 3

\_\_\_\_\_  
Signature of Co-author 3

Date: 21/08/2023

Michael Y. Mendoza  
Full name of Co-author 4

\_\_\_\_\_  
Signature of Co-author 4

Date:  
07/08/2023

Md. Zakaria Quadir  
Full name of Co-author 5

\_\_\_\_\_  
Signature of Co-author 5

17 Aug 23  
Date:

To whom it may concern,

I, Ricardo Santamaria, contributed by conducting the research, interpreting the obtained data and writing the contents in the publication entitled **“Stress corrosion cracking behavior of austenitic stainless steel 316L produced using laser-based powder bed fusion”**.

  
\_\_\_\_\_

Date: 04/08/2023

Signature of candidate

I, as Co-Author, endorse that this level of contribution by the candidate indicated above is appropriate.

Ke Wang  
Full name of Co-author 1

\_\_\_\_\_  
Signature of Co-author 1

Date: 08/08/2023

Mobin Salasi  
Full name of Co-author 2

\_\_\_\_\_  
Signature of Co-author 2

Date:  
10-Aug-2023

Mehdi Salem  
Full name of Co-author 3

\_\_\_\_\_  
Signature of Co-author 3

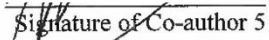
Date: August 10th, 2023

Philippe Lours  
Full name of Co-author 4

\_\_\_\_\_  
Signature of Co-author 4

Date: August 5th, 2023

Mariano Iannuzzi  
Full name of Co-author 5

  
Signature of Co-author 5

Date: 24/08/2023

Md. Zakaria Quadir  
Full name of Co-author 6

  
Signature of Co-author 6

17 Aug 23  
Date:

To whom it may concern,

I, Ricardo Santamaria, contributed by conducting the research, interpreting the obtained data and writing the contents in the publication entitled “**Microstructure and mechanical behaviour of 316L stainless steel produced using sinter-based extrusion additive manufacturing**”.

\_\_\_\_\_

Date: **04/08/2023**

Signature of candidate

I, as Co-Author, endorse that this level of contribution by the candidate indicated above is appropriate.

Mobin Salasi  
Full name of Co-author 1

\_\_\_\_\_  
Signature of Co-author 1

10-Aug-2023  
Date:

Sam Bakhtiari  
Full name of Co-author 2

\_\_\_\_\_  
Signature of Co-author 2

10-Aug-2023  
Date:

Garry Leadbeater  
Full name of Co-author 3

\_\_\_\_\_  
Signature of Co-author 3

10 August 2023  
Date:

Mariano Iannuzzi  
Full name of Co-author 4

*[Signature]*  
Signature of Co-author 4

Date: *21/08/23*

Md Zakaria Quadir  
Full name of Co-author 5

*[Signature]*  
Signature of Co-author 5

17 Aug 23  
Date:

To whom it may concern,

I, Ricardo Santamaria, contributed by conducting the research, interpreting the obtained data and writing the contents in the publication entitled **“Crystallographic Texture and Substructural Phenomena in 316 Stainless Steel Printed by Selective Laser Melting”**.

Date: 04/08/2023

\_\_\_\_\_  
Signature of candidate

I, as Co-Author, endorse that this level of contribution by the candidate indicated above is appropriate.

Mobin Salasi  
Full name of Co-author 1

\_\_\_\_\_  
Signature of Co-author 1

10-Aug-2023  
Date:

William D. A. Rickard  
Full name of Co-author 2

\_\_\_\_\_  
Signature of Co-author 2

16-Aug-2023  
Date:

Kod Pojtanabuntoeng  
Full name of Co-author 3

\_\_\_\_\_  
Signature of Co-author 3

Date: 15 August 2023

Garry Leadbeater  
Full name of Co-author 4

\_\_\_\_\_  
Signature of Co-author 4

10 August 2023  
Date:

Mariano Iannuzzi  
Full name of Co-author 5

\_\_\_\_\_  
Signature of Co-author 5

Date: 21/08/2023

Steven M. Reddy  
Full name of Co-author 6

\_\_\_\_\_  
Signature of Co-author 6

Date: 17 August 2023

Md Zakaria Quadir  
Full name of Co-author 7

\_\_\_\_\_  
Signature of Co-author 7

Date: 17 Aug 2023

## Appendix 2: Copyrights statements

© 2023 Spring Nature owns the copyright of the article reproduced with permission in Chapter 2.

Santamaria R, Salasi M, Bakhtiari S, Leadbeater G, Iannuzzi M, Quadir MZ. Microstructure and mechanical behaviour of 316L stainless steel produced using sinter-based extrusion additive manufacturing. *Journal of Materials Science*. 2022 Jun 1:1-7

<https://doi.org/10.1007/s10853-021-06828-8>

According to Spring Nature policies, authors may reuse their article's Version of Record, in whole or part, in their own thesis without any additional permission required, provided the original publication is properly cited and includes the following acknowledgment "Reproduced with permission from Spring Nature". Below is a screenshot of the email response from [journalpermissions@springnature.com](mailto:journalpermissions@springnature.com).

**RE: Copyright Permission - Request to reuse my published article in my PhD thesis**

Journalpermissions &lt;journalpermissions@springernature.com&gt;

Tue 2023-08-08 12:14 AM

To: Ricardo Santamaria Torres &lt;ricardo.santamar@postgrad.curtin.edu.au&gt;

Dear Ricardo,

Thank you for your recent email. Springer Nature journal authors may reuse their article's Version of Record, in whole or in part, in their own thesis without any additional permission required, provided the original publication is properly cited and includes the following acknowledgement "Reproduced with permission from Springer Nature". This includes the right to make a copy of your thesis available in your academic institution's repository, or other repository required by your awarding institution. For more information please visit see our FAQs [here](#).

If your awarding institution requires formal permission, please locate your article on either nature.com or link.springer.com. At the end of the article page you will find the 'Reprints and Permissions' link; clicking on this will redirect you to our CCC RightsLink service where you may input the details of your request. Please ensure you select "reuse in a thesis/dissertation" as your type of use, and to tick the box that asks whether you are the author.

During the process, you will need to set up an account with RightsLink. You will be able to use your RightsLink account in the future to request permissions from Springer Nature and from other participating publishers. RightsLink will also email you confirmation of your request with a link to your printable licence.

If you have any further questions, please do not hesitate to get in touch.

Kind Regards,

André

**André Buller**

Permissions Assistant

**SpringerNature**

The Campus, 4 Crinan Street, London N1 9XW, United Kingdom

T: [+442070146466]

E [andre.buller@springernature.com](mailto:andre.buller@springernature.com)<http://www.nature.com><http://www.springernature.com>

---

**From:** Ricardo Santamaria Torres <ricardo.santamar@postgrad.curtin.edu.au>**Sent:** 04 August 2023 06:06**To:** Journalpermissions <journalpermissions@springernature.com>**Subject:** Copyright Permission - Request to reuse my published article in my PhD thesis

---

Dear Sir/Madam,

I am the lead author of the following article and wish to seek permission to include the published version in my PhD thesis, currently being undertaken at Curtin University.

**Santamaria R, Salasi M, Bakhtiari S, Leadbeater G, Iannuzzi M, Quadir MZ. Microstructure and mechanical behaviour of 316L stainless steel produced using sinter-based extrusion additive manufacturing. Journal of Materials Science. 2022 Jun 1:1-7 <https://doi.org/10.1007/s10853-021-06828-8>**

09/08/2023, 21:28

Mail - Ricardo Santamaría Torres - Outlook

Once completed, the thesis will be made available (subject to any applicable embargo periods) via Curtin University's Institutional Repository [espace](#). As per University policies, deposit of my thesis into espace is a requirement of my award.

Thank you for taking the time to consider this request.

I look forward to your response.

Best regards,

Ricardo

<https://outlook.office.com/mail/inbox/id/AAQkAGVINGQ5NTI3LWU2YWEiNDIxY1IiMDIxLTNiYjhZGYzYjI5OAAQADxDbK6xv1pLkPu4Ae0JxbM%...> 2/2

© 1996 - 2023 MDPI owns the copyright of the article reproduced with permission in Chapters 3 and 4.

Santamaria R, Salasi M, Rickard WD, Pojtanabuntoeng K, Leadbeater G, Iannuzzi M, Reddy SM, Quadir MZ. Crystallographic Texture and Substructural Phenomena in 316 Stainless Steel Printed by Selective Laser Melting. *Materials*. 2023 Jun 9;16(12):4289.

<https://doi.org/10.3390/ma16124289>

Santamaria R, Wang K, Salasi M, Iannuzzi M, Mendoza MY, Quadir MZ. Stress Corrosion Cracking of 316L Stainless Steel Additively Manufactured with Sinter-Based Material Extrusion. *Materials*. 2023 May 26;16(11):4006. <https://doi.org/10.3390/ma16114006>

According to MDPI Open Access Information and Policy, all articles published by MDPI are made immediately available worldwide under an open access license, meaning everyone is free to re-use the published material if proper accreditation/citation of the original publication is given. Moreover, no special permission is required to reuse all or part of article published by MDPI, including figures and tables. For articles published under an open access Creative Common CC BY license, any part of the article may be reused without permission provided that the original article is clearly cited. Reuse of an article does not imply endorsement by the authors or MDPI. Below is a screenshot of the email response from the journal relations specialist, [rhys.pumphrey@mdpi.com](mailto:rhys.pumphrey@mdpi.com).



**Re: Request to reuse my published articles in my PhD thesis**

Rhys Pumphrey &lt;rhys.pumphrey@mdpi.com&gt;

Thu 2023-08-10 11:53 PM

To: Ricardo Santamaria Torres &lt;ricardo.santamar@postgrad.curtin.edu.au&gt;

Cc: materials@mdpi.com &lt;materials@mdpi.com&gt;

Dear Ricardo,

Thank you for your email.

The works you referred to were published under a CC BY license, which means you can use the work in your thesis without permission, as long as the original source is appropriately cited. You can find more information here:

<https://creativecommons.org/licenses/by/4.0/>

If you have any further questions, please feel free to email me.

Best regards,

Rhys Pumphrey  
Journal Relations Specialist, MDPI Manchester  
E-Mail: rhys.pumphrey@mdpi.com

1 New York Street, Suite B,  
3rd Floor, M1 4HD Manchester, UK  
Tel: +44 0161 513 4078

[www.mdpi.com](http://www.mdpi.com)

The information and files contained in this message are confidential and intended solely for the use of the individual or entity to whom they are addressed. If you have received this message in error, please notify me and delete this message from your system. You may not copy this message in its entirety or in part, or disclose its contents to anyone.

> ----- Forwarded Message -----

> Subject: Request to reuse my published articles in my PhD thesis

> Date: Thu, 10 Aug 2023 03:00:24 +0000

> From: Ricardo Santamaria Torres

> <ricardo.santamar@postgrad.curtin.edu.au>

> To: Editorial Office <materials@mdpi.com>

>

>

>

> CAUTION - EXTERNAL: This email originated from outside of MDPI  
> organisation. BE CAUTIOUS especially to click links or open attachments.

>

> Dear Sir/Madam,

>



CORROSION® The Journal of Science & Engineering owns the copyright of the article reproduced with permission in Chapters 5.

Santamaria R, Wang K, Salasi M, Salem M, Lours P, Iannuzzi M, Quadir MZ. Stress corrosion cracking behavior of austenitic stainless steel 316L produced using laser-based powder bed fusion. Corrosion. 2023;4311. <https://doi.org/10.5006/4311>

According to CORROSION, authors may include their articles in their thesis or dissertation as long as it is properly cited. Below is a screenshot of the email response from the Managing Editor in Chief [sammy.miles@ampp.org](mailto:sammy.miles@ampp.org).

**RE: A Request for August Publication**

Sammy Miles &lt;Sammy.Miles@ampp.org&gt;

Thu 2023-08-10 11:07 PM

To: Marlene Walters &lt;Marlene.Walters@ampp.org&gt;; Ricardo Santamaria Torres &lt;ricardo.santamar@postgrad.curtin.edu.au&gt;

Hi Ricardo,

As Marlene mentioned, authors may reuse their original figures, tables, and images in any subsequent publication, although they must request permission to reuse the full text or large passages in other works. Specifically related to inclusion of your article in your thesis or dissertation, you may include your *CORROSION* journal article. You may use the layout version in any printed copies, although we request that you use the as-accepted version (non-formatted) in any digital copies of the work with a link to the final published version.

Best regards,  
Sammy



Sammy Miles | Managing Editor in Chief, *CORROSION* journal  
Association for Materials Protection and Performance  
Tel: +1 281-228-6440 | [Sammy.Miles@ampp.org](mailto:Sammy.Miles@ampp.org)  
[ampp.org](http://ampp.org) | [corrosionjournal.org](http://corrosionjournal.org)

---

**From:** Marlene Walters <Marlene.Walters@ampp.org>  
**Sent:** Thursday, August 10, 2023 7:51 AM  
**To:** Ricardo Santamaria Torres <ricardo.santamar@postgrad.curtin.edu.au>  
**Cc:** Sammy Miles <Sammy.Miles@ampp.org>  
**Subject:** RE: A Request for August Publication

Good day Ricardo,

Our website allows authors to re-use their original work in future work so long as it is cited properly back to the journal. Sammy, will you confirm that is good for Ricardo's request with his thesis as well?

Thank you Ricardo for your submission and all the best with your PhD.

Marlene



Marlene Walters | Publications Production & Circulation Mgr  
Association for Materials Protection and Performance  
Tel: +1 281-228-6471 |  
[ampp.org](http://ampp.org)  
[coatingspromag.com](http://coatingspromag.com) | [materialsperformance.com](http://materialsperformance.com) |  
[corrosionjournal.org](http://corrosionjournal.org)

---


**From:** Ricardo Santamaria Torres <[ricardo.santamar@postgrad.curtin.edu.au](mailto:ricardo.santamar@postgrad.curtin.edu.au)>  
**Sent:** Wednesday, August 9, 2023 8:54 PM  
**To:** Marlene Walters <[Marlene.Walters@ampp.org](mailto:Marlene.Walters@ampp.org)>  
**Subject:** Re: A Request for August Publication

CAUTION: This email originated from outside of the organization. Do not click links or open attachments unless you recognize the sender and know the content is safe.

**Appendix 3: Original reprint of the publication included in  
Chapter 2**



## Microstructure and mechanical behaviour of 316L stainless steel produced using sinter-based extrusion additive manufacturing

Ricardo Santamaria<sup>1,\*</sup> , Mobin Salasi<sup>1</sup>, Sam Bakhtiari<sup>1</sup>, Garry Leadbeater<sup>1</sup>, Mariano Iannuzzi<sup>1</sup>, and Md Zakaria Quadir<sup>1,2</sup>

<sup>1</sup> Curtin Corrosion Centre, Curtin University, Perth, WA, Australia

<sup>2</sup> John de Laeter Centre, Curtin University, Perth, WA, Australia

Received: 19 September 2021

Accepted: 14 December 2021

© The Author(s), under exclusive licence to Springer Science+Business Media, LLC, part of Springer Nature 2021

### ABSTRACT

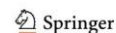
Specimens were additively manufactured in 316L stainless steel (SS316L) with a technology that combines the extruding method of fused filament fabrication (FFF) with the strengthening stages of metal injection moulding (MIM). A thorough metallographic analysis and tensile testing were carried out to investigate the effect of sintering in the final microstructures, mechanical properties, and fracture modes of the manufactured material. SS316L wrought specimens were also characterised and tested for comparison. Results showed that the sinter-based technology produced a near-fully dense material with a porosity of 1.27% v/v, and a microstructure and mechanical properties comparable to the standard requirements of the UNS S31603 grade. The sintered specimens were characterised at as annealed condition, with fully austenitic microstructures, annealing twins, and sintering defects such as (1) scattered round microporosity, (2) elongated macroporosity, (3) spherical inclusions rich in Si, Mn and O —also found in the precursor powder— and (4) irregular inclusions rich in Cr, Mn and O. The average mechanical properties of the printed SS316L were Young's modulus (E) 196 GPa, 0.2% offset yield strength (Sy) 166 MPa, tensile strength (Su) 524 MPa, elongation after fracture 85% and reduction of area 51%. Based on the findings, a mechanism is outlined explaining the departure from the typical cup-and-cone ductile fracture in the necked region observed in the printed samples.

Handling Editor: M. Grant Norton.

Address correspondence to E-mail: ricardo.santamar@postgrad.curtin.edu.au

<https://doi.org/10.1007/s10853-021-06828-8>

Published online: 03 January 2022



## Introduction

Additive manufacturing (AM), also known as 3D printing, is a general term covering those technologies that allow the fabrication of complex physical objects from digital data by the successive addition of material [1–3]. Regardless of the type of feedstock or binding mechanism, current AM technologies are classified into seven basic categories, i.e. (1) binder jetting, (2) direct energy deposition (DED), (3) material extrusion, (4) material jetting, (5) powder bed fusion (PBF), (6) sheet lamination and (7) vat photopolymerisation [2–4].

SS316L is a widely used stainless steel in the resource sector, due to its favourable corrosion behaviour and good formability. Studies on SS316L fabricated via PBF and DED showed that the manufacturing parameters have a direct impact on the final microstructures, porosity characteristics and mechanical properties [5–15]. Issues with these AM technologies include their initial capital costs, safety concerns in relation to the handling of loose powder and high energy sources, and also, the anisotropic nature of microstructures producing columnar grains [6–8, 15, 16]. Hence, in recent years, investigations have been carried out to address these issues by combining the low cost of extrusion 3D printing techniques using fused filament fabrication (FFF) with the strengthening process of metal injection moulding (MIM). This combined AM technology is referred as metal FFF [3, 17–22].

Manufacturing of SS316L via metal FFF starts with loading the feedstock of pre-alloyed powder embedded in a binder into the 3D printer. The feedstock is then heated just above its binder's melting point, 210 to 290 °C [22–25], allowing it to be extruded line-by-line and layer-by-layer [2–4]. The as-printed object, known as green-part, lacks all the mechanical properties of the final densified metal. To achieve the required strength, the green-part subsequently undergoes a series of post-print processing stages similar to those used in MIM and powder metallurgy (PM) technologies [3, 20, 23, 24]. Solvent debinding is the first stage in metal FFF. Debinding involves removing the primary binder material by dissolving it in a suitable solvent, typically a liquid or gas [13, 24, 26, 27]. The obtained structure, known as brown-part, undergoes the next stage of the process inside a furnace. During this next stage, the

remaining secondary binder is burnt off through the porous structures at 425 to 600 °C temperature range, a process known as thermal debinding [21, 23, 25, 27]. The heating rate during thermal debinding is optimised to avoid blistering or cracking of the part. A vacuum atmosphere is used to prevent the oxidation of the steel particles; however, a reducing atmosphere using hydrogen gas can also be employed [24–27]. During the final stage, i.e. sintering, the temperature reaches between 1250 and 1380 °C [23, 25, 26]. During sintering, the specimen is held at this peak temperature for 120 to 180 min [13, 21, 23, 24, 26, 27]. Finally, the sintered part is cooled down to room temperature either inside the furnace or by air quenching [13, 21]. It has been observed that a higher peak temperature and a longer sintering result in microstructures with larger grains and reduced porosity [24, 28, 29].

Recent investigations have reported the microstructure and mechanical properties of FFF fabricated SS316L [13, 17, 18, 21–27, 30–33]. Results show that metal FFF produces porous sintered materials [21, 24, 27], with a relatively large distribution of austenitic grains [13, 24, 27] displaying a ductile behaviour [21, 22] with varying other tensile properties, which are a function of the building orientation [13, 17, 21]. For instance, the porosity varied between < 1% and 16% [17, 26], the average grain size ranged between 25 and 75  $\mu\text{m}$  [13, 17], the yield strength ( $S_y$ ) varied between 93 and 252 MPa [18, 23], and the tensile strength ( $S_u$ ) ranged between 219 and 561 MPa [18, 30].

The objective of this work was to investigate the relationship between the microstructures, tensile properties and the fracture mechanism of the FFF additively manufactured SS316L. A detailed morphological and microstructural characterisation was carried out using scanning and transmission electron microscopy (SEM and TEM, respectively) and microanalytical techniques, such as electron backscattered diffraction (EBSD) and energy dispersive spectroscopy (EDS). The wrought condition of the SS316L specimens was also tested and analysed, and the results were compared to gain a better understanding of the mechanical and chemical performance of the sintered SS316L material. Results were benchmarked with the literature covering SS316L manufactured by PBF and DED.

## Experimental

### Manufacturing technology

The SS316L used in this investigation was additively manufactured with a sinter-based extrusion process known as Bound Metal Deposition™ (Desktop Metal®, DM) using the Studio System™ (DM) technology. The system comprises three units, printer, debinder and sintering furnace. The printer uses cartridges containing the feedstock in the form of  $6 \times 150$  mm rods made of pre-alloyed SS316L powder embedded in the wax- and polymer-based binders. The Studio Printer comprises a build volume of  $300 \times 200 \times 200$  mm<sup>3</sup> and a dual extrusion capability for the ceramic-based media. This media creates an interface between the part and its support structures that is removed after sintering. Once the printing of an object is done, it is moved to the Studio Debinder unit which is an atmospheric pressure, low emission, vapour and odour-tight distillation tank that uses a proprietary solvent solution at 50 °C to remove the wax-based binder and create an open-pore structure. Then, the debound part is moved to the Studio Furnace for sintering. The furnace, which operates under vacuum in an argon-rich atmosphere, eliminates the remaining binder in the brown-part during the heating process and then sinters the part at high temperature, followed by some degree of densification. The entire process is controlled by the cloud-based software Fabricate™ (DM).

### Sample manufacture

The dimensions of the SS316L samples for microscopy analysis were  $10 \times 10 \times 3$  mm. Subsize tensile specimens were produced per the ASTM E8 recommendations [34], i.e. 100 mm overall length, 6 mm width, 32 mm length in the parallel section, and a 3 mm thickness. All specimens were 3D printed in the XY orientation and Z-direction with the longest dimension laying parallel to the X-axis as shown in schematic Fig. 1a. The extruded line width was 500 µm, the deposited layer height was 150 µm, and the contour shell thickness was 1.5 mm. The top-to-bottom bulk volume was achieved with a linear raster pattern than changed its extruding direction +45° and -45° with respect to the Y-axis with each deposited layer. The other printing parameters were: extruding temperature 175 °C, extrusion nozzle size

400 µm diameter, extrusion rate 30 mm/s, and build plate temperature 65 °C. The sinter scale factors were  $X = 1.16$ ,  $Y = 1.16$  and  $Z = 1.15$ . This indicates the material allowance of the green-part to compensate for the contractions during the sintering stage. The solvent debinding was conducted for 15 h and the thermal debinding at 550 °C for 2 h. The sintering was performed at a peak temperature of 1350 °C with a dwell time of 2 h. The process ended with furnace-cooling the sintered parts down to room temperature. Figure 1b shows the sintering furnace temperature profile.

### Microscopy sample preparation

Feedstock rods (cut longitudinally), brown-part and sintered samples were mounted in cold epoxy resin. Then, they were wet ground from 80 to 1200 grit SiC abrasive paper and then mechanically polished down to a final polish with 0.02 µm alumina suspension. All polished samples were rinsed with ethanol, sonicated in deionized water, dried with nitrogen and placed inside a vacuum desiccator for at least 12 h before the microscopy analysis. Sintered samples for electron backscattered diffraction (EBSD) analysis were additionally ion-milled for 30 min using a beam voltage of 8 kV at a glancing angle of 4° with full cycle rotational movements (TECHNOORG Linda, SEMPRep2). Transmission electron microscopy (TEM) samples were prepared using the focussed ion beam (FIB) lift-out technique on a Dual Beam FIB/SEM instrument (FEI Helios Nanolab G3 CX). The prepared TEM lamella was a strip of  $10 \times 10$  µm<sup>2</sup> with a thickness below 100 nm. A carbon protective layer was deposited on top of the region of interest using an ion beam with a 30 kV voltage and 0.43 nA current. Trenching, cutting, and thinning steps were carried out at 30 kV and ion beam currents of 9.50–0.23 nA, as the thinning was progressed. After thinning the TEM lamella to a thickness of 100 nm at 30 kV, a final cleaning was applied in two steps: the first step was at a lower voltage of 5 kV for 1 min on each side, followed by a low voltage of 2 kV cleaning for 30 s on either side.

### Microstructure investigation

The chemical composition of the powder used in this investigation was verified by quantitative energy-dispersive X-ray spectroscopy (EDS). The analysis



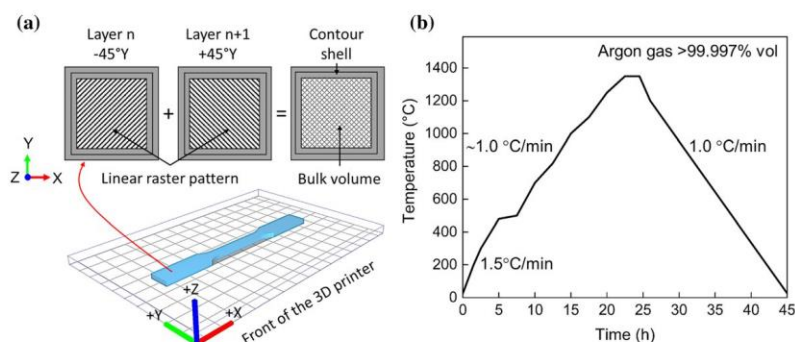


**Figure 1** a Test specimen 3D printing strategy, and b thermal profile used for sintering.

was performed on exposed particles on a section of a brown-part. Measurements were taken with a cobalt calibrated standard using a high sensitivity Oxford EDS detection system coupled to a field emission-scanning electron microscope (FE-SEM) (TESCAN system, CLARA). The quantification was conducted using the Oxford Aztec software. The chemical composition of a SS316L wrought sample was also quantified for comparison. The microstructure of the sintered material was imaged using the SE detector in the FE-SEM, and its chemical composition was mapped using EDS. The microstructure of the SS316L wrought sample was also obtained by FE-SEM for comparison. The particle size of the SS316L powder was measured with the open-source ImageJ software by analysing the FE-SEM images of the feedstock taken at different magnifications using both secondary electron (SE) and backscatter (BS) detectors. Imaging and elemental analysis at nanoscale were conducted on a TEM sample with a Field Emission TEM operating at 200 kV beam voltage (FEL, Talos).

The phases present in the SS316L powder and SS316L sintered material were identified via X-ray diffraction (XRD) analysis using a Cobalt K alpha powder diffractometer radiation source operating at 35 kV 40 mA using a LynxEye detector (Bruker D8 Discover). The XRD data were collected over an angular range of 15° to 135° at a step size of 0.015° and a time interval of 0.7 s. Likewise, a SS316L wrought sample was also analysed in the same analytical conditions for comparison.

The volumetric porosity fraction of the SS316L sintered material was determined with X-ray micro-

computed tomography (micro-CT) in a  $5 \times 5 \times 3$  mm<sup>3</sup> sample cut from the corner of a square specimen to ensure having part of its contour shell and bulk volume. The analysis was conducted using a 3D X-ray microscope with an exposure energy of 140 kV, during an exposure time of 24 h and at a pixel resolution of 2.2 μm (Zeiss 520 Versa). The fraction area of the samples' porosity was quantified with ImageJ by analysing cross-sectional SEM images at different magnifications. The density of the SS316L sintered material was calculated using the Archimedes principle, as described in ASTM B311 [35].

The crystallographic orientation of the SS316L sintered microstructures was mapped with respect to the build direction (Z) using an Oxford symmetry EBSD detector in the Tescan Clara FE-SEM. The data were acquired at 2 μm step size, 28 kV beam energy, and 21.2 mm working distance. Both EDS and EBSD data acquisition were conducted with Aztec data acquisition software, and the EDS and EBSD data post-processing was undertaken using the Aztec and AztecCrystal software, respectively. A clean-up process was applied to the EBSD data to assimilate any non- or mis-indexed points into the surrounding neighbourhood grains. Less than 10% of the points were modified in the process. The grain boundaries were detected with a threshold misorientation of 10° in conjunction with a minimum of 8 pixel of fractional difference of misorientation variation and a kernel size of 3 by 3. The grain size was measured as the maximum Feret diameter. The average grain aspect ratio was calculated as the fitted ellipse aspect ratio with the Σ3 twins (<111>/60°) boundaries

excluded. The same analysis was conducted on a SS316L wrought sample for comparison.

### Mechanical properties

The mechanical properties (yield and tensile strength) of the sintered SS316L samples were measured by tensile testing on triplicate specimens at room temperature (25 °C). Tests were conducted on rectangular subsize specimens using a 50 kN universal testing machine (UTM, Shimadzu) equipped with 50 kN manual non-shift wedge grips. The UTM crosshead speed was set to 0.48 mm/min within the elastic region, while the displacement was measured using an axial extensometer with a gauge length of 25 mm and a travel range of + 100% (Epsilon Tech Corp). The test was paused once the proportional limit was reached, the extensometer was then removed, and the test was resumed at a UTM crosshead speed of 1.6 mm/min until the specimen fractured. Data were collected at a rate of 10 Hz in the elastic region and 5 Hz in the plastic region. The test was monitored with the Trapezium X software. The tensile test, the dimensions of the specimens, and the method to calculate the 0.2% offset yield strength ( $S_y$ ), tensile strength ( $S_u$ ), elongation after fracture and reduction of area were conducted as per standard ASTM E8 [34]. The elongation at fracture was calculated from the engineering stress–strain curve. The Young's modulus ( $E$ ) was approximated using the least-squares method from 25 to 100 MPa using the stress–strain data as recommended in the standard ASTM E111 [36]. All fracture specimens were cut transversely (YZ plane) to a length of 10 mm, sonicated in ethanol, rinsed with deionised water, dried with nitrogen and placed inside a vacuum desiccator for at least 12 h before the microscopy analysis. Fractured surfaces were imaged using the SE detector, and micro-chemical analysis was conducted by EDS. The wrought SS316L specimens used for comparison were wire-cut with the same dimensions from a 3-mm-thick plate and similarly tested and analysed.

## Results

### Microstructures and analysis

Table 1 presents the chemical composition of SS316L powder and SS316L wrought samples measured by quantitative EDS along with the nominal composition of UNS S31603 as per standard ASTM A240 [37]. From comparisons, the analysed powder metal met the UNS S31603 requirements. A representative FE-SEM image of the feedstock is shown in Fig. 2. The measured average particle size distribution was  $d_{50}$  1.4  $\mu\text{m}$  and  $d_{90}$  5.0  $\mu\text{m}$ . A representative TEM image and corresponding EDS map of the SS316L precursor powder in Fig. 3 show the presence of spherical Si-, Mn- and O-rich inclusions. The inclusion size varies between 0.02 and 0.23  $\mu\text{m}$ .

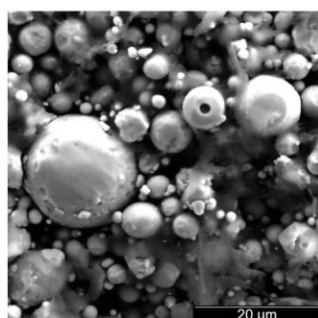
The XRD spectra of representative SS316L powder and sintered samples measured with respect to its build direction (Z) are shown in Fig. 4. The SS316L wrought data were added for comparison. It can be seen from the figure that the SS316L powder consisted mainly of  $\gamma$  (FCC) austenite phase with a subtle presence of retained  $\delta$  (BCC) ferrite. According to T. Kurzynowski et al. [6], the retention of  $\delta$ -ferrite in the powder feedstock results from the rapid solidification of molten SS316L during the gas atomisation process, when the  $\delta$ -ferrite stabilisers, such as Cr, Mo and Si, segregate to create later localised site-specific metastable conditions in the austenitic matrix [6]. The XRD data of the SS316L sintered sample solely shows  $\gamma$  (FCC) austenitic phase confirming the full dissipation of the  $\delta$ -ferrite. Wrought data was added for comparison.

Figure 5 shows a large field of view SEM images of the SS316L wrought and sintered samples. The grayscale contrasts indicate the presence of larger austenitic grains in the sintered sample than the wrought sample. Both samples comprise twin boundaries. There is a high porosity and oxide inclusion content in the sintered sample.

The micro-CT reconstruction in Fig. 6 reveals the presence of the elongated defects correlated with the printing raster pattern. The scan from the contour shell shows a cumulative stack of parallel lines as expected from the layer-by-layer print built up. The total scanned volume was  $6.9 \times 10^9 \mu\text{m}^3$ , in which the porosity volume was  $8.75 \times 10^7 \mu\text{m}^3$ , i.e. 1.27% v/v. The total amount of macro- and microporosity were 0.85% and 0.43%, respectively. The threshold

**Table 1** Quantitative EDS chemical composition of SS316L powder, SS316L wrought and nominal UNS S31603

Chemical composition in wt%						
Material	Fe	Cr	Ni	Mo	Mn	Si
SS316L Powder	Bal	17.1	10.0	2.3	1.3	0.6
SS316L Wrought	Bal	17.8	10.0	2.1	1.6	0.5
UNS S31603 [37]	Bal	16–18	10–14	2–3	2 max	0.75 max



**Figure 2** FE-SEM image of the feedstock showing the SS316L powder with a particle size distribution of d50 1.4  $\mu\text{m}$  and d90 5.0  $\mu\text{m}$ .

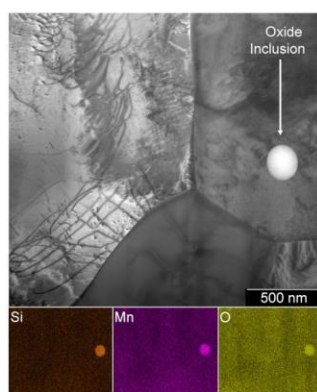


**Figure 3** TEM image and corresponding EDS map of a SS316L particle showing a spherical inclusion rich in Si, Mn and O content found in the SS316L precursor powder.

used to define micropores was  $< 10,000 \mu\text{m}^3$ . The fractional area of porosity measured from post-processed SEM cross-sectional images was  $4.8\% \pm 1.4$ .

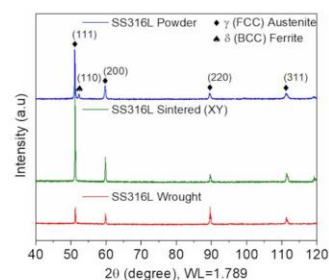


**Figure 4** XRD spectra of SS316L powder showing an  $\gamma$  (FCC) austenite phase with a small presence of retained  $\delta$  (BCC) ferrite (top), SS316L sintered sample (XY plane) showing a fully  $\gamma$  (FCC) austenite phase (middle), and SS316L wrought also showing a fully  $\gamma$  (FCC) (bottom).

The density of the sintered sample obtained using the Archimedes principle was  $7.43 \text{ g/cm}^3 \pm 0.07$ .

A SEM image of a SS316L sintered sample with corresponding EDS elemental maps is given in Fig. 7. The images show the presence of two types of inclusions, namely (1) irregular Cr-rich particles with an average size of  $3 \mu\text{m}$  and (2) spherical Si-rich particles with an average size of  $1.4 \mu\text{m}$ . Both types contain Mn and O. Identical findings are also reported in other investigations in 3D printed SS316L produced via PBF [38] and DED [12]. According to P. Deng et al. [38], the Si–Mn–O particles in the precursor powder were generated during the gas atomisation process [38]. Yan et al. [39] observed both inclusion types in PBF manufactured SS316L and concluded the particles were Rhodonite ( $\text{MnSiO}_3$ ) and Spinel ( $\text{MnCr}_2\text{O}_4$ ) [39]. However, the absence of these phases in the XRD spectra might suggest an amorphous nature of these inclusions, which deserves further investigations.

Figure 8 shows a wide area EBSD map of the Z-cross section (normal to the built direction) of a sintered sample is shown with the corresponding colour-coded inverse pole, indicating a weakly

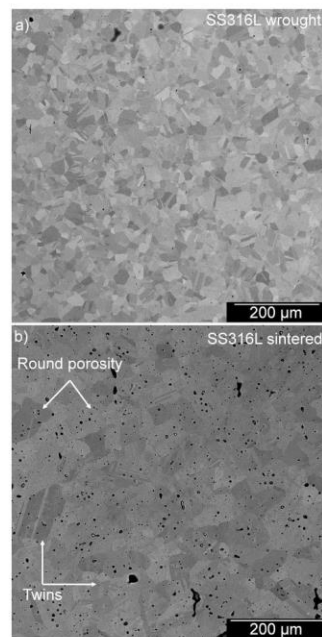


**Figure 5** SEM images showing large recrystallised microstructures in the **a** SS316L wrought, and **b** sintered samples, with the later showing distributed porosity, inclusions and twin interfaces.

textured almost random orientation distribution. The almost random orientation is also consistent with the low intensity ( $\times 1.26$  random) in the  $\{111\}$  pole figure. It should be noted that the EBSD area covered is inadequate for the measured grain size, but as a non-textured characteristic was found, it was not regarded as critical. The twin content was measured as the length fraction of the  $\Sigma 3$  boundaries in the microstructure, which was 52.3% of  $> 10^\circ$  boundaries. This finding is identical to the 53% reported by Irukuvarghula et al. [40] in hot isostatic pressing (HIP) processed SS316L steels [40]. The quantification made from the grain size measurement is shown in Table 2. In comparison, the SS316L wrought sample showed a slight strengthening of the texture as seen in the  $\{111\}$  pole figure, assumed to be caused by the processing history of the sample, the detail of which

is beyond the scope of the manuscript. The grain size measurements are shown in Table 2.

### Mechanical properties

Representative engineering stress–strain curves of both SS316L sintered and SS316L wrought samples are shown in Fig. 9, along with the dimensions of the test specimens. Results have shown that the sintered specimens performed in a ductile manner, which is represented by an initial linear elastic deformation followed by a non-linear permanent deformation. The calculated average Young's modulus ( $E$ , 196 GPa  $\pm$  28) matched with other's measurements, i.e. 202 GPa conducted at 25 °C room temperature [42]. The tensile strength ( $S_u$ , 524 MPa  $\pm$  1) and elongation at fracture (96%  $\pm$  1) met and exceeded the UNS S31603 standard requirements [37]. The 0.2% offset yield strength ( $S_y$ , 166 MPa  $\pm$  2) was slightly ( $\sim$  2%) lower than the minimum required. The mechanical properties are summarised in Table 3.

SEM images of the fractured surface of both SS316L wrought and sintered tensile specimens are presented in Fig. 10. The sintered specimens had a ductile fracture, which was characterised by small inclusions located inside the uniformly distributed spherical dimples. The magnified image at the contour shell and bulk volume shows the presence of elongated macro-porosity. No evidence of secondary central cracks or parabolic dimples, usually found from a shear fracture, was observed in the sintered sample; however, these features were found in the fractured surface of the SS316L wrought specimens. A SEM image and corresponding EDS map from the fractured surface of the SS316L sintered specimen confirming the presence of a Si–Mn–O-rich inclusion inside a spherical dimple can be seen in Fig. 11. Finally, photographs of both SS316L sintered and wrought fractured tensile specimens are given in Fig. 12. While both sintered and wrought sample fractured in a ductile manner, the sintered specimen had a smaller necked region. A typical cup-and-cone characteristic is observed in the wrought specimen.

### Discussion

The mechanical properties of the 3D printed SS316L in this work were compared with the literature of SS316L additively manufactured via FFF, PBF and

**Figure 6** Micro-CT scans of a SS316L sintered sample showing the presence of elongated macroporosity, **a** as a 3D mesh-like pattern at the bulk volume, **b** as a layer-by-layer pattern at the contour shell, and **c** as a layer-by-layer pattern skewed 45° in the XY plane at the bulk.

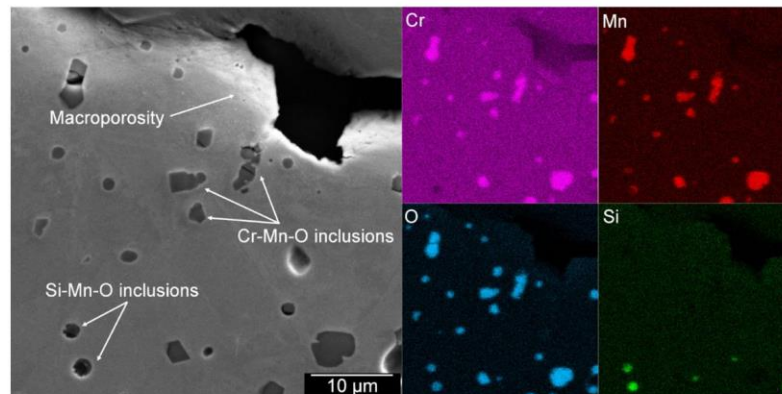
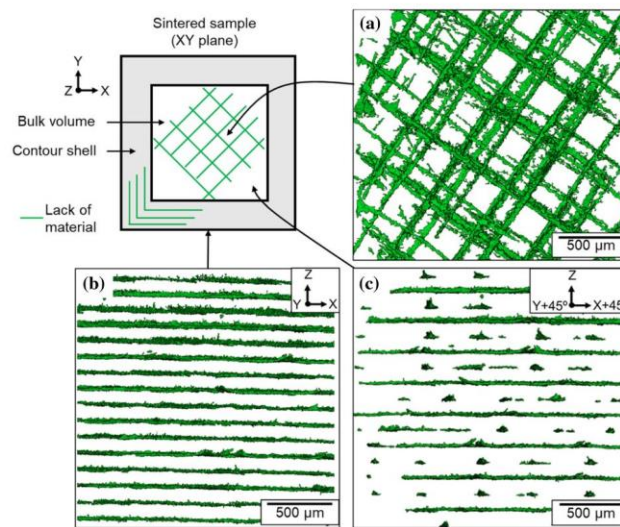


**Figure 7** SEM image of a SS316L sintered sample and corresponding EDS elemental maps showing the distribution of Si-Mn-O-rich spherical and Cr-Mn-O-rich irregular inclusions.

DED techniques. The results are summarised in Table 4 which also includes the typical properties obtained from well-established powder-based processes such as MIM and PM. The MIM-316L and UNS standard requirements for the S31603 grade were also added for comparison. Ultimately, some

characteristics obtained from the literature such as the size of the precursor powder as well as the average grain size and amount of porosity of the densified SS316L obtained with FFF, PBF and DED processes are given in Table 4 for comparison.

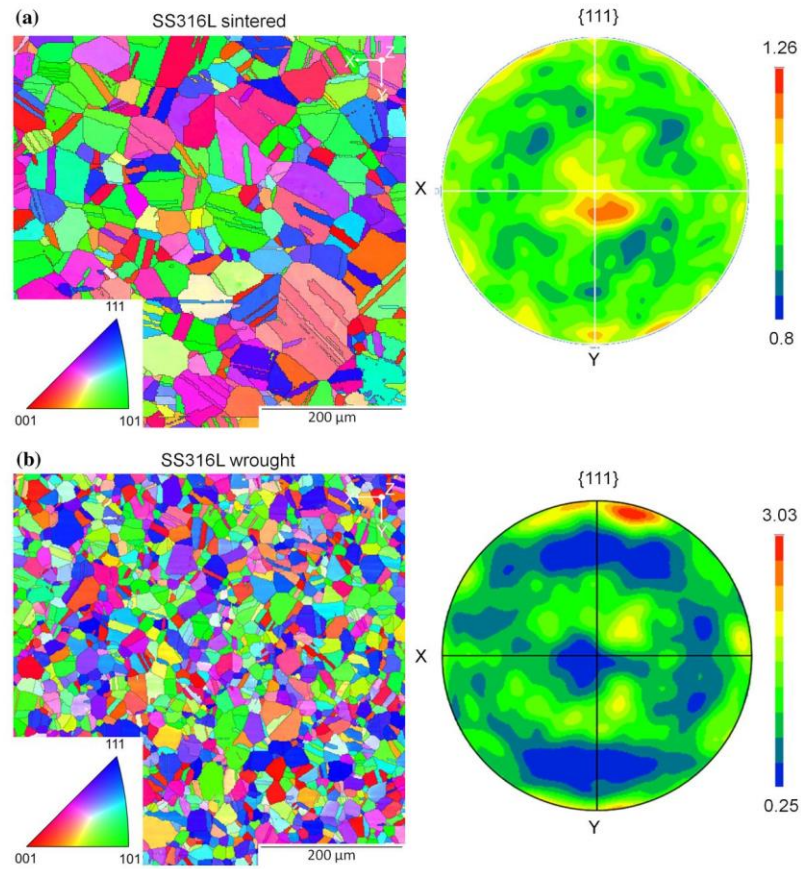


**Figure 8** EBSD measured inverse pole figure maps of the **a** SS316L sintered and **b** SS316L wrought sample with corresponding {111} pole figures.

**Table 2** Grain size measurements of SS316L sintered and SS316L wrought samples

Material	Overall grain size distribution (μm)	Average grain size (μm)	ASTM grain size No [41]	Average grain aspect ratio
SS316L sintered	d50 35, d90 71	40 ± 23	7.5	3.0 ± 2.4
SS316L wrought	d50 18, d90 34	20 ± 10	9.5	2.3 ± 1.3

**Figure 9** Engineering stress–strain curves of both sintered and wrought SS316L materials along with the dimensions of the test specimens.

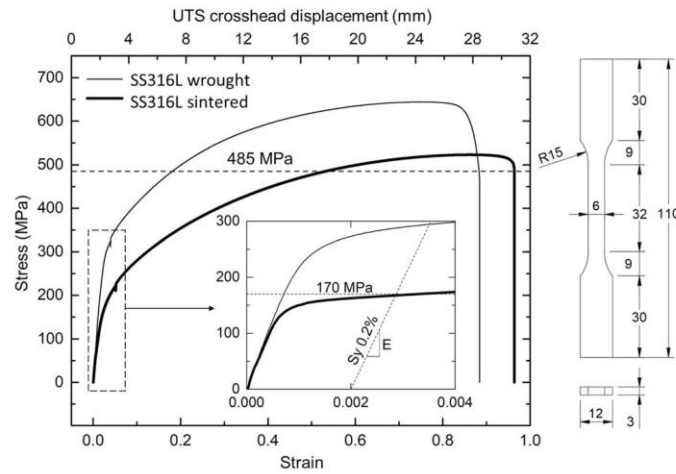


**Table 3** Mechanical properties of the SS316L sintered and SS316L wrought samples

Mechanical properties							
Material		Young's modulus (E) (GPa)	Offset Yield strength (Sy) (MPa)	Tensile strength (Su) (MPa)	Elongation at fracture (%)	Elongation after fracture in 32 mm (%)	Reduction of area (%)
SS316L Sintered	Avg	196	166	524	96	85	51
	Min	156	163	523	95	80	50
	Max	216	168	524	96	88	52
	Std Dev	28	2	1	1	3	1
SS316L Wrought	Avg	240	286	644	88	86	55
UNS S31603 [37]		202 [42]	min. 170	min. 485	min. 40	n/a	min. 40

**Influence of sintering on the microstructure**

This study revealed that the thermal profile in Fig. 1-b for sintering yield an average grain size of 40 μm, which is larger than the observed in the wrought sample. This can be seen in Figs. 5 and 8. The grain growth most likely took place as a result of the high temperature and long dwelling time inside the furnace. Similar grain growth has been reported in other FFF investigations [13, 17, 23]. It is pertinent to note that the grain growth did not led to the formation of a growth-dependent texture. In contrast, due to

different thermal processings with the PBF and DED involving a rapid melting followed by a rapid solidification, the produced material is strongly textured, and the microstructure is also asymmetric containing elongated columnar grains in the build direction along with much smaller grains that could grow preferentially along the scanning directions [10, 43].

The micro-CT analysis showed that after sintering, the final porosity of the additively manufactured SS316L was 1.27% v/v, which appears consistent with the findings by Y. Thompson et al. showing less porosity is produced after sintering at higher peak

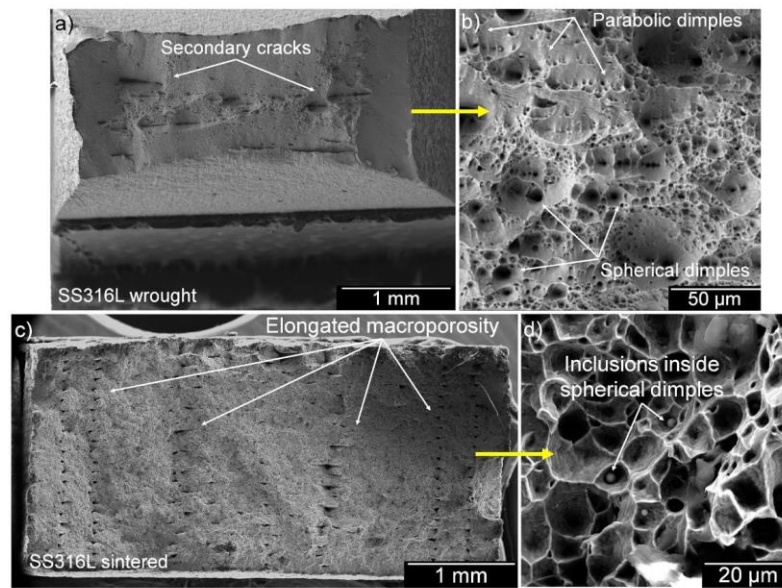


**Figure 10** SEM images of the tensile fractured surfaces in the a SS316L wrought and b sintered specimen showing their microscopy features.

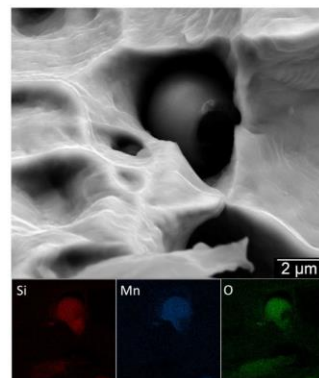


**Figure 11** SEM image of a SS316L sintered fractured specimen and corresponding EDS elemental map showing a Si-Mn-O inclusion inside a spherical dimple.

temperatures and longer dwell time [24]. The porosity content also depends on the built orientation and



**Figure 12** Photographic image of both fractured SS316L sintered tensile specimen (top) and SS316L wrought specimen (bottom) showing two types of necked regions.

printing raster patterns, as it was reported by Damon et al., and Suwanpreecha et al. [17, 19]. Similar effects were also found for PBF and DED [7, 9]. The size of the pre-alloyed powder used for making the feed material used in this investigation was 8 to 30 times smaller than the particles generally used in vast majority investigations with PBF and DED. Therefore, it would be a subject of research how PBF and DED can produce denser objects with a porosity as low as 0.2% [6, 10, 11]. The elongated macroporosity found in the manufactured sintered SS316L is a common defect of the FFF technique due to the inherent nature of the line-by-line and layer-by-layer



**Table 4** Summary of mechanical properties, powder size, grain size and final porosity of SS316L manufactured by Metal FFF, PBF, DED, MIM, PM and standard requirements for UNS S31603 and MIM-316L grade

	Young's modulus (E)	Yield strength (Sy)	Tensile strength (Su)	Elongation at fracture	Powder size	Grain size	Final porosity
Manufacturing technology	(GPa)	(MPa)	(MPa)	(%)	( $\mu\text{m}$ )	( $\mu\text{m}$ )	(%)
S316L sintered (this work)	196	166	524	96	d90 5.0	40 $\pm$ 23	1.27
Metal FFF [13]	93–154	168–187	409–499	17–37	n/s	75 $\pm$ 20	1.9 – 2.1
Metal FFF [17]	185 $\pm$ 5	155–165	500–520	32–37	n/s	25 $\pm$ 3	0.5 – 1.7
Metal FFF [18]	n/s	93–105	219–312	6–13	n/s	n/s	4.6
Metal FFF [21]	n/s	n/s	412	56.3	3–15	n/s	7.5
Metal FFF [22]	157.2 $\pm$ 4.5	148.0 $\pm$ 4.5	443.9 $\pm$ 5.9	43.3 $\pm$ 2.5	1–10	n/s	9.8
Meta FFF [23]	198	252 $\pm$ 7	521 $\pm$ 16	9	20–53	45 $\pm$ 5	7
Metal FFF [26]	132 $\pm$ 65	n/s	296 $\pm$ 78	32 $\pm$ 16	n/s	n/s	16
Metal FFF [30]	n/s	251	561	53	n/s	n/s	n/s
Metal FFF [31]	n/s	194 $\pm$ 19	441 $\pm$ 27	29.5 $\pm$ 3.8	30–50	n/s	7.8
Metal FFF [32]	152	167	465	31	n/s	n/s	1.5
PBF [6]	219 $\pm$ 41	517 $\pm$ 38	687 $\pm$ 40	32 $\pm$ 5	20–63	n/s	< 0.2
PBF [7]	n/s	430–536	509 – 668	12 – 25	20–50	1	1.4–4.8
DED [9]	204 – 218	201 – 284	457 – 509	27 – 42	44 – 106	n/s	< 1.0
DED [10]	n/s	388 $\pm$ 42	588 $\pm$ 53	48 $\pm$ 6	50 – 150	$\leq$ 10	0.1 – 0.2
SS316L Wrought (this work)	240	286	644	88	n/a	20	n/a
PM SS316L [28]	103–144	176–289	308–468	11–19	typ. 12	n/s	12.7–20.6
MIM SS316L [29]	185	180	520	40	n/s	n/s	n/s
UNS S31603 ASTM A240 [37]	202 [42]	min. 170	min. 485	min. 40	n/a	n/s	n/a
MIM-316L ASTM B883 [63]	190	min. 450 typ. 540	min. 450 typ. 520	min. 40 typ. 50	n/s	n/s	n/s

process, regardless of the feedstock or post-processing [2, 44, 45]. This pattern of porosity can be seen in Fig. 6, creating a 3D mesh-like structure inside the bulk volume, and a stack of lines resembling the layer-by-layer printing process in the contour shell of the specimen. The same type of FFF defect is reported elsewhere [17, 19, 21, 22, 27, 33, 46].

Spherical nanosized Si-, Mn- and O-rich inclusions, shown in Fig. 3, were observed in the original feedstock before sintering, which might alter or create a new set of inclusions. Similar findings in the feed powder of additive manufacturing and powder metallurgy processes have been reported elsewhere [28, 38, 39, 47]. Some investigations suggest that these inclusions are formed in the powder during its atomisation process [38, 47]. During sintering, these inclusions may undergo physical and chemical changes and may evolve into a new set of particles, as

shown in Fig. 7. The presence of this new type of irregular inclusions rich in Cr, Mn and O, suggests the importance of the sintering process on their morphology. The transformation from the fairly stable Si–Mn–O into the Cr–Mn–O type after the heat treatment of Fe–Cr alloys has also been studied elsewhere [48–51]. These investigations observed that the chemical composition of the Si–Mn–O-type inclusions present in the as-cast Fe–Cr alloys will either remain or change during heat treatment between 1000 and 1300 °C, depending on the initial content of Cr and Si in the steel matrix. Further changes associated with new transformation phenomena—as those occurring post-sintering in the 1100–1200 °C range for the PBF manufactured SS316L alloy—make the matter more complex [51]. The dwell time at peak temperature during the heat treatment

was also found to play important roles for the transformation [48, 51].

### Influence of sintering on the mechanical properties

The results presented herein showed that a sinter-based extrusion technology can be used to additively manufacture SS316L with a tensile strength ( $S_u$ ) and ductility in agreement with the standard requirements for the UNS S31603 grade, and a yield strength ( $S_y$ ) slightly lower ( $\sim 2\%$ ) than the minimum specified [37]. The higher yield strength ( $S_y$ ) of SS316L wrought, shown in Table 3, can be a contribution of the smaller grain size distribution as per the Hall–Petch equation [52, 53]. However, it should be noted here that many interdependent factors contribute the yield phenomena, and therefore, it should not be further discussed based on the grain size only.

An attempt was made to predict the minimum grain size requirement to attain the UNS S31603 standard benchmark of 170 MPa, assuming the other factors remains constant. The analysis was done using the Hall–Petch parameters experimentally obtained for SS316L wrought alloys in the literature [54, 55]. However, it becomes clear that none of the reported data fit the performance of the sintered material of the present study, i.e. the calculated yield strength ( $S_y$ ) for a 40  $\mu\text{m}$  grain size was much higher than the 166 MPa obtained herein. The discrepancy of the results with those of the published data could be explained by the fact that there is a significant presence of twin boundaries that were not taken into account in the Hall–Petch calculations. Also, as it is noted earlier, while Hall–Petch provides a great framework for strength prediction, the complexity of the present materials due to the presence of porosity and inclusions makes it difficult to predict and it requires a dedicated approach to simulate.

In order to shed light on the effect of porosity on mechanical properties, it was shown that the PBF and DED processes can produce SS316L with a porosity content that can be as low as 0.2% [6, 10, 11] and hence can exhibit improved yield and tensile strength. Porosity has a detrimental effect on these strength and ductility parameters because of the reduced area supporting the load and the stress concentration factor at each pore [28]. However, an investigation on the effects of sintering conditions on the mechanical properties of MIM SS316L showed

that only the tensile strength and elongation were dependent on the porosity content [56]. Further details on the influence of porosity in the strength of an additively manufactured SS316L via PBF and DED can be seen elsewhere [7, 57].

Regarding ductility, this study indicated that the elongation at fracture of the sintered tensile specimens was in average 70% higher than other metal FFF studies, as shown in Table 4. However, in some of these studies, the reported elongation was not calculated as per the ASTM E8 standard [34], which might explain the difference. When compared to the reported data of PBF and DED manufacturing, the elongation obtained in this study was 20% to 80% higher. The reason might be due to the fact that there is a significant strain field in the PBF and DED manufactured samples that makes a drop in ductility. Some improvements in ductility from the presence of annealing twins have also been reported elsewhere [57–60].

### Influence of sintering on the fracture

The SS316L sintered specimens were fractured in a ductile manner. The spherical dimples observed in Fig. 10-d appeared similar in size and uniformly distributed throughout the fractured surface. This mode of fracture is predicted to be caused by the presence of oxide inclusions, as shown in Fig. 7, which acted as the void nucleation sites [52]. The inclusion content, compared to SS316L wrought, is suspected to have led to the voids coalescence into a single crack that lead to the fracture during in tension. As a result, no secondary central cracks nor parabolic dimples were found in the fractography. It is pertinent to note that the presence of parabolic dimples indicates shear fracture [61]. Therefore, the absence of these features in the sintered fracture structure suggests that the material failed in pure tension [61]. The presence of larger voids indicates coalescence in both the wrought and sintered tensile specimens, as shown in Fig. 10b and d, respectively.

Another characteristic observation in the fracture surface of the SS316L sintered specimen was the lack of a cup-and-cone shape at the necked region, as shown in Fig. 12, which is a common feature of a ductile fracture [52, 53]. The reason can be explained by the tensile flow instability phenomena [52]. In short, for a tensile specimen with a rectangular cross section two types of tensile flow instabilities can take

place, i.e. diffuse and localised necking. The transition from diffuse to localised necking, as well as the final extent of each instability mode, depends on the capacity of the material to accommodate strains before the geometrical softening cancels its strain hardening [52]. In other words, when comparing two metals, the one with the higher strain-hardening exponent ( $n$ ) will tend to maintain the rectangular shape of its cross section for a longer period during the tensile test before the fracture, than the metal with the smaller  $n$ -value. The  $n$ -value was calculated for both sintered and wrought materials to predict the mode of behaviour by using the tensile test data and following the procedure reported in [52]. The values were 0.56 and 0.44 for the sintered and wrought materials, respectively. It can be seen from the different necked regions in the sintered and wrought specimens in Fig. 12 that the final instability mode was affected by the different  $n$ -values. As a result, the sintered specimen showed a larger localised necking than the wrought. Furthermore, when comparing the present investigation results with those from pure copper (99.99%) rectangular tensile specimens, it was found that the instability of the copper specimens was dominated by localised necking, making no cup-and-cone shape [62], because copper has an identical  $n$ -value of 0.54 [52].

### Conclusions

316L stainless steel was additively manufactured with a sinter-based extrusion technology. A detailed microstructure characterisation, tensile tests, and fractography were conducted to investigate the effects of sintering in the final microstructures and mechanical behaviour of the manufactured materials. Based on the results, the following conclusions can be drawn:

1. The SS316L sintered samples revealed an annealed microstructure composed of fully austenitic grains with an average grain size of 40  $\mu\text{m}$  and 1.27% v/v of combined porosity. Non-metallic particles, such as Si–Mn–O and Cr–Mn–O inclusions, were also obtained. Nanosized Si–Mn–O-type was found in the SS316L powder, probably as a sub-product of its atomisation process. Further research is required to elucidate the mechanism responsible for the transformation

of the Si–Mn–O inclusions into the Cr–Mn–O particles during sintering. Thermodynamic stability studies followed by different stages of sintering and in-depth microstructural analyses using methods, such as TEM-based techniques, will bring new insights into this complex phenomenon.

2. The SS316L sintered samples had a Young's modulus, tensile strength, and ductility comparable to those of a standard UNS S31603 grade; nevertheless, with a yield strength 2% lower than the specified minimum value. The main reason for the lower yield strength was attributed to the relatively large grains as defined by the general Hall–Petch relationship. The detrimental effect of porosity content requires further investigation.
3. The SS316L sintered samples revealed a ductile fracture in pure tension with two distinctive features: i) a fractured surface with uniformly distributed spherical dimples and no secondary cracks, and ii) a necked region without the typical cup-and-cone shape. The first type of fracture surface was proposed to be the product of the larger number of oxide inclusions present in the microstructure compared to the wrought case, leading to the formation of multiple voids coalescing into a single crack. The second fracture surface case was associated with the capacity of the sintered samples to accommodate a larger amount of strain-hardening during the tensile test, compared to the SS316L wrought specimens, which reduced the effect of the diffuse necking while promoting the localised necking instead as the dominating instability mode.

### Acknowledgements

The authors acknowledge the financial support of Woodside Energy, as well as the access to the instruments of the Microscopy and Microanalysis Facility (MMF) at Curtin University and the Centre for Microscopy, Characterisation and Analysis (CMCA) from the University of Western Australia.

### Author contributions

RS: was involved in conceptualisation, methodology, validation, investigation, writing—original draft. MS:

contributed to conceptualisation, supervision, writing—review and editing. SB: was involved in conceptualisation, investigation, data curation. GL: contributed to conceptualisation, writing—review and editing. MI: was involved in writing—review and editing, funding acquisition. MZQ: contributed to supervision, writing—review & editing.

### Funding

The fund was provided by Curtin University Grant number (4610000822).

### Declarations

**Conflict of interest** The authors declare that they have no known competing financial interests or personal relationships that could have appeared to influence the work reported in this paper.

### References

- [1] ISO/ASTM-52900 (2015) Additive manufacturing — General principles — Terminology. ISO, CH-1211 Geneva 20
- [2] Yang L, Hsu K, Baughman B, Godfrey D, Medina F, Menon M, Wiener S (2017) Additive manufacturing of metals: the technology, materials, design and production. Springer, Berlin
- [3] Redwood B, Schöffner F, Garret B (2017) The 3D printing handbook: technologies, design and applications. 3D Hubs B.V, Amsterdam
- [4] ISO-17296-2 (2015) Additive Manufacturing - General Principles - Part 2: Overview of process categories and feedstock. ISO International, CH-1211 Geneva 20
- [5] Rankouhi B, Bertsch KM, Meric de Bellefon G, Thevamaran M, Thoma DJ, Suresh K (2020) Experimental validation and microstructure characterization of topology optimized, additively manufactured SS316L components. *Mater Sci Eng, A* 776:139050. <https://doi.org/10.1016/j.msea.2020.139050>
- [6] Kurzynowski T, Gruber K, Stopyra W, Kuźnicka B, Chlebus E (2018) Correlation between process parameters, microstructure and properties of 316 L stainless steel processed by selective laser melting. *Mater Sci Eng, A* 718:64–73. <https://doi.org/10.1016/j.msea.2018.01.103>
- [7] Suryawanshi J, Prashanth KG, Ramamurty U (2017) Mechanical behavior of selective laser melted 316L stainless steel. *Mater Sci Eng, A* 696:113–121. <https://doi.org/10.1016/j.msea.2017.04.058>
- [8] Casati R, Lemke J, Vedani M (2016) Microstructure and fracture behavior of 316L austenitic stainless steel produced by selective laser melting. *J Mater Sci Technol* 32(8):738–744. <https://doi.org/10.1016/j.jmst.2016.06.016>
- [9] Kersten S, Praniewicz M, Kurfess T, Saldana C (2020) Build orientation effects on mechanical properties of 316SS components produced by directed energy deposition. *Procedia Manuf* 48:730–736. <https://doi.org/10.1016/j.promfg.2020.05.106>
- [10] Feenstra DR, Cruz V, Gao X, Molotnikov A, Birbilis N (2020) Effect of build height on the properties of large format stainless steel 316L fabricated via directed energy deposition. *Addit Manuf* 34:101205. <https://doi.org/10.1016/j.addma.2020.101205>
- [11] Benarji K, Ravi Kumar Y, Jinoop AN, Paul CP, Bindra KS (2021) Effect of heat-treatment on the microstructure, mechanical properties and corrosion behaviour of SS 316 structures built by laser directed energy deposition based additive manufacturing. *Met Mater Int* 27(3):488–499. <http://doi.org/10.1007/s12540-020-00838-y>
- [12] Aversa A, Saboori A, Librera E, de Chirico M, Biamino S, Lombardi M, Fino P (2020) The role of directed energy deposition atmosphere mode on the microstructure and mechanical properties of 316L samples. *Addit Manuf* 34:101274. <https://doi.org/10.1016/j.addma.2020.101274>
- [13] Caminero MÁ, Romero A, Chacón JM, Núñez PJ, García-Plaza E, Rodríguez GP (2021) Additive manufacturing of 316L stainless-steel structures using fused filament fabrication technology: mechanical and geometric properties. *Rapid Prototyp J* 27(3):583–591. <https://doi.org/10.1108/RPJ-06-2020-0120>
- [14] DebRoy T, Wei HL, Zuback JS, Mukherjee T, Elmer JW, Milewski JO, Beese AM, Wilson-Heid A, De A, Zhang W (2018) Additive manufacturing of metallic components – Process, structure and properties. *Prog Mater Sci* 92:112–224. <https://doi.org/10.1016/j.pmatsci.2017.10.001>
- [15] Yin S, Sun Q, Guo K, Wang X, Liu J, Sun J (2020) Effect of scanning strategies on the microstructure and mechanical behavior of 316L stainless steel fabricated by selective laser melting. *Mater Sci Eng, A* 793:139879. <https://doi.org/10.1016/j.msea.2020.139879>
- [16] Barkia B, Aubry P, Haghi-Ashtiani P, Auger T, Gosmain L, Schuster F, Maskrot H (2020) On the origin of the high tensile strength and ductility of additively manufactured 316L stainless steel: Multiscale investigation. *J Mater Sci Technol* 41:209–218. <https://doi.org/10.1016/j.jmst.2019.09.017>
- [17] Damon J, Dietrich S, Gorantla S, Popp U, Okolo B, Schulze V (2019) Process porosity and mechanical performance of fused filament fabricated 316L stainless steel. *Rapid*

- Prototyp J 25(7):1319–1327. <https://doi.org/10.1108/RPJ-01-2019-0002>
- [18] Ait-Mansour I, Kretschmar N, Chekurov S, Salmi M, Rech J (2020) Design-dependent shrinkage compensation modeling and mechanical property targeting of metal FFF. *Prog Addit Manuf* 5(1):51–57. <https://doi.org/10.1007/s40964-020-00124-8>
- [19] Suwanprecha C, Seensattayawong P, Vadhanakovint V, Manonukul A (2021) Influence of specimen layout on 17–4PH (AISI 630) alloys fabricated by low-cost additive manufacturing. *Metall Mater Trans A* 52(5):1999–2009. <https://doi.org/10.1007/s11661-021-06211-x>
- [20] Poszvek G, Stattler G, Markl E, Seemann R, Lackner M (2021) Fused filament fabrication of metallic components for semi-professional and home use. In: Durakbasa NM, Gencyilmaz MG (eds) *Digital conversion on the way to industry*. Springer International Publishing, Cham, pp 140–149. [https://doi.org/10.1007/978-3-030-62784-3\\_12](https://doi.org/10.1007/978-3-030-62784-3_12)
- [21] Wang Y, Zhang L, Li X, Yan Z (2021) On hot isostatic pressing sintering of fused filament fabricated 316L stainless steel – Evaluation of microstructure, porosity, and tensile properties. *Mater Lett* 296:129854. <https://doi.org/10.1016/j.matlet.2021.129854>
- [22] Tosto C, Tirillò J, Sarasini F, Cicala G (2021) Hybrid metal/polymer filaments for fused filament fabrication (FFF) to print metal parts. *Appl Sci* 11(4):1444. <https://doi.org/10.3390/app11041444>
- [23] Sadaf M, Bragaglia M, Nanni F (2021) A simple route for additive manufacturing of 316L stainless steel via fused filament fabrication. *J Manuf Process* 67:141–150. <https://doi.org/10.1016/j.jmapro.2021.04.055>
- [24] Thompson Y, Gonzalez-Gutierrez J, Kukla C, Felfer P (2019) Fused filament fabrication, debinding and sintering as a low cost additive manufacturing method of 316L stainless steel. *Addit Manuf* 30:100861. <https://doi.org/10.1016/j.addma.2019.100861>
- [25] Cerejo F, Gatões D, Vieira MT (2021) Optimization of metallic powder filaments for additive manufacturing extrusion (MEX). *Int J Adv Manuf Technol* 115(7):2449–2464. <https://doi.org/10.1007/s00170-021-07043-0>
- [26] Rosnitschek T, Seefeldt A, Alber-Laukant B, Neumeyer T, Altstädt V, Tremmel S (2021) Correlations of geometry and infill degree of extrusion additively manufactured 316L stainless steel components. *Materials* 14(18):5173. <https://doi.org/10.3390/ma14185173>
- [27] Jiang D, Ning F (2021) Additive manufacturing of 316L stainless steel by a printing-debinding-sintering method: effects of microstructure on fatigue property. *J Manuf Sci Eng* 143(9):091007. <https://doi.org/10.1115/1.4050190>
- [28] German RM (1998) *Powder metallurgy of iron and steel*. Wiley, 605 Third Ave, New York, NY 10016, USA, 1998. 496
- [29] Heaney DF (2012) *Handbook of metal injection molding*. Woodhead Publishing, Philadelphia, PA
- [30] Šafka J, Ackermann M, Machacek J, Seidl M, Věle F, Truxova V (2020) Fabrication process and basic material properties of the basf ultrafuse 316IX material. *MM Sci J* 2020:4216–4222. [https://doi.org/10.17973/MMSJ.2020\\_12\\_2020071](https://doi.org/10.17973/MMSJ.2020_12_2020071)
- [31] Liu B, Wang Y, Lin Z, Zhang T (2020) Creating metal parts by fused deposition modeling and sintering. *Mater Lett* 263:127252. <https://doi.org/10.1016/j.matlet.2019.127252>
- [32] Gong H, Snelling D, Kardel K, Carrano A (2019) Comparison of stainless steel 316L parts made by FDM- and SLM-Based additive manufacturing processes. *JOM* 71(3):880–885. <https://doi.org/10.1007/s11837-018-3207-3>
- [33] Gante Lokesh Renukaradhy K (2019) *Metal filament 3D printing of SS316L : focusing on the printing process*. Student thesis, KTH Royal Institute of Technology, Sweden
- [34] ASTM-E8 (2016) *Standard test methods for tension testing of metallic materials*. ASTM International, West Conshohocken, PA. Doi: [https://doi.org/10.1520/E0008\\_E0008M-16AE01](https://doi.org/10.1520/E0008_E0008M-16AE01)
- [35] ASTM-B311 (2017) *Standard Test Method for Density of Powder Metallurgy (PM) Materials Containing Less Than Two Percent Porosity*. ASTM International, West Conshohocken, PA, 2017. doi: <https://doi.org/10.1520/B0311-17>
- [36] ASTM-E111 (2017) *Standard test method for young's modulus, tangent modulus, and chord modulus*. ASTM International, West Conshohocken, PA. Doi: <https://doi.org/10.1520/E0111-17>
- [37] ASTM-A240 (2020) *Standard specification for chromium and chromium-nickel stainless steel plate sheet and strip for pressure vessels and for general applications*. ASTM International, West Conshohocken, PA. Doi: [https://doi.org/10.1520/A0240\\_A0240M-20A](https://doi.org/10.1520/A0240_A0240M-20A)
- [38] Deng P, Karadge M, Rebak RB, Gupta VK, Prorok BC, Lou X (2020) The origin and formation of oxygen inclusions in austenitic stainless steels manufactured by laser powder bed fusion. *Addit Manuf* 35:101334. <https://doi.org/10.1016/j.addma.2020.101334>
- [39] Yan F, Xiong W, Faierson E, Olson GB (2018) Characterization of nano-scale oxides in austenitic stainless steel processed by powder bed fusion. *Scripta Mater* 155:104–108. <https://doi.org/10.1016/j.scriptamat.2018.06.011>
- [40] Irukuvarghula S, Hassanin H, Cayron C, Attallah MM, Stewart D, Preuss M (2017) Evolution of grain boundary network topology in 316L austenitic stainless steel during powder hot isostatic pressing. *Acta Mater* 133:269–281. <https://doi.org/10.1016/j.actamat.2017.04.068>

- [41] ASTM-E2627 (2019) Standard practice for determining average grain size using electron backscatter diffraction (EBSD) in fully recrystallized polycrystalline materials. ASTM International, West Conshohocken, PA. Doi: <https://doi.org/10.1520/E2627-13R19>
- [42] Ledbetter HM (1981) Stainless-steel elastic constants at low temperatures. *J Appl Phys* 52(3):1587–1589. <https://doi.org/10.1063/1.329644>
- [43] Pham MS, Dovgvy B, Hooper PA (2017) Twinning induced plasticity in austenitic stainless steel 316L made by additive manufacturing. *Mater Sci Eng, A* 704:102–111. <https://doi.org/10.1016/j.msea.2017.07.082>
- [44] Colón Quintana JL, Redmann A, Mazzei Capote GA, Pérez-Irizarry A, Bechara A, Osswald TA, Lakes R (2019) Viscoelastic properties of fused filament fabrication parts. *Addit Manuf* 28:704–710. <https://doi.org/10.1016/j.addma.2019.06.003>
- [45] Montero M, Roundy S, Odell D, Ahn S-H, Wright PK (2001) Material characterization of fused deposition modeling (FDM) ABS by designed experiments. *Soc Manuf Eng* 10(13552540210441166):1–21
- [46] Singh P (2020) Materials-processing relationships for metal fused filament fabrication of Ti-6Al-4V alloy. University of Louisville
- [47] Klar E, Samal PK (2007) Powder metallurgy stainless steels: processing, microstructures, and properties. ASM international, Ohio
- [48] Shibata H, Kimura K, Tanaka T, Kitamura S-y (2011) Mechanism of change in chemical composition of oxide inclusions in Fe-Cr alloys deoxidized with Mn and Si by heat treatment at 1473 K. *ISIJ Int* 51(12):1944–1950. <https://doi.org/10.2355/isijinternational.51.1944>
- [49] Shibata H, Tanaka T, Kimura K, Kitamura SY (2010) Composition change in oxide inclusions of stainless steel by heat treatment. *Ironmak Steelmak* 37(7):522–528. <https://doi.org/10.1179/030192310X12700328925903>
- [50] Ren Y, Zhang L, Pistorius PC (2017) Transformation of oxide inclusions in type 304 stainless steels during heat treatment. *Metall and Mater Trans B* 48(5):2281–2292. <https://doi.org/10.1007/s11663-017-1007-8>
- [51] Laleh M, Hughes AE, Xu W, Cizek P, Tan MY (2020) Unanticipated drastic decline in pitting corrosion resistance of additively manufactured 316L stainless steel after high-temperature post-processing. *Corros Sci* 165:108412. <https://doi.org/10.1016/j.corsci.2019.108412>
- [52] Dieter GE, Bacon DJ (1976) *Mechanical metallurgy*. McGraw-hill, New York
- [53] Callister WD, Rethwisch DG, Blicblau A, Bruggeman K, Cortie M, Long J, Hart J, Marceau R, Ryan M, Parvizi R (2021) *Materials science and engineering: an introduction*. Wiley, Hoboken
- [54] Varin R, Kurzydowski K (1988) The effects of nitrogen content and twin boundaries on the yield strength of various commercial heats of type 316 austenitic stainless steel. *Mater Sci Eng, A* 101:221–226. [https://doi.org/10.1016/0921-5093\(88\)90068-8](https://doi.org/10.1016/0921-5093(88)90068-8)
- [55] Singh KK, Sangal S, Murty G (2002) Hall-Petch behaviour of 316L austenitic stainless steel at room temperature. *Mater Sci Technol* 18:165–172. <https://doi.org/10.1179/026708301125000384>
- [56] Yoon TS, Lee YH, Ahn SH, Lee JH, Lee CS (2003) Effects of sintering conditions on the mechanical properties of metal injection molded 316L stainless steel. *ISIJ Int* 43(1):119–126. <https://doi.org/10.2355/isijinternational.43.119>
- [57] Ronneberg T, Davies CM, Hooper PA (2020) Revealing relationships between porosity, microstructure and mechanical properties of laser powder bed fusion 316L stainless steel through heat treatment. *Mater Des* 189:108481. <https://doi.org/10.1016/j.matdes.2020.108481>
- [58] Ma S, Fu L, Shan A (2021) Enhancing strength-ductility of the aluminum bronze alloy by generating high-density ultrafine annealing twins. *Mater Charact* 177:111057. <https://doi.org/10.1016/j.matchar.2021.111057>
- [59] Deng HW, Xie ZM, Zhao BL, Wang YK, Wang MM, Yang JF, Zhang T, Xiong Y, Wang XP, Fang QF, Liu CS (2019) Tailoring mechanical properties of a CoCrNi medium-entropy alloy by controlling nanotwin-HCP lamellae and annealing twins. *Mater Sci Eng, A* 744:241–246. <https://doi.org/10.1016/j.msea.2018.11.143>
- [60] Kheiri S, Mirzadeh H, Naghizadeh M (2019) Tailoring the microstructure and mechanical properties of AISI 316L austenitic stainless steel via cold rolling and reversion annealing. *Mater Sci Eng, A* 759:90–96. <https://doi.org/10.1016/j.msea.2019.05.028>
- [61] Mills K, Davis JR (1987) *ASM Handbook, Volume 12-Fractography*. ASM International
- [62] Ifergane S, Barkay Z, Beeri O, Eliaz N (2010) Study of fracture evolution in copper sheets by in situ tensile test and EBSD analysis. *J Mater Sci* 45(23):6345–6352. <https://doi.org/10.1007/s10853-010-4596-z>
- [63] ASTM-B883 (2019) Standard specification for metal injection molded (MIM) materials. ASTM International, West Conshohocken, PA. Doi: <https://doi.org/10.1520/B0883-19>

**Publisher's Note** Springer Nature remains neutral with regard to jurisdictional claims in published maps and institutional affiliations.

**Appendix 4: Original reprint of the publication included in  
Chapter 3**

Article

# Crystallographic Texture and Substructural Phenomena in 316 Stainless Steel Printed by Selective Laser Melting

Ricardo Santamaría <sup>1</sup>, Mobin Salasi <sup>1</sup>, William D. A. Rickard <sup>2</sup>, Kod Pojtanabuntoeng <sup>1</sup>, Garry Leadbeater <sup>1,3</sup>, Mariano Iannuzzi <sup>1</sup>, Steven M. Reddy <sup>4</sup> and Md Zakaria Quadir <sup>2,3,\*</sup>

<sup>1</sup> Curtin Corrosion Centre, Curtin University, Perth, WA 6102, Australia;

ricardo.santamar@postgrad.curtin.edu.au (R.S.); mobin.salasi@curtin.edu.au (M.S.); thunyaluk.pojtanabuntoeng@curtin.edu.au (K.P.); g.leadbeater@exchange.curtin.edu.au (G.L.); mariano.iannuzzi@curtin.edu.au (M.I.)

<sup>2</sup> Microscopy and Microanalysis Facility, John de Laeter Centre (JdLC), Perth, WA 6845, Australia; w.rickard@curtin.edu.au

<sup>3</sup> School of Civil and Mechanical Engineering, Curtin University, Bentley, WA 6102, Australia

<sup>4</sup> School of Earth and Planetary Sciences, Curtin University, Bentley, WA 6102, Australia; s.reddy@curtin.edu.au

\* Correspondence: zakaria.quadir@curtin.edu.au; Tel.: +61-(808)-9266-1026

**Abstract:** There is a fast-growing interest in the use of selective laser melting (SLM) for metal/alloy additive manufacturing. Our current knowledge of SLM-printed 316 stainless steel (SS316) is limited and sometimes appears sporadic, presumably due to the complex interdependent effects of a large number of process variables of the SLM processing. This is reflected in the discrepant findings in the crystallographic textures and microstructures in this investigation compared to those reported in the literature, which also vary among themselves. The as-printed material is macroscopically asymmetric in terms of both structure and crystallographic texture. The  $\langle 101 \rangle$  and  $\langle 111 \rangle$  crystallographic directions align parallel with the SLM scanning direction (SD) and build direction (BD), respectively. Likewise, some characteristic low-angle boundary features have been reported to be crystallographic, while this investigation unequivocally proves them to be non-crystallographic, since they always maintain an identical alignment with the SLM laser scanning direction, irrespective of the matrix material's crystal orientation. There are also  $500 \pm 200$  nm columnar or cellular features, depending on the cross-section, which are generally found all over the sample. These columnar or cellular features are formed with walls made of dense packing of dislocations entangled with Mn-, Si- and O-enriched amorphous inclusions. They remain stable after ASM solution treatments at a temperature of 1050 °C, and therefore, are capable of hindering boundary migration events of recrystallization and grain growth. Thus, the nanoscale structures can be retained at high temperatures. Large 2–4 µm inclusions form during the solution treatment, within which the chemical and phase distribution are heterogeneous.

**Keywords:** selective laser melting (SLM); 3D printing; additive manufacturing (AM); 316 stainless steel (SS316); EBSD; TEM



**Citation:** Santamaría, R.; Salasi, M.; Rickard, W.D.A.; Pojtanabuntoeng, K.; Leadbeater, G.; Iannuzzi, M.; Reddy, S.M.; Quadir, M.Z. Crystallographic Texture and Substructural Phenomena in 316 Stainless Steel Printed by Selective Laser Melting. *Materials* **2023**, *16*, 4289. <https://doi.org/10.3390/ma16124289>

Academic Editor: Rainer J. Hebert

Received: 3 May 2023

Revised: 1 June 2023

Accepted: 6 June 2023

Published: 9 June 2023



**Copyright:** © 2023 by the authors. Licensee MDPI, Basel, Switzerland. This article is an open access article distributed under the terms and conditions of the Creative Commons Attribution (CC BY) license (<https://creativecommons.org/licenses/by/4.0/>).

## 1. Introduction

Selective laser melting (SLM) is a powder-based 3D printing/additive manufacturing (AM) technique for fabricating complex metallic parts with custom-designed internal and/or external structures. In SLM, a digital system drives a high-power laser beam, up to 1 kW, along a predesigned track to melt and fuse metallic powder particles layer by layer to build a complex metal/alloy shape and/or internal structures that otherwise would be impossible to fabricate with conventional metal processing techniques. SLM was initially developed almost two decades ago [1], but until recently, it has primarily been used in laboratory-scale and industrial prototyping [2–5]. Over the last ten years, the manufacturing sector has shown a keen interest in using SLM for industrial mass



production. This is primarily due to improvements in SLM printing hardware, e.g., laser precision, powder manufacturing, etc., thus reducing time and production costs, as well as increasing the inherent metallurgical benefits of SLM manufacturing [2–4]. SLM provides a high degree of freedom in alloy compositions, covering both conventional and exotic mixtures, e.g., high-entropy alloys, and provides for post-heating treatments [6–8]. There are also unique metallurgical benefits in terms of the lightweighting and strengthening of material via the control of solidification rates and compositional gradients. These benefits are not possible, or are highly restricted, in conventional metal casting and subsequent thermomechanical processing (TMP) [9–11]. As a result, the SLM technique is rapidly being incorporated into industrial manufacturing [12–14], particularly in the aerospace, automotive, biomedical and energy sectors [15–17].

The metallurgical process variables between conventional metal processing and SLM are significantly different [18,19]. Consequently, the material properties, structures (at macro, micro and nano scales), and application performance have large differences, even for the same alloy composition. Nevertheless, it should be noted that the majority of metal AM techniques are developed from the concept of conventional techniques such as casting, welding, powder processing and/or cladding. These conventional techniques are not ideal when developing additive manufacturing process parameters and variables, and Aboulkhair et al. [18] recently summarized the SLM process variables, and their differences compared to conventional processing. For instance, castability and weldability are considered the primary characteristics for a given alloy's suitability for SLM fabrication. Indeed, there are marked differences between the solidification rates and conventional welding parameters and those involved in SLM. Likewise, the remelting and rewelding during subsequent SLM scanning creates a thermal effect that has some similarities to conventional TMP [5].

Our current SLM knowledge is limited to a handful of alloy systems, including aluminum [19–22] and titanium [10,23,24] alloys, as well as some studies on stainless steel [25–28], nickel [29–32], cobalt [33–36], copper [37] and magnesium [38] alloys. Consistent and systematic investigations are essential to developing a detailed understanding of the effect of process variables on the microstructures and ultimate physical properties of SLM-printed materials; as such, it has taken many decades of research to reach the current level of knowledge for a given alloy system for a given conventional processing. The SLM journey has commenced, and the processes, microstructures and properties of materials processed in this way are in high demand because of the significant benefits and rapid growth of the technique. This paper presents a comprehensive analysis of the crystallography and composition of structures in an SLM-printed 316 stainless steel (SS316) in the macro to the nano scales for advancing and rectifying our understanding on the structural and crystallographic texture phenomena.

## 2. Materials and Methods

SLM printing was conducted with a 3D system Pro X DMP 320 machine by a commercial 3D printing service company (Amiga Engineering, Tullamarine, VIC, Australia). A SS316 powder feed supplied by TLS Technik GmbH & Co (Bitterfeld-Wolfen, Germany) with  $45 \pm 10 \mu\text{m}$  average size was used to print a rectangular block  $40 \times 40 \times 2 \text{ mm}$  (X:Y:Z), see the schematic in Figure 1a inset. The other SLM parameters were  $30 \mu\text{m}$  layer thickness, 250 W laser power, 900 mm/s laser speed,  $30 \mu\text{m}$  scan resolution, parallel raster pattern with  $0^\circ$  rotation, and high-purity argon as the shielding gas. The feed chemical composition was provided by the supplier as 0.02 wt.% C, 0.51 wt.% Si, 1.0 wt.% Mn, 17.5 wt.% Cr, 2.3 wt.% Mo, 11.1 wt.% Ni, and Fe balance.

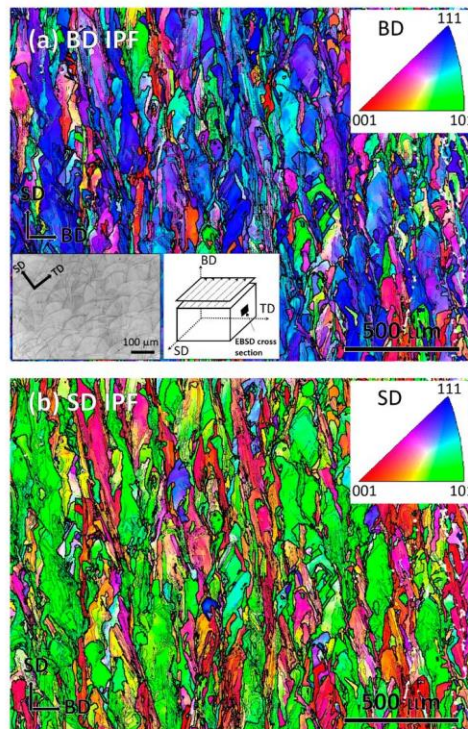


**Figure 1.** EBSD-measured color-coded IPF map of the as-printed SLM sample showing the orientation along the (a) BD and (b) SD. The insets in Figure 1a show the optical microscopy image and the EBSD cross-section.

The printed material was subjected to an isothermal solution treatment at 1050 °C for 4 h in an argon-purged furnace followed by immediate water-cooling. The longitudinal cross-section, see the schematic in Figure 1a inset, of both the as-printed and heat-treated samples were cut, mechanically polished down to colloidal silica finish, and then ion milled with a Technoorg Linda SEMPprep II system (Budapest, Hungary) to obtain a defect-free surface suitable for investigation by electron backscattered diffraction (EBSD) investigation. The ion milling parameters were 8 kV, 6° tilt and 360° rotation. EBSD was conducted with an Oxford Instruments Symmetry™ system attached to a Tescan Mira (Brno, The Czech Republic) field emission scanning electron microscope (FE SEM) operated at 15 kV beam energy. Iron FCC (face-centered cubic) phase from the Oxford database was used for indexing EBSD patterns and the Oxford Instruments' AztecCrystal software v.2.1.259 was used to post-process and analyze the EBSD data.

Site-specific transmission electron microscopy (TEM) samples were prepared from bulk samples using a Tescan Lyra Ga<sup>+</sup> (Brno, The Czech Republic) focused ion beam (FIB)-SEM. The final polishing step was performed with a low beam energy of 2 kV to minimize ion beam damage. A FEI Talos FS200X G2 (Waltham, MA, USA) FE TEM was used for the TEM investigation and was operated at 200 kV. Elemental mapping was conducted by an energy dispersive spectroscopy (EDS) attached as two pairs of a FEI Super X detection

system. Location-specific diffraction analysis was performed using selective area diffraction (SAD) with an aperture with a diameter of 200 nm and convergent beam electron diffraction (CBED). A double tilt holder was used to tilt the sample to the intended crystallographic zone axis by navigating through the CBED generated Kikuchi pattern. TEM imaging was conducted both in conventional and scanning TEM (STEM) modes. For STEM, the bright field (BF) and high-angle annular dark-field (HAADF) mode were used to enhance diffraction and atomic number contrast, respectively. TEM data acquisition and analysis was undertaken using Velox software and diffraction data analysis was conducted using the international center for diffraction data (ICDD) database.

### 3. Results and Discussion

#### 3.1. Structural Symmetry and Crystallographic Texture

Figure 1a,b show EBSD color-coded inverse pole figure (IPF) maps in the building direction (BD) and scanning direction (SD) in a BD-SD cross-section from an SLM-printed block. The investigated cross-section schematic is shown in the inset in Figure 1a, in which the terminology of the orthogonal print axes is shown, in convention with comparable studies, e.g., [39]. In Figure 1, the optical micrograph shows the characteristic print features in an SD-TD surface previously reported in numerous investigations [39–42]. From the IPF maps, it is clear that the BD and SD were predominantly oriented along the  $\langle 111 \rangle$  and  $\langle 101 \rangle$  crystal directions, respectively. It has been well-established that crystallographic texture in iron controls its anisotropy in mechanical, thermal, magnetic and optical properties. The observed macroscopic crystallographic texture is therefore likely to play a fundamental control on the anisotropy of physical properties in SLM-printed SS316. The thick and thin black lines in the EBSD map represent the high-angle ( $>15^\circ$ ) and low-angle ( $3\text{--}15^\circ$ ) misorientation boundaries, respectively. The high-angle boundaries are broadly parallel to the laser scanning tracks associated with printing. There was no evidence of the formation of the  $\Sigma 9$  twin boundary ( $\langle 111 \rangle 60^\circ$ ) in the as-printed sample. This finding is consistent with the other literature, where no twin boundaries were reported in SLM-printed SS316, although the wrought form of the material contained annealing twins [41,42]. The formation of twin boundaries is generally promoted by low solidification rates [43,44]. Therefore, in the case of SLM-manufactured SS316, where solidification occurs almost instantly at cooling rates ranging from  $10^3$  to  $10^7$  K/s [2,45–47], the formation of twin boundaries is hindered. This rapid cooling prevents sufficient time for the atoms to rearrange, which in turn delays the nucleation and growth of twin boundaries. This is in contrast to wrought SS316L, where cooling rates are much slower and facilitate the formation of twin boundaries [41,42].

In the IPF map presented in Figure 1b, there are thin  $\langle 001 \rangle$ -oriented layers, colored in red, between thicker  $\langle 101 \rangle$ -oriented printing tracks, colored in green. These green and red layers are called ‘major’ and ‘minor layers’ by Sun et al. [48] (pp. 89–93). The thickness of the major and minor layers varied between 100 and 200  $\mu\text{m}$  and 50 and 100  $\mu\text{m}$ , respectively, suggesting an overall crystallographic relationship between the major and minor layers. In both IPF maps, there are other orientations in the major layers, which are present in the red and green regions in Figure 1a, and red and blue regions in Figure 1b. EBSD analysis in the TD revealed mixed orientation, not presented in the Figure 1. These findings suggest that a sample-scale macroscopic crystallographic texture forms in SLM-printed SS316, which is consistent overall with the recent literature, but the reported textures vary in terms of crystal orientation [48–51]. An epitaxial growth mechanism between the major and minor layers is regarded as the origin of the overall texture development [48]. However, lattice epitaxy requires a perfect match between two lattice interfaces with common coincident sites, which is somewhat unrealistic to imagine in the SLM-printed material, because it contains a continuous change in orientation, as reflected by a gradual change in color within short distances in the EBSD maps. Hence, a separate in-depth investigation at a finer length scale is required to find out whether there are epitaxies over short distances, and if this collectively develops the overall texture.

In Figure 2a, the misorientation boundaries are elucidated in a higher-resolution, 100 nm step size, IPF map, whereby the SD is plotted as per the color-coded IPF section in the inset. As before, the high- ( $>15^\circ$ ) and low-angle ( $3\text{--}15^\circ$ ) boundaries are represented by thick and thin black lines, respectively. The corresponding Kernel average misorientation (KAM) map is shown in Figure 2b, in which each data point represents the mean orientation difference with the eight surrounding neighboring points. The blue–yellow–red legend in Figure 2b indicates the relative KAM intensity. There is a correlation between Figure 2a,b, viz., comparison of the white encircled areas shows that the high-stored-energy spots have a higher density of misorientation boundaries. This observation can be understood in relation to dislocation density because a higher dislocation density is required to accommodate any misorientation. There were also regions of low stored energy. One such example is encompassed with a white rectangular box, within which there is a small orientation variation, represented by a minor change in the IPF color variation. Such low misorientation variations indicate the presence of dislocation mesh and cell structures, which usually accommodate relatively less energy [52]. Therefore, the as-printed sample showed an overall heterogeneous distribution of the stored energy. This finding explains the spatial variation of the micro- and nano-scale mechanical data in the SLM-printed material [53,54].

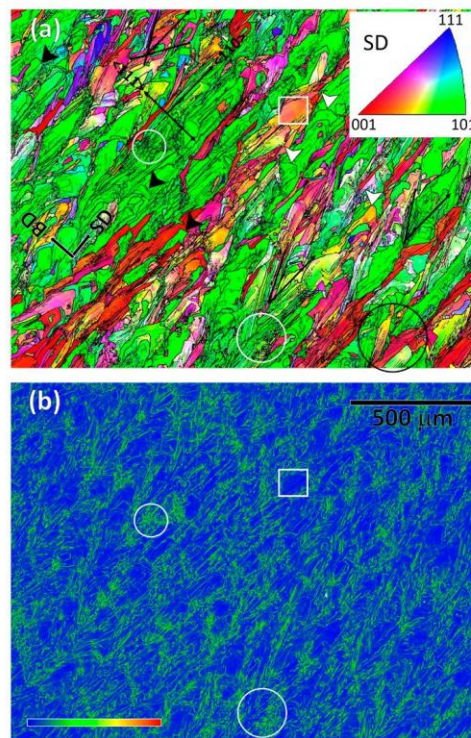


**Figure 2.** Higher-resolution EBSD maps of the as-printed SLM sample showing (a) color-coded IPF map of SD to illustrate the inhomogeneities in the high ( $>15^\circ$ ) and low-angle ( $3\text{--}15^\circ$ ) boundary distributions and their alignments with the SD and (b) the corresponding inhomogeneities in the KAM plot.

Figure 2a also reveals several other morphological features of the boundary. For example, the majority of the boundaries were straight, though there were several high-angle boundaries that had convoluted trajectories, some of which are indicated with white arrows. This phenomenon indicates the occurrence of a thermally induced restoration process, perhaps from the heat flow from the subsequent SLM scanning [52]. It is important to note that the boundaries depicted in Figure 2 are also present in Figure 1. However, Figure 1 provides a broader field of view, making the details of the boundaries less apparent. Figure 2 complements Figure 1 by offering a closer view (or finer scale) that provides additional information about the boundary features. There was no sign of recrystallization, as noted by an absence of a trailed region with a uniform orientation behind a migrating high-angle boundary [52]. The convoluted high-angle boundaries are expected to have formed during solidification or due to subsequent thermal restoration [52], although the process did not progress to the boundary migration stage of recrystallization.

### 3.2. Substructural Features

There is a profuse presence of straight misorientation boundaries in Figure 2a, which are aligned, within a certain angular range, with the SD, as indicated by the black lines. Some straight boundaries are aligned along the SD, as shown in Figure 2a, which is  $\langle 101 \rangle$  of the lattice direction. A small fraction also aligns at the right angle, in short segments indicated with the black arrows, which is along the BD  $\parallel \langle 111 \rangle$ . The remainder, accounting for the largest fraction of straight boundaries, are aligned in the  $\pm 30\text{--}45^\circ$  angular range, with the highest frequency being around  $\pm 35^\circ$ . Some boundary combinations also resemble a leaf vein structure, with changing directions; one such example is circled in black at the right bottom of Figure 2a. Therefore, the overall alignment of the straight boundaries is rather complex, which Dinda et al. [55] (pp. 2152–2160) described as a function of the laser scanning strategy. In some recent studies, the boundaries appeared to have a coincidence with the crystallographic planes, most commonly along the  $\{100\}$  plane trace, e.g., SS316-, Ni-25% (Mo, Nb and Ti)-, Al-, Ta-, Ti-Mo-Zr-Al- and Mo-Si-alloys [48,49,55–60]. A few mechanisms for the formation of these textures have been outlined in the published literature based on the formation of the solid/liquid interface in order to explain their crystallographic origin. The scan rate and laser energy have been reported to play a vital role in this regard [61]. In this investigation, however, the alignment of the straight boundaries invariably remained identical within an angular range with the SD, irrespective of the matrix orientation, as shown in Figure 2a. For instance, the boundary orientations in the blue-, located in the upper left, and red-oriented regions comprise the same angular alignments with SD as the boundaries found in the vast majority green regions. This suggests that the low-angle straight boundaries are non-crystallographic, viz., they do not preferentially form on a particular lattice plane trace(s). Although this conclusion is made based on unequivocal evidence, it should be noted that only a 3D EBSD can reveal the real crystallography of a 3D interface. There is evidence that 2D trace analysis of 3D boundary features may lead to misleading conclusions. One such example is the low-angle microband boundaries that form in high stacking fault energy materials that have been claimed to be both crystallographic [62] and non-crystallographic [63]. This debate continued until reconciliation was achieved on the basis of a 3D EBSD investigation [64,65].

A recent article by Pham et al. [51] (p. 749) accounts for the variations in boundary formation in SLM-printed SS316, such as those seen in Figure 2a. The fundamental basis remains identical to the previous reports, viz., the boundaries form along the solid–liquid interface during the solidification process [48,66,67]. In Pham et al.'s simulation work, it was demonstrated that side branching occurs, similarly to the current findings shown in Figures 1 and 2, during the solidification process, and thus alters the shape of the solidifying boundary front. As a result, the alignment of the solidification interface changes, and therefore, the formation of low-angle boundaries takes place over a wider angular range. The magnitude of side branching depends on a number of factors, primarily on the thermal gradient and heat flux, and the SLM parameters that control these two. Each narrative in

the literature on low-angle crystallographic boundary formation, including Pham et al.'s study, is overwhelmed by the assumption that the solid/liquid interface appears as a crystallographic lattice interface. However, physical details on the mechanism by which the habit plane or rotation axis correlate with a preferred crystal plane or direction are missing. Therefore, the mechanism of low-angle boundary formation is rather complicated, because of the simultaneous occurrence of rapid solidification with the complex mechanical interaction of the semi-solid pool by laser beam movement. In addition, there is thermal pulsing during the subsequent overlay of layers.

Numerous investigations have reported columnar structures that also appear as fine cellular structures in the transverse cross-section of SLM-printed SS316 [40,68,69]. An example of such a cell structure is shown as an SEM image in the inset of Figure 3a. Unlike the low- and high-angle boundary structures in Figures 1 and 2, this structure was found homogeneously throughout the sample. These cellular structures have been reported to vary in size from 0.25 to 1.2  $\mu\text{m}$ , with the actual size having an inverse relationship with the laser scanning speed. [46,70,71]. It has been observed that these structures exhibit a weaker strengthening effect compared to the grain boundaries of the microstructure [71]. Because of the submicron-scale fineness of the cellular structures, an electron-transparent TEM sample was prepared using FIB-SEM site-specific lift-out methods. Figure 3a shows an HAADF STEM image of the TEM sample, in which the columnar structures are sub-vertical in the cross-sectional lamellae. The walls of the columns are densely populated with dislocations, and the walls are spaced parallel at an average distance of 500 nm. These boundaries were also decorated with 5–30 nm spherical particles. The particles were tangled within the boundary dislocations, see higher magnification image in Figure 3b, and created a pinning effect. These particles are likely to have restricted any thermally activated migration, and thus, restricted the structures to the nanoscale. The dislocation walls were 50–150 nm in thickness and are expected to have created a strain field, which became apparent through the diffraction contrast in the BF STEM imaging in Figure 3c, which was taken after tilting the sample so that the boundaries were edge-on. These dislocation features are expected to provide elevated strengthening in the SLM-printed SS316 material over the conventionally processed grade that usually comprises large equiaxed grains, hundreds of  $\mu\text{m}$  in size, and twin boundaries. This is reflected in a 20–50% improvement in the tensile strength of SLM-printed SS316 over the conventional grade with an identical chemical composition [40]. The strength can also be improved by changing the laser strategy that works at a larger length scale. While further discussions of mechanical properties are outside the scope of this paper, it is expected from the results presented herein that superior strengthening at the micro and nano scale can be achieved in SLM-printed grade due to the retention of nanostructures and the formation of inclusions due to the rapid cooling ( $\sim 10^3\text{--}10^5$  K/s) of SLM solidification [72].

The darker appearance of the particles in the HAADF STEM images in Figure 3 indicates that they had a lower average atomic weight than the matrix. In Figure 4, an area was selected that contained larger particles, and these were subjected to elemental analysis by STEM-EDS. Elemental maps revealed that the particles were rich in Mn, Si and O. Significant efforts were devoted to determining the crystallographic identity of the inclusions using SAD and CBED diffraction techniques, but no diffraction spots were observed other than those from the FCC iron matrix, and therefore, these particles are likely amorphous. This finding is consistent with the report by Salman et al. [69] (pp. 205–212). It is pertinent to note that Shibata et al. [73] (pp. 522–528) found larger particles,  $\sim 1$   $\mu\text{m}$ , with identical morphologies in cast SS316. These were characterized as MnO–SiO<sub>2</sub> particles, solely based on the chemical ratio measured by electron probe microanalysis and thermodynamic calculations. In some cases, they also found a small association of Cr<sub>2</sub>O<sub>3</sub>. In regard to the current study, it is important to note that Cr was not measured within the particles, and no Cr–C crystalline diffraction patterns were observed. Therefore, Cr is expected to remain in the solid solution to provide the intended stainless property in the SLM-printed SS316.

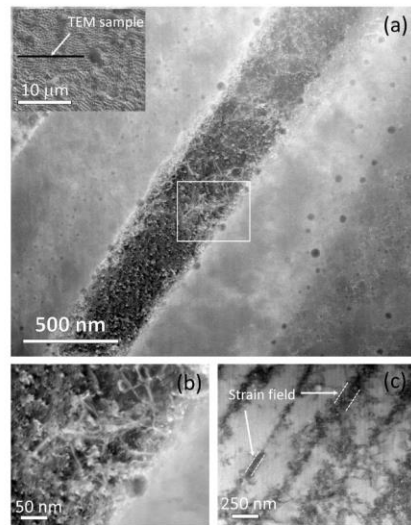


**Figure 3.** HAADF STEM images showing (a) particle decorations in the dislocation-constituted boundaries of the commonly found fine cell structures (in the inset) in the SLM-printed sample. (b) Particle pinning at the dislocation boundary in a higher-magnification HAADF STEM image of the white rectangular area located in subfigure (a). (c) BF STEM image showing the strain field width of the dislocation boundaries at the boundaries edge on tilted condition.

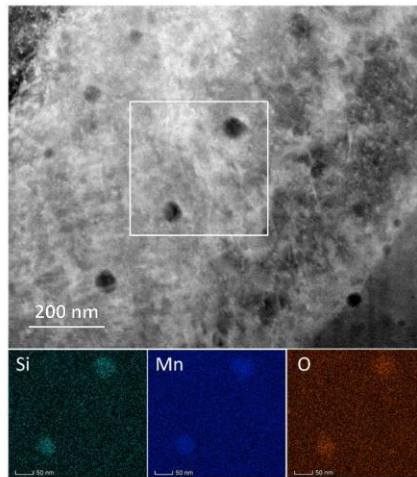


**Figure 4.** HAADF STEM image (top) of the nanoparticles and corresponding EDS-measured elemental maps (bottom) of the white rectangular area, showing that the particles are rich in Si, Mn and O content in the as-printed SLM sample.

### 3.3. Solution Treatment Structures

A solution treatment at 1050 °C for 4 h, per ASM [74] recommendations, of the as-printed sample is expected to anneal any thermally unstable microstructures, and to ensure a uniform Cr dissolution into the matrix. It is pertinent to note that the stainless properties are impaired in conventional-grade SS316 because of the inadequate presence of atomic Cr in the solution that occurs due to Cr-C formation. The solution treatment brings the Cr atoms back to the matrix as solutes. Cr-containing inclusions were not observed in the samples in this study, see Figures 3 and 4, which suggests that the solution treatment is not needed for Cr dissolution purposes in the SLM material. However, the heterogeneous boundary structures shown in Figure 2 may result in an uneven Cr distribution, because dislocations are naturally preferable sites for solute atoms. Therefore, the solution treatment may indeed promote an even Cr concentration.

Interestingly, only a subtle change took place in the substructures during the 1050 °C solution treatment. Figure 5a,b present a comparative view in the form of KAM maps that reveal an overall reduction in the KAM-intensive boundary density after the solution treatment. The solution-treated structure is also shown in the BF STEM micrograph in Figure 5c, in which the dislocation-constituted boundaries underwent a thermal relaxation process, compared with Figure 3, viz., the boundaries were curved and the dislocations were dissociated. The rectangular area in Figure 5c is magnified in the HAADF STEM image in Figure 5d. Analysis revealed boundary pinning by the inclusions that were found in the as-printed sample in Figures 3 and 4. They were measured to contain Mn, Si and O as per the as-printed sample. Overall, the inclusion density was significantly reduced by the solution treatment, perhaps because of some degree of dissolution and/or agglomeration. The high stability of the inclusions after the solution treatment at 1050 °C explains why recrystallization and grain growth did not take place in the SLM-printed material. Previously, Shibata et al. [73] (pp. 522–528) reported that amorphous Mn-Si-O particles remain stable even after 1200 °C solution treatment in cast SS316, where grain growth was not prevented because the density was low and the inclusions size was large, >1 µm.

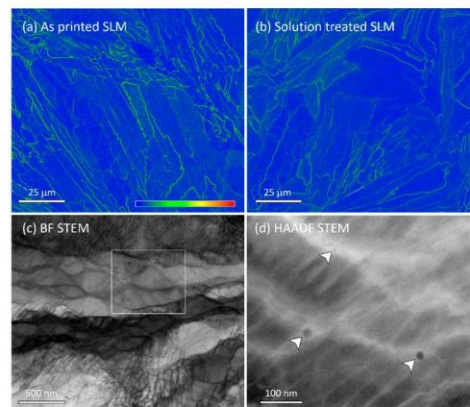


**Figure 5.** EBSD-measured high-resolution KAM map showing the differences in the stored energy distributions between the (a) as-printed and (b) solution-treated SLM samples in the BD-SD cross-section. TEM investigation of the solution-treated sample shows (c) the changes in the dislocation boundary structures in a BF STEM image and (d) the retention of boundaries by particle (arrowed) pinning in a magnified HAADF STEM image of the rectangular area marked in subfigure (c).



It is important to note that inclusions 2–4  $\mu\text{m}$  in size were also observed in the solution-treated sample that were absent under as-printed conditions. An example is shown in the upper inset in Figure 6a, whereby a TEM lamella was prepared by FIB and presented as a STEM HAADF image (Figure 6a) in order to determine the chemical distribution within the inclusion. The surrounding iron matrix appears brighter. It should be noted that it was identified via TEM-EDS that the inclusions were rich in Mn, Si, and O, although there were also Cr- and O-rich regions within the inclusions, which can also be seen as brighter regions, as indicated by arrows, in the darker overall matrix. An SAD pattern was taken of the marked area and indexed as  $\text{Cr}_3\text{O}_4$ , as illustrated in the lower inset of Figure 6a. The iron matrix also contained Cr, which was expected as the solute. These findings suggest that during the solution treatment, a large fraction of the nano-sized inclusions agglomerate into large 2–4  $\mu\text{m}$  inclusions. The Cr from the solid solution also diffused and participated in the formation of inclusions, since Cr was not found in the inclusions in the as-printed sample. Overall, the localized corrosion resistance of the as-printed SLM-manufactured SS316 is excellent, which can be attributed to factors such as the absence of sulphides, the presence of a more stable passive film, lower rates of metastable pitting, and a higher pitting potential compared to its wrought counterpart [75–77]. However, the presence of these large inclusions with heterogeneous chemical and structural distribution after heat treatment, as reported in this work, has been shown to be detrimental to the alloy's resistance to localized corrosion by decreasing its pitting potential [78]. Therefore, the solution treatment recommended by ASM [74] for conventional SS316 is, indeed, expected to be detrimental to the SLM-printed material.

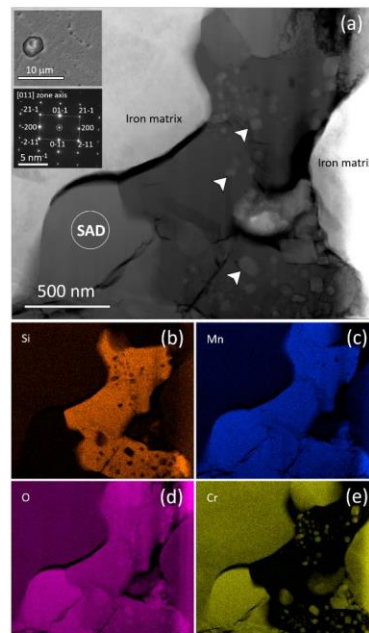


**Figure 6.** The structural and chemical heterogeneity of inclusions in the solution-treated SLM-printed sample is shown in (a) the HAADF STEM image, and (b–e) the corresponding elemental mapping for Si, Mn, O, and Cr, respectively. The insets in (a) show the inclusion from which the TEM sample was prepared, and the indexed SAD pattern of  $\text{Cr}_3\text{O}_4$  from the SAD-labeled area.

SLM-manufactured SS316 components have shown excellent mechanical properties [40,79,80] and localized corrosion resistance [75–77], often surpassing their conventionally manufactured wrought counterparts. Therefore, it is crucial to evaluate their performance against common damage mechanisms observed in the energy sector, such as stress corrosion cracking (SCC) or hydrogen-induced cracking (HIC), in both as-printed and heat-treated microstructures. Additionally, exploring the optimization of properties through variations in printing parameters or the utilization of post-processing steps would be of great significance.

#### 4. Conclusions

In this investigation, a thorough microscopic characterization of SLM SS316s/s under as-printed and solution-annealed conditions was conducted at the macro, micro and nano scales. The findings suggest some of the existing findings are inconclusive or imprecise, and require further investigation to mature our knowledge in this area. The conclusions of this study can be summarized as follows:

1. SLM-printed material possesses an asymmetric crystallographic texture and material structure. The microstructure has a distinctive structural morphology along the orthogonal axes of the sample, and develops crystallographic textures in  $SD \parallel \langle 101 \rangle$  and  $BD \parallel \langle 111 \rangle$ .
2. Heterogeneous distributions of misorientation boundaries and stored energy were found throughout the SLM-printed structures. Twin boundary formation was not observed in either the as-printed or solution-annealed samples.
3. In the as-printed structures, the typical straight misorientation boundaries were characterized as being non-crystallographic. The boundaries maintained general alignment with the SD within an angular range, irrespective of the matrix's crystal orientation, although there were occasional coincidences with crystal plane traces.
4. The high-angle boundaries in the SLM substructures underwent thermal restoration, which was activated by the heat originating from the printing of the subsequent layer. Pinning by the nano inclusions hindered classical recrystallization, and thus, prevented the formation of a defect-free annealing structure, even after 4 h of solution treatment at 1050 °C.
5. A nano-scale lamellar structure with a width of  $500 \pm 200$  nm formed homogeneously throughout the printed material. Depending on the orientation, the structures appeared with cellular or columnar morphologies in SEM and TEM images. Their boundaries contained dense dislocation structures tangled with fine amorphous inclusions containing Mn, Si and O. Cr was not found above the limit of detection in the inclusions. Hence, Cr remains in the matrix to provide the stainless properties.
6. Some degree of dissociation of the dislocation boundaries occurred during the solution treatment, but the overall refined structures were retained. Additionally, inclusions with a size of 2–4  $\mu\text{m}$  formed, consisting of composite structures and chemical distributions. These inclusions can have detrimental effects on the localized corrosion resistance of the alloy.

**Author Contributions:** Conceptualization, R.S., M.Z.Q., M.S., W.D.A.R., K.P. and S.M.R.; methodology, M.Z.Q., M.S., W.D.A.R., K.P. and M.I.; validation, M.Z.Q., W.D.A.R. and S.M.R.; formal analysis, R.S., M.S. and M.Z.Q.; investigation, R.S. and M.Z.Q.; resources, M.Z.Q.; data curation, R.S. and M.Z.Q.; writing—original draft preparation, R.S. and M.Z.Q.; writing—review and editing, M.S., G.L., M.I. and S.M.R.; visualization, R.S., W.D.A.R. and M.Z.Q.; supervision, M.Z.Q. All authors have read and agreed to the published version of the manuscript.

**Funding:** This research received no external funding.

**Institutional Review Board Statement:** Not applicable.

**Informed Consent Statement:** Not applicable.

**Data Availability Statement:** This article contains all the data that was generated and is presented in the form of Figures.

**Acknowledgments:** The advanced characterization facility at Curtin’s centralized research infrastructure hub, John de Laeter Centre (JdLC) is acknowledged for providing access to SEM, EBSD, TEM, FIB and sample preparation tools.

**Conflicts of Interest:** The authors declare no conflict of interest.

## References

- Meiners, W.; Wissenbach, K.; Gasser, A. Shaped Body Especially Prototype or Replacement Part Production. DE Patent DE19649865C1, 12 February 1998.
- DebRoy, T.; Wei, H.L.; Zuback, J.S.; Mukherjee, T.; Elmer, J.W.; Milewski, J.O.; Beese, A.M.; Wilson-Heid, A.; De, A.; Zhang, W. Additive manufacturing of metallic components—Process, structure and properties. *Prog. Mater. Sci.* **2018**, *92*, 112–224. [\[CrossRef\]](#)
- Harun, W.; Kamariah, M.; Muhamad, N.; Ghani, S.; Ahmad, F.; Mohamed, Z. A review of powder additive manufacturing processes for metallic biomaterials. *Powder Technol.* **2018**, *327*, 128–151. [\[CrossRef\]](#)
- Song, B.; Dong, S.; Deng, S.; Liao, H.; Coddet, C. Microstructure and tensile properties of iron parts fabricated by selective laser melting. *Opt. Laser Technol.* **2014**, *56*, 451–460. [\[CrossRef\]](#)
- Olakanmi, E.O.; Cochrane, R.F.; Dalgarno, K.W. A review on selective laser sintering/melting (SLS/SLM) of aluminium alloy powders: Processing, microstructure, and properties. *Prog. Mater. Sci.* **2015**, *74*, 401–477. [\[CrossRef\]](#)
- Liu, Z.; Zhang, D.; Sing, S.; Chua, C.; Loh, L. Interfacial characterization of SLM parts in multi-material processing: Metallurgical diffusion between 316L stainless steel and C18400 copper alloy. *Mater. Charact.* **2014**, *94*, 116–125. [\[CrossRef\]](#)
- Shi, R.; Khairallah, S.A.; Roehling, T.T.; Heo, T.W.; McKeown, J.T.; Matthews, M.J. Microstructural control in metal laser powder bed fusion additive manufacturing using laser beam shaping strategy. *Acta Mater.* **2020**, *184*, 284–305. [\[CrossRef\]](#)
- Mower, T.M.; Long, M.J. Mechanical behavior of additive manufactured, powder-bed laser-fused materials. *Mater. Sci. Eng. A* **2016**, *651*, 198–213. [\[CrossRef\]](#)
- Maconachie, T.; Leary, M.; Lozanovski, B.; Zhang, X.; Qian, M.; Faruque, O.; Brandt, M. SLM lattice structures: Properties, performance, applications and challenges. *Mater. Des.* **2019**, *183*, 108137. [\[CrossRef\]](#)
- Maskery, I.; Aremu, A.; Simonelli, M.; Tuck, C.; Wildman, R.; Ashcroft, I.; Hague, R. Mechanical properties of Ti-6Al-4V selectively laser melted parts with body-centred-cubic lattices of varying cell size. *Exp. Mech.* **2015**, *55*, 1261–1272. [\[CrossRef\]](#)
- Maskery, I.; Aboulkhair, N.; Aremu, A.; Tuck, C.; Ashcroft, I.; Wildman, R.D.; Hague, R. A mechanical property evaluation of graded density Al-Si10-Mg lattice structures manufactured by selective laser melting. *Mater. Sci. Eng. A* **2016**, *670*, 264–274. [\[CrossRef\]](#)
- Hamilton, R.F.; Bimber, B.A.; Andani, M.T.; Elahinia, M. Multi-scale shape memory effect recovery in NiTi alloys additive manufactured by selective laser melting and laser directed energy deposition. *J. Mater. Process. Technol.* **2017**, *250*, 55–64. [\[CrossRef\]](#)
- Visser, C.W.; Pohl, R.; Sun, C.; Römer, G.W.; Huis in ‘t Veld, B.; Lohse, D. Toward 3D printing of pure metals by laser-induced forward transfer. *Adv. Mater.* **2015**, *27*, 4087–4092. [\[CrossRef\]](#) [\[PubMed\]](#)
- Li, Y.; Gu, D. Parametric analysis of thermal behavior during selective laser melting additive manufacturing of aluminum alloy powder. *Mater. Des.* **2014**, *63*, 856–867. [\[CrossRef\]](#)
- Averyanova, M.; Cicala, E.; Bertrand, P.; Grevey, D. Experimental design approach to optimize selective laser melting of martensitic 17-4 PH powder: Part I—single laser tracks and first layer. *Rapid Prototyp. J.* **2012**, *18*, 28–37. [\[CrossRef\]](#)
- Lott, P.; Schleifenbaum, H.; Meiners, W.; Wissenbach, K.; Hinke, C.; Bültmann, J. Design of an optical system for the in situ process monitoring of selective laser melting (SLM). *Phys. Procedia* **2011**, *12*, 683–690. [\[CrossRef\]](#)
- Brecher, C. *Advances in Production Technology*; Springer Nature: Berlin, Germany, 2015.
- Aboulkhair, N.T.; Simonelli, M.; Parry, L.; Ashcroft, I.; Tuck, C.; Hague, R. 3D printing of Aluminium alloys: Additive Manufacturing of Aluminium alloys using selective laser melting. *Prog. Mater. Sci.* **2019**, *106*, 100578. [\[CrossRef\]](#)
- Aboulkhair, N.T.; Everitt, N.M.; Ashcroft, I.; Tuck, C. Reducing porosity in AlSi10Mg parts processed by selective laser melting. *Addit. Manuf.* **2014**, *1*, 77–86. [\[CrossRef\]](#)
- Langelaar, M. Topology optimization of 3D self-supporting structures for additive manufacturing. *Addit. Manuf.* **2016**, *12*, 60–70. [\[CrossRef\]](#)
- Read, N.; Wang, W.; Essa, K.; Attallah, M.M. Selective laser melting of AlSi10Mg alloy: Process optimisation and mechanical properties development. *Mater. Des.* **2015**, *65*, 417–424. [\[CrossRef\]](#)
- Aboulkhair, N.T.; Everitt, N.M.; Maskery, I.; Ashcroft, I.; Tuck, C. Selective laser melting of aluminum alloys. *MRS Bull.* **2017**, *42*, 311–319. [\[CrossRef\]](#)
- Simonelli, M.; Tse, Y.Y.; Tuck, C. Effect of the build orientation on the mechanical properties and fracture modes of SLM Ti-6Al-4V. *Mater. Sci. Eng. A* **2014**, *616*, 1–11. [\[CrossRef\]](#)
- Simonelli, M.; Tse, Y.Y.; Tuck, C. On the texture formation of selective laser melted Ti-6Al-4V. *Metall. Mater. Trans. A* **2014**, *45*, 2863–2872. [\[CrossRef\]](#)

25. Kamath, C.; El-Dasher, B.; Gallegos, G.F.; King, W.E.; Sisto, A. Density of additively-manufactured, 316L SS parts using laser powder-bed fusion at powers up to 400 W. *Int. J. Adv. Manuf. Technol.* **2014**, *74*, 65–78. [[CrossRef](#)]
26. Garibaldi, M.; Ashcroft, I.; Lemke, J.; Simonelli, M.; Hague, R. Effect of annealing on the microstructure and magnetic properties of soft magnetic Fe-Si produced via laser additive manufacturing. *Scr. Mater.* **2018**, *142*, 121–125. [[CrossRef](#)]
27. Garibaldi, M.; Ashcroft, I.; Simonelli, M.; Hague, R. Metallurgy of high-silicon steel parts produced using Selective Laser Melting. *Acta Mater.* **2016**, *110*, 207–216. [[CrossRef](#)]
28. Lemke, J.; Simonelli, M.; Garibaldi, M.; Ashcroft, I.; Hague, R.; Vedani, M.; Wildman, R.; Tuck, C. Calorimetric study and microstructure analysis of the order-disorder phase transformation in silicon steel built by SLM. *J. Alloys Compd.* **2017**, *722*, 293–301. [[CrossRef](#)]
29. Catchpole-Smith, S.; Aboulkhair, N.; Parry, L.; Tuck, C.; Ashcroft, I.A.; Clare, A. Fractal scan strategies for selective laser melting of 'unweldable' nickel superalloys. *Addit. Manuf.* **2017**, *15*, 113–122. [[CrossRef](#)]
30. Choi, J.-P.; Shin, G.-H.; Yang, S.; Yang, D.-Y.; Lee, J.-S.; Brochu, M.; Yu, J.-H. Densification and microstructural investigation of Inconel 718 parts fabricated by selective laser melting. *Powder Technol.* **2017**, *310*, 60–66. [[CrossRef](#)]
31. Marchese, G.; Garmendia Colera, X.; Calignano, F.; Lorusso, M.; Biamino, S.; Minetola, P.; Manfredi, D. Characterization and comparison of Inconel 625 processed by selective laser melting and laser metal deposition. *Adv. Eng. Mater.* **2017**, *19*, 1600635. [[CrossRef](#)]
32. Carter, L.N.; Martin, C.; Withers, P.J.; Attallah, M.M. The influence of the laser scan strategy on grain structure and cracking behaviour in SLM powder-bed fabricated nickel superalloy. *J. Alloys Compd.* **2014**, *615*, 338–347. [[CrossRef](#)]
33. Ciurana, J.; Hernandez, L.; Delgado, J. Energy density analysis on single tracks formed by selective laser melting with CoCrMo powder material. *Int. J. Adv. Manuf. Technol.* **2013**, *68*, 1103–1110. [[CrossRef](#)]
34. Pupo, Y.; Delgado, J.; Serenó, L.; Ciurana, J. Scanning space analysis in selective laser melting for CoCrMo powder. *Procedia Eng.* **2013**, *63*, 370–378. [[CrossRef](#)]
35. Monroy, K.; Delgado, J.; Ciurana, J. Study of the pore formation on CoCrMo alloys by selective laser melting manufacturing process. *Procedia Eng.* **2013**, *63*, 361–369. [[CrossRef](#)]
36. Takaichi, A.; Nakamoto, T.; Joko, N.; Nomura, N.; Tsutsumi, Y.; Migita, S.; Doi, H.; Kurosu, S.; Chiba, A.; Wakabayashi, N. Microstructures and mechanical properties of Co–29Cr–6Mo alloy fabricated by selective laser melting process for dental applications. *J. Mech. Behav. Biomed. Mater.* **2013**, *21*, 67–76. [[CrossRef](#)] [[PubMed](#)]
37. Yadroitsev, I.; Gusarov, A.; Yadroitsava, I.; Smurov, I. Single track formation in selective laser melting of metal powders. *J. Mater. Process. Technol.* **2010**, *210*, 1624–1631. [[CrossRef](#)]
38. Zhang, B.; Liao, H.; Coddet, C. Effects of processing parameters on properties of selective laser melting Mg–9% Al powder mixture. *Mater. Des.* **2012**, *34*, 753–758. [[CrossRef](#)]
39. Galy, C.; Le Guen, E.; Lacoste, E.; Arvieu, C. Main defects observed in aluminum alloy parts produced by SLM: From causes to consequences. *Addit. Manuf.* **2018**, *22*, 165–175. [[CrossRef](#)]
40. Suryawanshi, J.; Prashanth, K.G.; Ramamurthy, U. Mechanical behavior of selective laser melted 316L stainless steel. *Mater. Sci. Eng. A* **2017**, *696*, 113–121. [[CrossRef](#)]
41. Michiuchi, M.; Kokawa, H.; Wang, Z.; Sato, Y.; Sakai, K. Twin-induced grain boundary engineering for 316 austenitic stainless steel. *Acta Mater.* **2006**, *54*, 5179–5184. [[CrossRef](#)]
42. Godec, M.; Zaefferer, S.; Podgornik, B.; Sinko, M.; Tchernychova, E. Quantitative multiscale correlative microstructure analysis of additive manufacturing of stainless steel 316L processed by selective laser melting. *Mater. Charact.* **2020**, *160*, 110074. [[CrossRef](#)]
43. Mahata, A.; Zaeem, M.A. Evolution of solidification defects in deformation of nano-polycrystalline aluminum. *Comput. Mater. Sci.* **2019**, *163*, 176–185. [[CrossRef](#)]
44. Shen, J.; Gonçalves, R.; Choi, Y.T.; Lopes, J.G.; Yang, J.; Schell, N.; Kim, H.S.; Oliveira, J.P. Microstructure and mechanical properties of gas metal arc welded CoCrFeMnNi joints using a 308 stainless steel filler metal. *Scr. Mater.* **2023**, *222*, 115053. [[CrossRef](#)]
45. Ma, M.; Wang, Z.; Zeng, X. A comparison on metallurgical behaviors of 316L stainless steel by selective laser melting and laser cladding deposition. *Mater. Sci. Eng. A* **2017**, *685*, 265–273. [[CrossRef](#)]
46. Diaz Vallejo, N.; Lucas, C.; Ayers, N.; Graydon, K.; Hyer, H.; Sohn, Y. Process Optimization and Microstructure Analysis to Understand Laser Powder Bed Fusion of 316L Stainless Steel. *Metals* **2021**, *11*, 832. [[CrossRef](#)]
47. Tsutsumi, Y.; Ishimoto, T.; Oishi, T.; Manaka, T.; Chen, P.; Ashida, M.; Doi, K.; Katayama, H.; Hanawa, T.; Nakano, T. Crystallographic texture- and grain boundary density-independent improvement of corrosion resistance in austenitic 316L stainless steel fabricated via laser powder bed fusion. *Addit. Manuf.* **2021**, *45*, 102066. [[CrossRef](#)]
48. Sun, S.-H.; Ishimoto, T.; Hagihara, K.; Tsutsumi, Y.; Hanawa, T.; Nakano, T. Excellent mechanical and corrosion properties of austenitic stainless steel with a unique crystallographic lamellar microstructure via selective laser melting. *Scr. Mater.* **2019**, *159*, 89–93. [[CrossRef](#)]
49. Sun, S.-H.; Hagihara, K.; Nakano, T. Effect of scanning strategy on texture formation in Ni-25 at.% Mo alloys fabricated by selective laser melting. *Mater. Des.* **2018**, *140*, 307–316. [[CrossRef](#)]
50. Thijs, L.; Sistiaga, M.L.M.; Wauthele, R.; Xie, Q.; Kruth, J.-P.; Van Humbeeck, J. Strong morphological and crystallographic texture and resulting yield strength anisotropy in selective laser melted tantalum. *Acta Mater.* **2013**, *61*, 4657–4668. [[CrossRef](#)]

51. Pham, M.-S.; Dovggy, B.; Hooper, P.A.; Gourlay, C.M.; Piglione, A. The role of side-branching in microstructure development in laser powder-bed fusion. *Nat. Commun.* **2020**, *11*, 749. [[CrossRef](#)]
52. Humphreys, F.; Hatherly, M. Chapter 12-recrystallization textures. In *Recrystallization and Related Annealing Phenomena*, 2nd ed.; Elsevier: Oxford, UK, 2004; p. 379e413.
53. Prashanth, K.; Shahabi, H.S.; Attar, H.; Srivastava, V.; Ellendt, N.; Uhlenwinkel, V.; Eckert, J.; Scudino, S. Production of high strength Al85Nd8Ni5Co2 alloy by selective laser melting. *Addit. Manuf.* **2015**, *6*, 1–5. [[CrossRef](#)]
54. Qi, T.; Zhu, H.; Zhang, H.; Yin, J.; Ke, L.; Zeng, X. Selective laser melting of Al7050 powder: Melting mode transition and comparison of the characteristics between the keyhole and conduction mode. *Mater. Des.* **2017**, *135*, 257–266. [[CrossRef](#)]
55. Dinda, G.; Dasgupta, A.; Mazumder, J. Evolution of microstructure in laser deposited Al–11.28% Si alloy. *Surf. Coat. Technol.* **2012**, *206*, 2152–2160. [[CrossRef](#)]
56. Wei, H.; Mazumder, J.; DebRoy, T. Evolution of solidification texture during additive manufacturing. *Sci. Rep.* **2015**, *5*, 16446. [[CrossRef](#)] [[PubMed](#)]
57. Bhattacharya, S.; Dinda, G.P.; Dasgupta, A.K.; Mazumder, J. A comparative study of microstructure and mechanical behavior of CO<sub>2</sub> and diode laser deposited Cu–38Ni alloy. *J. Mater. Sci.* **2014**, *49*, 2415–2429. [[CrossRef](#)]
58. Parimi, L.L.; Ravi, G.; Clark, D.; Attallah, M.M. Microstructural and texture development in direct laser fabricated IN718. *Mater. Charact.* **2014**, *89*, 102–111. [[CrossRef](#)]
59. Yadollahi, A.; Shamsaei, N.; Thompson, S.M.; Seely, D.W. Effects of process time interval and heat treatment on the mechanical and microstructural properties of direct laser deposited 316L stainless steel. *Mater. Sci. Eng. A* **2015**, *644*, 171–183. [[CrossRef](#)]
60. Dinda, G.; Dasgupta, A.; Bhattacharya, S.; Natu, H.; Dutta, B.; Mazumder, J. Microstructural characterization of laser-deposited Al 4047 alloy. *Metall. Mater. Trans. A* **2013**, *44*, 2233–2242. [[CrossRef](#)]
61. Ishimoto, T.; Hagihara, K.; Hisamoto, K.; Sun, S.-H.; Nakano, T. Crystallographic texture control of beta-type Ti–15Mo–5Zr–3Al alloy by selective laser melting for the development of novel implants with a biocompatible low Young’s modulus. *Scr. Mater.* **2017**, *132*, 34–38. [[CrossRef](#)]
62. Winther, G.; Jensen, D.J.; Hansen, N. Dense dislocation walls and microbands aligned with slip planes—Theoretical considerations. *Acta Mater.* **1997**, *45*, 5059–5068. [[CrossRef](#)]
63. Hurley, P.; Bate, P.; Humphreys, F. An objective study of substructural boundary alignment in aluminium. *Acta Mater.* **2003**, *51*, 4737–4750. [[CrossRef](#)]
64. Afrin, N.; Quadir, M.Z.; Xu, W.; Ferry, M. Spatial orientations and structural irregularities associated with the formation of microbands in a cold deformed Goss oriented Ni single crystal. *Acta Mater.* **2012**, *60*, 6288–6300. [[CrossRef](#)]
65. Afrin, N.; Quadir, M.Z.; Bassman, L.; Driver, J.; Albou, A.; Ferry, M. The three-dimensional nature of microbands in a channel die compressed Goss-oriented Ni single crystal. *Scr. Mater.* **2011**, *64*, 221–224. [[CrossRef](#)]
66. Wei, H.; Elmer, J.; DebRoy, T. Origin of grain orientation during solidification of an aluminum alloy. *Acta Mater.* **2016**, *115*, 123–131. [[CrossRef](#)]
67. Wang, Y.; Shi, J. Developing very strong texture in a nickel-based superalloy by selective laser melting with an ultra-high power and flat-top laser beam. *Mater. Charact.* **2020**, *165*, 110372. [[CrossRef](#)]
68. Wang, Y.M.; Voisin, T.; McKeown, J.T.; Ye, J.; Caltà, N.P.; Li, Z.; Zeng, Z.; Zhang, Y.; Chen, W.; Roehling, T.T. Additively manufactured hierarchical stainless steels with high strength and ductility. *Nat. Mater.* **2018**, *17*, 63–71. [[CrossRef](#)] [[PubMed](#)]
69. Salman, O.; Gammer, C.; Chaubey, A.; Eckert, J.; Scudino, S. Effect of heat treatment on microstructure and mechanical properties of 316L steel synthesized by selective laser melting. *Mater. Sci. Eng. A* **2019**, *748*, 205–212. [[CrossRef](#)]
70. Gao, S.; Hu, Z.; Duchamp, M.; Krishnan, P.S.R.; Tekumalla, S.; Song, X.; Seita, M. Recrystallization-based grain boundary engineering of 316L stainless steel produced via selective laser melting. *Acta Mater.* **2020**, *200*, 366–377. [[CrossRef](#)]
71. Kong, D.; Dong, C.; Ni, X.; Zhang, L.; Li, X. Cellular size dependence on the strength of additively manufactured austenitic stainless steel. *Mater. Lett.* **2020**, *279*, 128524. [[CrossRef](#)]
72. Huang, C.; Yan, X.; Zhao, L.; Liu, M.; Ma, W.; Wang, W.; Soete, J.; Simar, A. Ductilization of selective laser melted Ti6Al4V alloy by friction stir processing. *Mater. Sci. Eng. A* **2019**, *755*, 85–96. [[CrossRef](#)]
73. Shibata, H.; Tanaka, T.; Kimura, K.; Kitamura, S.-Y. Composition change in oxide inclusions of stainless steel by heat treatment. *Ironmak. Steelmak.* **2010**, *37*, 522–528. [[CrossRef](#)]
74. Dossett, J.; Totten, G. Heat Treating of Austenitic and Duplex Stainless Steels. In *Heat Treating of Irons and Steels*; ASM International: Cleveland, OH, USA, 2014. [[CrossRef](#)]
75. Man, C.; Dong, C.; Liu, T.; Kong, D.; Wang, D.; Li, X. The enhancement of microstructure on the passive and pitting behaviors of selective laser melting 316L SS in simulated body fluid. *Appl. Surf. Sci.* **2019**, *467–468*, 193–205. [[CrossRef](#)]
76. Shaeri Karimi, M.H.; Yeganeh, M.; Alavi Zaree, S.R.; Eskandari, M. Corrosion behavior of 316L stainless steel manufactured by laser powder bed fusion (L-PBF) in an alkaline solution. *Opt. Laser Technol.* **2021**, *138*, 106918. [[CrossRef](#)]
77. Sander, G.; Thomas, S.; Cruz, V.; Jurg, M.; Birbilis, N.; Gao, X.; Brameld, M.; Hutchinson, C.R. On The Corrosion and Metastable Pitting Characteristics of 316L Stainless Steel Produced by Selective Laser Melting. *J. Electrochem. Soc.* **2017**, *164*, C250–C257. [[CrossRef](#)]
78. Wang, K.; Chao, Q.; Annasamy, M.; Hodgson, P.D.; Thomas, S.; Birbilis, N.; Fabijanic, D. On the pitting behaviour of laser powder bed fusion prepared 316L stainless steel upon post-processing heat treatments. *Corros. Sci.* **2022**, *197*, 110060. [[CrossRef](#)]

79. Kurzynowski, T.; Gruber, K.; Stopyra, W.; Kuźnicka, B.; Chlebus, E. Correlation between process parameters, microstructure and properties of 316 L stainless steel processed by selective laser melting. *Mater. Sci. Eng. A* **2018**, *718*, 64–73. [[CrossRef](#)]
80. Chao, Q.; Thomas, S.; Birbilis, N.; Cizek, P.; Hodgson, P.D.; Fabijanic, D. The effect of post-processing heat treatment on the microstructure, residual stress and mechanical properties of selective laser melted 316L stainless steel. *Mater. Sci. Eng. A* **2021**, *821*, 141611. [[CrossRef](#)]

**Disclaimer/Publisher's Note:** The statements, opinions and data contained in all publications are solely those of the individual author(s) and contributor(s) and not of MDPI and/or the editor(s). MDPI and/or the editor(s) disclaim responsibility for any injury to people or property resulting from any ideas, methods, instructions or products referred to in the content.

**Appendix 5: Original reprint of the publication included in  
Chapter 4**

Article

# Stress Corrosion Cracking of 316L Stainless Steel Additively Manufactured with Sinter-Based Material Extrusion

Ricardo Santamaria <sup>1</sup>, Ke Wang <sup>1</sup>, Mobin Salasi <sup>1</sup>, Mariano Iannuzzi <sup>1,†</sup>, Michael Y. Mendoza <sup>2</sup> and Md Zakaria Quadir <sup>1,3,\*</sup>

<sup>1</sup> Curtin Corrosion Centre, Curtin University, Perth, WA 6102, Australia; ricardo.santamar@postgrad.curtin.edu.au (R.S.); ke.wang2@curtin.edu.au (K.W.); mobin.salasi@curtin.edu.au (M.S.); mariano.iannuzzi@curtin.edu.au (M.I.)

<sup>2</sup> Institute of Naval and Maritime Science, Universidad Austral de Chile, Valdivia 5090000, Los Rios, Chile; michael.mendoza@uach.cl

<sup>3</sup> John de Laeter Centre, Curtin University, Perth, WA 6845, Australia

\* Correspondence: zakaria.quadir@curtin.edu.au

† Current address: Alcoa Corporation, P.O. Box 252, Applecross, WA 6953, Australia.

**Abstract:** This study investigates the stress corrosion cracking (SCC) behavior of type 316L stainless steel (SS316L) produced with sinter-based material extrusion additive manufacturing (AM). Sinter-based material extrusion AM produces SS316L with microstructures and mechanical properties comparable to its wrought counterpart in the annealed condition. However, despite extensive research on SCC of SS316L, little is known about the SCC of sinter-based AM SS316L. This study focuses on the influence of sintered microstructures on SCC initiation and crack-branching susceptibility. Custom-made C-rings were exposed to different stress levels in acidic chloride solutions at various temperatures. Solution-annealed (SA) and cold-drawn (CD) wrought SS316L were also tested to understand the SCC behavior of SS316L better. Results showed that sinter-based AM SS316L was more susceptible to SCC initiation than SA wrought SS316L but more resistant than CD wrought SS316L, as determined by the crack initiation time. Sinter-based AM SS316L showed a noticeably lower tendency for crack-branching than both wrought SS316L counterparts. The investigation was supported by comprehensive pre- and post-test microanalysis using light optical microscopy, scanning electron microscopy, electron backscatter diffraction, and micro-computed tomography.

**Keywords:** chloride stress corrosion cracking (CSCC); crack-branching; C-ring specimen; porosity; residual stresses; transgranular cracking



**Citation:** Santamaria, R.; Wang, K.; Salasi, M.; Iannuzzi, M.; Mendoza, M.Y.; Quadir, M.Z. Stress Corrosion Cracking of 316L Stainless Steel Additively Manufactured with Sinter-Based Material Extrusion. *Materials* **2023**, *16*, 4006. <https://doi.org/10.3390/ma16114006>

Academic Editor: Rainer J. Hebert

Received: 3 May 2023

Revised: 22 May 2023

Accepted: 24 May 2023

Published: 26 May 2023



**Copyright:** © 2023 by the authors. Licensee MDPI, Basel, Switzerland. This article is an open access article distributed under the terms and conditions of the Creative Commons Attribution (CC BY) license (<https://creativecommons.org/licenses/by/4.0/>).

## 1. Introduction

Additive manufacturing (AM) encompasses the technologies used to create physical objects from digital data by successively joining materials [1]. Sinter-based material extrusion, one of the AM technologies categorized by the International Organization for Standardization (ISO) [2], is gaining popularity due to its ease of use, low running and maintenance costs, and reduced safety risks [3,4]. Sintered-based AM involves a multi-step approach that incorporates the principles of fused filament fabrication (FFF), also known as fused deposition modelling (FDM), powder metallurgy (PM), and metal injection molding (MIM). The process starts by heating the pre-alloyed powder-bound feedstock to the binder's melting point, and then extruding it through a nozzle to fabricate the so-called "green part". In the subsequent step, the primary binder is removed through full immersion in a solvent bath that leaves a component consisting of powder held by the secondary binder. This so-called "brown part" is still incomplete in terms of engineering properties. Therefore, in the final step, the component is strengthened by heating it just below the alloy's melting point, allowing the metal particles to sinter and create a structure that requires minimal post-processing or machining. The resulting sintered microstructure has



been reported to have a weak crystallographic texture, relatively large equiaxed grains, and populated with twin boundaries, pores, and oxide inclusions [5–9]. These characteristics diverge from the typical columnar grains found in other AM technologies where the heat follows the dissipation route, such as laser-engineered net shaping (LENS) [10,11], electron beam additive manufacturing (EBAM) [12,13], and laser-based powder bed fusion (LPBF) [14,15].

Stress corrosion cracking (SCC) is a form of environmentally-assisted cracking (EAC), typically nucleating from localized corrosion sites when susceptible materials are exposed above a threshold stress in specific corrosive environments [16–20]. For instance, in conventional austenitic stainless steels, cracks originate from pits that create the stress concentration and acidic environment required for cracking [21–27]. The trajectory of the crack is determined by the energy associated with its propagation process. Therefore, secondary cracks, or crack-branching, occur due to the presence of an obstacle or a more energetically favorable path [28]. The presence of a tensile stress, either residual, applied, or both, along with a specific corrodent, are required for SCC to occur. Moreover, the cracks can grow and propagate at much lower stress levels than those needed to fracture the material without the corrodent [16,18,29–32]. Therefore, brittle SCC fracture can occur on otherwise highly ductile materials [16,29,33].

Austenitic stainless steel UNS S31603 (SS316L) is considered an excellent material for engineering applications due to its exceptional ductility, weldability, and corrosion resistance [16,34,35]. Its low carbon content (max. 0.035% [36]) has largely eliminated sensitization of its microstructure, which is responsible for intergranular SCC [16,34,35]. However, when exposed to hot environments containing halides, stressed SS316L can still experience transgranular SCC [17,19,32,37]. Consequently, SCC poses a significant threat to the integrity and reliability of equipment in the energy sector. Thus, it is crucial to understand the influence of the AM process on SCC susceptibility.

Among the AM technologies, there has been a significant increase in the use of LPBF to investigate SCC in SS316L due to its ability to produce an alloy with a fully austenitic microstructure [38–40], extremely low porosity [40–42], excellent resistance to localized corrosion [43–46], and outstanding mechanical properties [40–42]. This is due to the distinctive manufacturing process of LPBF, in which a high-intensity laser is programmed to melt layers of powder feedstock that solidify into near-net-shape parts [2,3,47] at cooling rates ranging from  $10^3$  to  $10^7$  K/S [48–51]. However, this heating and cooling cycle at each deposited layer results in LPBF-manufactured SS316L with high residual stresses [40,52,53], which are known to increase its susceptibility to SCC [52,54,55].

The objective of this work was to determine the SCC behavior of SS316L additively manufactured with sinter-based material extrusion when exposed to different stress levels and temperatures in an acidic chloride environment. The study focused on the impact of the sintered microstructure on the SCC initiation and crack-branching susceptibility. The SCC response was compared with those obtained from similarly tested wrought SS316L samples in solution-annealed (SA), and cold-drawn (CD) conditions. The investigation was supported by comprehensive pre- and post-test microanalyses that included light optical microscopy (LOM), scanning electron microscopy (SEM), electron backscattered diffraction (EBSD), and micro-computed tomography (micro-CT).

## 2. Materials and Methods

### 2.1. Materials

The AM SS316L samples used in this investigation were fabricated using Bound Metal Deposition (BMD) (Desktop Metal, Studio System; Burlington, MA, USA). The technology includes the following: (i) rods of pre-alloyed SS316L powder held in a mix of polymer and wax binder, (ii) an FDM 3D printer, (iii) a solvent-based debinding unit, (iv) a sintering furnace, and (v) a cloud-based software (Live Studio v3.0) to control the process from digital object to sintered part. Further information regarding the manufacturing process can be found in a previous publication by Santamaria, R., et al. (2021) [9]. All BMD SS316L

specimens for tensile and SCC testing were produced with the parameters summarized in Table 1. For comparison, commercially available SA wrought SS316L seamless tubes and CD wrought SS316L rod bars were included in the investigation. The tubes were 22 mm in diameter and 2 mm in thickness, while the rod bars were 25 mm in diameter. The dimensions of all BMD-manufactured specimens, including thickness, width, and length, were within 10% of the original design after sintering.

**Table 1.** Summary of parameters used to manufacture all BMD SS316L test specimens.

Printing Parameters		Debinding Parameters	
Extrude line width:	0.5 mm	Debinding time:	15 h
Deposited layer height:	0.15 mm	Debinding temperature:	50 °C
Contour shell thickness:	1.50 mm	Debinding pressure:	Atmospheric
Extrusion nozzle size:	0.40 mm	Sintering parameters	
Extrusion rate:	30 mm/s	Heating rate:	~1.0 °C/min
Extrusion temperature:	175 °C	Thermal debinding temperature:	550 °C
Build plate temperature:	60 °C	Thermal debinding dwell time:	2 h
Sintering scale factors:	X = Y = Z = 1.15	Sintering temperature:	1350 °C
Bulk volume raster pattern:	+45° / -45° each layer	Sintering atmosphere:	Ar > 99.997% vol.
Infill density:	100%	Sintering dwell time:	2 h
Print orientation:	Vertical (Z)	Cooling rate:	Furnace cooling

## 2.2. Analytical Characterization

Table 2 presents the elemental composition of the BMD SS316L used in this investigation determined with inductively coupled plasma atomic emission spectroscopy (ICP-AES) analysis. The chemical compositions of SA wrought SS316L and CD wrought SS316L, as given in their material test reports (MTR), are also presented in Table 2. The UNS S31603 nominal chemical composition range is added for comparison.

**Table 2.** Elemental composition in wt% of BMD SS316L, SA wrought SS316L, CD wrought SS316L, and nominal composition of UNS S31603.

Alloy	Source	Fe	C	Cr	Ni	Mo	Si	Mn	P	S
BMD SS316L	ICP-AES	Bal.	0.020	16.3	10.4	2.12	0.61	1.22	0.010	0.010
SA SS316L	MTR	Bal.	0.012	16.1	10.1	2.03	0.46	0.92	0.036	0.002
CD SS316L	MTR	Bal.	0.019	16.7	10.1	2.03	0.41	1.72	0.024	0.025
UNS S31603	ASTM A213 [36]	Bal.	Max. 0.035	16.0 18.0	10.0 14.0	2.00 3.00	Max. 1.00	Max. 2.00	Max. 0.045	Max. 0.030

The constituent phases were identified via X-ray diffraction (XRD) analysis using a Cobalt K alpha ( $\lambda = 0.179$  nm) powder diffractometer radiation source operating at 35 kV 40 mA with a LynxEye detector (Bruker, Billerica, MA, USA, D8 Discover). All XRD data were collected within  $2\theta$  ranging from  $40^\circ$  to  $130^\circ$ , using a step size of  $0.015^\circ$ , and a time interval of 0.7 s. Content of  $\gamma$ -austenite (FCC) and  $\delta$ -ferrite (BCC) phases were quantified from the XRD patterns as the area of each crystalline peak over the total area of crystalline peaks. Micro-CT analysis was performed on a  $2 \times 2 \times 2$  mm<sup>3</sup> cut sample using a 3D X-ray microscope with an exposure energy of 140 kV, during an exposure time of 24 h, and at a pixel resolution of 2.2  $\mu$ m (Zeiss 520 Versa, Oberkochen, Germany).

Microstructural characterization was conducted on representative samples, which were cut, mounted in cold epoxy resin, manually wet-ground with SiC abrasive papers,

and mechanically polished down to 1  $\mu\text{m}$  surface finish. Light optical microscopy (LOM) analysis was conducted on samples chemically etched with a solution containing 100 mL  $\text{H}_2\text{O}$ , 10 mL  $\text{HNO}_3$ , and 100 mL HCl. The concentration of nitric acid and hydrochloric acid was 70% and 32%, respectively.

Electron backscatter X-ray diffraction (EBSD) analysis was conducted on samples that were polished to a mirror surface finish with 0.02  $\mu\text{m}$  colloidal silica, and then ion-milled for 30 min using a beam voltage of 8 kV at a glancing angle of  $4^\circ$  with full cycle rotational movements (TECHNOORG Linda, Budapest, Hungary, SEMPRep2). Samples were surface-coated with a carbon film 5  $\mu\text{m}$  thick to prevent electrostatic charging. Microstructures were imaged using secondary electron (SE) and backscatter (BS) detectors coupled to a field emission scanning electron microscope (FE-SEM) (TESCAN system, CLARA, Brno, Czech Republic). Elemental composition was mapped with a high-sensitivity Oxford energy-dispersive X-ray spectroscopy (EDS) detection system attached to the FE-SEM. The content of non-metallic inclusions was quantified from EDS elemental maps by dividing the area of oxides or sulfides over the total area of the map, per ASTM E1245 [56].

EBSD was conducted with an Oxford symmetry EBSD detector in the FE-SEM on  $70^\circ$  tilted samples, at a working distance of 20 mm, with a beam energy of 28 kV, and a beam current of 1 nA. A clean-up process was applied to the data to assimilate any non- or mis-indexed points, ensuring that a maximum of 10% of the points were modified. Grain boundaries were detected with a threshold misorientation of  $10^\circ$  in conjunction with a minimum of 8 pixels of fractional difference of misorientation variation and a kernel size of 3 by 3. Kernel average misorientation (KAM) maps were used to investigate the presence of local strain in the microstructures. This analysis was conducted using a 3 by 3 kernel size, a square kernel shape, and a maximum misorientation angle of  $5^\circ$ .

The average grain size was measured as the maximum Feret diameter. The average grain aspect ratio was calculated as the fitted ellipse aspect ratio. Twin content was measured as the fraction length of  $\Sigma 3$  ( $\langle 111 \rangle / 60^\circ$ ) boundaries over the total length of  $\gamma$ -austenite (FCC) boundaries. The Schmid factor on the  $\gamma$ -austenite (FCC) phase was measured in the plane/direction  $\langle 111 \rangle / \langle 110 \rangle$ . All data acquisition and subsequent post-processing were conducted using the software Aztec v.5.1 and AztecCrystal v.2.1.259, respectively.

### 2.3. Mechanical Testing

Tensile tests were conducted according to ASTM E8 [57]. BMD SS316L and CD wrought SS316L were tested with rectangular specimens, while SA wrought SS316L was tested using tubular specimens with metallic plugs inserted in their ends to ensure a proper grip. All tests were conducted with a 50 kN universal testing machine (UTM, Shimadzu, Kyoto, Japan, AGS-X series). Displacements were measured using an axial extensometer with 25 mm of gauge length and +25 mm of travel length (Epsilon TechCorp, Jackson, WY, USA). The UTM crosshead speed was set to 0.375 mm/min, and the test was stopped once a clear deviation from the initial linear behavior was observed. The actual yield strength (AYS) of each alloy was calculated by intersecting their corresponding stress–strain curves with an 0.2% offset line running parallel to their elastic portion, as per ASTM E8 requirements [57]. Figure 1 shows the geometries and dimensions of the tensile specimens.

Microhardness was measured on cut samples of untested C-rings prepared similarly to the microstructural characterization procedure that removes the sample preparation induced artifacts. The samples were obtained from the middle of the uppermost curved surface of the C-ring. This test was conducted as per ASTM E384 [58] using a microhardness tester (Duramin-4, Struers, Copenhagen, Denmark), an applied load of 2 Kg (HV2), and a dwell time of 15 s. The bulk density was determined according to ASTM B962 [59] using a density kit coupled to an analytical balance with a readability of 0.001 g and a linearity of  $\pm 0.002$  g (Mettler-Toledo, ME203, Columbus, OH, USA). The relative bulk porosity content was calculated as the ratio of the measured bulk density and the standard density of UNS S31603 given in ASTM G15 [60].

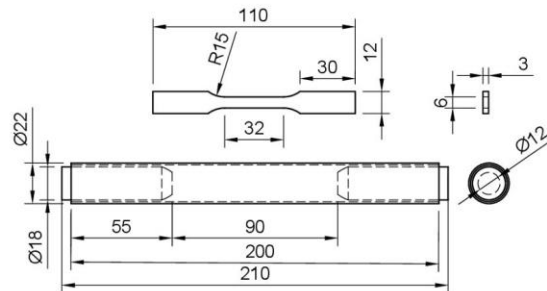


**Figure 1.** Drawings of the specimens used for tensile testing BMD SS316L and CD wrought SS316L (top), and SA wrought SS316L with snug-fitting metallic plugs (bottom). Units in millimeters.

#### 2.4. SCC Susceptibility and Crack-Branching

The SCC susceptibility of BMD SS316L and its wrought SS316L counterparts was investigated by exposing C-ring samples to different applied stresses and temperatures. The C-rings were designed following ASTM G38 guidelines [61], see Figure 2. This type of specimen was selected due to its versatility to be elastically deformed at different magnitudes, unlike the U-bent type suggested by ASTM G123 [62]. Duplicate BMD and wrought SS316 C-ring specimens were stressed to 60% and 90% of their AYS to study the effect of stress level on SCC susceptibility. Unstressed C-rings, i.e., 0% AYS, were also tested for comparison and to investigate the possible influence of residual stresses on SCC. Tests were performed in a 25% (by mass) sodium chloride (NaCl) solution, which was acidified to pH 1.5 with phosphoric acid ( $H_3PO_4$ ), as per ASTM G123 [62]. In addition to the standard boiling condition, tests were conducted at different temperatures, i.e., 30, 60, and 80 °C, to define stress–temperature SCC thresholds.

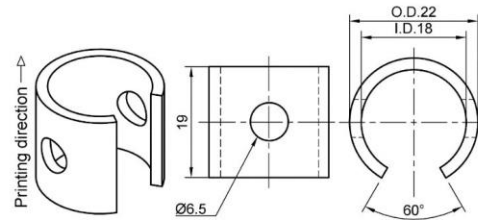


**Figure 2.** Drawings of the C-ring type specimen used to investigate the SCC susceptibility in the BMD SS316L and its wrought SS316L counterparts. Units in millimeters.

BMD SS316L C-rings were 3D printed in the vertical direction as shown in Figure 2. All surfaces were wet-ground from 80-grit to 600-grit with SiC abrasive paper, avoiding any excessive removal of material. Subsequently, C-rings were constant-strained to the required level, as per ASTM G38 [61]. The constant-strain setup, which is shown in Figure 3, consisted of two PEEK washers, two M6 titanium flat washers, one M6 titanium socket cap bolt, one M6 titanium flanged lock nut, and a strip of clear PTFE heat shrinkable tube molded to the bolt. The required strain level was obtained by attaching a 0.3 mm circumferential strain gauge (Tokyo Measuring Instruments, Tokyo, Japan, FLAB-03-11-1LJC-F) to the uppermost curved surface at the middle of the C-ring's arc and width, as shown in Figure 3. Then, the bolt was tightened until the reading in the data logger (Ahlborn, Sayner, WI, USA, Almemo 2590) indicated the required strain value corresponding to 60% and 90% AYS. All traces of the strain gauges and adhesive were manually removed with 600-grit

SiC abrasive paper. The electrical insulation between the titanium bolt and the C-ring was verified with a digital multimeter. The C-rings tested at 0% AYS were also prepared, as shown in Figure 3, but no strain was applied in this case. SA wrought SS316L and CD wrought SS316L C-rings were prepared following an identical procedure.

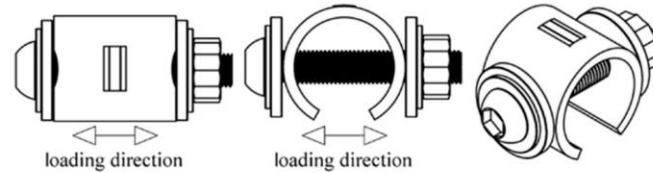


**Figure 3.** Schematics of the constant-strain setup used to stress the C-rings under different levels of AYS. The circumferential strain gauge is located at the uppermost curved surface of the C-ring.

SCC tests were conducted by immersing the C-rings in a series of Erlenmeyer flasks containing 750 mL of solution at the set constant temperatures. Each temperature was monitored regularly with a thermocouple. Duplicate specimens of stressed and unstressed BMD SS316L C-rings and their wrought counterparts were immersed in the solution. Each Erlenmeyer flask contained three different C-rings, i.e., one from each alloy stressed at the same level. The volume of solution per exposed C-ring surface area ratio was 11 mL/cm<sup>2</sup>, which is twice the minimum ratio according to the ASTM G123 standard [62]. All C-rings were standing on their washers to prevent stagnant solution spots at the contact points. C-rings were removed weekly from the solution and inspected for cracks at a magnification of 20× using a LOM. If no cracks were observed, the specimens continued the test in a freshly prepared solution. If cracks were found, cracked specimens were removed from the test and prepared for microscopy analysis. The tests continued for a maximum of six weeks, as per ASTM G123 [62]. The degree of crack-branching was calculated by dividing the total crack length, which includes both the primary and secondary cracks, by the length of the primary crack. LOM images at 10× magnifications were used for this purpose. This approach is consistent with other investigations [52,63]. Size and depth of pits were measured according to the ASTM G46 standard [64].

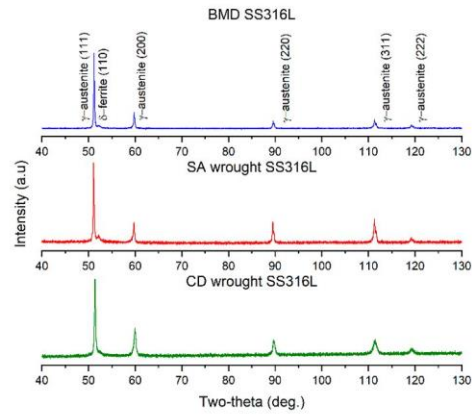
### 3. Results

#### 3.1. Analytical Characterization

Representative BMD and wrought SS316 XRD patterns are presented in Figure 4, as indicated. The XRD patterns indicated that all the alloys contained almost entirely  $\gamma$ -austenite (FCC) with a minor presence of  $\delta$ -ferrite (BCC) phase. The amount of  $\delta$ -ferrite is summarized in Table 3. Retained  $\delta$ -ferrite in a relatively low temperature powder-based additively manufactured SS316L can originate from the gas atomization process of the pre-alloyed powder feedstock due to the ferrite-stabilizer effect of Cr, Mo, and Si [41]. Therefore, the small amount of  $\delta$ -ferrite found in BMD SS316L suggests that its allotropic transformation into the  $\gamma$ -austenite was incomplete during the sintering stage.

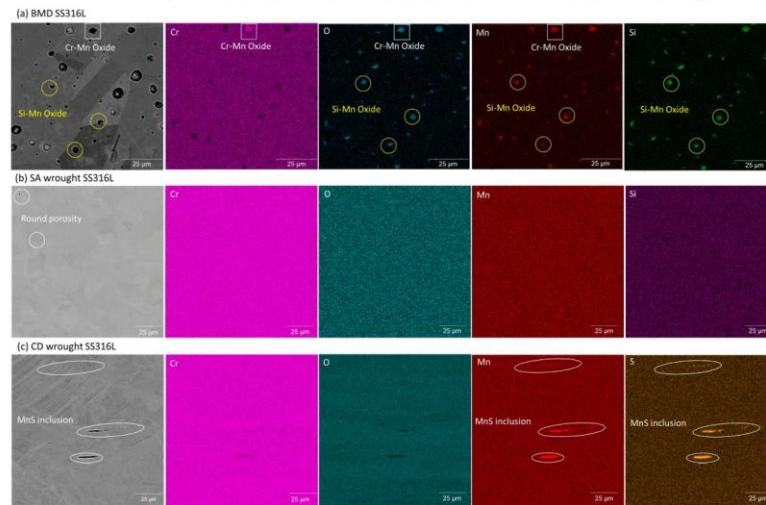
**Table 3.** Content of non-metallic inclusions,  $\delta$ -ferrite (BCC) phase, and grain size measurements of BMD SS316L, SA wrought SS316L, and CD wrought SS316L.

Alloy	Non-Metallic Inclusions (%)	$\delta$ -Ferrite Phase (%)	Average Grain Size ( $\mu\text{m}$ )	Aspect Ratio	Twin Boundaries (%)	Schmid Factor $\{111\}\langle 110 \rangle$
BMD SS316L	3.23	6.09	$40.8 \pm 23.8$	$3.1 \pm 2.4$	53.2	0.69
SA SS316L	0.01	7.86	$16.2 \pm 8.5$	$2.2 \pm 1.3$	45.5	0.94
CD SS316L	0.39	0.95	$43.5 \pm 33.6$	$3.9 \pm 3.6$	39.4	0.96



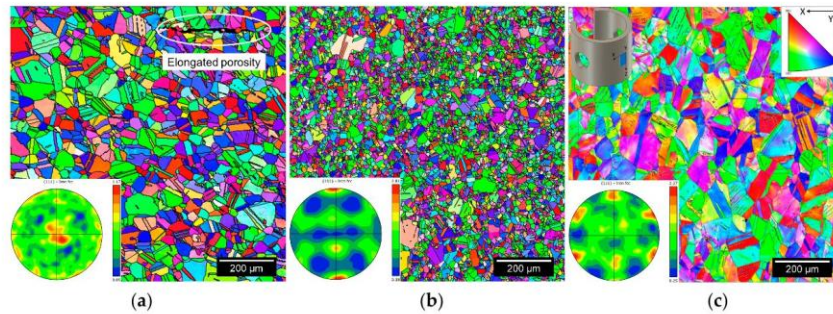
**Figure 4.** Representative XRD patterns of BMD SS316L, SA wrought SS316L, and CD SS316L showing predominance of the  $\gamma$ -austenitic with small fractions of  $\delta$ -ferrite.

SEM-EDS analysis showed no evidence of sensitization, i.e., Cr depletion in the vicinity of the grain boundaries, in any of the SS316L alloys, as illustrated in the elemental map in Figure 5. BMD SS316L contained non-metallic particles rich in O, Si, Mn, and Cr, as seen in Figure 5a, which are inherent to PM and MIM manufacturing processes [65–67]. SA wrought SS316L had an almost negligible amount of round pores, and no oxide inclusions were found, Figure 5b. CD wrought SS316L contained manganese sulfide inclusions (MnS), Figure 5c, common in cold-worked austenitic stainless steels [35,68,69]. Table 3 summarizes the content of non-metallic inclusions in BMD SS316L and its wrought counterparts.



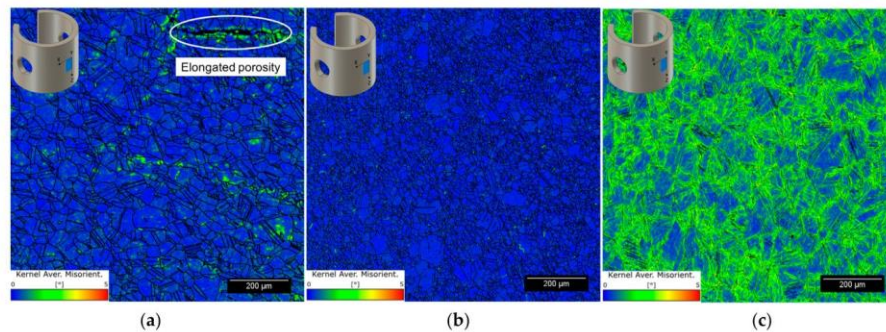
**Figure 5.** Representative EDS elemental map of (a) BMD SS316L showing inclusions rich in O, Si, Mn, and Cr, (b) SA wrought SS316L showing slight presence of round pores and lack of non-metallic inclusions, and (c) CD wrought SS316L showing elongated MnS inclusions.

Figure 6 shows representative inverse pole figure EBSD maps with respect to the build direction (Y-axis) of BMD SS316L and its wrought SS316L counterparts. The corresponding BMD SS316L {111} pole figures in Figure 6a show a weakly textured, almost randomly oriented distribution with low intensity ( $\times 1.17$  random). In comparison, Figure 6b,c shows a slight texture strengthening in wrought SS316L ( $\times 2.81$  random) and CD wrought SS316 ( $\times 2.27$  random), as indicated. These texture developments are assumed to be caused by the processing history, which is beyond the scope of this study. Figure 6a also shows an elongated pore in the BMD SS316L sample, perpendicular to its build direction. This type of porosity is inherent to the extruding nature of FDM manufacturing [70,71].



**Figure 6.** Representative EBSD maps with corresponding {111} pole figures of (a) BMD SS316L, (b) SA wrought SS316L, and (c) CD wrought SS316L C-rings taken from their uppermost curved surfaces.

Figure 7 shows the KAM maps of the corresponding EBSD scans in Figure 6, illustrating areas of slight local plastic deformation, i.e., residual stresses, in the microstructure of BMD SS316L. Figure 7b shows negligible local straining in SA wrought SS316L, as opposed to CD wrought SS316L which contained substantial residual stresses, Figure 7c. The distinct degree of residual stresses observed in the wrought materials is caused by their processing conditions [72], which are also beyond the scope of this study. Grain measurements, such as average grain size, aspect ratio, twin boundary content, and Schmid factors are included in Table 3. Further information regarding the influence of the sintering process on the microscopy of the BMD-manufactured SS316L can be found in a previous publication by Santamaria, R., et al. (2021) [9].



**Figure 7.** Representative KAM maps with a maximum misorientation angle of  $5^\circ$  in (a) BMD SS316L, (b) SA wrought SS316L, and (c) CD wrought SS316L C-rings taken from their uppermost curved surfaces.

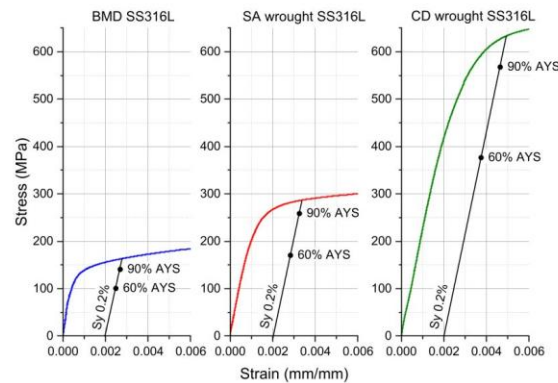
### 3.2. Mechanical Testing

Figure 8 presents the elastic regions of the engineering stress–strain curves of BMD SS316L and SA and CD wrought SS316L, indicating their corresponding 60% and 90% AYS values. As shown in Figure 8, CD wrought SS316L had the highest average AYS due to cold working, i.e.,  $646 \pm 8$  MPa, followed by the SA wrought SS316L, i.e.,  $293 \pm 6$  MPa, and lastly, the BMD SS316L with an AYS of  $167 \pm 2$  MPa. Similar values of AYS in AM sinter-based SS316L have been reported elsewhere [8,73–75]. Table 4 summarizes microhardness, bulk density, and relative bulk porosity content.

Santamaria et al. (2021) [9] conducted a detailed investigation on the impact of the sintering process on the tensile properties and fracture behavior of the BMD-manufactured SS316L. They found that the AM SS316L had a lower yield and tensile strength, caused by its relatively larger grain sizes. However, AM SS316L showed excellent ductility attributed to the abundance of twin boundaries. The AM SS316L fractured in a ductile manner, with spherical dimples uniformly distributed throughout the fracture surface, containing evidence of oxide inclusions. No secondary cracks or parabolic dimples were observed, indicating that the fracture was due to pure tension. Additionally, the necked region exhibited no cup and cone shape, attributed to the tensile flow instability phenomena.

**Table 4.** Average mechanical properties of BMD SS316L and its wrought counterparts.

Alloy	AYS (MPa)	Microhardness (HV2)	Bulk Density (g/cm <sup>3</sup> )	Relative Bulk Porosity (%)
BMD SS316L	$167 \pm 2$	$117.1 \pm 3.2$	$7.564 \pm 0.013$	5.21
SA SS316L	$293 \pm 6$	$163.9 \pm 2.5$	$7.935 \pm 0.025$	0.57
CD SS316L	$646 \pm 8$	$277.3 \pm 3.2$	$7.953 \pm 0.027$	0.35



**Figure 8.** Stress–strain curves within the elastic region of BMD SS316L, SA wrought SS316L, and CD wrought SS316L showing their corresponding 60% and 90% AYS.

### 3.3. Pitting and Cracking Susceptibility

Figure 9 summarizes the susceptibility to pitting and cracking initiation of BMD and SA and CD wrought SS316L at different stress and temperature levels over six weeks, as indicated. In Figure 9, cells colored in green represent no pitting, cells colored in yellow indicate that pitting was observed, and cells colored in red indicate SCC had occurred. At 30 °C, none of the C-rings showed evidence of pitting for the duration of the tests. However, pits were observed in all alloys within the first week when exposed to higher temperatures, i.e., 60 °C and above. In boiling solution (~106 °C), pits quickly (Week 1)



transitioned into cracks for BMD and CD wrought SS316L at 90% AYS. The SCC resistance of all alloys decreased with increasing time, stress, and temperature, in agreement with the literature [18,20,33,76]. Figure 9 also shows that SA wrought SS316L had the highest SCC resistance, as indicated by only 2 out of 12 conditions that led to cracking, followed by BMD SS316L with 4 conditions, and finally, CD wrought SS316L with 7 conditions. It is noteworthy to mention that in stressed CD wrought SS316L specimens, all cracks started from the sharp edges of their curved surface, whereas in unstressed specimens, cracks initiated at their flat surface. The difference in crack initiation location was attributed to the residual stresses introduced during the manufacturing process and subsequent machining of the C-rings [76–79].

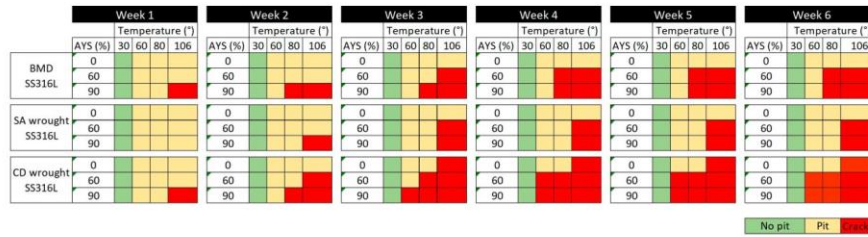


Figure 9. Pitting and cracking susceptibility map of BMD SS316L and its wrought SS316L counterparts at different test conditions over a period of six weeks.

Figure 10 illustrates the size and distribution of corrosion pits in unstressed BMD and SA and CD wrought SS316L C-rings on their flat and curved surfaces after a week of exposure to the boiling solution. As shown in Figure 10, the printed material had the largest pits, while both wrought counterparts exhibited smaller pits that were similar in size. However, CD wrought SS316L had more pits than the other two alloys. Figure 10 also confirmed that residual stresses were sufficient to cause SCC in the unstressed CD wrought SS316L specimens after a week of immersion in the boiling solution. Table 5 summarizes the average pit size measurements made on unstressed C-rings after one week in boiling solution, as well as the average pit depth in cracked specimens under stress. As seen in Table 5, BMD SS316L had the largest and deepest pits in both measured conditions, while SA wrought had the smallest ones.

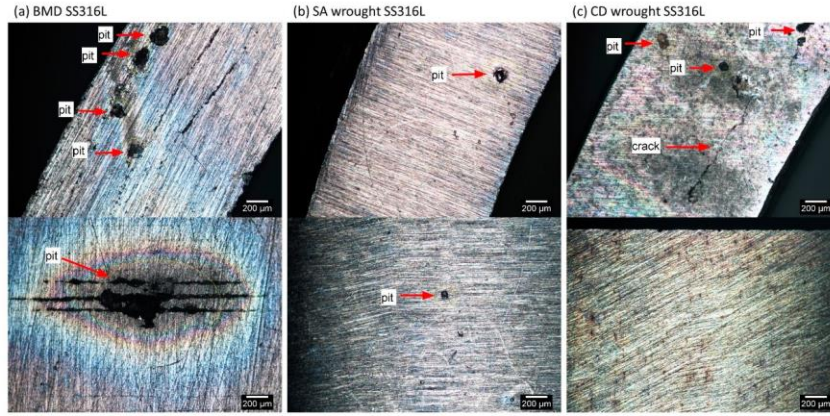
Table 5. Average pit size and pit depth measurements made on stressed and unstressed BMD SS316L C-rings and wrought counterparts.

Alloy	Unstressed C-Ring (0%AYS) in Boiling Solution after 1 Week		Stressed C-Ring (90%AYS) in Boiling Solution after Cracking	
	Pit Size (µm) in Flat Surface	Pit Size (µm) in Curved Surface	Pit Size (µm)	Pit Depth (µm)
BMDSS316L	112 ± 117	89 ± 154	406 ± 359	190 ± 135
SA SS316L	31 ± 27	28 ± 16	213 ± 178	58 ± 27
CD SS316L	88 ± 61	27 ± 11	205 ± 118	130 ± 84

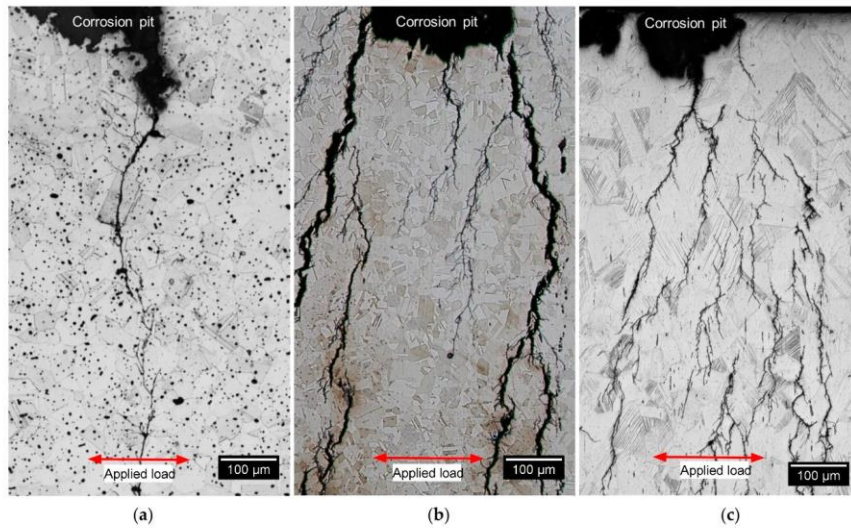
### 3.4. Crack-Branching Susceptibility

Figure 11 shows transgranular SCC in BMD, SA and CD wrought SS316L after exposure to the boiling solution under a stress of 90% AYS. Identical crack morphology was observed in all specimens regardless of the applied stress and temperature. SCC started from pits and propagated perpendicularly to the applied stress direction, in agreement with the literature [33,76,80,81]. Figure 11 also shows that BMD SS316L had the least

amount of crack-branching while both wrought SS316L counterparts cracked in a similar fashion. The calculated crack-branching ratio for BMD and SA and CD wrought SS316L was  $1.84 \mu\text{m}/\mu\text{m}$ ,  $4.29 \mu\text{m}/\mu\text{m}$ , and  $4.64 \mu\text{m}/\mu\text{m}$ , respectively.



**Figure 10.** LOM images of unstressed C-rings after one week in boiling solution, showing different sizes of corrosion pits in (a) BMD SS316L, (b) SA wrought SS316L, and (c) CD wrought SS316L. The top images correspond to the C-rings' flat surfaces, while the curved ones are presented at the bottom.



**Figure 11.** LOM images of etched microstructures in (a) BMD SS316L, (b) SA wrought SS316L, and (c) CD wrought SS316L C-rings after exposure to boiling solution, showing SCC initiated from pits and propagated perpendicular to the applied stress of 90% AYS.

The transgranular nature of SCC in BMD SS316L was also confirmed by the EBSD analysis shown in Figure 12, which include all Euler map, KAM, and phase distributions along with the overlaid band contrast images to facilitate locating crack propagation through the grains. Figure 12 also illustrates some of the characteristic features of the BMD SS316L microstructure, such as twin boundaries, round porosity, oxide inclusions, and  $\delta$ -ferrite (BCC). Additionally, Figure 13 shows an SEM image of a crack that propagated through elongated pores of a BMD SS316L sample without branching. The lack of branching was attributed to the arresting effect of the pores, which is also visible in the micro-CT scan in Supplementary Video S1.

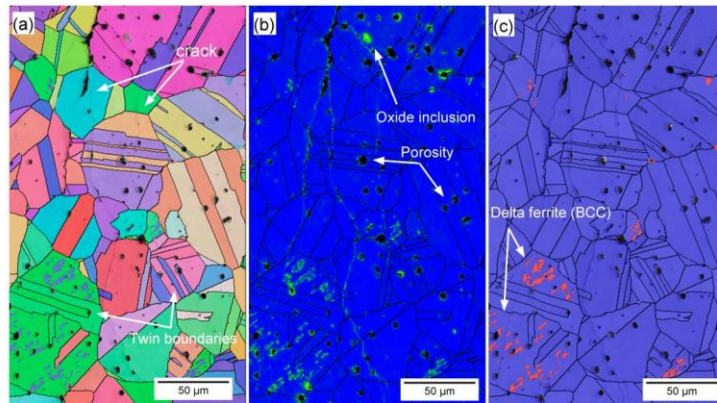


**Figure 12.** Representative (a) EBSD map, (b) KAM map, and (c) phase map with overlaid band contrast of BMD SS316L, showing transgranular cracking, twin boundaries, oxide inclusions, round porosity, and area of  $\delta$ -ferrite.

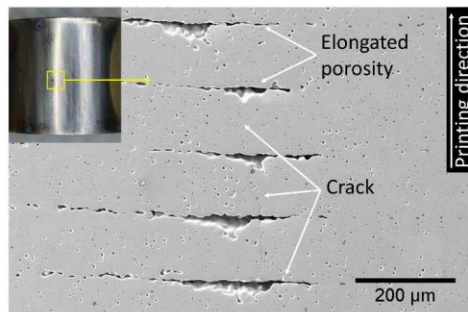


**Figure 13.** Photographic and SEM image of the curved surface of a BMD SS316L C-ring after exposure to boiling solution under 90% AYS, showing SCC crossing perpendicular to the elongated porosity.

#### 4. Discussion

The results from this study are consistent with the established body of knowledge showing that non-sensitized austenitic stainless steels under tensile stress are susceptible to transgranular SCC when exposed to hot acidic chloride solutions, i.e., 60 °C or above [16,18,20,34]. Additionally, results demonstrated that, when tested under the same conditions, BMD SS316L was more susceptible to SCC initiation than SA wrought SS316L.

but, given its much lower strength, more resistant than CD wrought SS316L, Figure 9. It is important to note that samples were stressed at a fixed percentage of their AYS. Thus, the actual stress level of CD wrought SS316L was substantially higher at 60% and 90% AYS (i.e., 388 MPa and 581 MPa) than SA wrought (i.e., 176 MPa and 264 MPa) and BMD (i.e., 100 MPa and 150 MPa) samples. Nevertheless, the results are considered valid since the loading conditions represent the reasonable utilization values for the materials in service, where designers take advantage of the higher yield strength of the CD wrought material. Results of unstressed samples also highlighted the influence of residual stresses on SCC susceptibility, with CD wrought samples experiencing SCC cracks after three weeks of exposure to the boiling conditions.

The manufacturing route influenced SCC morphology. Highly branched cracks are a frequent SCC characteristic of austenitic SS in chloride solutions [33,37,82]. SA and CD wrought samples exhibited the expected branched morphology. In contrast, BMD SS316L showed transgranular cracking with little to no branching, Figure 11. Given that all alloy compositions met the requirements of the UNS S31603 alloy type [36], the different crack morphologies can be attributed to differences in alloy microstructure features such as defects and chemistry-phase-crystallography distributions.

#### 4.1. Susceptibility to SCC Initiation: Pit-to-Crack Transition

The susceptibility map in Figure 9 shows that CD wrought SS316L had the lowest SCC resistance. As discussed above, SCC susceptibility depends on the extent of plastic deformation of the cold-worked condition [35,82,83]. Cold working introduced substantial residual stresses, as shown in the KAM map in Figure 7, promoting SCC nucleation [77]. High-strength SSs, such as CD wrought SS316L, are known to have a low threshold stress intensity factor for SCC ( $K_{I,SCC}$ ), an indication of their low SCC arrest capacity [16,27,31,84]. Due to their lower strength and applied loads, SA wrought and BMD SS316L had improved resistance to SCC initiation. However, BMD exhibited a relatively lower SCC resistance than SA wrought SS316L, especially considering the AM samples' lower strength.

The lower SCC resistance of BMD SS316L was attributed to the higher content of microstructural heterogeneities, such as pores and oxide inclusions, Figure 5 and Tables 3 and 4. These defects serve as preferred stable pit nucleation sites [67,85–88]. Faster sharp pit propagation, in turn, facilitates the so-called pit-to-crack transition [21–26]. The more extensive and deeper pits in BMD SS316L, Figure 10 and Table 5, negatively affected SCC resistance. The SCC resistance of BMD SS316L could be markedly improved by decreasing porosity and oxide inclusions. Strategies to reduce SCC susceptibility include using low-oxygen powder feedstock and prolonging the sintering time to reduce pore size, albeit at the expense of grain growth [65–67]. Post-processing steps such as high isostatic pressure (HIP) could also be introduced to close the bulk porosity [5,89–92]. Lastly, shot-peening could also close surface pores and introduce compressive residual stresses [93–96].

#### 4.2. Crack-Branching

The noticeable difference in SCC morphology between wrought and BMD SS316L samples, illustrated in Figure 11, was attributed to the presence of randomly oriented equiaxed grain aggregates—with minimal or no influence of special boundaries—and to a high content of twin boundaries in the BMD microstructure, Figure 6 and Table 3. These features are commonly found in materials processed with sinter-based manufacturing technologies [5,8,9,73–75], which act as barriers for crack-branching of transgranular SCC.

The weakly crystallographic textured microstructure of BMD SS316L resulted in an overall reduction of the Schmid factor, as given in Table 3. The Schmid factor indicates the increased resolved shear stress to initiate the slip across grains [97–101]. Furthermore, the equiaxed grains are crystallographically randomly oriented and comprise a larger amount of twin boundary fractions in BMD SS316L, thus enhancing the resistance to crack propagation via branching in non-localized directions [98,100–103]. In addition, the

higher porosity in BMD SS316L acted as an obstacle to crack-branching. A similar arrestor effect, caused by the blunting of the crack tips, has been reported elsewhere in additively manufactured porous alloys [104–106]. The influence of the non-metallic inclusions and retained  $\delta$ -ferrite (BCC) on the resistance to crack-branching could not be determined since no clear relationship was observed.

## 5. Conclusions

This work determined the SCC behavior of SS316L additively manufactured by sinter-based material extrusion. Tests were conducted in an acidified chloride solution (25 wt% NaCl, pH 1.50) at different stress levels and temperatures to identify SCC thresholds. Results were compared with the SCC response of conventional SA and CD wrought SS316L. Results were supported by a thorough characterization that included LOM, SEM-EDS, EBSD, and micro-CT. The following conclusions were drawn based on the evidence presented above:

1. SCC resistance increased in the following order: SA wrought > BMD > CD wrought SS316L.
2. The sinter-based manufacturing process used to produce BMD SS316L resulted in lower residual stresses and lower strength, contributing to a higher SCC initiation resistance than the highly stressed CD wrought condition.
3. The large grain aggregates, equiaxed grain morphology, weak crystallographic texture, and a large content of twin boundaries decreased the SCC crack-branching of BMD SS316L when compared to SA and CD wrought SS316L.
4. The porosity distribution of BMD SS316L had a mixed impact on its SCC resistance. While these defects facilitated the pit-to-crack transition, they also acted as crack arrestors by blunting the crack tips.

**Supplementary Materials:** The following supporting information can be downloaded at: <https://www.mdpi.com/article/10.3390/ma16114006/s1>, Video S1: Micro-CT scan of BMD SS316L with respect to its build direction (Z) showing the propagation of the secondary cracks being arrested by the elongated porosity.

**Author Contributions:** Conceptualization, R.S., K.W., M.S., M.I. and M.Z.Q.; methodology, R.S., M.S. and M.I.; validation, K.W., M.S. and M.Z.Q.; formal analysis, R.S., K.W., M.S. and M.Y.M.; investigation, R.S.; resources, M.I. and M.Z.Q.; writing—original draft preparation, R.S.; writing—review and editing, K.W., M.S., M.Y.M. and M.Z.Q.; supervision, K.W., M.S. and M.Z.Q.; funding acquisition, M.I. and M.Z.Q. All authors have read and agreed to the published version of the manuscript.

**Funding:** This research was funded by the Curtin University of Technology and Woodside Energy, grant number 4610000822.

**Institutional Review Board Statement:** Not applicable.

**Informed Consent Statement:** Not applicable.

**Data Availability Statement:** This article contains all the data that was generated and is presented in the form of Figures, Tables, or Supplementary Materials.

**Acknowledgments:** The authors would like to express their gratitude to Woodside Energy for the financial support provided. They also appreciate the access to the instruments at the Microscopy and Microanalysis Facility (MMF) at the John de Laeter Centre at Curtin University and the Centre for Microscopy, Characterization and Analysis (CMCA) at the University of Western Australia. Additionally, they extend their thanks to Sam Bakhtiari from the Curtin Corrosion Centre for conducting the micro-CT analysis.

**Conflicts of Interest:** The authors declare no conflict of interest.

## References

1. ISO/ASTM-52900; Additive Manufacturing—General Principles—Fundamentals and Vocabulary. ISO: Geneva, Switzerland, 2015. [[CrossRef](#)]
2. ISO-17296-2; Additive Manufacturing—General Principles—Part 2: Overview of Process Categories and Feedstock. ISO International: Geneva, Switzerland, 2015.
3. Redwood, B.; Schöffer, F.; Garret, B. *The 3D Printing Handbook: Technologies, Design and Applications*; 3D Hubs B.V.: Amsterdam, The Netherlands, 2017.
4. Poszvek, G.; Stattler, G.; Markl, E.; Seemann, R.; Lackner, M. Fused Filament Fabrication of Metallic Components for Semi-professional and Home Use. In *Digital Conversion on the Way to Industry 4.0*; Durakbasa, N.M., Gençylmaz, M.G., Eds.; Springer International Publishing: Cham, Switzerland, 2021; pp. 140–149. [[CrossRef](#)]
5. Wang, Y.; Zhang, L.; Li, X.; Yan, Z. On hot isostatic pressing sintering of fused filament fabricated 316L stainless steel—Evaluation of microstructure, porosity, and tensile properties. *Mater. Lett.* **2021**, *296*, 129854. [[CrossRef](#)]
6. Thompson, Y.; Gonzalez-Gutierrez, J.; Kukla, C.; Felfer, P. Fused filament fabrication, debinding and sintering as a low cost additive manufacturing method of 316L stainless steel. *Addit. Manuf.* **2019**, *30*, 100861. [[CrossRef](#)]
7. Jiang, D.; Ning, F. Additive Manufacturing of 316L Stainless Steel by a Printing-Debinding-Sintering Method: Effects of Microstructure on Fatigue Property. *J. Manuf. Sci. Eng.* **2021**, *143*, 091007. [[CrossRef](#)]
8. Caminero, M.Á.; Romero, A.; Chacón, J.M.; Núñez, P.J.; García-Plaza, E.; Rodríguez, G.P. Additive manufacturing of 316L stainless-steel structures using fused filament fabrication technology: Mechanical and geometric properties. *Rapid Prototyp. J.* **2021**, *27*, 583–591. [[CrossRef](#)]
9. Santamaria, R.; Salasi, M.; Bakhtiari, S.; Leadbeater, G.; Iannuzzi, M.; Quadir, M.Z. Microstructure and mechanical behaviour of 316L stainless steel produced using sinter-based extrusion additive manufacturing. *J. Mater. Sci.* **2022**, *57*, 9646–9662. [[CrossRef](#)]
10. Mendoza, M.Y.; Samimi, P.; Brice, D.A.; Martin, B.W.; Rolchigo, M.R.; LeSar, R.; Collins, P.C. Microstructures and grain refinement of additive-manufactured Ti-xW alloys. *Metall. Mater. Trans. A* **2017**, *48*, 3594–3605. [[CrossRef](#)]
11. Zietala, M.; Durejko, T.; Polański, M.; Kuncze, I.; Płociński, T.; Zieliński, W.; Łazińska, M.; Stępniewski, W.; Czujko, T.; Kurzydowski, K.J.; et al. The microstructure, mechanical properties and corrosion resistance of 316L stainless steel fabricated using laser engineered net shaping. *Mater. Sci. Eng. A* **2016**, *677*, 1–10. [[CrossRef](#)]
12. Edwards, P.; O’Conner, A.; Ramulu, M. Electron Beam Additive Manufacturing of Titanium Components: Properties and Performance. *J. Manuf. Sci. Eng.* **2013**, *135*, 061016. [[CrossRef](#)]
13. Wang, X.; Chou, K. EBSD study of beam speed effects on Ti-6Al-4V alloy by powder bed electron beam additive manufacturing. *J. Alloys Compd.* **2018**, *748*, 236–244. [[CrossRef](#)]
14. Zaharia, S.M.; Lancea, C.; Chicco, L.A.; Pop, M.A.; Caputo, G.; Serra, E. Mechanical properties and corrosion behaviour of 316L stainless steel honeycomb cellular cores manufactured by selective laser melting. *Trans. FAMENA* **2017**, *41*, 11–24. [[CrossRef](#)]
15. Guzmán-Nogales, R.; Estupiñán-López, F.; Gaona-Tiburcio, C.; Lopez-Botello, O.E.; Ramírez-Rodríguez, J.G.; Zambrano-Robledo, P.C. Corrosion Resistance Measurement of 316L Stainless Steel Manufactured by Selective Laser Melting. *Materials* **2021**, *14*, 4509. [[CrossRef](#)] [[PubMed](#)]
16. Jones, D.A. *Principles and Prevention of Corrosion*, 2nd ed.; New international edition; Pearson: Essex, UK, 1996.
17. Newman, R.C. *Stress-Corrosion Cracking Mechanisms*; Corrosion Technology: New York, NY, USA; Basel, Switzerland, 2002; Volume 17, pp. 399–450.
18. McCafferty, E. *Introduction to Corrosion Science*; Springer Science & Business Media: Cham, Switzerland, 2010.
19. Zhang, W.; Fang, K.; Hu, Y.; Wang, S.; Wang, X. Effect of machining-induced surface residual stress on initiation of stress corrosion cracking in 316 austenitic stainless steel. *Corros. Sci.* **2016**, *108*, 173–184. [[CrossRef](#)]
20. Spencer, D.; Edwards, M.; Wenman, M.; Tsitsios, C.; Scatigno, G.; Chard-Tuckey, P. The initiation and propagation of chloride-induced transgranular stress-corrosion cracking (TGSCC) of 304L austenitic stainless steel under atmospheric conditions. *Corros. Sci.* **2014**, *88*, 76–88. [[CrossRef](#)]
21. Bryan, C.R.; Dingreville, R.P.M.; Enos, D. *Estimating Bounding Corrosion Pit Sizes on Stainless Steel SNF Interim Storage Canisters*; Sandia National Lab. (SNL-NM): Albuquerque, NM, USA, 2016.
22. Martin, U.; Bastidas, D.M. Stress corrosion cracking failure analysis of AISI 1018 carbon steel reinforcing bars in carbonated and chloride contaminated environment. *Eng. Fail. Anal.* **2023**, *147*, 107159. [[CrossRef](#)]
23. Horner, D.A.; Connolly, B.J.; Zhou, S.; Crocker, L.; Turnbull, A. Novel images of the evolution of stress corrosion cracks from corrosion pits. *Corros. Sci.* **2011**, *53*, 3466–3485. [[CrossRef](#)]
24. Katona, R.; Karasz, E.; Schaller, R. A Review of the Governing Factors in Pit-to-Crack Transitions of Metallic Structures. *Corrosion* **2023**, *79*, 72–96. [[CrossRef](#)] [[PubMed](#)]
25. Huang, X.-G.; Xu, J.-Q. 3D analysis for pit evolution and pit-to-crack transition during corrosion fatigue. *J. Zhejiang Univ. Sci. A* **2013**, *14*, 292–299. [[CrossRef](#)]
26. Fang, B.Y.; Eadie, R.L.; Chen, W.X.; Elboujdaini, M. Pit to crack transition in X-52 pipeline steel in near neutral pH environment Part 1—Formation of blunt cracks from pits under cyclic loading. *Corros. Eng. Sci. Technol.* **2010**, *45*, 302–312. [[CrossRef](#)]
27. Marcus, P. *Corrosion Mechanisms in Theory and Practice*; CRC Press: Boca Raton, FL, USA, 2011.
28. Scatigno, G.G.; Ryan, M.P.; Giuliani, F.; Wenman, M.R. The effect of prior cold work on the chloride stress corrosion cracking of 304L austenitic stainless steel under atmospheric conditions. *Mater. Sci. Eng. A* **2016**, *668*, 20–29. [[CrossRef](#)]

29. Russell, H.J. *Stress Corrosion Cracking*; The Materials Information Society, ASM International: Materials Park, OH, USA, 1992.
30. Sedriks, A.J. *Corrosion of Stainless Steels*, 2nd ed.; John Wiley & Sons, Inc.: New York, NY, USA, 1996.
31. Revie, R.W. *Uhlig's Corrosion Handbook*, 3rd ed.; The Electrochemical Society Series; John Wiley & Sons: Pennington, NJ, USA, 2011.
32. Raja, V.; Shoji, T. *Stress Corrosion Cracking: Theory and Practice*; Woodhead Publishing Limited: Cambridge, UK, 2011.
33. Jones, R.H. *Stress-Corrosion Cracking: Materials Performance and Evaluation*; ASM International: Materials Park, OH, USA, 2017. [\[CrossRef\]](#)
34. Khatak, H.S.; Raj, B. *Corrosion of Austenitic Stainless Steels: Mechanism, Mitigation and Monitoring*; Woodhead Publishing: Cambridge, UK, 2002.
35. McGuire, M.F. *Stainless Steels for Design Engineers*; ASM International: Materials Park, OH, USA, 2008.
36. ASTM-A213; Standard Specification for Seamless Ferritic and Austenitic Alloy-Steel Boiler, Superheater, and Heat-Exchanger Tubes. ASTM International: West Conshohocken, PA, USA, 2022. Available online: [https://www.astm.org/a0213\\_a0213m-18.html](https://www.astm.org/a0213_a0213m-18.html) (accessed on 25 May 2022).
37. Newman, R.C. Stress-corrosion cracking mechanisms. In *Corrosion Mechanisms in Theory and Practice*; CRC Press: Boca Raton, FL, USA, 2011; pp. 511–556.
38. Liverani, E.; Toschi, S.; Ceschini, L.; Fortunato, A. Effect of selective laser melting (SLM) process parameters on microstructure and mechanical properties of 316L austenitic stainless steel. *J. Mater. Process. Technol.* **2017**, *249*, 255–263. [\[CrossRef\]](#)
39. Woźniak, A.; Adamiak, M.; Chladek, G.; Kasperski, J. The Influence of the Process Parameters on the Microstructure and Properties SLM Processed 316L Stainless Steel. *Arch. Metall. Mater.* **2020**, *65*, 73–80. [\[CrossRef\]](#)
40. Chao, Q.; Thomas, S.; Birbilis, N.; Cizek, P.; Hodgson, P.D.; Fabijanic, D. The effect of post-processing heat treatment on the microstructure, residual stress and mechanical properties of selective laser melted 316L stainless steel. *Mater. Sci. Eng. A* **2021**, *821*, 141611. [\[CrossRef\]](#)
41. Kurzynowski, T.; Gruber, K.; Stopyra, W.; Kuźnicka, B.; Chlebus, E. Correlation between process parameters, microstructure and properties of 316 L stainless steel processed by selective laser melting. *Mater. Sci. Eng. A* **2018**, *718*, 64–73. [\[CrossRef\]](#)
42. Suryawanshi, J.; Prashanth, K.G.; Ramamurty, U. Mechanical behavior of selective laser melted 316L stainless steel. *Mater. Sci. Eng. A* **2017**, *696*, 113–121. [\[CrossRef\]](#)
43. Man, C.; Dong, C.; Liu, T.; Kong, D.; Wang, D.; Li, X. The enhancement of microstructure on the passive and pitting behaviors of selective laser melting 316L SS in simulated body fluid. *Appl. Surf. Sci.* **2019**, *467–468*, 193–205. [\[CrossRef\]](#)
44. Shaeri Karimi, M.H.; Yeganeh, M.; Alavi Zaree, S.R.; Eskandari, M. Corrosion behavior of 316L stainless steel manufactured by laser powder bed fusion (L-PBF) in an alkaline solution. *Opt. Laser Technol.* **2021**, *138*, 106918. [\[CrossRef\]](#)
45. Sander, G.; Thomas, S.; Cruz, V.; Jurg, M.; Birbilis, N.; Gao, X.; Brameld, M.; Hutchinson, C.R. On The Corrosion and Metastable Pitting Characteristics of 316L Stainless Steel Produced by Selective Laser Melting. *J. Electrochem. Soc.* **2017**, *164*, C250–C257. [\[CrossRef\]](#)
46. Lodhi, M.J.K.; Deen, K.M.; Haider, W. Corrosion behavior of additively manufactured 316L stainless steel in acidic media. *Materialia* **2018**, *2*, 111–121. [\[CrossRef\]](#)
47. Bian, L.; Shamsaei, N.; Usher, J.M. *Laser-Based Additive Manufacturing of Metal Parts: Modeling, Optimization, and Control of Mechanical Properties*; CRC Press: Boca Raton, FL, USA, 2017.
48. DebRoy, T.; Wei, H.L.; Zuback, J.S.; Mukherjee, T.; Elmer, J.W.; Milewski, J.O.; Beese, A.M.; Wilson-Heid, A.; De, A.; Zhang, W. Additive manufacturing of metallic components—Process, structure and properties. *Prog. Mater. Sci.* **2018**, *92*, 112–224. [\[CrossRef\]](#)
49. Ma, M.; Wang, Z.; Zeng, X. A comparison on metallurgical behaviors of 316L stainless steel by selective laser melting and laser cladding deposition. *Mater. Sci. Eng. A* **2017**, *685*, 265–273. [\[CrossRef\]](#)
50. Diaz Vallejo, N.; Lucas, C.; Ayers, N.; Graydon, K.; Hyer, H.; Sohn, Y. Process Optimization and Microstructure Analysis to Understand Laser Powder Bed Fusion of 316L Stainless Steel. *Metals* **2021**, *11*, 832. [\[CrossRef\]](#)
51. Tsutsumi, Y.; Ishimoto, T.; Oishi, T.; Manaka, T.; Chen, P.; Ashida, M.; Doi, K.; Katayama, H.; Hanawa, T.; Nakano, T. Crystallographic texture- and grain boundary density-independent improvement of corrosion resistance in austenitic 316L stainless steel fabricated via laser powder bed fusion. *Addit. Manuf.* **2021**, *45*, 102066. [\[CrossRef\]](#)
52. Dong, P.; Vecchiato, F.; Yang, Z.; Hooper, P.A.; Wenman, M.R. The effect of build direction and heat treatment on atmospheric stress corrosion cracking of laser powder bed fusion 316L austenitic stainless steel. *Addit. Manuf.* **2021**, *40*, 101902. [\[CrossRef\]](#)
53. Bian, P.; Shi, J.; Liu, Y.; Xie, Y. Influence of laser power and scanning strategy on residual stress distribution in additively manufactured 316L steel. *Opt. Laser Technol.* **2020**, *132*, 106477. [\[CrossRef\]](#)
54. Yazdanpanah, A.; Franceschi, M.; Bergamo, G.; Bonesso, M.; Dabalà, M. On the exceptional stress corrosion cracking susceptibility of selective laser melted 316L stainless steel under the individual effect of surface residual stresses. *Eng. Fail. Anal.* **2022**, *136*, 106192. [\[CrossRef\]](#)
55. Yazdanpanah, A.; Lago, M.; Gennari, C.; Dabalà, M. Stress corrosion cracking probability of selective laser melted 316L austenitic stainless steel under the effect of grinding induced residual stresses. *Metals* **2021**, *11*, 327. [\[CrossRef\]](#)
56. ASTM-E1245; Standard Practice for Determining the Inclusion or Second-Phase Constituent Content of Metals by Automatic Image Analysis. ASTM International: West Conshohocken, PA, USA, 2016. [\[CrossRef\]](#)
57. ASTM-E8; Standard Test Methods for Tension Testing of Metallic Materials. ASTM International: West Conshohocken, PA, USA, 2016. [\[CrossRef\]](#)

58. ASTM-E384; Standard Test Method for Microindentation Hardness of Materials. ASTM International: West Conshohocken, PA, USA, 2017. [CrossRef]
59. ASTM-B962; Standard Test Methods for Density of Compacted or Sintered Powder Metallurgy (PM) Products Using Archimedes' Principle. ASTM International: West Conshohocken, PA, USA, 2017. [CrossRef]
60. ASTM-G15; Standard Terminology Relating to Corrosion and Corrosion Testing. ASTM International: West Conshohocken, PA, USA, 2010. [CrossRef]
61. ASTM-G38; Standard Practice for Making and Using C-Ring Stress-Corrosion Test Specimens. ASTM International: West Conshohocken, PA, USA, 2013. Available online: <https://www.astm.org/g0038-01r21.html> (accessed on 27 October 2022).
62. ASTM-G123; Standard Test Method for Evaluating Stress-Corrosion Cracking of Stainless Steel Alloys with Different Nickel Content in Boiling Acidified Sodium Chloride Solution. ASTM International: West Conshohocken, PA, USA, 2015. [CrossRef]
63. Matsuda, F.; Nakagawa, H.; Kato, I.; Murata, Y. Effects of ferrite content and microsegregation on solidification crack susceptibility of duplex stainless steel weld metals. *Weld. Int.* **1988**, *2*, 529–535. [CrossRef]
64. ASTM-G46; Standard Guide for Examination and Evaluation of Pitting Corrosion. ASTM International: West Conshohocken, PA, USA, 2018. [CrossRef]
65. German, R.M. *Powder Metallurgy of Iron and Steel*; John Wiley & Sons, Inc.: New York, NY, USA, 1998; 496p.
66. Heaney, D.F. *Handbook of Metal Injection Molding*; Woodhead Publishing: Philadelphia, PA, USA, 2012.
67. Klar, E.; Samal, P.K. *Powder Metallurgy Stainless Steels: Processing, Microstructures, and Properties*; ASM International: Materials Park, OH, USA, 2007.
68. Verhoeven, J.D. *Steel Metallurgy for the Non-Metallurgist*; ASM International: Materials Park, OH, USA, 2007.
69. Hosford, W.F. *Iron and Steel*; Cambridge University Press: Cambridge, UK, 2012.
70. Yang, L.; Hsu, K.; Baughman, B.; Godfrey, D.; Medina, F.; Menon, M.; Wiener, S. *Additive Manufacturing of Metals: The Technology, Materials, Design and Production*; Springer: Berlin/Heidelberg, Germany, 2017.
71. Colón Quintana, J.L.; Redmann, A.; Mazzei Capote, G.A.; Pérez-Irizarry, A.; Bechara, A.; Osswald, T.A.; Lakes, R. Viscoelastic properties of fused filament fabrication parts. *Addit. Manuf.* **2019**, *28*, 704–710. [CrossRef]
72. Ravi Kumar, B.; Mahato, B.; Singh, R. Influence of Cold-Worked Structure on Electrochemical Properties of Austenitic Stainless Steels. *Metall. Mater. Trans. A* **2007**, *38*, 2085–2094. [CrossRef]
73. Damon, J.; Dietrich, S.; Gorantla, S.; Popp, U.; Okolo, B.; Schulze, V. Process porosity and mechanical performance of fused filament fabricated 316L stainless steel. *Rapid Prototyp. J.* **2019**, *25*, 1319–1327. [CrossRef]
74. Liu, B.; Wang, Y.; Lin, Z.; Zhang, T. Creating metal parts by Fused Deposition Modeling and Sintering. *Mater. Lett.* **2020**, *263*, 127252. [CrossRef]
75. Gong, H.; Snelling, D.; Kardel, K.; Carrano, A. Comparison of Stainless Steel 316L Parts Made by FDM- and SLM-Based Additive Manufacturing Processes. *JOM* **2019**, *71*, 880–885. [CrossRef]
76. Ghosh, S.; Rana, V.P.S.; Kain, V.; Mittal, V.; Baveja, S.K. Role of residual stresses induced by industrial fabrication on stress corrosion cracking susceptibility of austenitic stainless steel. *Mater. Des.* **2011**, *32*, 3823–3831. [CrossRef]
77. Acharyya, S.G.; Khandelwal, A.; Kain, V.; Kumar, A.; Samajdar, I. Surface working of 304L stainless steel: Impact on microstructure, electrochemical behavior and SCC resistance. *Mater. Charact.* **2012**, *72*, 68–76. [CrossRef]
78. Turnbull, A.; Mingard, K.; Lord, J.D.; Roebuck, B.; Tice, D.R.; Mottershead, K.J.; Fairweather, N.D.; Bradbury, A.K. Sensitivity of stress corrosion cracking of stainless steel to surface machining and grinding procedure. *Corros. Sci.* **2011**, *53*, 3398–3415. [CrossRef]
79. Wenman, M.R.; Trethewey, K.R.; Jarman, S.E.; Chard-Tuckey, P.R. A finite-element computational model of chloride-induced transgranular stress-corrosion cracking of austenitic stainless steel. *Acta Mater.* **2008**, *56*, 4125–4136. [CrossRef]
80. Turnbull, A.; McCartney, L.N.; Zhou, S. A model to predict the evolution of pitting corrosion and the pit-to-crack transition incorporating statistically distributed input parameters. *Corros. Sci.* **2006**, *48*, 2084–2105. [CrossRef]
81. Turnbull, A.; McCartney, L.N.; Zhou, S. Modelling of the evolution of stress corrosion cracks from corrosion pits. *Scr. Mater.* **2006**, *54*, 575–578. [CrossRef]
82. Dieter, G.E.; Bacon, D.J. *Mechanical Metallurgy*; McGraw-Hill: New York, NY, USA, 1976; Volume 3.
83. Callister, W.D.; Rethwisch, D.G.; Blicblau, A.; Bruggeman, K.; Cortie, M.; Long, J.; Hart, J.; Marceau, R.; Ryan, M.; Parvizi, R. *Materials Science and Engineering: An Introduction*; Wiley: Hoboken, NJ, USA, 2021.
84. Galvele, J.; Duffó, G. *Procesos de Corrosión*; Cursos ECOMAR, Comisión Nacional de Energía Atómica: Buenos Aires, Argentina, 1975.
85. Abbass, M.K.; Ajeel, S.A.; Wadullah, H.M. Biocompatibility, bioactivity and corrosion resistance of stainless steel 316L nanocoated with TiO<sub>2</sub> and Al<sub>2</sub>O<sub>3</sub> by atomic layer deposition method. *J. Phys. Conf. Ser.* **2018**, *1*, 012017. [CrossRef]
86. Abdullah, Z.; Ismail, A.; Ahmad, S. The influence of porosity on corrosion attack of Austenitic stainless steel. *J. Phys. Conf. Ser.* **2017**, *1*, 012013. [CrossRef]
87. García, C.; Martín, F.; de Tiedra, P.; Cambroner, L.G. Pitting corrosion behaviour of PM austenitic stainless steels sintered in nitrogen–hydrogen atmosphere. *Corros. Sci.* **2007**, *49*, 1718–1736. [CrossRef]
88. Deng, P.; Karadge, M.; Rebak, R.B.; Gupta, V.K.; Prorok, B.C.; Lou, X. The origin and formation of oxygen inclusions in austenitic stainless steels manufactured by laser powder bed fusion. *Addit. Manuf.* **2020**, *35*, 101334. [CrossRef]
89. Mao, Y.; Yuan, J.; Heng, Y.; Feng, K.; Cai, D.; Wei, Q. Effect of hot isostatic pressing treatment on porosity reduction and mechanical properties enhancement of 316L stainless steel fabricated by binder jetting. *Virtual Phys. Prototyp.* **2023**, *18*, e2174703. [CrossRef]



90. Atkinson, H.; Davies, S. Fundamental aspects of hot isostatic pressing: An overview. *Metall. Mater. Trans. A* **2000**, *31*, 2981–3000. [[CrossRef](#)]
91. Teng, Q.; Xie, Y.; Sun, S.; Xue, P.; Long, A.; Wu, T.; Cai, C.; Guo, J.; Wei, Q. Understanding on processing temperature-metallographic microstructure-tensile property relationships of third-generation nickel-based superalloy WZ-A3 prepared by hot isostatic pressing. *J. Alloys Compd.* **2022**, *909*, 164668. [[CrossRef](#)]
92. Cai, C.; Gao, X.; Teng, Q.; Kiran, R.; Liu, J.; Wei, Q.; Shi, Y. Hot isostatic pressing of a near  $\alpha$ -Ti alloy: Temperature optimization, microstructural evolution and mechanical performance evaluation. *Mater. Sci. Eng. A* **2021**, *802*, 140426. [[CrossRef](#)]
93. Damon, J.; Dietrich, S.; Vollert, F.; Gibmeier, J.; Schulze, V. Process dependent porosity and the influence of shot peening on porosity morphology regarding selective laser melted AlSi10Mg parts. *Addit. Manuf.* **2018**, *20*, 77–89. [[CrossRef](#)]
94. AlMangour, B.; Yang, J.-M. Improving the surface quality and mechanical properties by shot-peening of 17-4 stainless steel fabricated by additive manufacturing. *Mater. Des.* **2016**, *110*, 914–924. [[CrossRef](#)]
95. Rautio, T.; Jaskari, M.; Gundgire, T.; Iso-Junno, T.; Vippola, M.; Järvenpää, A. The Effect of Severe Shot Peening on Fatigue Life of Laser Powder Bed Fusion Manufactured 316L Stainless Steel. *Materials* **2022**, *15*, 3517. [[CrossRef](#)]
96. Jemaa, N.; Shu, J.; Kaliaguine, S.; Grandjean, B.P. Thin palladium film formation on shot peening modified porous stainless steel substrates. *Ind. Eng. Chem. Res.* **1996**, *35*, 973–977. [[CrossRef](#)]
97. Lépinoux, J.; Magnin, T. Stress corrosion microcleavage in a ductile f.c.c. alloy. In *Fundamental Aspects of Dislocation Interactions*; Kostorz, G., Calderon, H.A., Martin, J.L., Eds.; Elsevier: Amsterdam, The Netherlands, 1993; pp. 266–269. [[CrossRef](#)]
98. Qu, H. Effect of Crystallography on Stress Corrosion Cracking Growth in Austenitic Stainless Steels. Master's Thesis, Purdue University Graduate School, West Lafayette, IN, USA, 2020.
99. Hosford, W. Mechanical testing. In *Mechanical Behavior of Materials*; Pearson: London, UK, 2009; pp. 36–64.
100. Haidemenopoulos, G.N. *Physical Metallurgy: Principles and Design*; CRC Press: Boca Raton, FL, USA, 2018.
101. Qu, H.J.; Tao, F.; Gu, N.; Montoya, T.; Taylor, J.M.; Schaller, R.F.; Schindelholz, E.; Wharry, J.P. Crystallographic effects on transgranular chloride-induced stress corrosion crack propagation of arc welded austenitic stainless steel. *npj Mater. Degrad.* **2022**, *6*, 43. [[CrossRef](#)]
102. Koyama, M.; Ogawa, T.; Yan, D.; Matsumoto, Y.; Tazan, C.C.; Takai, K.; Tsuzaki, K. Hydrogen desorption and cracking associated with martensitic transformation in Fe-Cr-Ni-Based austenitic steels with different carbon contents. *Int. J. Hydrogen Energy* **2017**, *42*, 26423–26435. [[CrossRef](#)]
103. Anderson, T.L. *Fracture Mechanics: Fundamentals and Applications*; CRC Press: Boca Raton, FL, USA, 2017.
104. Conway, K.M.; Kunka, C.; White, B.C.; Pataky, G.J.; Boyce, B.L. Increasing fracture toughness via architected porosity. *Mater. Des.* **2021**, *205*, 109696. [[CrossRef](#)]
105. Kumar, P.; Jayaraj, R.; Suryawanshi, J.; Satwik, U.R.; McKinnell, J.; Ramamurthy, U. Fatigue strength of additively manufactured 316L austenitic stainless steel. *Acta Mater.* **2020**, *199*, 225–239. [[CrossRef](#)]
106. Vieille, B.; Keller, C.; Mokhtari, M.; Briatta, H.; Breteau, T.; Nguejio, J.; Barbe, F.; Ben Azzoune, M.; Baustert, E. Investigations on the fracture behavior of Inconel 718 superalloys obtained from cast and additive manufacturing processes. *Mater. Sci. Eng. A* **2020**, *790*, 139666. [[CrossRef](#)]

**Disclaimer/Publisher's Note:** The statements, opinions and data contained in all publications are solely those of the individual author(s) and contributor(s) and not of MDPI and/or the editor(s). MDPI and/or the editor(s) disclaim responsibility for any injury to people or property resulting from any ideas, methods, instructions or products referred to in the content.

**Appendix 6: Original reprint of the publication included in  
Chapter 5**

# Stress Corrosion Cracking Behavior of Austenitic Stainless Steel 316L Produced Using Laser-Based Powder Bed Fusion

Ricardo Santamaría,<sup>\*,\*\*</sup> Ke Wang,<sup>\*</sup> Mobin Salasi,<sup>\*</sup> Mehdi Salem,<sup>\*\*\*</sup> Philippe Lours,<sup>\*\*\*</sup> Mariano Iannuzzi,<sup>\*</sup> and Md Zakaria Quadir<sup>\*\*</sup>

Austenitic stainless steel UNS S31603 (SS316L) is widely used in the resources industry due to its excellent corrosion resistance, ductility, and weldability. Recently, laser-based powder bed fusion (LPBF) manufacturing has gained popularity for creating SS316L components with complex geometries and superior mechanical properties. However, the rapid melting and solidification of the deposited layers during the thermal cycle of LPBF produce residual stresses. Components manufactured through LPBF are frequently used under applied stress in corrosive environments. Thus, it is crucial to understand their susceptibility to stress corrosion cracking (SCC) and the impact of residual stresses. This study investigated the combined effects of applied stress and temperature on the SCC behavior of LPBF SS316L using custom-made C-ring test specimens. Cold-drawn wrought SS316L was included for comparison. Stress relief heat treatment, microhardness testing, partial immersion testing, and microanalysis techniques, such as light optical microscopy, scanning electron microscopy, and electron backscattered diffraction were used to quantify the SCC behavior. The outcomes of this study showed that stressed and unstressed LPBF SS316L specimens were highly susceptible to cracking around their printed holes. The SCC susceptibility was attributed to the residual stresses introduced by the printed supports, as both polished and as-printed holes showed similar cracking behavior. This work provides valuable insights and lays a foundation for further research into the impact of using C ring samples to investigate SCC susceptibility and sheds light on the SCC susceptibility of as-printed components of complex geometry printed with supports due to the influence of residual stresses.

KEY WORDS: additive manufacturing, crack initiation, printed support structure, residual stress, selective laser melting

## INTRODUCTION

Additive manufacturing (AM) encompasses the technologies used to produce physical objects from digital data by adding layers upon layers of material.<sup>1-3</sup> Compared to traditional manufacturing, AM has the potential to reduce complexity in the supply chain in terms of quality, impact, cost, speed, and innovation.<sup>4</sup> AM technologies include binder jetting, direct energy deposition, material extrusion, material jetting, sheet lamination, vat photopolymerization, and powder bed fusion (PBF).<sup>2-3,5</sup> Nowadays, it is common to use AM to produce engineering-grade metals such as copper,<sup>6-8</sup> stainless steels,<sup>9-12</sup> titanium-based,<sup>13-16</sup> aluminum-based,<sup>17-19</sup> and nickel-based alloys.<sup>20-22</sup> Thus, AM technologies have gathered growing interest from different industries such as biomedical, transport, aerospace, and energy among others.<sup>4,23-27</sup>

Stainless steel SS316L (UNS S31603<sup>(1)</sup>) is widely known for its ductility, weldability, and good corrosion resistance in certain oxidizing conditions.<sup>28-31</sup> However, when exposed to halides, such as chloride ions, while being stressed under tension, SS316L can be susceptible to stress corrosion cracking (SCC).<sup>32-38</sup> SCC is a form of environmentally assisted cracking

that occurs when a susceptible material is exposed to a specific environment above a certain tensile stress level. Cracks often nucleate from localized corrosion; thus, SCC occurs when the service temperature exceeds a critical localized corrosion temperature.<sup>35,39-42</sup> In SCC, cracks can initiate and propagate at much lower stress levels than those required to fracture the material in the absence of a corrosive, i.e., once the cracking initiates, it propagates until the applied stress exceeds the fracture strength of the remaining ligament.<sup>32-33</sup> Therefore, using AM technologies, such as PBF, to produce SS316L components with improved properties is of great interest.<sup>43-46</sup>

In PBF, a high-intensity energy source, such as a laser (LPBF) or an electron beam (EB) PBF, is used to melt layers of powdered feedstock that solidify at a calculated rate of approximately  $10^3$  K/s to  $10^7$  K/s<sup>47-50</sup> into near net shape parts.<sup>3,5,51</sup> LPBF-manufactured SS316L is known to be produced with fully austenitic microstructures,<sup>12,52-53</sup> extremely low porosity content,<sup>43,53-54</sup> and nanosize nonmetallic inclusions.<sup>53,55-56</sup> Moreover, LPBF SS316L has shown excellent localized corrosion resistance<sup>56-58</sup> and outstanding tensile properties.<sup>43,53-54</sup>

Submitted for publication: February 24, 2023. Revised and accepted: May 30, 2023. Preprint available online: May 30, 2023, <https://doi.org/10.5006/4311>.

<sup>\*</sup> Corresponding author. E-mail: ricardo.santamar@postgrad.curtin.edu.au.

<sup>\*\*</sup> Curtin Corrosion Centre, Curtin University, Perth, Western Australia, 6102, Australia.

<sup>\*\*\*</sup> John de Laeter Centre, Curtin University, Perth, Western Australia, 6845, Australia.

<sup>\*\*\*\*</sup> IMT Mines Albi, Institut Mines-Telecom, Albi, Tarn, 81013, France.

<sup>(1)</sup> UNS numbers are listed in *Metals & Alloys in the Unified Numbering System*, published by the Society of Automotive Engineers (SAE International) and cosponsored by ASTM International.

**Table 1.** Elemental Composition of the Prealloyed SS316L Powder, LPBF-Manufactured SS316L, CD Wrought SS316L, and Nominal Composition of UNS S31603

Chemical Composition in wt%										
Material	Source	Fe	C	Cr	Ni	Mo	Si	Mn	P	S
Powder SS316L	Material certificate	Bal.	0.01	17.7	12.6	2.36	0.65	0.90	0.007	0.01
LPBF SS316L	ICP-AES analysis	Bal.	0.02	17.5	12.3	2.02	0.06	0.62	<0.01	0.01
CD wrought SS316L	Material certificate	Bal.	0.02	16.7	10.1	2.03	0.04	1.72	0.024	0.02
UNS S31603	ASTM A276 <sup>93</sup>	Bal.	Max. 0.03	16.0 18.0	10.0 14.0	2.00 3.00	Max. 1.00	Max. 2.00	Max. 0.045	Max. 0.03

However, the cyclic process of melting and rapid cooling through the deposited layers leaves LPBF SS316L parts with a metastable microstructure containing a high degree of residual stresses.<sup>53,59-60</sup> These stresses, which can be between 250 MPa (36 ksi) and 500 MPa (72 ksi),<sup>53,59,61-63</sup> usually start as tension loads at the external surfaces of the component, and gradually turn into compressive loads at its core.<sup>53,60</sup> The magnitude of these process-induced residual stresses in LPBF-manufactured SS316L can be high enough for SCC to start at an applied stress lower than the material's yield strength or even in the absence of an externally applied load.<sup>42,59,64</sup> In addition, residual porosity and a rough surface finish, which are inherent in the LPBF manufacturing process, are factors known to increase the SCC susceptibility,<sup>65-69</sup> as they facilitate localized corrosion initiation.<sup>70-75</sup> Yazdanpanah, et al.,<sup>76</sup> observed that SCC in LPBF-manufactured SS316L with high levels of residual stress started from microstructural heterogeneities, such as melt pool boundaries and grain boundaries, and from machining marks and pore sites, whereas for annealed specimens, only pitting was observed. Therefore, it is possible to decrease the SCC susceptibility by improving the surface finish of the printed material throughout grinding or machining. However, the localized plastic deformation from these processes may also introduce additional residual stresses that could further increase their SCC susceptibility.<sup>35,38,69,76-78</sup> A more practical route to improve the SCC resistance of LPBF-manufactured components is reducing their intrinsic residual stresses by optimizing the printing parameters such as laser power, scanning strategy, and printing orientation,<sup>60,79-82</sup> or by adding postprocessing steps to the as-printed object, e.g., stress relief heat treatment<sup>53,83-86</sup> or shock peening.<sup>63,87-89</sup>

This study investigated how the residual stresses on LPBF-manufactured SS316L C rings printed with supports influenced their high SCC susceptibility. To assess this, stressed and unstressed test specimens were immersed in an acidified chloride solution at boiling temperature, and their time-to-crack was monitored. Furthermore, stress relief heat treatment and partial immersion tests were conducted to mitigate the impact of residual stresses on the SCC susceptibility around the printed holes. A detailed post-testing characterization was performed using light optical microscopy (LOM), scanning electron microscopy (SEM), and electron backscattered diffraction (EBSD) analysis. The cracking behavior of cold-drawn wrought SS316L C rings was used as a comparison.

<sup>1</sup> Trade name.

## EXPERIMENTAL PROCEDURES

### 2.1 | Materials

The SS316L used in this investigation was produced with LPBF. The material was additively manufactured using fresh nitrogen-atomized prealloyed SS316L powder with an average particle size of 35.7  $\mu\text{m}$ , and a particle size distribution of D50 33.1  $\mu\text{m}$  and D90 55.2  $\mu\text{m}$ . The SS316L powder was kept for at least 12 h in an oven at 50°C (122°F) to remove moisture prior to use. Before printing, the build plate was preheated at 100°C (212°F) to decrease thermal gradients, the oxygen content was reduced to less than 0.2%, and the chamber was filled with high-purity argon. All LPBF SS316L specimens were produced with a layer thickness of 50  $\mu\text{m}$ , no fill contour, no down-skin layer, and using a zig-zag pattern without rotation between layers to achieve the bulk volume. The laser power (P) was 275 W, the scanning speed (V) was 700 mm/s, and the hatching space (h) was 120  $\mu\text{m}$ . Commercially available cold-drawn (CD) wrought SS316L, which is known for its high-yield strength and residual stresses resulting from its plastic deformation process,<sup>90-92</sup> was used for comparison.

The LPBF SS316L elemental composition was determined with inductively coupled plasma atomic emission spectroscopy (ICP-AES). Table 1 summarizes the elemental composition of the prealloyed SS316L powder used in the LPBF process and the CD wrought SS316L rod bar, as reported in their manufacturer certificates. Table 1 also shows the externally analyzed composition of the as-printed LPBF SS316L and the nominal composition of UNS S31603 for comparison.

### 2.2 | Microstructure Characterization

The phased composition of the LPBF and CD wrought SS316L were identified via x-ray diffraction (XRD) using a Cobalt K alpha powder diffractometer radiation source operating at 35 kV and 40 mA with a LynxEye<sup>1</sup> detector (Bruker D8 Discover<sup>1</sup>). The XRD data were collected over an angular range of 40° to 130°, a step size of 0.015°, and a time interval of 0.7 s. The microscopy analysis was conducted on tested and untested samples that were cut, mounted in cold epoxy resin, wet ground with SiC abrasive paper, and mechanically polished down to a 1  $\mu\text{m}$  surface finish. Samples intended for LOM analysis were chemically etched with a solution containing 100 mL H<sub>2</sub>O, 10 mL HNO<sub>3</sub>, and 100 mL HCl. The concentration of nitric acid and hydrochloric acid was 70% and 32%, respectively. Samples for EBSD analysis were polished to a mirror surface finish with 0.02  $\mu\text{m}$  colloidal silica and then ion-milled for 30 min using a beam voltage of 8 kV at a glancing angle of 4° with full cycle rotational movements (TECHNOORG Linda, SEMPRep2<sup>1</sup>).

## SCIENCE SECTION

All samples for EBSD analysis were surface coated with a 5  $\mu\text{m}$  carbon film to prevent electrostatic charging.

The microstructures were imaged using secondary electron (SE) and backscatter (BS) detectors in a field emission-scanning electron microscope (FE-SEM) (TESCAN system, CLARA<sup>1</sup>). The crystallographic orientations were mapped using an Oxford<sup>2</sup> symmetry EBSD detector in the FE-SEM, on samples tilted 70°, with a working distance of 20 mm, a beam energy of 28 kV, and a beam current of 1 nA. A clean-up process was applied to the EBSD data to assimilate any non or misindexed points into the surrounding neighborhood grains, ensuring that less than 10% of the points were modified. Grain boundaries were detected with a threshold misorientation of 10°, a minimum of 8 pixels of fractional difference of misorientation variation, and a kernel size of 3 × 3. Grain size was measured as the maximum Feret diameter. The kernel average misorientation (KAM) maps were obtained using 3 × 3 square kernels and a maximum misorientation angle of 5°. All data acquisition and subsequent postprocessing were conducted using the software Aztec<sup>3</sup> and Aztec Crystal<sup>4</sup>, respectively.

### 2.3 | Mechanical Properties

Mechanical properties, including yield strength ( $S_y$ ), tensile strength ( $S_u$ ), elongation at fracture, elongation after fracture, reduction of area, and elastic modulus ( $E$ ), were measured at room temperature. The tests were conducted in triplicate specimens. The LPBF SS316L, provided by IMT Mines Albi (France), was tested using rectangular specimens that were 55 mm (2.20 in) long, 8 mm (0.30 in) wide, and 2 mm (0.08 in) thick manufactured in the horizontal orientation. The displacement during the tensile test was measured using an axial extensometer with a 15 mm (0.60 in) gauge length and +5 mm (0.20 in) travel length (Epsilon TechCorp<sup>5</sup>). The crosshead speed in the universal testing machine (UTM) was set to 0.225 mm/min within the elastic region and 0.750 mm/min within the plastic region. The CD wrought SS316L was tested according to ASTM<sup>(2)</sup> E8<sup>94</sup> using custom rectangular subsize tensile specimens that were 100 mm (4 in) long, 6 mm (0.24 in) wide, and 3 mm (0.12 in) thick, also as per ASTM E8. The specimens were machined from a 25 mm (1 in) diameter rod bar. The displacement during the tensile test was measured with an axial extensometer with a 25 mm (1 in) gauge length and +25 mm (1 in) travel length (Epsilon TechCorp<sup>5</sup>). The UTM crosshead speed was set to 0.375 mm/min within the elastic region and 1.25 mm/min within the plastic region. The displacement rates were different in both materials as their gauge lengths were different, as defined in ASTM E8. Figure 1 shows the geometry and dimensions of the LPBF SS316L and CD wrought SS316L tensile specimens.

All tensile tests were conducted using a 50 kN Shimadzu<sup>7</sup> UTM equipped with 50 kN manual nonshift wedge grips. All data were collected at a rate of 10 Hz using the Trapezium X<sup>1</sup> software. The actual yield strength (AYS) of the LPBF SS316L and the wrought SS316L were calculated by intersecting their corresponding engineering stress-strain curves with an 0.2% offset line running parallel to the elastic portion of their curves, per ASTM E8.<sup>94</sup> The slope of the offset line, i.e., an approximation of the material's elastic modulus ( $E$ ), was calculated using the least-squared method per ASTM E111.<sup>95</sup> The microhardness was measured according to ASTM E384<sup>96</sup> using a microhardness tester (Duramin-4, Struers<sup>8</sup>), an applied load of 2 Kg (HV2), and a dwell time of 15 s. The bulk density was calculated using the Archimedes principle per standard ASTM B962<sup>97</sup> with a density

<sup>(2)</sup> ASTM International, 100 Barr Harbor Dr., West Conshohocken, PA 19428-2959.

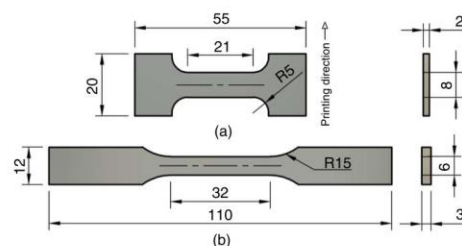


**FIGURE 1.** Geometry of the rectangular specimens used for the tensile tests (a) LPBF-manufactured SS316L and (b) machined CD wrought SS316L. Units in millimeters.

kit coupled to an analytical balance with a readability of 0.001 g and a linearity of  $\pm 0.002$  g (ME203, Mettler-Toledo).

### 2.4 | Stress Corrosion Cracking

The SCC behavior was investigated by monitoring the time required by the materials to crack when subjected to a stress level corresponding to 60% and 90% of their AYS while immersed in a boiling solution, i.e., 106°C (223°F). Unstressed specimens, i.e., 0% AYS, were also tested for comparison. The test solution was 25 wt% NaCl acidified to pH 1.50 with phosphoric acid ( $\text{H}_3\text{PO}_4$ ), per ASTM G123.<sup>98</sup> The test specimens used in this investigation were C rings designed per ASTM G38.<sup>99</sup> The LPBF SS316L C rings were manufactured, as shown in Figure 2(a), and their holes were re-bored with a slightly larger drill

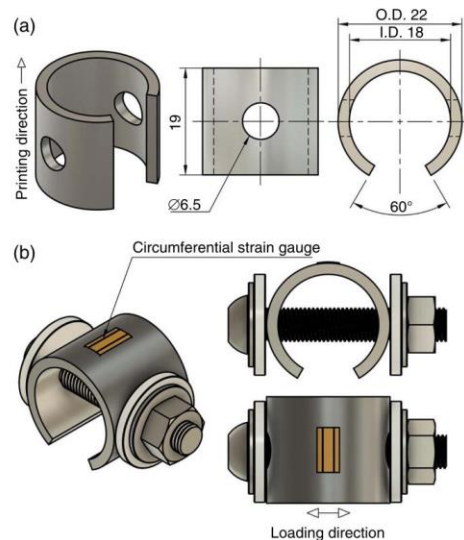


**FIGURE 2.** (a) Geometry of the custom C-ring specimen used to investigate the SCC susceptibility of LPBF and CD wrought SS316L and (b) schematics of the constant-strain assembly according to ASTM G38.

bit to remove the printed supports. All surfaces of the C rings were sequentially wet-ground with abrasive papers from 80- to 600-grit SiC. Although the dimensions of the C rings were not measured after surface finishing, the grinding process produced no excessive material removal. Notably, during the initial stages of this investigation, the printed holes were left in their as-printed condition. However, after preliminary results (not shown), it was decided to polish them in the same way as the rest of the C ring. All tests were performed at least in duplicate, as explained below.

The C rings were stressed to their corresponding material's AYS using a constant-strain setup, per ASTM G38.<sup>99</sup> The assembly, shown in Figure 2(b), consisted of two PEEK washers, two M6 titanium flat washers, one M6 titanium socket cap bolt, one M6 titanium flanged lock nut, and a strip of clear PTFE heat shrinkable tube molded to the bolt. The stress levels of 60% and 90% AYS were obtained by attaching a 0.3 mm (1/64 in) circumferential strain gauge (FLAB-03-11-1LJC-F, Tokyo Measuring Instruments) to the middle of the uppermost curved surface of the C ring, as shown in Figure 2(b). Then, the bolt was tightened until the reading in the data logger (Almemo 2590, Ahlborn) indicated the strain value corresponding to the required stress level. This procedure was conducted according to the stress considerations outlined in ASTM G38,<sup>99</sup> which states that the nominal stress exists only along a line that runs across the C ring at the middle of its arc. Therefore, the strain should be measured at that location, where the strain is maximum. However, the circumferential stress may vary across the width of the C ring, and the extent of the variation depends on the width-to-thickness and diameter-to-thickness ratios of the specimen. In general, the stress is greater at the edges than in the middle, but only finite element modeling (FEM) can determine the actual location of the maximum stress for a given C-ring's configuration, which was outside the scope of our work. All traces of the strain gauges were manually removed with 600-grit SiC abrasive paper. The electrical insulation between the bolt and the C ring was verified with a digital multimeter. All of the C rings tested at 0% AYS were also prepared, as shown in Figure 2(b), although no stress was applied to the bolt. The CD-wrought SS316L C rings were similarly prepared and included as a control.

Each test condition consisted of a flask containing 750 mL of the test solution and two C rings, one from each material stressed to the same corresponding AYS. The ratio of the volume of solution per exposed surface area of specimens was 17 mL/cm<sup>2</sup> (109 mL/in<sup>2</sup>), which is more than threefold the minimum required by ASTM G123.<sup>98</sup> The SCC susceptibility of each material was assessed as the time required to observe the first cracks. Therefore, longer exposure times without cracking indicated a lower SCC susceptibility. All C rings were removed from their test solution weekly, cleaned, and inspected for cracks at a magnification of 20× using LOM. C rings showing SCC were cut and prepared for post-test microscopy analysis, while C rings with no cracks continued the test in freshly prepared solution until the next inspection for a maximum of 6 weeks, per ASTM G123.<sup>98</sup> As removing the specimens for inspection is expected to disturb the local corrosion cells and may affect the results,<sup>98</sup> and due to the aggressive nature of the test solution for most stainless steels, a 1-week inspection frequency was considered sufficient to determine the onset of cracking.

Two different methods were used to investigate how residual stresses affect the cracking behavior of LPBF-manufactured SS316L. The first method involved subjecting

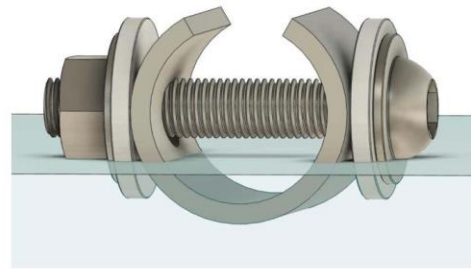


FIGURE 3. Schematic of the partial immersion test applied to the as-printed LPBF SS316L C ring.

duplicate C rings to a stress relief heat treatment in a vertical tube furnace under vacuum at 650°C (1,200°F) for 2 h. After stress relieving, the C rings were manually wet ground down to 600-grit using SiC abrasive paper, left overnight to recover the passive film, and tested unstressed, i.e., 0% AYS, in boiling solution (approximately 106°C [223°F]). In the second method, duplicate C rings were manually wet-ground down to 600 grit, stressed to 90% of their AYS, and left to passivate overnight. The specimens were then partially immersed in boiling solution while hanging upside-down, with the uppermost curved surface immersed in the solution, while the printed holes were kept

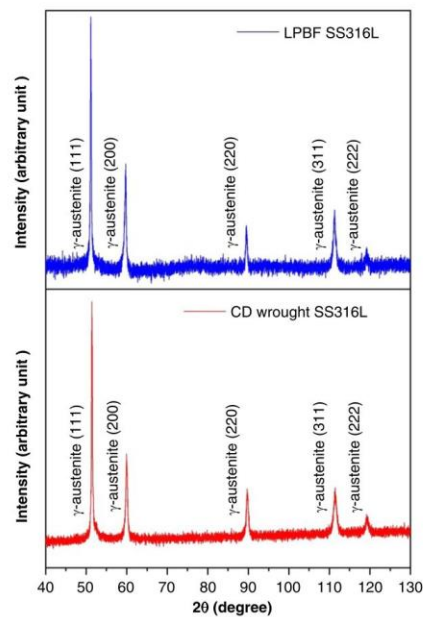


FIGURE 4. XRD patterns of LPBF and CD wrought SS316L showing the presence of  $\gamma$  (fcc) austenite as the only phase in their microstructures.

above the solution level, Figure 3. Weekly inspections were conducted on all C rings to determine the onset of cracking.

RESULTS

3.1 | Microstructure Characterization

Figure 4 shows representative XRD patterns of LPBF and CD wrought SS316L. Both materials consisted entirely

of  $\gamma$ -austenite (fcc), i.e.,  $\delta$ -ferrite (bcc) was not detected within the resolution of the technique. Figure 5 shows EBSD maps perpendicular to the build direction and corresponding color-coded inverse pole figures (IPF) of the LPBF and the CD wrought SS316L microstructures obtained from untested C rings. The IPF showed strongly textured LPBF and wrought SS316L microstructures indicated by the high-intensity poles in the  $\{111\}$  pole figure, i.e., 2.32 and 2.27 times

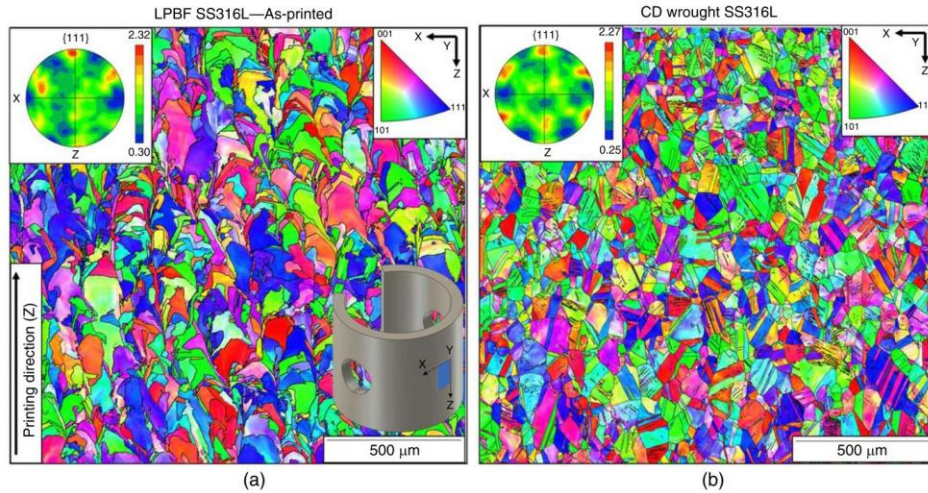


FIGURE 5. EBSD maps and color-coded inverse pole figures of untested C rings showing textured microstructures in the (a) as-printed LPBF SS316L perpendicular to its printing direction and (b) CD wrought SS316L.

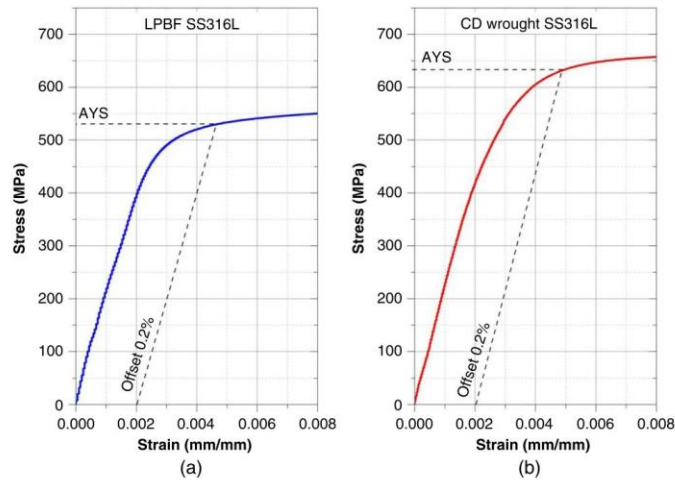


FIGURE 6. Engineering stress-strain curves within the elastic region of (a) LPBF SS316L and (b) CD wrought SS316L along with the location of their corresponding AYS.

random, respectively. Figure 5 also indicates relatively large austenitic grains in the LPBF and the CD-wrought SS316L microstructures. Their average grain sizes were 57±52 μm in the LPBF SS316L and 44±34 μm in the CD wrought SS316L. The overall grain size distributions were D<sub>50</sub> 39 μm and D<sub>90</sub> 124 μm for the LPBF SS316L, and D<sub>50</sub> 34 μm and D<sub>90</sub> 90 μm for the CD wrought SS316L. The fitted ellipse aspect ratios were 3.0±1.8 for the LPBF SS316L and 3.9±3.6 for the CD wrought SS316L.

3.2 | Mechanical Properties

Figure 6 shows representative engineering stress-strain curves of LPBF SS316L and its CD wrought counterpart in their elastic regions and corresponding AYS. The AYS of LPBF and CD wrought SS316L were 529 MPa (77 ksi) and 646 MPa (94 ksi), respectively. Although the displacement rates differed for each material due to their different gauge lengths, which may affect their tensile properties,<sup>94</sup> the C rings were stressed to their corresponding material's AYS, which allowed a proper

Table 2. Mechanical Properties of As-Printed LPBF SS316L, CD-Wrought SS316L, and Standard Requirements for UNS S31603

Materials	Elastic Modulus (E)	Yield Strength (Sy)	Tensile Strength (Su)	Elongation at Fracture	Elongation After Fracture	Reduction of Area	Bulk Density
	GPa (ksi)	MPa (ksi)	MPa (ksi)	%	%	%	g/cm <sup>3</sup>
LPBF SS316L	211±12 (30.6±1.7) 10 <sup>3</sup>	529±4 (77±0.6)	656±7 (95±1.0)	43±1	12±2	45±1	7.894±0.013
CD wrought SS316L	214±7 (31.0±1.0) 10 <sup>3</sup>	646±8 (96±1.2)	717±6 (104±0.9)	49±5	13±2	66±2	7.953±0.027
UNS S31603 <sup>93</sup>	202 <sup>100</sup> (29.3) 10 <sup>3</sup>	Min. 170 (25)	Min. 485 (70)	Min. 40	n/a	Min. 40	7.98 <sup>101</sup>
UNS S31603 (strain-hardened) <sup>102</sup>	202 <sup>100</sup> (29.3) 10 <sup>3</sup>	Min. 450 (65)	Min. 585 (85)	Min. 30	n/a	Min. 40	n/a

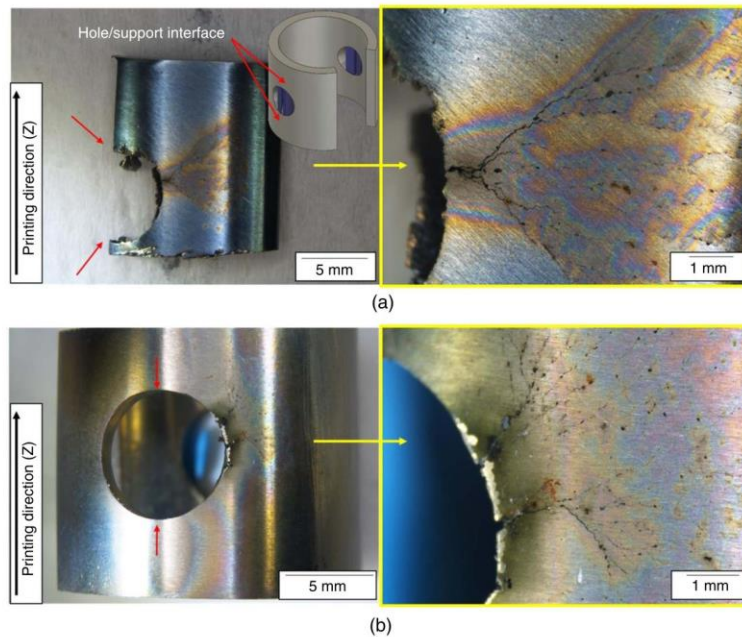


FIGURE 7. Photographs of as-printed LPBF SS316L C rings fully immersed in boiling solution showing similar SCC morphologies under (a) unstressed (0% AYS) and (b) stressed (90% AYS) conditions. The red arrows indicate the location of the hole/support interfaces.



**SCIENCE SECTION**

evaluation of SCC susceptibility despite the difference in geometry and displacement rates.  
 The bulk density of LPBF and CD wrought SS316L were  $7.894 \pm 0.013 \text{ g/cm}^3$  and  $7.953 \pm 0.027 \text{ g/cm}^3$ , respectively.

The bulk porosity of LPBF SS316L was less than 1%. Table 2 summarizes additional tensile properties, such as elastic modulus, tensile strength, elongation at fracture, elongation after fracture, and reduction of area. The average microhardness of

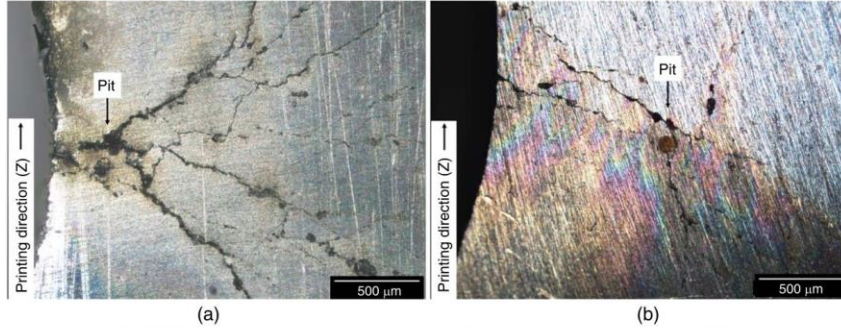


**FIGURE 8.** Photographs of LPBF SS316L C rings with (a) as-printed holes and (b) polished holes, showing similar SCC that initiated from pits near their printed holes in the unstressed (0% AYS) and stressed (90% AYS) conditions, respectively.

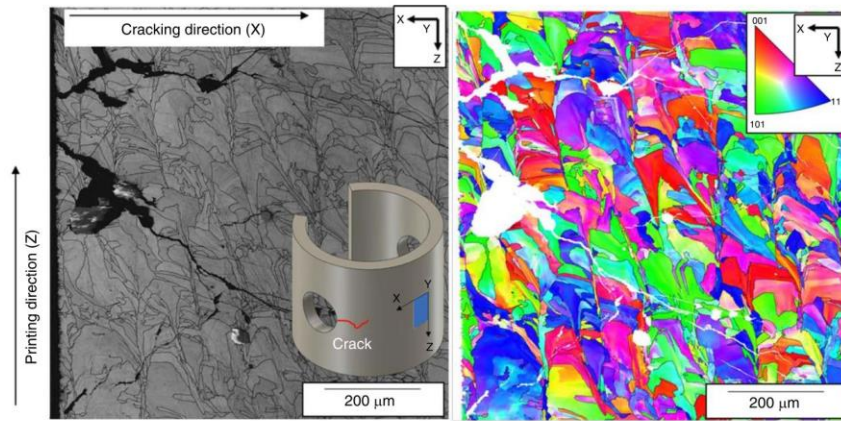


**FIGURE 9.** Band contrast image and corresponding EBSD map of SCC in as-printed unstressed (0% AYS) LPBF SS316L specimens after full immersion in boiling solution showing transgranular cracking.

**Table 3.** SCC Behavior of LPBF SS316L and CD Wrought SS316L C Rings Tested at Different Conditions in Acidified Chloride Boiling Solution.<sup>(A)</sup>

Stainless Steel 316L C Rings in Boiling Solution				
	Partially Immersed		Fully Immersed	
Stress level	LPBF as-printed	Wrought cold-drawn	LPBF as-printed	LPBF stress-relieved
0% AYS	–	3 week	1 week	2 week
60% AYS	–	2 week	2 week	–
90% AYS	2 week	1 week	3 week	–
Crack location	Arch	Arch	Hole	Hole

<sup>(A)</sup> The number in the cells corresponded to the week when the cracks were observed. Ndash correspond to untested conditions.

Downloaded from <http://meridian.allenpress.com/corrosion/article-pdf/doi/10.5006/431132438504311> pdf by Curtin University user on 03 August 2023

the as-printed LPBF SS316L, the stress-relieved LPBF SS316L, and the CD wrought SS316L were  $224 \pm 3$  HV2,  $195 \pm 2$  HV2, and  $282 \pm 3$  HV2, respectively.

### 3.3/ Stress Corrosion Cracking

Evidence of SCC in the as-printed LPBF SS316L C rings tested in boiling solution while stressed to 0% and 90% AYS is shown in Figures 7(a) and (b), respectively. The figures show that regardless of the applied stress, the stressed and unstressed C rings cracked with similar morphology, initiating from corrosion pits near the edges of their printed holes. Figure 8(a) illustrates the results of one of the initial C ring tests with as-printed holes, whereas Figure 8(b) corresponds to one with the as-printed surface removed by grinding. Interestingly, both initiation sites were perpendicular to the hole/support interfaces, as depicted by the inset images in Figure 9. Highly branched SCC initiated near the printed holes from corrosion pits on unstressed and stressed LPBF SS316L C rings with the holes in as-printed and polished conditions, respectively (Figure 8). SCC is initiated from the polished surface of the C ring near the holes regardless of the stress state and surface condition. Figure 9 shows an EBSD map and corresponding band contrast, revealing transgranular SCC in an unstressed (0% AYS) LPBF SS316L C ring that cracked from the same location around the printed holes. The SCC behavior of fully immersed as-printed LPBF and CD wrought SS316L C rings under different applied stress levels is summarized in Table 3. As seen in Table 3, a trend was observed between the immersion condition and time to crack initiation. In this regard, fully immersed as-printed LPBF C rings took longer to crack when stressed to higher stress levels than partially immersed samples. Nevertheless, cracks always initiated near the same locations around their printed holes and perpendicular to the printed supports, regardless of the applied stress. The SCC resistance of the CD wrought SS316L decreased with applied load, in agreement with the literature<sup>33,41-42,103</sup> and the cracks always initiated on the curved surface.

The role of residual stresses on the unexpected SCC behavior in LPBF SS316L C ring samples was investigated by conducting a stress relief heat treatment on as-printed C rings. Figure 10 shows KAM maps perpendicular to the build direction of the as-printed and stress-relieved LPBF SS316L C rings, as indicated. The as-printed LPBF SS316L microstructure contained local strain around their grain boundaries caused by its processing history. This local strain, depicted by the green areas in Figure 10(a), indicates a high degree of residual stress.<sup>104-105</sup> Inversely, the microstructure of the heat-treated LPBF SS316L showed fewer areas with local strain, Figure 10(b). A quantitative representation of the reduction in residual stresses due to the heat treatment is shown in Figure 10(c). As seen in this figure, the stress relief effect of the heat treatment reduced the magnitude of the KAM angles. The overall KAM distributions went from  $D_{50}$  0.96°,  $D_{90}$  1.89° in the as-printed LPBF SS316L, to  $D_{50}$  0.64°,  $D_{90}$  1.43° in the heat-treated LPBF SS316L. A Kolmogorov-Smirnov (K-S) test using OriginLab's<sup>1</sup> statistical tools was conducted to confirm that both distributions were significantly different, and the results are presented in Figure 10(c).

Figure 11 illustrates the SCC of a stress-relieved LPBF SS316L C ring when tested in boiling solution without applied stress, i.e., 0% AYS. As shown in Figure 11, in the absence of applied stress, cracking still occurred at the same locations near the printed holes and perpendicular to the printed supports. Moreover, the crack morphology was similar to its as-printed

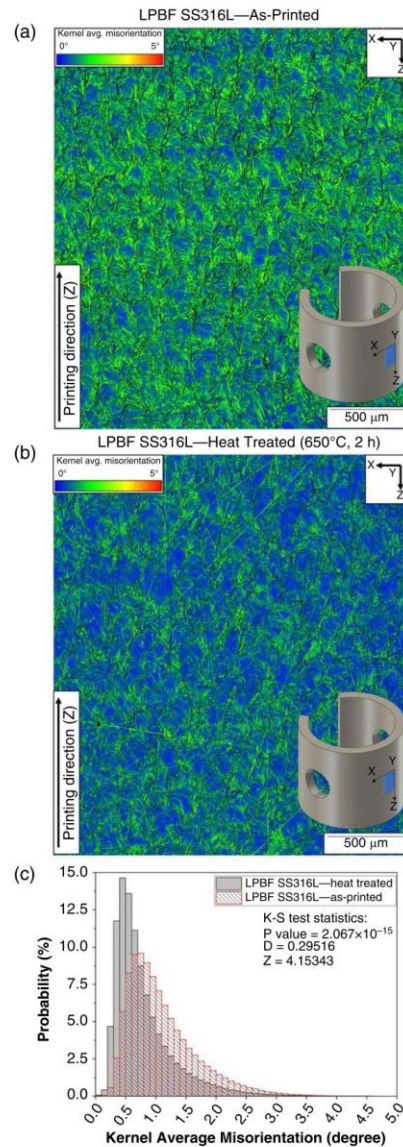


FIGURE 10. KAM maps of untested LPBF SS316L C rings in their (a) as-printed and (b) stress-relieved conditions. The KAM histogram in (c) shows the redistribution of local misorientations after the stress relief process.

Downloaded from <http://meridian.allenpress.com/corrosion/article-pdf/doi/10.5006/43113243850/4311> pdf by Curtin University user on 03 August 2023

SCIENCE SECTION

counterparts, although the initial main crack propagated longer before branching in the annealed specimen. As seen in Table 3, the heat-treated specimens cracked 1 week after the as-printed counterparts. These findings indicated that the SCC resistance of unstressed LPBF SS316L C rings slightly improved after stress relief.

The as-printed LPBF SS316L C rings stressed to 90% AYS were also partially immersed in boiling 25% NaCl (pH 1.5), as shown in Figure 3. As the dissolved oxygen concentration is much lower at the boiling temperature (106°C [223°F]) than at room temperature,<sup>106</sup> pitting and SCC were supported by the hydrogen evolution reaction rather than the oxygen reduction reaction, which allows a direct comparison between fully and

partially immersed tests. After exposure, the partially immersed printed material cracked transgranularly from its uppermost curved surface, i.e., where the nominal applied stress is maximum,<sup>99,107</sup> Figure 12. Figure 13 shows the SCC behavior of the fully immersed 90% AYS CD wrought samples. As seen in Figure 13, the CD-wrought SS316L samples cracked perpendicular to the direction of the applied stress from its curved surface. However, cracking initiated from the edges of the C ring rather than from its middle area. Cracking from the edges of the samples was attributed to the residual stresses introduced during the machining process.<sup>35,38,108</sup> Nevertheless, both materials cracked along the line of maximum applied stress when stressed to 90% AYS. Notably, the percentage of the total

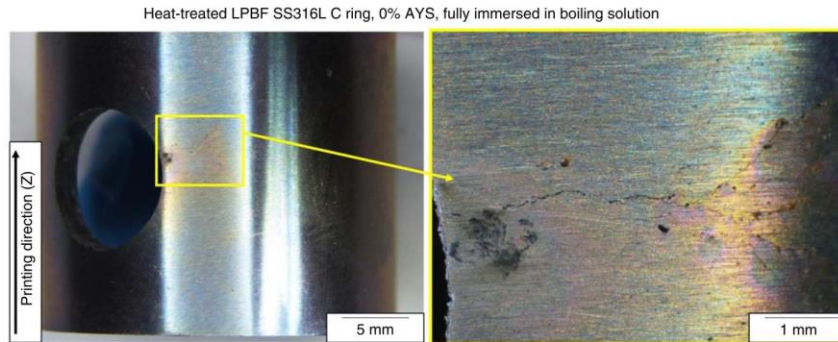


FIGURE 11. Photographs of an unstressed (0% AYS) stress-relieved LPBF SS316L C ring after full immersion in boiling solution showing identical SCC morphology and crack location as its as-printed counterparts.

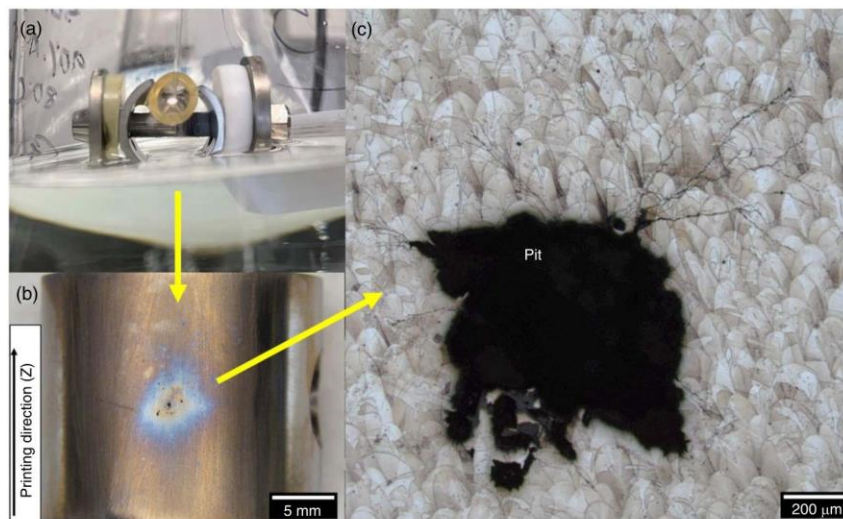


FIGURE 12. As-printed LPBF SS316L C ring stressed at 90% AYS showing (a) its partial immersion setup, (b) SCC located at the middle of its uppermost curved surface, and (c) an etched image showing the resulting transgranular SCC morphology.

Downloaded from <http://meridian.allenpress.com/corrosion/article-pdf/doi/10.5006/431132438504311> pdf by Curtin University user on 03 August 2023



**FIGURE 13.** CD-wrought SS316L 90% C ring showing (a) full immersion setup, (b) photograph illustrating SCC that started from the edge of the uppermost curved surface, and (c) a micrograph showing the resulting transgranular SCC morphology.

pitted area in the fully immersed samples (approximately 0.22%) was, on average, 4 to 5 times higher than the percentage of pitted area in the partially immersed samples (approximately 0.05%). Therefore, considering that the immersed area of the fully immersed sample is about three times larger compared to the partially immersed sample, this suggests that the difference in the immersed surface of the samples had no impact on the distribution of pitting or the onset of cracking.

## DISCUSSION

All LPBF SS316L C rings manufactured with printed supports were consistently susceptible to SCC. Regardless of whether the specimens were stressed (90% AYS) or unstressed (0% AYS), as-printed or heat-treated, they all developed cracks from the same location near the printed holes and perpendicular to the hole/support interface, as illustrated in Figures 7, 8, and 11. All cracks exhibited a highly branched morphology, indicating a similar fracture behavior across the different test conditions and, thus, suggesting the presence of highly localized residual stresses at the cracking sites. The stress relief heat treatment applied to the specimens reduced residual stresses, as evidenced by the KAM maps and distribution shown in Figure 10, as well as the 13% reduction in microhardness. Interestingly, the stress-relieved specimens exhibited a slightly different cracking behavior than their as-printed counterparts, as can be seen in Figures 7 and 11, in which the length of the main crack before branching was around three times longer than in the as-printed condition. Nevertheless, the cracking location remained consistent near the printed holes, indicating that the stress relief process was only partially effective at reducing SCC susceptibility. The surface finish of the printed holes did not play a role in SCC initiation, as evidenced by

Figures 7 and 8, where all cracks occurred in the same location—i.e., from pits located on the polished surface of the C rings and near the printed holes—regardless of the hole's surface roughness. These observations suggested that factors other than the hole's surface roughness, particularly residual stresses, may be influencing the SCC behavior of the LPBF SS316L C rings.

The influence of residual stresses around the printed holes was further demonstrated through partial immersion tests conducted on stressed C rings (90% AYS). As the printed holes were positioned above the solution line, Figure 3, the specimens cracked along the axis of maximum applied stress, Figure 12. This SCC behavior, characterized by highly branched transgranular cracks, was comparable to that observed in CD wrought C rings, Figure 13, although the wrought specimens cracked from the edges instead of the center or the curved surface. The different crack initiation site was attributed to the residual stresses introduced during the machining process of the CD-wrought SS316L C rings.<sup>35,38,69,76-78</sup> These results underscore the significant role of residual stresses in dictating the path of crack propagation, regardless of the manufacturing method used.

The results from the partial immersion tests summarized in Table 3 indicated that the LPBF C rings developed SCC 1 week after the CD wrought samples. Notably, no cracks were observed at the printed holes, confirming the absence of residual stress influencing the SCC of the material at those locations. This apparent marginal improvement in the SCC resistance of the printed material compared to its wrought counterpart could be attributed, for instance, to a delay in pit nucleation and the lower applied stress.<sup>109-110</sup> However, to provide a comprehensive understanding of this phenomenon, further analysis would be

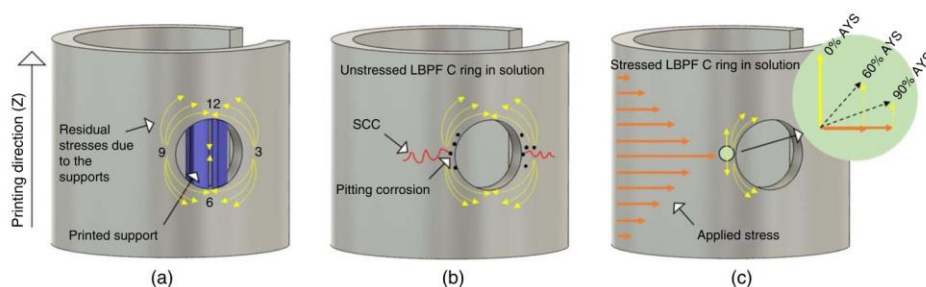


**FIGURE 14.** Hypothesized: (a) residual stresses produced in the hole/support interface of the C rings, (b) unstressed C ring with SCC initiating from corrosion pits at the 3 and 9 o'clock sites, and (c) "stress relieving" effect of the applied load over the residual stresses.

necessary, for instance, by including testing LPBF C rings manufactured at different orientations and specimens with drilled holes instead of printed ones.

It is hypothesized that the hole/support interface, located at the 12 and 6 o'clock positions, as shown in Figure 14, experienced volumetric contraction during the rapid cooling from the melting temperatures during the production of the C rings, resulting in the observed residual stress effect. This phenomenon may have introduced compressive stresses through the supporting structure, forming two additional sites of maximum tensile residual stress at the 3 and 9 o'clock positions, as shown in Figure 14. This stress effect, resembling a "C ring within the C ring" scenario, is believed to be the primary cause of the systematic cracking of the C rings at the 3 and 9 o'clock positions.

Finally, this study found that the SCC susceptibility of the LPBF C rings decreased as the applied stress increased, particularly in the unstressed LPBF C rings, which exhibited faster crack initiation than their stressed counterparts, as reported in Table 3. In the absence of rigorous FEM, which is beyond the scope of this investigation, these unexpected results can be explained using vector analysis. In this regard, the 3 and 9 o'clock positions are the locations of the highest tensile residual stress in unstressed C ring, Figures 14(a) and (b). In contrast, in stressed C rings, Figure 14(c), the stress acts perpendicular to the main component of the residual stress, reducing the magnitude and changing the direction of the stress. This unintentional "stress relieving" effect is hypothesized to have lowered the SCC propensity (measured as a longer crack initiation time) around the printed holes. Nevertheless, as all stressed LPBF C rings continued to crack at their printed holes suggests that the resulting "vector stress" in this area was above the externally applied stress.

## CONCLUSIONS

This study investigated the SCC behavior of LPBF-manufactured SS316L using stressed and unstressed C rings immersed in boiling, 106°C (223°F), 25% NaCl (pH 1.5). The analysis included a stress relief heat treatment and a partial immersion test to elucidate the effect of residual stresses, as well as a comprehensive microstructure characterization to analyze the cracking behavior. The following conclusions were drawn based on the results presented above:

> Localized residual stresses introduced by the printed supports reduced the SCC resistance of SS316L C rings manufactured by LPBF. This observation has important

implications, as it suggests that LPBF-manufactured components with complex geometries that require printed supports may also contain residual stresses, leading to decreased SCC resistance.

> Provided that the effect of residual stresses is mitigated or removed by a stress relief heat treatment, LPBF SS316L had a marginally better SCC resistance than CD wrought SS316L when stressed at 90% of their corresponding AYS values, as determined by a 1 week delay in crack initiation time.

> A stress relief heat treatment improved the SCC resistance of LPBF SS316L. However, more research is needed to determine the degree of improvement that can be achieved and to identify the best temperature and duration of the heat-treatment process.

## ACKNOWLEDGMENTS

The authors acknowledge the financial support of Woodside Energy, as well as the access to the instruments of the Microscopy and Microanalysis Facility (MMF) at Curtin University, and the LPBF SS316L manufactured C rings supplied by IMT Mines Albi, Institut Mines-Telecom in France.

## References

- ASTM52900-21, "Additive Manufacturing—General Principles—Fundamentals and Vocabulary" (Geneva, Switzerland: ISO, 2015).
- L. Yang, K. Hsu, B. Baughman, D. Godfrey, F. Medina, M. Menon, S. Wiener, *Additive Manufacturing of Metals: The Technology, Materials, Design and Production* (New York, NY: Springer, 2017).
- B. Redwood, F. Schöffer, B. Garret, *The 3D Printing Handbook: Technologies, Design and Applications* (Amsterdam, Netherlands: 3D Hubs B.V., 2017).
- M. Attaran, *Bus. Horiz.* 60, 5 (2017): p. 677-688.
- ISO 17296-2:2015, "Additive Manufacturing—General Principles—Part 2: Overview of Process Categories and Feedstock" (Geneva, Switzerland: ISO International, 2015).
- S.D. Jadhav, L.R. Goossens, Y. Kinds, B. Van Hooreweder, K. Vanmeensel, *Addit. Manuf.* 42 (2021): p. 101990.
- H. Miyajima, D. Ma, M.A. Atwater, K.A. Darling, V.H. Hammond, C.B. Williams, *Addit. Manuf.* 32 (2020): p. 100960.
- J. Huang, X. Yan, C. Chang, Y. Xie, W. Ma, R. Huang, R. Zhao, S. Li, M. Liu, H. Liao, *Surf. Coat. Technol.* 395 (2020): p. 125936.
- R. Santamaria, M. Salasi, S. Bakhtiari, G. Leadbeater, M. Iannuzzi, M.Z. Qadir, *J. Mater. Sci.* 57 (2022): p. 1-17.
- D. Karlsson, C.-Y. Chou, N.H. Pettersson, T. Helander, P. Harlin, M. Sahlberg, G. Lindwall, J. Odqvist, U. Jansson, *Addit. Manuf.* 36 (2020): p. 101580.
- J.W. Elmer, J. Vaja, J.S. Carpenter, D.R. Coughlin, M.J. Dvornak, P. Hochanadel, P. Gurung, A. Johnson, G. Gibbs, *Weld. J.* 99, LLNL-JRNL-771645; LA-UR-19-23147 (2020).

12. E. Liverani, S. Toschi, L. Ceschini, A. Fortunato, *J. Mater. Process. Technol.* 249 (2017): p. 255-263.
13. Z. Lin, K. Song, X. Yu, *J. Manuf. Process.* 70 (2021): p. 24-45.
14. B. Dutta, F.S. Froes, *Met. Powder Rep.* 72, 2 (2017): p. 96-106.
15. D. Zhang, D. Qiu, M.A. Gibson, Y. Zheng, H.L. Fraser, D.H. StJohn, M.A. Easton, *Nature* 576, 7785 (2019): p. 91-95.
16. M.Y. Mendoza, P. Samimi, D.A. Brice, B.W. Martin, M.R. Rolchigo, R. LeSar, P.C. Collins, *Metall. Mater. Trans. A* 48, 7 (2017): p. 3594-3605.
17. N.T. Aboulkhair, M. Simonelli, L. Parry, I. Ashcroft, C. Tuck, R. Hague, *Prog. Mater. Sci.* 106 (2019): p. 100578.
18. E. Louvis, P. Fox, C.J. Sutcliffe, *J. Mater. Process. Technol.* 211, 2 (2011): p. 275-284.
19. L. Pantélev, D. Koutrný, D. Paloušek, J. Kaiser, *Mater. Sci. Forum* 891 (2017): p. 343-349.
20. C.Y. Yap, H.K. Tan, Z. Du, C.K. Chua, Z. Dong, *Rapid Prototyp. J.* 23 (2017): p. 750-757.
21. L.N. Carter, C. Martin, P.J. Withers, M.M. Attallah, *J. Alloys Compd.* 615 (2014): p. 338-347.
22. E. Martin, A. Natarajan, S. Kottilingam, R. Batmaz, *Addit. Manuf.* 39 (2021): p. 101894.
23. S.C. Altiparmak, B. Xiao, *J. Manuf. Process.* 68 (2021): p. 728-738.
24. A.J. Pinkerton, *Opt. Laser Technol.* 78 (2016): p. 25-32.
25. C. Fredriksson, *Proc. Manuf.* 33 (2019): p. 139-144.
26. A.J. Sheoran, H. Kumar, P.K. Arora, G. Moona, *Proc. Manuf.* 51 (2020): p. 663-670.
27. T.D. Ngo, A. Kashani, G. Imbalzano, K.T. Nguyen, D. Hui, *Compos. B Eng.* 143 (2018): p. 172-196.
28. P. Marshall, *Austenitic Stainless Steels: Microstructure and Mechanical Properties* (New York, NY: Springer Science & Business Media, 1984).
29. A. Di Schino, ed., in *Manufacturing and Applications of Stainless Steels*, vol. 10 (Basel, Switzerland: MDPI, 2020), p. 327.
30. A. Outokumpu Stainless, *Avesta Resarch Centre, Avesta, Sweden* (2013).
31. M.F. McGuire, *Stainless Steel for Design Engineers* (Materials Park, OH: ASM International, 2008).
32. R.C. Newman, in *Corrosion Mechanisms in Theory and Practice* (Boca Raton, FL: CRC Press, 2011), p. 511-556.
33. R.H. Jones, *Stress-Corrosion Cracking: Materials Performance and Evaluation*, ed. R.H. Jones (Materials Park, OH: ASM International, 2017).
34. H.J. Russell, *Stress Corrosion Cracking* (Materials Park, OH: ASM International, 1992).
35. W. Zhang, K. Fang, Y. Hu, S. Wang, X. Wang, *Corros. Sci.* 108 (2016): p. 173-184.
36. S. Ghosh, "Effect of Surface Working Operations on Electrochemical Corrosion and Susceptibility to Stress Corrosion Cracking of 304L Stainless Steel" (Doctoral thesis diss., Homi Bhabha National Institute, 2012), p. 157.
37. S.G. Acharyya, A. Khandelwal, V. Kain, A. Kumar, I. Samajdar, *Mater. Charact.* 72 (2012): p. 68-76.
38. S. Wang, Y. Hu, K. Fang, W. Zhang, X. Wang, *Corros. Sci.* 126 (2017): p. 104-120.
39. D.A. Jones, *Principles and Prevention of Corrosion, New International Edition*, 2nd ed. (Essex, England: Pearson, 1996).
40. R.C. Newman, "Stress-Corrosion Cracking Mechanisms," *Corrosion Technology*, vol. 17 (New York, Basel, 2002), p. 399-450.
41. E. McCafferty, *Introduction to Corrosion Science* (New York, NY: Springer Science & Business Media, 2010).
42. D. Spencer, M. Edwards, M. Wenman, C. Tsitsios, G. Scatigno, P. Chard-Tuckey, *Corros. Sci.* 88 (2014): p. 76-88.
43. J. Suryawanshi, K.G. Prashanth, U. Ramamurthy, *Mater. Sci. Eng. A* 696 (2017): p. 113-121.
44. R. Casati, J. Lemke, M. Vedani, *J. Mater. Sci. Technol.* 32, 8 (2016): p. 738-744.
45. Y.n. Song, Q. Sun, K. Guo, X. Wang, J. Liu, J. Sun, *Mater. Sci. Eng. A* 793 (2020): p. 139879.
46. T. Ronneberg, C.M. Davies, P.A. Hooper, *Mater. Des.* 189 (2020): p. 108481.
47. T. DebRoy, H.L. Wei, J.S. Zuback, T. Mukherjee, J.W. Elmer, J.O. Milewski, A.M. Beese, A. Wilson-Heid, A. De, W. Zhang, *Prog. Mater. Sci.* 92 (2018): p. 112-224.
48. M. Ma, Z. Wang, X. Zeng, *Mater. Sci. Eng. A* 685 (2017): p. 265-273.
49. N. Diaz Vallejo, C. Lucas, N. Ayers, K. Graydon, H. Hyer, Y. Sohn, *Metals* 11, 5 (2021): p. 832.
50. Y. Tsutsumi, T. Ishimoto, T. Oishi, T. Manaka, P. Chen, M. Ashida, K. Doi, H. Katayama, T. Hanawa, T. Nakano, *Addit. Manuf.* 45 (2021): p. 102066.
51. L. Bian, N. Shamsaei, J.M. Usher, *Laser-Based Additive Manufacturing of Metal Parts: Modeling, Optimization, and Control of Mechanical Properties* (Boca Raton, FL: CRC Press, 2017).
52. A. Woźniak, M. Adamiak, G. Chladek, J. Kasperski, *Arch. Metall. Mater.* 65 (2020): p. 73-80.
53. Q. Chao, S. Thomas, N. Birbilis, P. Cizek, P.D. Hodgson, D. Fabijanic, *Mater. Sci. Eng. A* 821 (2021): p. 141611.
54. T. Kurzynowski, K. Gruber, W. Stopyra, B. Kuznicka, E. Chlebus, *Mater. Sci. Eng. A* 718 (2018): p. 64-73.
55. V.B. Vukkum, J. Christudasjustus, A.A. Darwish, S.M. Storck, R.K. Gupta, *npj Mater. Degrad.* 6, 1 (2022): p. 2.
56. C. Man, C. Dong, T. Liu, D. Kong, D. Wang, X. Li, *Appl. Surf. Sci.* 467-468 (2019): p. 193-205.
57. M.H. Shaeri Karimi, M. Yeganeh, S.R. Alavi Zaree, M. Eskandari, *Opt. Laser Technol.* 138 (2021): p. 106918.
58. G. Sander, S. Thomas, V. Cruz, M. Jurg, N. Birbilis, X. Gao, M. Brameld, C.R. Hutchinson, *J. Electrochem. Soc.* 164, 6 (2017): p. C250-C257.
59. P. Dong, F. Vecchiato, Z. Yang, P.A. Hooper, M.R. Wenman, *Addit. Manuf.* 40 (2021): p. 101902.
60. P. Bian, J. Shi, Y. Liu, Y. Xie, *Opt. Laser Technol.* 132 (2020): p. 106477.
61. R.J. Williams, F. Vecchiato, J. Kelleher, M.R. Wenman, P.A. Hooper, C.M. Davies, *J. Manuf. Process.* 57 (2020): p. 641-653.
62. A.S. Wu, D.W. Brown, M. Kumar, G.F. Gallegos, W.E. King, *Metall. Mater. Trans. A* 45, 13 (2014): p. 6260-6270.
63. N. Alharbi, *Int. J. Adv. Manuf. Technol.* 119, 3 (2022): p. 2285-2299.
64. T. Magnin, A. Chambreuil, B. Bayle, *Acta Mater.* 44, 4 (1996): p. 1457-1470.
65. D. Kong, C. Dong, X. Ni, X. Li, *npj Mater. Degrad.* 3, 1 (2019): p. 24.
66. X-q. Ni, D.-c. Kong, Y. Wen, L. Zhang, W.-h. Wu, B.-b. He, L. Lu, D.-x. Zhu, *Int. J. Miner. Metall. Mater.* 26 (2019): p. 319-328.
67. Y. Liu, Y. Yang, D. Wang, *Int. J. Adv. Manuf. Technol.* 87 (2016): p. 647-656.
68. X. Lou, M. Song, P.W. Emigh, M.A. Othon, P.L. Andresen, *Corros. Sci.* 128 (2017): p. 140-153.
69. A. Yazdanpanah, M. Franceschi, G. Bergamo, M. Bonesso, M. Dabalà, *Eng. Fail. Anal.* 136 (2022): p. 106192.
70. C.R. Bryan, R.P.M. Dingreville, D. Enos, "Estimating Bounding Corrosion Pit Sizes on Stainless Steel SNF Interim Storage Canisters," Sandia National Lab. (SNL-NM), report no. SAND2016-10823C, 2016.
71. U. Martin, D.M. Bastidas, *Eng. Fail. Anal.* 147 (2023): p. 107159.
72. D.A. Horner, B.J. Connolly, S. Zhou, L. Crocker, A. Turnbull, *Corros. Sci.* 53, 11 (2011): p. 3466-3485.
73. R. Katona, E. Karasz, R. Schaller, *Corrosion* 79, 1 (2023): p. 72-96.
74. X-g. Huang, J.-q. Xu, *J. Zhejiang Univ. Sci. A* 14, 4 (2013): p. 292-299.
75. B.Y. Fang, R.L. Eadie, W.X. Chen, M. Elboudjaini, *Corros. Eng. Sci. Technol.* 45, 4 (2010): p. 302-312.
76. A. Yazdanpanah, M. Lago, C. Gennari, M. Dabalà, *Metals* 11, 2 (2021): p. 327.
77. A. Yazdanpanah, F.R. Biglari, A. Fallahi Arezoodar, M. Dabalà, *Corros. Eng. Sci. Technol.* 56, 1 (2021): p. 81-92.
78. A. Turnbull, K. Mingard, J.D. Lord, B. Roebuck, D.R. Tice, K.J. Mottershead, N.D. Fairweather, A.K. Bradbury, *Corros. Sci.* 53, 10 (2011): p. 3398-3415.
79. J. Hajnys, M. Pagáč, J. Měsíček, J. Petru, M. Król, *Materials* 13, 7 (2020): p. 1659.
80. X. Yan, J. Pang, Y. Jing, *Materials* 12, 17 (2019): p. 2719.
81. E. Malekipour, H. El-Mounayri, "Scanning Strategies in the PBF Process: A Critical Review," *ASME International Mechanical Engineering Congress and Exposition (New York, NY: American Society of Mechanical Engineers, 2020)*, p. V02AT02A055.
82. P. Pant, *Residual Stress Distributions in Additively Manufactured Parts: Effect of Build Orientation*, vol. 1869 (Linköping, Sweden: Linköping University Electronic Press, 2020).
83. M. Kumaran, V. Senthilkumar, T. Sathies, C.T. Justus Panicker, *Mater. Lett.* 313 (2022): p. 131766.

84. M. Kamariah, W. Harun, N. Khalil, F. Ahmad, M. Ismail, S. Sharif, *IOP Conf. Ser.* 257 (2017): p. 012021.
85. K. Burdová, H. Jirková, L. Kučerová, I. Zetková, J. Mach, *Manufac. Technol.* 22, 3 (2022): p. 261-266.
86. S. Leuders, T. Lieneke, S. Lammers, T. Tröster, T. Niendorf, *J. Mater. Res.* 29, 17 (2014): p. 1911-1919.
87. T. Gundgire, T. Jokiah, S. Santa-aho, T. Rautio, A. Järvenpää, M. Vippola, *Mater. Charact.* 191 (2022): p. 112162.
88. N. Kalentics, E. Boillat, P. Peyre, C. Gorny, C. Kenel, C. Leinenbach, J. Jhabvala, R.E. Logé, *Mater. Des.* 130 (2017): p. 350-356.
89. N. Kalentics, E. Boillat, P. Peyre, S. Čirić-Kostić, N. Bogojević, R.E. Logé, *Addit. Manufac.* 16 (2017): p. 90-97.
90. M.F. McGuire, *Stainless Steels for Design Engineers* (Materials Park, OH: ASM International, 2008).
91. G.E. Dieter, D.J. Bacon, *Mechanical Metallurgy*, vol. 3 (New York, NY: McGraw-Hill, 1976).
92. W.D. Callister, D.G. Rethwisch, A. Blicblau, K. Bruggeman, M. Cortie, J. Long, J. Hart, R. Marceau, M. Ryan, R. Parvizi, *Materials Science and Engineering: An Introduction* (New York, NY: John Wiley, & Sons, 2021).
93. ASTM A276-13a, "Standard Specification for Stainless Steel Bars and Shapes" (West Conshohocken, PA: ASTM International, 2015).
94. ASTM E8/E8M-22, "Standard Test Methods for Tension Testing of Metallic Materials" (West Conshohocken, PA: ASTM International, 2016).
95. ASTM E111-17, "Standard Test Method for Young's Modulus, Tangent Modulus, and Chord Modulus" (West Conshohocken, PA: ASTM International, 2017).
96. ASTM E384-17, "Standard Test Method for Microindentation Hardness of Materials" (West Conshohocken, PA: ASTM International, 2017).
97. ASTM B962-17, "Standard Test Methods for Density of Compacted or Sintered Powder Metallurgy (PM) Products Using Archimedes' Principle" (West Conshohocken, PA: ASTM International, 2017).
98. ASTM G123-0, "Standard Test Method for Evaluating Stress-Corrosion Cracking of Stainless Steel Alloys with Different Nickel Content in Boiling Acidified Sodium Chloride Solution" (West Conshohocken, PA: ASTM International, 2015).
99. ASTM G38-01, "Standard Practice for Making And Using C-ring Stress-Corrosion Test Specimens" (West Conshohocken, PA: ASTM International, 2013).
100. H.M. Ledbetter, *J. Appl. Phys.* 52, 3 (1981): p. 1587-1589.
101. ASTM G15-06, "Standard Terminology Relating to Corrosion and Corrosion Testing" (West Conshohocken, PA: ASTM International, 2010).
102. ASTM A479, "Standard Specification for Stainless Steel Bars and Shapes for Use in Boilers and Other Pressure Vessels" (West Conshohocken, PA: ASTM International, 2021).
103. S. Ghosh, V.P.S. Rana, V. Kain, V. Mittal, S.K. Baveja, *Mater. Des.* 32, 7 (2011): p. 3823-3831.
104. M. Tong, X. Di, C. Li, D. Wang, *Mater. Charact.* 144 (2018): p. 631-640.
105. M. Calcagnotto, D. Ponge, E. Demir, D. Raabe, *Mater. Sci. Eng. A* 527, 10-11 (2010): p. 2738-2746.
106. W. Xing, M. Yin, Q. Lv, Y. Hu, C. Liu, J. Zhang, in *Rotating Electrode Methods and Oxygen Reduction Electrocatalysts*, eds. W. Xing, G. Yin, J. Zhang (Amsterdam, Netherlands: Elsevier, 2014), p. 1-31.
107. S. Huzni, M. Ridha, A.K. Ariffin, *Key Eng. Mater.* 462-463 (2011): p. 194-199.
108. D.Y. Jang, T.R. Watkins, K.J. Kozaczek, C.R. Hubbard, O.B. Cavin, *Wear* 194, 1 (1996): p. 168-173.
109. Q. Chao, V. Cruz, S. Thomas, N. Birbilis, P. Collins, A. Taylor, P.D. Hodgson, D. Fabijanic, *Scr. Mater.* 141 (2017): p. 94-98.
110. G. Sander, S. Thomas, V. Cruz, M. Jurg, N. Birbilis, X. Gao, M. Brameld, C. Hutchinson, *J. Electrochem. Soc.* 164, 6 (2017): p. C250.